LBL-26537 c.2

Lawrence Berkeley Laboratory

UNIVERSITY OF CALIFORNIA

RECEIVED
SEP 1 9 1989
DOCUMENTS SECTION

Materials & Chemical Sciences Division

Reaction of Oxygen with Allene

S. Huang
(Ph.D. Thesis)

July 1988

TWO-WEEK LOAN COPY

This is a Library Circulating Copy which may be borrowed for two weeks.

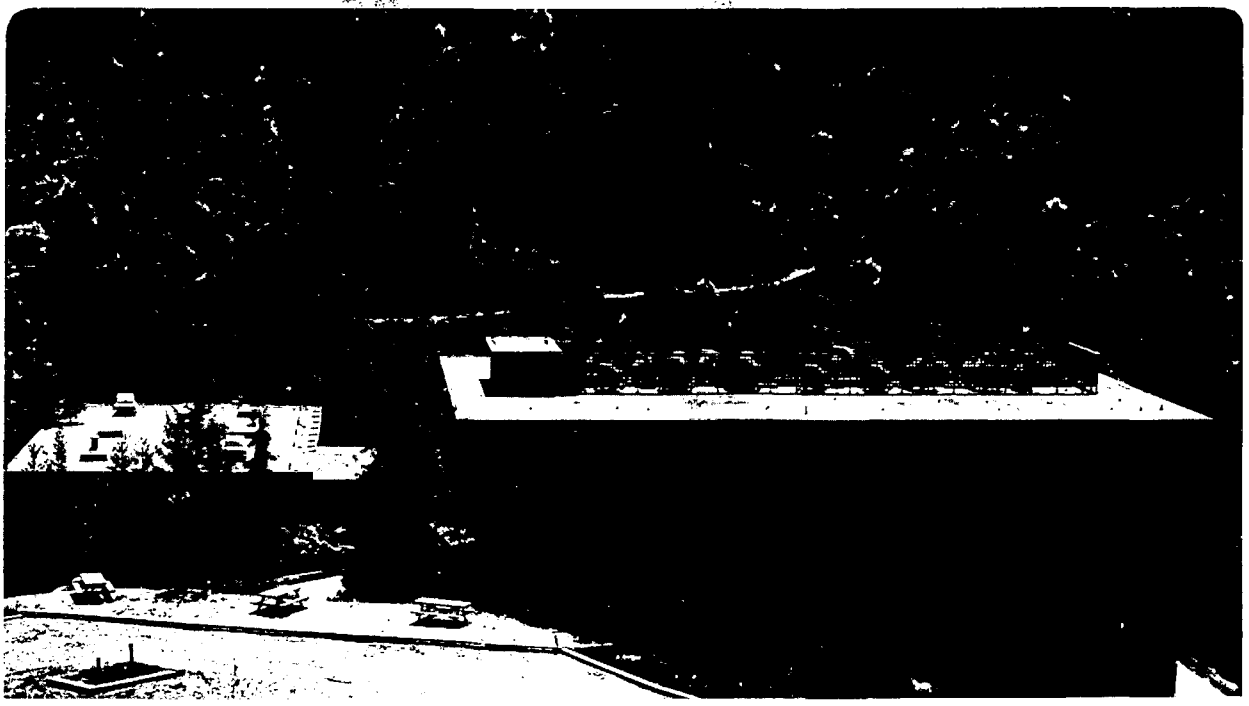

LBL-26537 c.2

Prepared for the U.S. Department of Energy under Contract Number DE-AC03-76SF00098.

DISCLAIMER

This document was prepared as an account of work sponsored by the United States Government. While this document is believed to contain correct information, neither the United States Government nor any agency thereof, nor the Regents of the University of California, nor any of their employees, makes any warranty, express or implied, or assumes any legal responsibility for the accuracy, completeness, or usefulness of any information, apparatus, product, or process disclosed, or represents that its use would not infringe privately owned rights. Reference herein to any specific commercial product, process, or service by its trade name, trademark, manufacturer, or otherwise, does not necessarily constitute or imply its endorsement, recommendation, or favoring by the United States Government or any agency thereof, or the Regents of the University of California. The views and opinions of authors expressed herein do not necessarily state or reflect those of the United States Government or any agency thereof or the Regents of the University of California.

LBL-26537

Reaction of Oxygen with Allene

Sheng-yu Huang
(Ph.D. Thesis)

Department of Chemistry
University of California
and
Materials and Chemical Sciences Division
Lawrence Berkeley Laboratory
1 Cyclotron Road
Berkeley, California 94720

July 1988

Supported by the U.S. Department of Energy under Contract Number DE-AC03-76SF00098.

Reaction of Oxygen with Allene

Sheng-yu Huang

ABSTRACT

Elastic scattering studies carried out independently of the work related to the title forms the first section of the dissertation. The low-energy elastic scattering of He with Ar, Kr, Xe has been studied by molecular beam techniques. Using a specially designed beam source the experiments were carried out at nozzle temperatures of 15.2 K and 35.7 K for He + Ar, 25.5 K for He + Kr, 15.2 K and 35.7 K for He + Xe. Two potential forms, exponential-spline-Morse-Morse-spline-van der Waals (ESMMSV) and Simon-Parr-Finlan-Dunham (SPFD), have been used to fit the measured differential cross section. The intermolecular potentials parameters determined from experiments ϵ and r_m (well depth and equilibrium separation) are: 32.83 K and 3.469 Å for He + Ar, 34.46 K and 3.671 Å for He + Kr, 35.2 K and 3.92 Å for He + Xe. Elastic scattering theory and experimental details are introduced.

The reactive scattering of $O(^3P)$ with allene has been studied using crossed molecular beams. Differing from the well known central-carbon-attack (CCA) mechanism in which the final products, carbon monoxide and ethylene, are obtained via a ring intermediate, a new mechanism, terminal-carbon-attack (TCA), has been observed. Under 5-8 kcal/mole collision energy the identified products are allenyloxy radicals and hydrogen atoms. The production of $O(^3P)$ atoms by radio frequency discharge is also introduced.

To assist understanding of the experiments a multi-configuration self-consistent-

field (MCSCF) study of the reaction of $O(^3P)$ with allene has been carried out. The key feature of the oxygen-allene potential energy surface for both CCA and TCA channels has been calculated with single-zeta (SZ), double-zeta (DZ), and double-zeta plus polarization (DZP) basis sets. In the CCA channel, a triplet intermediate, oxyallyl, possessing planar geometry and lying 23.52 kcal/mole lower in energy than the reactant has been found. On the triplet surface, the barrier for the CCA channel is 16.68 kcal/mole and the barrier for the TCA channel is 27 kcal/mole. The interesting behavior of the diradicals, which are general intermediates in reaction of oxygen with unsaturated hydrocarbons, have been studied in both CCA and TCA channels. Many near-degenerate states with different symmetries and spin multiplets are found. Transitions between many of these states are facilitated by inter-system crossing via the spin-orbit interaction.

Finally, an algorithm for optimizing the trial wavefunction in quantum Monte Carlo calculations has been developed. With the application of group theory, a symmetry-constrained optimization process can yield an improved trial wavefunction for the calculation of excited electronic state energies as well as the ground-state energy. Several applications are discussed.

Table of Contents

Acknowlegements v

Part One: Experimental Study

I. Crossed Molecular Beam Technique 1

Figure 6

II. Low-Energy Elastic Study of He + Ar (Kr, Xe)

A. Introduction 7

B. Scattering Theory

1. Classical Mechanics 10

2. Partial Wave Method and the Phase Shift 13

3. Perturbation Model 15

C. Experiment

1. Beam Sources 20

2. Experimental Condition 22

3. Zero Degree Angle Offset 25

D. Measured DFCS and Potential Fittings

1. Potential Forms 27

2. Data and Fitting 31

3. Analysis and Discussion 33

Appendix 1: Classical Trajectory Calculation 36

Appendix 2: Computal Program for Zero Degree Offset 38

References 40

Tables 42

Caption and Figures 60

III. Reactive Scattering of $O(^3P) + C_3H_4$

A. Introduction 84

B. Oxygen Beam Source

1. Radio Frequency Discharge 88

2. Plasma Mechanism

a. Low Pressure Ignition 90

b. Hot Plasma and Critical Phenomenon 94

c. Inductive Discharge 96

3. Operation of Apparatus

a. Matching 100

b. Non-resistive Matching 102

c. Resistive Matching 105

d. Trouble-shooting 106

C. Preliminary Experiment 109

Appendix: Butch's Theorem 112

References 114

Tables 116

Caption and Figures 118

Part Two: Theoretical Study

IV. MCSCF Study of $O(^3P) + C_3H_4$

A. Introduction 131

B. Allene 134

C. CCA Channel 136

D. Singlet Cyclopropanone and Triplet Oxyallyl 138

E. TCA Channel 142

F. Allenyloxy Radicals 147

G. Intersystem Crossing

1. Spin-Orbital Interaction 149

2. Resonance Structure of Radicals 152

3. Conclusion 153

H. Summary 154

References 156

Tables 160

Caption and Figures 170

V. Optimized Trial Functions for Quantum Monte Carlo

A. Introduction 187

B. Quantum Monte Carlo Method 190

C. Optimization

1. Correlation Function 193

2. Virial Theorem 195

3. Algorithm 200

D. Symmetry Restrained by Group Theory

1. Projection Operator: Point Group 203

2. Projection Operator: Permutational Group 205

E. Application to H_4 207

F. Summary 208

Appendix 1: Molecular Orbitals and Projection Operator for Pyramidal H_4 209

Appendix 2: H_4 Wavefunction from Permutation Group Projection Operator 212

References 214

Tables 218

Caption and Figures 225

Acknowledgements

First of all, I would like to thank my adviser, Professor William A. Lester Jr., who provided me the opportunity to study theoretical chemistry. I have had many pleasant times in his group and many helpful discussions. Especially, he has given me much encouragment and guidance in my scientific studies. His rigorous scientific approach, a broad knowledge of information, and the judgment has deep influnce in my learning to do research.

I also would like to thank Professor Yuan T. Lee who provided me the opportunity of the experimental study with molecular beams. He helps every student in technique detail and gives a precise advise in need. His great intelligence, remarkable memory, and very energetic working style set an example for me in achieving success in scientific career.

During my stay in Berkeley, I have received the help from a dozens of graduate students and post-doctoral fellows. Among them, I would like to thank Anne-Marie Schmolter, my co-worker of experimental study. She spent much time reading each chapter of this dissertation, knew very well what I wanted to express, and gave me many good suggestions. I also want to thank Dr. Peter Felder, Dr. Jan ven der Biensen, Dr. Mathu Vernon for their helps in elastic scattering study, and R. Bruzynski for reactive scattering study. During my theoretical studies, Brian Hammond is the first person who showed me how to do *ab initio* calculations. Chris Dateo helped me a lot in using the HONDO code. I also want to thank the other members of the Lester group, Dr. Peter Reynolds, Dr. Randy Grimes, Kent

Owen, Robert Barnett. Finally, I want to thank my co-worker, Dr. Zhiwei Sun, who did the programming of the QMC optimization.

PART ONE:

Experimental Study

Chapter I. Crossed Molecular Beam Technique

The development of the crossed molecular beam technique has deeply changed the study of chemical kinetics. It provides an opportunity to "look" at the dynamic picture at the molecular collision level. It separates the elementary process from many complicated and fast chemical reactions, and makes these processes observable and measureable. It removes many ambiguities with clear evidence. It gives a precise quantitative measurement under well-defined conditions. This technique has been widely applied to elastic, inelastic, chemical reaction, and photochemical studies. The experimental studies in this thesis: (1) intermolecular potential of rare gases, (2) combustion reaction of oxygen with allene are two of these examples.

The basic idea of this technique is to establish a vacuum environment in which the mean free path is large enough to prevent secondary collisions, to generate two high intensity and well defined molecular beams of interest which cross at a right angle, and a sophisticated detector system to measure intensity, velocity, and angular distribution. Figure 1.1 is a typical schematic diagram of a molecular beam machine. The two beams (He and Ar) are triply differential pumped before they cross in the main chamber ($p \approx 10^{-6} - 10^{-7}\tau$). The two beams are first collimated by a skimmer and the divergence angles (He, 1.0° and Ar, 1.8°) are finally defined by two slits which are placed at the entrances of the main chamber. Notice that the secondary beam (Ar) is usually positioned closer to the collision center in order to obtain higher intensity signal. A tuning fork chopper (CP,f = 150 hz) is used to modulate the secondary beam, the comparison of two channels, beam blocked and

unblocked, eliminates the background noise. A rotatable quadrupole mass spectometer (DT) provides an angular measurement and also a velocity measurement combined with a time-of-flight (TOF) technique. The detector is also triply pumped but to an even lower pressure ($10^{-10}\tau$) than the main chamber's.

Several universal molecular beam machines of differing sizes, and a rotating source machine have been designed and manufactured in the Y. T. Lee group to meet various needs. All the machines consist of four parts: (1) main body with pumping system; (2) beam sources; (3) detector; and (4) electronic display and controller. The present paper will not discuss parts (1), (3), and (4) since the details are well described elsewhere.[1] I present here a brief discussion about beam sources.

The most convenient feature desired is that the beam source be easily removable. This provides flexibility and room to develop beam sources for various purposes. It could be as simple as a tube with a nozzle at the end. It could also be a complex structure. For instance,

1. *Low-temperature*: It can be achieved by a simple liquid nitrogen cooled heat exchanger (77 - 150 K, Ar source), or as complicate as a commercial refrigerator cooling system consisting of a helium compressor, an expander used to cool the beam (7 - 77 K, He source), and a temperature controller.

2. *High temperature*: It can be achieved using heating wires or microwave radiation.

3. *Excited states*: A laser beam can be used to cross the molecular beam before

it reaches the collision center. The molecules are pumped to excited electronic states, ions, or led to dissociate.

4. *Plasma*: Oxygen atoms can be generated in a hot plasma by applying a radio-frequency (RF) discharge. A coil and a capacitor form a LC discharge circuit. A RF generator, a linear amplifier (LA), and an interlock are needed to assemble such an aparatus. Both the coil and the quartz tube containing the plasma are water-cooled. (there will be a more detail description in Chapt. III)

Two major measurements are usually carried out:

(1) Angular distribution: DT can be rotated within an angular range (-10° to 110°) with regard to the primary beam, and the scattered molecules can be detected by mass spectrometer. By a laboratory-to-center-of-mass (LAB-CM) coordinate transformation the differential cross section (DFCS) of elastic, inelastic, or reactive scattering can be obtained.

(2) Time-of-flight: By placing a rotating slotted disk (frequency = 400 hz) in front of the the detector entrance a time-of-flight (TOF) distribution is obtained which can be converted to a velocity distribution.

With these measurements the following results can be obtained:

(1) Intermolecular potential by the anlysis of the DFCS of elastic scttering.

(2) Reactive products identification and reaction channel determination.

(3) Reaction entrance and exit barrier.

(4) Reaction products translational energy. By comparing with the total energy of reactants one gets the partition of energies among the product's degrees of

freedom.

(5) The life-time of intermediate complex relative to the rotational period by analyzing a 2-dimensional angular distribution. The symmetric contour map may indicate a thoroughly randomizing before dissociation.

Many physical and geometric factors can be varied to optimize experimental conditions. For instance, a large collision volume results in higher signal, but decreased resolution. High intensity beams (using a big nozzle aperture, or high stagnation pressure) yields a stronger signal, but the intensity is limited by the pumping speed. The tuning fork chopper may lead the beam opening to the main chamber at only half time while detector is counting. Also, the pulsed nozzles allow higher instantaneous beam intensity at the same overall pumping load.

Another difficulty is stability of the experimental condition. In the elastic scattering of He + Ar, for example, a scanning angular distribution measurement needs 30 seconds for each point at the small angle range, and 300 seconds for the large angle range. Since the detector rotation and data recording are done manually and many scans are needed to improve the signal-to-noise ratio, the whole measurement (100 points scanned 5 times each) for one collision energy lasts more than 30 hours. During this long time, changes of temperature or stagnation pressure might occur, or one of the nozzles might be clogged by some impurity. Any systematic shift may also cause errors or, at least, uncertainty in the results. Increasing the counting time can reduce the error bar according to a square root relation, but it also increases the chance of fluctuation and accidant. As an improvement, computer

program control and automatic recording would be one possible way to reduce the experimental time. Another improvement that could be done is to design an easier installation of equipments when the experiment is frequently switched from angular distribution measurement to TOF measurement. The present procedure requires venting the machine and re-pumping repeatedly. It causes the disadvantages in two aspects: long waiting time and the risk of disturbing experimental condition. In a newly designed rotating source machine the equipment switching can be done without venting. It certainly helps a lot for efficiently using this technique.

Chapter II. Low-Energy Elastic Scattering Study of He + Ar (Kr, Xe)

A. Introduction

The difficulty in determining the well-depth ϵ and the equilibrium distance r_m of the intermolecular potential between helium and other noble gases is the very weak van der Waals interaction. Using second-order perturbation theory the long-range force coefficients C_6 (dipole-dipole interaction), C_8 (dipole-quadrupole interaction), and C_{10} (quadruploe-quadrupole and dipole-octupole interaction) can be calculated accurately.[2] But the computational accuracy of very sophisticated *ab initio* calculation with heavy atoms, such as Ar, Kr, Xe, fails to match the demand of less than 0.06 kcal/mole which is a general scale for the well depth of an intermolecular potential involving He. Thermodynamic transport properties measurement provides a good test of a given potential, but by no means allows the determination of potential by inversion. Scattering experiments seem the best way to "measure" the ϵ and r_m since in the advanced molecular beam machine the trajectory bending caused by interaction of molecules within 10^{-8} cm is observable by a high resolution detector. There should be no difficulty for quantum mechanics to simulate the dimensionless atoms collision. The update speedy computer can generate the phase shift up to enough partial waves and calculate an accurate DFCS for comparison with experimental data. The developments in both experimental technique and computal tool make the elastic scattering study be possible and straightforward.

In 1973 Chen *et al.* carried out an elastic scattering experiment[3] involving helium cooled to liquid nitrogen temperature (77 K). The ϵ and r_m obtained by fitting a multiparameter potential to experimental data and second virial coefficients are 24.2 K, * 3.54 Å(He-Ar), 24.7 K, 3.75 Å(He-Kr), 25.2 K, 4.15 Å(He-Xe), respectively. In 1977 Smith *et al.* did both low-energy (0.42 kcal/mole) and high-energy (1.37 kcal/mole) scattering of He + Ar.[4] The ϵ and r_m were determined to be 30.2 K and 3.46 Å. In 1978 Keil *et al.* [5] and later on, Aziz *et al.*[6] did the scattering experiment of He + Ar on a molecular beam machine at room temperature. The results were $\epsilon = 29.4$ K (which is 44% deeper than Keil's) and $r_m = 3.47$ Å, obtained by fitting to the SPFD form[7,8]. (see expression in Sec. D, pp. 28) The collision energy in their experiment was 26.9 times the well depth ϵ. Since the impact under this collision energy is mostly acted on repulsive part of potential rather than attractive well part, an analysis should be done on testifying how much information on the potential well can actually be obtained by scattering at these relatively high collision energy.

Applying a refrigerator-cooled He beam source we have reached a 20 K beam temperature for He (may be the lowest in He + rare gases experiment as we know sofar). Several scatterings for He + Ar, He + Kr, He + Xe under different collision energies have been performed. Before introducing the detail of our low-energy elastic scattering experiment a theoretical background both classical and quantum mechanical is given in Sec. B. A perturbation model is also applied in analyzing the

* The energy unit K (=0.001989 kcal/mole) for shallow well depth will be employed throughout this thesis.

interfering phenomena and testing the effect of potential to the DFCS. The details of the experiment are in Sec. C. The results and analysis are in Sec. D.

B. Scattering Theories

1. Classical

The "quantum effect" of low-energy elastic scattering involving light atoms, such as hydrogen and helium, is not negligible. The *de Broglie* wavelength of helium atoms at 10 K is 2.5 Å, which is dimensionally comparable with the potential well (3 - 5 Å). In such a case, a wave packet description for incident particles rather than particles hitting a certain point of the potential curve is more realistic. In other words, we should treat a phase shift at each point as a contribution by a range of potential curve, and the differential cross section (DFCS) caused by a collective effect. However, a simple classical model is still good enough to understand the experimental DFCS signal, and especially interfering phenomena.

As shown in Fig. 2.1, Ar atom is the target, and the He atom approaches Ar parallel to the z-axis with an impact parameter b (defined as the distance between Z-axis and the the incoming direction line of He atom). Several trajectories with positive deflection angle ($\alpha > 0$) are made by He hitting the repulsive wall (shaded area, V > 0). With larger b ($> 4\mathring{A}$) the trajectory is attractive ($\beta < 0$). Note that there is a trajectory ($\theta = 0$) with a critical impact parameter b_g in which the zero-deflection is made by the net cancellation of attractive and repulsive force of the potential. The interfering between the contribution from b_g and that from non-interaction (b = ∞) usually causes a glory resonance.

Fig. 2.2 shows trajectories at different collision energies: (a) $E_c = \epsilon$; (b) and (c) correspond to our experimental condition in which the He beams are cooled to 20

K ($E_c = 2.32\epsilon$) and 40 K ($E_c = 3.89\epsilon$) respectively (see details in Sec. C.2); and (d) is under room temperature which is the condition of Aziz *et al.*[6] By comparision one may find that the large attractive deflection only occurs at low-energy collision and less features are shown in the trajectory plot at room temperature condition (d).

The deflection function curve vs impact parameter is shown in Fig. 2.3. One should notice that in the attractive region (negative deflection angle) there are two points (b_2 and b_3) which cause the same deflection angle. Assuming a DT is located at a fixed angle θ, in general, there may be three impact parameters (one from the repulsive region, two from the attractive region) which make contributions to the signal at this angle. Interference of these partial waves with different phase shifts it results in an oscillatory angular distribution. Study of this interference may provide the information of both repulsive and attractive well range. Fig. 2.4 shows deflection functions for four collision energies ($E_c = \epsilon$, 2.32ϵ, 3.89ϵ, 26.9ϵ as shown in Fig. 2.2). From these functions one may see that the lower the collsion energy, the wider the negative deflection angle range. For instance, the maximum negative deflection angle at $E_c = 2\epsilon$ is 80° and with $E_c = 10\epsilon$ is only 20°. That means that the signal measured at $E_c = 10\epsilon$ beyond 20° does not contain information on the attractive well.

There are two interesting features at low collision energies:

(1) *orbiting trajectories*: In Fig. 2.4 the $E_c = \epsilon$ curve shows an infinite deflection at b = 5.2 Å. This can be understood as a orbiting trajectory caused

by attactive force of potential. This may happen at lower collision energies (for instance, when b = 6.7 Å at $E_c = 0.18\epsilon$), but does not exist at collision energies higher than 2ϵ.

(2) *discontinuity of the turning point and the phase shift*: The classical turning point is obtained by solving the following equation:

$$\frac{dr}{dt} = \pm v\sqrt{1 - \frac{b^2}{r^2} - \frac{V(r)}{E_c}} = 0 \tag{2.1}$$

The detailed classical trajectory calculation is shown in appendix 1. Here Eq. (2.1) is the same with Eq. (A8). The JWKB[9] phase shift formular is given in Sec. B.2. The JWKB phase shift as a function of impact parameter b with several collision energies is shown in Fig. 2.5. Both formular (2.1) and (2.16) are related to the square root of the following expression

$$B(r) = 1 - \frac{b^2}{r^2} - \frac{V(r)}{E_c} \tag{2.2}$$

When E_c is larger than 0.83ϵ B(r) has always a single root. But when the collision energy is less than $0.83epsilon$ the problem becomes complicated. Fig. 2.7 shows a B(r) function for several b at $E_c = 0.18\epsilon$. At b = 7.68 Å the second root occurs at r = 5.6 Å. Therefore the turning point suddenly jumps from 3.25 to 5.6 Å because a negative B(r) is forbidden. The calculated phase shift has a discontinuity at this critical point. Tab. 2.1 shows all the critical points with several E_cs less than 0.83ϵ. It would be interesting to observe this discontinuity experimentally. But unfortunately our experiment can not reach the E_c below 2ϵ sofar.

2. Partial Wave Method and the Phase Shifts

A scattering problem can be described by a two-body Schrödinger equation[10,11]

$$(-\frac{1}{2\mu}\nabla^2 + U)\Psi = E\Psi \tag{2.3}$$

where $\mu = m_1 m_2/(m_1 + m_2)$ is the reduced mass of the two particles which collide with each other, and U is the intermolecular potential. The incident particles may be described by a plane wave function

$$\Psi_1 = Ae^{ikz} \tag{2.4}$$

and the outgoing particles may be written as a outgoing spherical wave function

$$\Psi_2 = f(\theta)\frac{e^{ikr}}{r} \tag{2.5}$$

Asymptotically the wavefunction

$$\Psi = \Psi_1 + \Psi_2 \tag{2.6}$$

It is easy to prove[8] that the amplitude $f(\theta)$ is simply related to DFCS by

$$\frac{d\sigma}{d\Omega} = \mid f(\theta) \mid^2 \tag{2.7}$$

To solve Eq. (2.3) one may expand Ψ in partial waves

$$\Psi(r,\theta,\phi) = \sum_{l=0}^{\infty} R_l(r) Y_{lm}(\theta,\phi). \tag{2.8}$$

Due to the cylindrical symmetry with Z-axis the ϕ dependence can be eliminated

$$\Psi(r,\theta) = \sum_{l=0}^{\infty} R_l(r) P_l(cos\theta) \tag{2.9}$$

Eq. (2.3) can be written as

$$\frac{1}{r}\frac{d}{dr}(r^2\frac{dR_l(r)}{dr}) + (k^2 - V(r) - \frac{l(l+1)}{r^2})R_l(r) \;=\; 0 \tag{2.10}$$

The solution in the asymptotic region approaches

$$\Psi(r,\theta) \underset{r\to\infty}{\longrightarrow} \sum_{l=0}^{\infty} \frac{A_l'}{r} sin(kr + \delta_l')P(cos\theta) \;=\; \frac{A_l sin(kr - \frac{1}{2}l\pi + \delta_l)}{kr} \tag{2.11}$$

where $A_l \;=\; kA_l'$ and $\delta_l \;=\; \delta_l' + \frac{1}{2}l\pi$. Also, expanding Ψ_1 in partial waves as well

$$e^{ikz} \;=\; e^{ikr\ cos\theta} \;=\; \sum_{l=0}^{\infty}(2l+1)i^l j_l(kr)P_l(cos\theta) \tag{2.12}$$

where

$$j_l(kr) \;=\; \sqrt{\frac{\pi}{2kr}}J_{l+\frac{1}{2}}(kr) \tag{2.13}$$

is the spherical Bessel function of the first kind that asymptotically tends to

$$\frac{1}{kr}sin(kr - \frac{1}{2}l\pi) \tag{2.14}$$

Now substitue Eq. (2.4) (Ψ_1) by partial wave expansion (2.12), and let it tend to the asymptotic form Eq. (2.14). Also add Eq. (2.5) (Ψ_2) with the asymptotic form of Ψ_1 and substitue the sum into Eq. (2.6). By comparing this result with Eq. (2.11),the asymptotic solution of Schrödinger equation (2.10) and using $\sin\alpha \;=\; (e^{i\alpha} - e^{-i\alpha})/2i$ we may get

$$f(\theta) \;=\; \frac{1}{2ki}\sum_{l=0}^{\infty}(2l+1)P_l(cos\theta)(e^{2i\delta_l} - 1) \tag{2.15}$$

where δ_l is partial wave shift. It can be calculated either by exactly solving Schrödinger equation or by the following JWKB[9] formular

$$\delta(k,b) \;=\; k\lim_{R\to\infty}\left(\int_{r_c}^{R}\sqrt{1 - \frac{b^2}{r_2} - \frac{V(r)}{E}}dr \;-\; \int_{b}^{R}\sqrt{1 - \frac{b^2}{r^2}}dr\right) \tag{2.16}$$

where k is the wave number, E is the collision energy, b = (l+1/2)/$\hbar$ is the impact parameter, and r_c is the classical turning point radius.

With a given intermolecular potential V(r), the partial phase shift δ_l can be therefore calculated up to a necessary wave number (60 is good enough for low-energy collision). By using Eqs. (2.15) and (2.7) the DFCS can be evalued at each angle in CM coordinate system. A simple CM-LAB coordinate transform makes it possible for comparison with experimental data.

3. Perturbation Model

In general, it is not appropriate to treat low-energy scattering as a perturbation problem. However, due to the very weak intermolecular potential ($\approx$ 30 K) between He and other rare gas atoms, a first order approximation is good enough to describe many scattering features, such as interference phenomena etc.. Since this is a quantum mechanical model, it gives a better description than the classical model. In the other hand, this model does not go to phase shift calculation as exact Schrödinger solution does but makes a direct link between the potential and the DFCS signal. That makes a more clear picture in understanding the scattering process. Especially, as a simple model, it is useful to test the effects of all potential parameters (ϵ, r_m, etc.) to the DFCS before starting to fit the experimental data.

By first order perturbation consideration the DFCS at each angle can be thought as a transition probability from incident wavefunction and outgoing wave packet at this angle (θ, ϕ)

$$\frac{d\sigma}{d\Omega} = \frac{2\pi}{\hbar} |< i \mid V \mid f >|^2 \tag{2.17}$$

where $< i \mid$ can be written as a plane wave along the Z-axis and the outgoing

wavefunction $| f >$ is deflected by an angle θ (see Fig. 2.7).

$$< i | = \frac{1}{(2\pi\hbar)^{3/2}} exp(-\vec{k}_i \cdot \vec{r}) \tag{2.18.1}$$

$$| f > = \frac{1}{(2\pi\hbar)^{3/2}} exp(\vec{k}_f \cdot \vec{r}) \tag{2.18.2}$$

and in an elastic collision

$$k = | \vec{k}_i | = | \vec{k}_f | \tag{2.19}$$

and

$$K = 2k \cdot sin\frac{\theta}{2} \tag{2.20}$$

By substituting (2.18.1) and (2.18.2) into (2.17)

$$\frac{d\sigma}{d\Omega} = \frac{4\mu^2}{K\hbar^4} | \int_0^\infty r \ sin(Kr) \ U(r) \ dr |^2 \tag{2.21}$$

where

$$U(r) = \frac{\hbar^2}{2\mu} V(r) \tag{2.22}$$

Using the integral formula

$$\int r \ sin(Kr) \ dx = \frac{1}{K^2} sin(Kr) - \frac{r}{K} cos(Kr) \tag{2.22}$$

performing partial integration of (2.21), and assuming that U(r) satisfies:

$$\lim_{r \to \infty} rU(r) = 0 \tag{2.23.1}$$

and

$$\lim_{r \to 0} V(r) \ sin(Kr) = 0 \tag{2.23.2}$$

thus

$$\frac{d\sigma}{d\Omega} = \frac{4\mu^2}{K\hbar^4} \mid \int_0^\infty \frac{dU(r)}{dr} \left(\frac{r}{K} cos(Kr) - \frac{1}{K^2} sin(Kr) \right) dr \mid^2 \tag{2.24}$$

or

$$= \frac{4\mu^2}{K^5\hbar^4} \mid \int_0^\infty \frac{dU(r)}{dr} A(r) cos(Kr + \delta)\ dr \mid^2 \tag{2.25}$$

where

$$A(r) = \sqrt{1 + (Kr)^2}$$

and

$$\delta = tg^{-1} \frac{1}{Kr}$$

From Eq. (2.25) the following information can be learnd:

(1) The DFCS signal at each angle θ is caused by an interaction involving the whole potential field. Therefore it is a quantum mechanical rather than a classical model.

(2) The gradient of the potential dU(r)/dr plays a role as a weight factor. The steepest descent (or ascent) region of potential gives the largest contribution. Similar to the the case when light travels in media where the sudden change of density causes a large bending of light path. One may have the experience when drives on freeway dring a sunny day, the hot road surface may causes a large temperature gradient and therefore a large density gradient in the air near the road surface. The reflection of sky may be mistaken as some "water" but the "water" dissapears anyway when you move closer.

(3) K is a monotonic function of θ (Eq. (2.21)). Making the approximation $\theta \approx 2sin\frac{\theta}{2}$ the factor $cos(Kr + \delta)$ in integrand causes an oscillation vs angle θ with

a frequency $\omega = kr$. Consider the weight factor du(r)/dr there are three regions: (a) repulsive wall, (b) well with r less than r_m, and (c) between r_m and van Der Waals portion may cause three major oscillations with different frequencies (due to different r) and different sign ((a),(b) are negative and (c) is positive). This results in a interference to DFCS we have seen in classical model (Sec.II (B)).

(4) The dependence of collision energy (k) shows the lower energy results in an angular distribution curve with lower oscillation frequency. It is observed by experiment and quantum mechanical calculation.

(5) The oscillated DFCS curve has a damping factor K^{-5}. Since K is proportional to θ each peak of DFCS curve is descended according the approximate relation of θ^{-5} as θ increases.

As a example, we take a square well potential (Fig. 2.4). The DFCS calculated by Eq. (2.25) is

$$\frac{d\sigma}{d\Omega} = \frac{4\mu^2}{K^5\hbar^4}(Ka(\epsilon_1 + \epsilon_2)cos(Ka)$$

$$-\epsilon_2 Kbcos(Kb) + \epsilon_2(sin(Kb) - sin(Ka)))^2 \qquad (2.26)$$

There are two terms one from the descent edge (r = a, with amount $\epsilon_1 + \epsilon_2$ and the other from ascent edge (r = b, with amount ϵ_2). The effects of parametrs ϵ_1, ϵ_2, a, and b are shown in Fig. 2.8. One can see the following effects: (a) ϵ *effect*: Deeper well depth makes larger amplitute of oscillation. The peak vertically raises up apparently at larger angle. (b) *a effect*: Smaller repulsive wall position makes oscillation more relax. The oscillater curve has motion horizontally rather than vertically. (c) *b effect*: In high collision enrgy or shallow well depth case,

larger back step position (it can be induced by larger r_m) causes a similar vertical amplitute change like increasing well depth, but slightly different (see the uppest and lowest panel of Fig. 2.5). Therefore the correct position of each peak should bring the information of well depth, but be careful to recognize the ϵ and r_m effects. Otherwise, the larger ϵ with smaller r_m (or vise versa) effects may cancel each other to give a incorrect result.

C. Experiment

1. Beam Sources

1. *Helium-Beam Source*:

Fig. 2.9 is a schematic diagram of He-beam source. Basically, it is built based on a commercial refrigerator (made by *Air Product Co.*) which consists of (a) circulate helium compressor, (b) motor drived piston expander with two step cooling system, and (c) thermal couple meter and temperature controller. Helium is first cooled to 60 K by a tube coil attached to the pre-cooling part of the expander, then arrives at a noozle which is well contacted with the tip of expander. The further cooling makes He temperature be possibly 10 K. To eliminate impurity a liquid N_2 cooled trap is settled in the inlet line.

To combine the commercial refrigerator with the beam source a special designing has been made. The drawing diagram is shown in Fig. 2.10. The expander with a nozzle in the tip is setteled inside a reducer as source chamber. A diffusion pump which is located at the bottom of reducer can pump the source chamber down to $10^{-4} - 10^{-5}\tau$. A skimmer placed in front of nozzle makes the extrance of secondary vacuum chamber. In order to hold the expander and to insulate the working part (cooling part, tube coil, and nozzle) from atmosphere a container is designed. The major body of expander with all the accessory connection (power supply wire, circulate helium hose, and thermal couple wire) are placed inside the container which is open to atmosphere. In the front part of container the working part passes through a round window with O-ring which seals the source chamber

outside the container. The container is fasten to the reducer via a flange connection. Three adjustable screws may determine the container position in order to calibrate the nozzle. Helium gas flows through a tube T, which passes through a flange (A) to enter the vacuum chamber. A tube coil is made for pre-cooling and the tube ends with nozzle to form molecular beam. In order to get better heat exchange the nozzle is made of copper , and there is an Indium foil between the nozzle and the tip of expander. The tip of nozzle is soldered with a Plutonium aperture (d=30μ). There are two thermal couples attached, one at the tip of refrigerator (D), and the other at the nozzle (E).

In test runs, the lowest temperature reached was 7.1 K without gas flow and 9.6 K with a beam. At such low temperatures it is hard to auto-control the temperature and the nozzle clogs frequently. The stable temperature we eventually chose were 20 K and 40 K.

2. *Argon-Beam Source*:

Differing from He it is easy for heavier atoms Ar (Kr, Xe) to form dimers in low temperature. Since the velocity of the heavier atoms does not affect the collision energy very much, a liquid N_2 cooling temperature is good enough for scattering experiment. Fig. 2.11 shows the low-temperature Ar beam source with heat exchanger. A tube with nozzle in the end is well contacted by two pieces of copper plate B. The other copper plate A above B is soldered with a tube through which liquid N_2 passes. Eight copper screws are used to conduct the heat between the two plates A and B. A thermal couple is attached to the nozzle to measure

the temperature. During the experiment, the following problems were found and need improvement in the future: (1) In the course of experiment diffusion pump oil tends to fill the gap of each junction point which leads to a worse contact. As the long time experiment going on the nozzle temperature raise up graduately. (2) This beam source should also be equipped with a temperature controller.

With this beam source the stable low temperature achieved is 146-148 K.

2. Experimental Condition

As described in the schematic diagram of Chapt. I, the two beams each of that is triply pumped are crossed at a right angle in the main chamber. The geometric parameters are listed in Tab.2.2. Note that the secondary beam (2°) is placed more closer to the collision center (2.09 in.) than the primary He beam (1°) (3.61 in.) in order to obtain larger signal intensity without loss of resolusion. The divengent angles defined by each rectangular slot are 1° for He and 1.8° for Ar. The resulting collision volumn is 0.065×0.065 in^2. in the beam crossing plane and a height of 0.13 in. In the quantum mechanical simulation several sampling points are taken within this volumn. The twice larger dimension of height may double the signal intensity but does not disturb the resolution since there is few change of Newton diagram along the direction perpendicular to the collision plane.

The He, Ar, Kr, and Xe gases are products of *Mathson Co.* and have been used without further purification. To prevent any impurity from clogging the He-nozzle the gas is led to flow through a liquid N_2 cooled trap. Before running the experiment the source system is tested by flowing N_2 for a while to make sure no water and

dirty stuff in it. The stagnation pressure behind the He nozzle is regulated to 11.5 psi and the pressure is 300 τ for Ar. A time-of-flight (TOF) measurement for testing the dimer ratio of Ar was made. At T = 145 K and P = 200 τ the ratio is less than 0.1%.

The experiment is started by evacuating the molecular beam machine to about $10^{-7}\tau$ and cooling the beam source to a desired temperature. The refrigerator cools the He beam at a speed of $-4°$ per minute. In about 1.5 hour the desired stable low temperature is reached. The temperature is measured and automatively controlled. The digital reading error is ± 0.1 K and the reference environment temperature may cause ± 0.5 K variance. Cooling of the Ar-beam with liquid N_2 takes several hours. The Ar nozzle temperature is measured with a thermol couple and an ice-water reference.

Five elastic scatterings between He and other rare gases have been studied. They are:

(1) He (20 K) + Ar (148 K) (Ar20)

(2) He (40 K) + Ar (146 K) (Ar40)

(3) He (30 K) + Kr (room temperature) (Kr30)

(3) He (20 K) + Xe (room temperature) (Xe20)

(3) He (40 K) + Xe (room temperature) (Xe40)

The temperatures listed above are determined using thermolcouples. The more accurate temperatures are measured by TOF technique.[1] The total flight time is

calculated by the following formula:

$$t = \delta \times n - t_a - t_{ofst} - 2\sqrt{m} \tag{2.27}$$

where $\delta = 3\ \mu s$ is the channel width, n is the channel number, $t_a = 3\ \mu s$ is the trigger advance time, t_{ofst} is the offset determined by measuring with wheel spining clockwise and counter-clockwise direction, m is the moleculat mass. The last term describes the flight time of the ions produced by electron bombardment. The offset term corrects for geometric inperfections of the wheel assembly. The total length of the flight path is determined by a Ne TOF measurement at room temperature. We got $\Delta l = 17.8$ cm. By using the simple formula

$$v = \frac{\Delta l}{t} \tag{2.28}$$

we can get the beam velocity and distribution.

The measured velocities and distribution for each of the five experiments are given in Tab. 2.3 where subscript 1 and 2 represents primary and secondary beam respectively. The corresponding temperatures are also listed. The scattering DFCS data are taken between 3° and 50° Lab angle. To account for fluctuations during the extremely long experiment time, after 5-10 data points are measured we return to a fixed reference angle. The angle is chosen as the position of the first peak of the distribution at small angles (it is 15° for Ar40, 12° for Ar20, etc.). The angle interval is 0.5°. Several scans had been carried out and the data were averaged. The counting time for small angles is 30-60 seconds, and for large angles 300-400 seconds. The whole measurement takes about 30 hours. To measure the rapid

increased intensity of small angle (3-7°) signal we adjust the ionizer current from 10 mA to 3.5 mA. At 6°, 6.5°, and 7° measurements are taken at both current settings to determine the proper scaling factor.

3. Zero Degree Angle Offset

Due to a calibration error or an equipmental problem there might be a zero degree angle offset, however, it should be very small ($< 1°$). But the small angle DFCS signal varies over one order of magnitude within 5°, therefore the angular shift can cause a large error. An easy way to obtain the amount of the offset is to measure the DFCS signal at negative angles in the Lab coordinate system (LCS), then compare these data with the positive angle signal in the following manner.

Fig. 2.12 is a Newton diagram for elastic scattering of He and Ar. v_1 = OA and v_2 = OB are the beam velocities of He and Ar respectively. $\vec{v}_c$ = OC is the velocity of center of mass.

$$\vec{v}_c = \frac{m_1\vec{v}_1 + m_2\vec{v}_2}{m_1 + m_2} \tag{2.29}$$

The center of mass coordinate system (CMCS) is constructed with the origin at C and X'-axis along CA direction. The transformation from CMCS to LCS can be written

$$x = x'cos\gamma + y'sin\gamma + x_c \tag{2.30.1}$$

$$y = -x'sin\gamma + y'cos\gamma + y_c \tag{2.30.2}$$

where

$$\gamma = tg^{-1}\frac{v_2}{v_1}$$

and

$$x_c = \frac{m_1}{m_1 + m_2} v_1 \qquad y_c = \frac{m_2}{m_1 + m_2} v_2$$

are the components of $\vec{v}_c$.

By inversion of Eq. (2.30) it is easy to get the CMCS angle α^- from the LCS angle β^-. In the CMCS due to the symmetry of elastic scattering

$$\beta^+ = -\beta^- \tag{2.31}$$

F (in Fig. 2.12) is the reduced point from the negative angle point E. By using the transformationf Eq. (2.30) one easily gets the positive LBCS angle α^+. The following relation will give a way to reduce negtive angles to positive angles.

$$\alpha^- \rightarrow \beta^- \rightarrow \beta^+ \rightarrow \alpha^+ \tag{2.32}$$

Before getting the reduced signal one must consider the geometric Jacobi factor. The intensity of the signal is proportional[11] to a factor C

$$C = \frac{I^+}{I^-} = \frac{v_{LB}^-}{v_{LB}^+} \cdot \frac{cos\xi^+}{cos\xi^-} \tag{2.33}$$

A program which transforms the negative Lab angle signal to the reduced positive angle signal is shown in Appendix 2.2.

Fig. 2.13 shows the DFCS signal of He-Ar elastic scattering measurements from 3 to 42° and -4 to -10°. The arrow indicates the reduced signal from negative angles. It does not fit the original positive signal well when the adjustment is not taken ($\delta = 0$). This means that there is indeed a zero degree offset.

Fig. 2.13 also shows reduced data assuming angular offset $\delta = 0.1, 0.2, 0.3, 0.4, 0.5, 0.6, 0.7, 0.8, 0.9$ degrees each (dotted line) compared with the original positive

signal (points). In this case the best fitting occurs at $\delta = 0.4°$. Thus the machine zero degree offset is obtained.

D. Measured DFCS and Potential Fittings

1. Potential Forms

There are many potential forms have been suggested and applied to fit the experimental DFCS data. Among them, the simple Lennard-Jones (n,6)[5] and Exponential-6 (exp-6)[5] form were early applied. It is essentially a combination of a repulsive and a dispersion term. It does not describe the well region well, and even in the long range dispersion it is too high since the dipole-quadrupole (r^{-8}) and quadrupole-quadrupole (r^{-10}) interactions are not considered. Late on, several portional type forms[5] (MSV, M^2SV, ESMMSV, HFD etc.) were suggested. One of these forms may have one or two Morse functions to describe the well region near r_m and several major terms to describe van der Waals dispersion portion, and a smooth connection is made by spling function between the two regions. Usually, these forms have more than ten parameters to be adjusted, and each portion can be optimized independently to meet the reliable information. Also, a form with better flexibility, namely SPFD[7,8] (Simons-Parr-Finlan- Dunham) is recommanded in both quantum mechanical and bulk properties fitting. The two widely applied potential forms: (1) ESMMSV and (2) SPFD will be given later. Besides, a form suggested by Tang *et el.* recently is also given.

Before listing all these expressions several reduced parameters should be de-

fined. Throughout this section, v, r, and c_i represent the reduced potential, the reduced distance, and a reduced dispersion term coefficient respectively.

$$v \equiv \frac{V(R)}{\epsilon}, \quad r \equiv \frac{R}{r_m}, \quad c_i \equiv \frac{C_i}{\epsilon r_m^i} \tag{2.33}$$

where ϵ is the well depth, r_m is the equilibrium internuclear distance, and C_i (i = 6, 8, 10...) is a dispersion term coefficient.

1. *exponential-spline-Morse-Morse- spline-van der Waals*[5](ESMMSV):

$$v(r) = \left\{ \begin{array}{ll} A \cdot exp(-\alpha(r-1)) & 0 < r < r_1 \\ exp(a_1 + (r-r_1)(a_2 + (r-r_2)(a_3 + & \\ \qquad +(r-r_1)a_4))) & r_1 < r < r_2 \\ exp(-2\beta_1(r-1)) - 2exp(-\beta_1(r-1)) & r_2 < r < r_3 \\ exp(-2\beta_2(r-1)) - 2exp(-\beta_2(r-1)) & r_3 < r < r_4 \\ b_1 + (r-r_3)(b_2 + (r-r_4)(b_3 + (r-r_3)b_4)) & r_4 < r < r_5 \\ -(c_6 r^{-6} + c_8 r^{-8} + c_{10} r^{-10}) & r_5 < r < \infty \end{array} \right\} \tag{2.35}$$

2. *Simons-Parr-Finlan-Dunham*[7,8](SPFD):

$$v(r) = \left\{ \begin{array}{ll} h(r)A \cdot exp(-\alpha \cdot r) + (1 - h(r)) & \\ \qquad \times(b_o \lambda^2 (1 + \sum_{i=1}^{3} b_i \lambda^i) - 1) & r < r_f \\ -(c_6 r^{-6} + c_8 r^{-8} + c_{10} r^{-10}) & r > r_f \end{array} \right\} \tag{2.36}$$

where

$$h(r) = (1 + exp(\tau(r - r_o)))^{-1}$$

and

$$\lambda = 1 - r^{-1}$$

3. *Tang-Toennies*[22]:

$$v(r) = A \cdot exp(-br) - \sum_{n>3}^{\infty}(1 - \sum_{k=0}^{2n} \frac{(br)^k}{k!} exp(-br)) \frac{c_{2n}}{r^{2n}}$$

There is a question regarding these potential forms: Are these forms flexible enough to extract unbiased information from the experimental data? The firm positive answer is really doubtable. The simplest form (Lennard-Jones) is the worst. Because the important well region is built by the net cancellation between repusive and dispersion terms, there is no garentee for correct repulsive term and correct dispersion term making correct well shape. In this sense, the ESMMSV form makes a lot improvement since ϵ and r_m are well defined and the vicinity is better described by one or two Morse functions. But even though ϵ and r_m are often refered as two characteric parameters of potential well it is still no garentee for "correct" ϵ and r_m generating the correct DFCS. According to first order perturbation analysis (see my perturbation model formular Eq. (2.25)) It is the derivative of potential not potential itself to make the deflection force. In this sense the two steepest region (one between repulsive region and r_m, the other between r_m and van der Waals portion) which make the major contribution to DFCS are not well described. The flexibility of splining function is totally limited by the choice of parameters at the junction point. Good parameters for repulsive, dispersion, ϵ, and r_m may cause an incorrect spline connection, or a better spline connection may let the ϵ and r_m value "slip out". The potential form dependence can be seen from the discrepency of different fitting. For example, in the previous works[6] the He-Ar well depth ϵ ranges from 21.0 K to 35.7 K when the same data is fitted by different potential

forms.

The form bias is not the only problem to the difficulty of data fitting. A noticeable thing that can be found in almost all the interatomic potential studies[3-6] is that the larger r_m associated with smaller ϵ or, vise versa, the smaller r_m with larger ϵ can also fit the data well. In other words, there are a family of combinations of $r_m s$ and ϵs resulting in an ununique fitting. Especially, with the experimental uncertainty, it seems hard to tell which combination of r_m and ϵ is "better". The reason can be thought as: (1) The phase shift is produced by a convolution of potential contribution. The different conbination of parameters may result in a similar integral. There is no effective manner to deconvolute the contribution from each point of potential. (2) The nonlinear χ^2 regression may not be unique when the multi-parameter optimization is carried out along a non-sensitive subspace (like $\epsilon - r_m$ family).

The third problem is the small angle measurement. Due to the primary beam interference and the ultra-high intensity beam causing the nonlinear reacting of detector, in almost all the interatomic potential studies[1-4] the experimental data is always lower than the calculation at the angle less than 4°. Also, as I pointed in Sec. C.3, there might be a zero degree offset. It puzzles me a little that there was neither offset nor treatment reported in the previous works. Thinking of one order of magnititue change within 5° I found that the 0.1° offset will cause a different story in parameter fitting.

2. Data and Fitting

The measured DFCS data for Ar20, Ar40, Kr30, Xe20, and Xe40 (see Sec. C.2 for condition) are shown in Tabs. 2.4-2.8. All the data are taken by 3-8 scanned measurements. Unfortunately the negative angle measurement which is essential for zero degree angle offset determination was only carried out in Ar40. The inverse of the experimental error at each angle will be taken as the weight factor in χ^2 fitting.

The fitting program is written by M. F. Vernon.[13] The detailed description can be read through his doctorial thesis (1983). There are two options (exact and JWKB) for phase shift calculation, and four options (LJ, HFD, ESMMSV, and SPFD) for potential form selection in the grogram. The following geometric factors: (1) collision volume , (2) beam velocity distribution, and (3) DT entrance window dimension are considered and many sampling can be averaged in order to simulate the experimental condition. In phase shift calculation, 60 partial waves for lower collision energy (Ar20, Kr30, Xe20), and 75 for the others are counted and a test is made to make sure these number are good enough. The zero degree angle offset of Ar40 is determined by negative angle measurement (see Sec. C.3), and there are no information about zero degree angle offset in Ar20, Kr30, Xe20, and Xe40. The fitting for the other experiments except Ar40 are carried out by taking several guesses, then carefully compare the $\chi^2 s$ among these fully optimized results. Since the χ^2 is very sensitive to the offset choice a reasonable, but less reliable result can be extracted. The zero degree angle offset determined by this manner ranges from 0.062° to 0.65° (see Tab. 2.9).

The measured data and the fitting by ESMMSV and SPFD forms are ploted in Figs. 2.14-2.18. The corresponding potential are plotted in Figs. 2.19-2.21. The most plots look good in overall fittings. But as in general, the measured data at small angle are lower than the fitting curve. The arising question is that how many weight should we put into these small angle data. Aziz *et al.* said:"*given a set of scattering data, the attractive potential extracted depends largely on the way the data are analyzed*". They start to trust their data at angle larger than $3°-4°$ and put more error to reduce the weight at the small angle.

The other problem is how to treat the weak signal in the valley at large angle. The measurement at those rigion suffers from two aspects: (1) bad signal-to-noise ratio, (2) minimum is largely shifted by the temperature flunctuation. As I analyzed in my perturbation model, the curve ocsillate frequency ω is proportional to collision energy k or temperature T. 2% of tempertaure change may cause $1°$ signal shifting at $50°$. At each peak point, it does not hurt the measurement, because the derivative is small, $1°$ shifting makes no large difference and averaging from a bounch of shifted curves may still reproduce the correct shape well. But it is totally different in the valley region where the curve has a large derivative and the bottom is a sharp *cusp* point (derivative is not continue there. It can be understood by Eq. (2.25) where the absolute value makes the discontinuity.). Averaging in this point certainly makes the bottom higher and be incorrectly smooth. In the experiment the record shows each scanned data builds a sharp valley but the bottom occurs in different point at different time. This is the reason that causes the discrepency between the measured

data and the fitting curve in the third and fourth valley of Ar40 (Fig. 2.4).

Summarize the problems, my suggestion is: the χ^2 fitting should not take either equal weight, or the inverse of experimental error to be weight factor for each data. Because these errors reflect how the effort has been made rather than how trustable these data are. We should put more weight in the following region: (1) from 6° to the vicinity of the first peak, (2) the vicinity of each peak.

The van der Waals dispersion coefficients C_6, C_8, and C_{10} are taken from the theoretic resuls[2]. Tab. 2.10 is the calculated dipole-dipole, dipole-quadrupole, quadrupole-quadropole, and dipole-octupole interactions for He-Ar, He-Kr, and He-Xe. The optimized potential parameters are listed in Tab. 2.11. The results are analyzed and discussed in next Section.

3. Analysis and Discussion

The optimied ϵ for He-Ar interatomic potential in this study is 32.83 K, and the obtained r_m is 3.469 Å (see Tab. 2.1 for Ar40 by SPFD). The r_m is in good agreement with the result (3.47 Å) of Aziz *et al.* but the ϵ is 12% larger. We did an experiment (only He-Ar) one year before this study, it also gave the ϵ 10% larger than Aziz's. The ϵ obtained by Ar20 is even larger (35.74 K), but the result is less reliable for no negative angle data was measured. The $\epsilon - r_m$ are 34.46 K, 3.671 Å for He-Kr and 35.74 K, 3.898 Å for He-Xe. Compared with the results obtained by Chen *et al.* and Smith *et al* (24.7 K, 3.75 Å for He-Kr and 25.2 K, 4.15 Å for He-Xe) our r_ms are 2-6.5% smaller, but ϵs are 40% larger.

How do we think of the increasing of well depth for all the interatomic potential

by our experiment? Consider the Aziz's experiment (1979) for He-Ar, the ϵ they got (29.4 K) is already 21.5% increased compared with Chen's (1973) result (24.2 K). Our result is just 12% further increasing. The second explanation is: as I analyzed in Sec. D.2, the combination of a smaller ϵ with a larger r_m may result in a similar DFCS. The fitting by using those parameters of previous authors[3-6] is not too bad, but the present parameters are certainly better. Fig. 2.22 is the Ar40 fitted by Aziz's potential parameters. The fitting in small angle region looks good, but there are apparently discrepency in the third and fourth peaks since the height of the peak at large angle is sensitive to ϵ. It would not be recognized by higher collision energy experiment since I showed in classical model (Sec. B.1) there would not be information contained beyond 20° under the collision energy 10 times ϵ. If one carefully looks the fitting plot of Aziz *et al.* (Fig. 1. of ref. 6) the dscrepency exists already in the fourth peak by ESMMSV. Finnaly, I would like to say, it seems unlikely that there was mistaken by accident, since the five experiments with different pairs and different energies show uniquely the increasing trend.

The other discussion is about the combination rule. Chen *et al.* found[3] that the combination rule does not hold for unlike paired interatomic potential involving He. It was also found[14-21] in rare gas-alkali system, the system with the same rare gas atom and different alkali atoms the ϵ are nearly the same, but there are substantial differences in the ϵ for system with the same alkali atom and different rare gas atoms. The slight difference of ϵ between He-Ar and He-Kr (Xe) obtained in this study also suggests that the ϵ is mainly determined by He, the larger polarizability

of Kr and Xe seems not make much difference. The further mechanism study for explanation is beyond the goal of this study.

Appendix 1: Classical Trajectory Calculation

It is convenient to use a moving coordinate system instead of fixed coordinate system. Along the trajectory the unit vector $\hat{i}$ points in the radial direction with the target particle as the center and the unit vector $\hat{j}$ is tangential to the path of the moving particle. The derivatives of unit vectors are

$$\dot{\hat{i}} = \dot{\theta}\hat{j}$$

$$\dot{\hat{j}} = -\dot{\theta}\hat{i}$$

where the "dot" means the derivative is taken with respect to time. From Newton's Second Law the trajectory equation can be written as

$$\ddot{\vec{r}} = \ddot{r}\hat{i} + 2\dot{r}\dot{\hat{i}} + r\ddot{\hat{i}} \qquad (A1a)$$

$$= \ddot{r}\hat{i} + 2\dot{r}\dot{\theta}\hat{j} + r\ddot{\theta}\hat{j} - r(\dot{\theta})^2\hat{i} \qquad (A1b)$$

$$= (\ddot{r} - r(\dot{\theta})^2)\hat{i} + (r\ddot{\theta} + 2\dot{r}\dot{\theta})\hat{j} \qquad (A1c)$$

$$= -\frac{1}{\mu}\frac{\partial V(r)}{\partial r}\hat{i} \qquad (A1d)$$

Since $\hat{i}$ and $\hat{j}$ are linearly independent, Eqs. (A1c) and (A1d) yield

$$\ddot{r} - r(\dot{\theta})^2 = -\frac{1}{\mu}\frac{\partial V(r)}{\partial r} \qquad (A2a)$$

$$\frac{1}{r}\frac{d(r^2\dot{\theta})}{dt} = 0 \qquad (A2b)$$

Integrating Eq. (A2b) yields

$$r^2\dot{\theta} = C \qquad (A3)$$

where C is a constant, and the left hand side of the equation is twice the scanned area by the moving vector during unit time interval (see Fig. 2.15). Asymptotically

$$C = vb \qquad (A4)$$

where v is initial velocity and b is impact parameter of incident particle. Using Eqs. (A3) and (A4) we see that

$$\dot{\theta} = \frac{vb}{r^2} \tag{A5}$$

Therefore, Eq. (A2a) may be written as

$$\ddot{r} - \frac{v^2 b^2}{r^3} = -\frac{1}{\mu}\frac{\partial V(r)}{\partial r} \tag{A6}$$

Defining $u \equiv \dot{r}$ and noting that

$$\ddot{r} = u\frac{du}{dr}$$

Eq. (A5) becomes

$$udu = \left(\frac{v^2 b^2}{r^3} - \frac{1}{\mu}\frac{\partial V(r)}{\partial r}\right) dr \tag{A7}$$

Integrating both sides of Eq. (A7) and solving for u gives

$$u = \pm v\left(1 - \frac{b^2}{r^2} - \frac{V(r)}{E_c}\right)^{1/2} \tag{A8}$$

where the asymptotic value $u\,|_{r=\infty} = v$ is used and E_c is the collision energy. Dividing each side of Eq. (A8) by $\dot{\theta}$ and using Eq. (A5) on the right hand side yields

$$\frac{dr}{d\theta} = \frac{r^2}{b}\left(1 - \frac{b^2}{r^2} - \frac{V(r)}{E_c}\right)^{1/2} \tag{A9}$$

This equation is used to compute the classical trajectories of the particles.

Appendix 2: Computal Program for Zero Degree Offset

```
C-----------------------------------------------------------------C
C  This program can find out the zero degree offset by analyzing   C
C  the obtained negative degree scattering data. The output file,  C
C  ngpo.dat, can be used as an input file of telagraph to generate C
C  a plot.                                                         C
C -----------------------------------------------------------------C
      program ngpo
      dimension angle(20),data(20),cc(26),x(100),y(100),offset(10)
      data pi/3.14159265/
      open(3,file='ngpo.in',status='old')
      open(6,file='ngpo.ot',status='new')
C                                                                   C
C  Read in the experimental parameters and the scattering data.     C
C    am1, am2 - molecular masses of the two beams;                  C
C    v1 , v2  - the velocities of the two beams;                    C
C    nngdat   - number of the negative angle data;                  C
C    npodat   - number of the positive angle data;                  C
C    angle, data - negative angles and data;                        C
C    x,  y    - positive angles and data.                           C
C    offset   - 10 preset zero degree offsets.                      C
C                                                                   C
      read(3,*)am1,am2,v1,v2,nngdat,npodat
          read(3,*)(angle(k),data(k),k=1,nngdat)
      read(3,*)(x(k),y(k),k=1,npodat)
          read(3,*)(offset(k),k=1,10)
      write(6,*)'generate a plot.'
      write(6,*)'x axis label is "ANGLE IN OLD COOR. SYSTEM".'
      write(6,*)'y axis label is "DFCS (arbt. unit)".'
      write(6,*)'no legend.'
      write(6,*)'curve 11 symbol type 16.'
      write(6,*)'curve 11 symbol size 0.8.'
      write(6,*)'input data.'
      am=am1+am2
      v=sqrt(v1*v1+v2*v2)
      vc1=v1*am1/am
      vc2=v2*am2/am
      vc=sqrt(vc1*vc1+vc2*vc2)
      r=am2/am*v
      c=v1/v
      s=v2/v
      do 101 kk=1,10
          cor=offset(kk)
      do 100 ik=1,nngdat
      alabag=angle(ik)+cor
      tept=-pi/4.
      dis=pi/8.*5.
      l=1
13    if(l.eq.0)goto 15
      tept=tept+dis
      goto 16
15    tept=tept-dis
16    call tr(tept,r,c,s,afa,vlab,vc1,vc2)
      if(abs(afa-alabag).le..01)goto 70
      if(afa.le.alabag)goto 19
      l=0
      goto 20
19    l=1
```

```
20      dis=dis/2.
        goto 13
70      vlabn=vlab
        cosbtn=(vlab*vlab+r*r-vc*vc)/2./r/vlab
        call tr(-tept,r,c,s,afa,vlab,vc1,vc2)
        vlabp=vlab
        cosbtp=(vlab*vlab+r*r-vc*vc)/2./r/vlab
        coef=vlabp*cosbtn/vlabn/cosbtp
        dfcs=data(ik)*coef
        cc(2*ik-1)=afa-cor
        cc(2*ik)=dfcs
100     continue
        write(6,*)'"',cor,'"'
        write(6,45)cc
101     continue
        write(6,*)'"DATA"'
        write(6,45)(x(i),y(i),i=1,npodat)
45      format(6(1x,f8.3))
        write(6,*)'end of data.'
        write(6,*)'all curves count 0,dashed.'
        write(6,*)'go.'
        stop
        end
        subroutine tr(ang,r,c,s,afa,vlab,vc1,vc2)
        xxx=r*cos(ang)
        yyy=r*sin(ang)
        xx=c*xxx+s*yyy
        yy=-s*xxx+c*yyy
        x=xx+vc1
        y=yy+vc2
        afa=atan2(y,x)/3.14159265*180.
        vlab=sqrt(x*x+y*y)
        return
        end
```

References

(1) Y. T. Lee and Y. R. Shen, Phys. Today, **33**, 52-9 (1980).

(2) K. T. Tang, J. M. Norbeck, and P. R. Certain, J. Phys. Chem., **64**, 3063 (1976).

(3) C. H. Chen, P. E. Siska, and Y. T. Lee, J. Chem. Phys., **59**, 601 (1973).

(4) K. M. Smith, A. M. Rulis, G. Scoles, R. A. Aziz, and V. Nain, J. Chem. Phys., **67**, 152 (1977).

(5) M. Keil, J. T. Slankas, and A. Kuppermann, J. Chem. Phys., **70**, 482 (1979).

(6) R. A. Aziz, P. W. Riley, U. Buck, G. Maneke, J. Schleusener, G. Scoles, and U. Valbusa, J. Chem. Phys., **71**, 2637 (1979).

(7) G. Simon, R. G. Parr, and J. M. Finlan, L. Chem. Phys., **59**, 3229 (1973).

(8) R. W. Bickes and R. Bernstein, Chem. Phys. Lett., **26**, 457 (1973).

(9) J. S. Cohen, J. Chem. Phys., **68**, 1841 (1978).

(10) L. D. Landau and E. M. Lifshitz, "*Quantum Mechanics*", pp. 502-516, 1976.

(11) N. F. Mott and H. S. W. Massey, "*The Theory of Atomic Collisions*", 3rd ed. Oxford, 1965.

(12) R. D. Levine and R. B. Bernstein, "*Molecular Reaction Dynamics*", Oxford University, 1974.

(13) M. F. Vernon, Ph. D. thesis (1983).

(14) E. W. Rothe, P. K. Rol, and R. B. Bernstein, Phys. Rev. **130**, 2333 (1963).

(15) P. Barwig, U. Buck, E. Hundhausen, and H. Pauly, Z. Phys., **196**, 343 (1966).

(16) D. Beck and H. J. Loesch, Z. Phys., **195**, 444 (1966).

(17) M. Hollstein and H. Pauly, Z. Phys., **201**, 10 (1967).

(18) H. Hundhausen and H. Pauly, Z. Phys., **187**, 305 (1965).

(19) P. Casavecchia, G. Z. He, R. K. Sparks, and Y. T. Lee, J. Chem. Phys., **75**, 710 (1981).

(20) P. T. Pack, J. J. Valentini, C. H. Becker, R. J. Buss, and Y. T. Lee, J. Chem. Phys., **77**, 5475 (1982).

(21) P. Casavecchia, G. Z. He, R. K. Sparks, and Y. T. Lee, J. Chem. Phys., **77**, 1878 (1982).

(22) K. T. Tang and J. P. Toennies, J. Chem. Phys., **80**, 3726 (1984).

Table 2.1 Orbiting impact parameters vs collision energies. At these points the derivatives of classical turning point and phase shift are discontinue (see text).

collision energies	impact parameters	collision energies	impact parameters
ϵ^*	Å	ϵ	Å
0.18	7.0	0.53	6.0
0.23	6.8	0.58	5.8
0.28	6.6	0.63	5.8
0.33	6.2	0.68	5.8
0.43	6.2	0.73	5.6
0.48	6.0	0.83	5.4

* well depth.

Table 2.2 Geometric parameters of crossed beams (length in inch).

beam	nozzle-skimmer	skimmer-wall	wall-collision	total
1°	0.22	2.49	0.90	3.61
2°	0.26	1.54	0.55	2.09

Table 2.3 TOF measured velocities and distributions for five experiments.

expt.	v_1	β_1	v_2	β_2	true temp.
	$10^4 cm \cdot s^{-1}$		$10^4 cm \cdot s^{-1}$		K
Ar20	3.97	230	3.92	19.10	15.2
Ar40	6.09	190	3.90	19.80	35.7
Kr30	5.15	200	3.87	10.17	25.5
Xe20	3.97	230	3.06	20.14	15.2
Xe40	6.09	190	3.09	19.80	35.7

Table 2.4 Angular distribution of the scattered intensity I(θ) as a function of the laboratory angle θ for He (20 K) scattered by Ar.

θ	$I(\theta)$	ΔI	θ	$I(\theta)$	ΔI
3.062	17.7095	0.6181	12.562	0.8241	0.0167
3.562	16.6652	0.4360	13.062	0.9029	0.0260
4.062	15.2515	0.4022	13.562	0.9743	0.0148
4.562	12.9485	0.1953	14.062	0.9923	0.0097
5.062	11.3730	0.2249	14.562	1.0000	0.0010
5.562	9.3256	0.2720	15.062	0.9825	0.0123
6.062	7.4704	0.1171	15.562	0.9004	0.0095
6.562	5.8238	0.0731	16.062	0.8059	0.0185
7.062	4.4573	0.0530	16.562	0.6799	0.0152
7.562	3.2538	0.0758	17.062	0.5677	0.0138
8.062	2.3779	0.0498	17.562	0.4544	0.0164
8.562	1.6284	0.0665	18.062	0.3353	0.0140
9.062	1.0927	0.0230	18.562	0.2191	0.0116
9.562	0.7828	0.0119	19.062	0.1618	0.0060
10.062	0.6100	0.0126	19.562	0.1238	0.0076
10.562	0.5410	0.0062	20.062	0.0898	0.0068
11.062	0.5477	0.0116	20.562	0.0878	0.0045
11.562	0.6072	0.0150	21.062	0.1194	0.0078
12.062	0.7278	0.0106	21.562	0.1286	0.0078

Table 2.4 (continue)

θ	$I(\theta)$	ΔI	θ	$I(\theta)$	ΔI
22.062	0.1831	0.0079	32.062	0.0826	0.0097
22.562	0.2007	0.0073	32.562	0.0899	0.0044
23.062	0.2527	0.0094	33.062	0.0992	0.0067
23.562	0.2971	0.0115	33.562	0.1305	0.0051
24.062	0.3205	0.0118	34.062	0.1234	0.0060
24.562	0.3207	0.0106	34.562	0.1408	0.0040
25.062	0.3281	0.0147	35.062	0.1339	0.0064
25.562	0.3030	0.0060	35.562	0.1281	0.0092
26.062	0.2920	0.0100	36.062	0.1351	0.0080
26.562	0.2468	0.0099	36.562	0.1152	0.0059
27.062	0.2088	0.0066	37.062	0.1010	0.0065
27.562	0.1532	0.0093	37.562	0.0671	0.0080
28.062	0.1133	0.0068	38.062	0.0578	0.0091
28.562	0.0962	0.0080	38.562	0.0307	0.0057
29.062	0.0694	0.0084	39.062	0.0398	0.0070
29.562	0.0172	0.0077	39.562	0.0264	0.0101
30.062	0.0204	0.0053	40.062	0.0095	0.0047
30.562	0.0237	0.0074	40.562	0.0243	0.0085
31.062	0.0130	0.0117	41.062	0.0289	0.0073
31.562	0.0592	0.0078	41.562	0.0359	0.0061

Table 2.4 (continue)

θ	$I(\theta)$	$\triangle I$	θ	$I(\theta)$	$\triangle I$
42.062	0.0460	0.0088	45.562	0.0636	0.0090
42.562	0.0483	0.0060	46.062	0.0633	0.0069
43.062	0.0628	0.0093	46.562	0.0794	0.0068
43.562	0.0758	0.0060	47.062	0.0504	0.0083
44.062	0.0732	0.0069	47.562	0.0345	0.0106
44.562	0.0751	0.0067	48.062	0.0517	0.0065
45.062	0.0681	0.0087			

Table 2.5 Angular distribution of the scattered intensity I(θ) as a function of the laboratory angle θ for He (40 K) scattered by Ar.

θ	$I(\theta)$	ΔI	θ	$I(\theta)$	ΔI
4.4	9.1217	0.1014	13.9	0.5819	0.0150
4.9	7.3476	0.0050	14.4	0.4464	0.0073
5.4	5.5750	0.1648	14.9	0.3198	0.0010
5.9	3.8026	0.0389	15.4	0.1886	0.0059
6.4	2.6430	0.0706	15.9	0.1342	0.0092
6.9	1.8471	0.0316	16.4	0.0959	0.0189
7.4	1.2910	0.0264	16.9	0.0712	0.0145
7.9	0.9211	0.0240	17.4	0.1009	0.0125
8.4	0.7749	0.0101	17.9	0.1052	0.0082
8.9	0.7669	0.0001	18.4	0.1564	0.0096
9.4	0.7778	0.0137	18.9	0.1873	0.0107
9.9	0.8812	0.0117	19.4	0.2403	0.0125
10.4	0.9495	0.0163	19.9	0.2623	0.0134
10.9	0.9877	0.0225	20.4	0.2537	0.0113
11.4	1.0000	0.0000	20.9	0.2723	0.0001
11.9	0.9874	0.0112	21.4	0.2606	0.0119
12.4	0.9557	0.0010	21.9	0.2304	0.0102
12.9	0.8386	0.0138	22.4	0.1970	0.0093
13.4	0.6938	0.0010	22.9	0.1472	0.0097

Table 2.5 (continue)

θ	$I(\theta)$	ΔI	θ	$I(\theta)$	ΔI
23.4	0.1198	0.0108	30.4	0.1067	0.0056
23.9	0.0808	0.0115	30.9	0.1026	0.0059
24.4	0.0476	0.0079	31.4	0.0816	0.0062
24.9	0.0265	0.0065	31.9	0.0753	0.0071
25.4	0.0241	0.0048	32.4	0.0623	0.0075
25.9	0.0250	0.0067	32.9	0.0306	0.0074
26.4	0.0392	0.0092	33.9	0.0221	0.0064
26.9	0.0478	0.0075	34.9	0.0228	0.0076
27.4	0.0569	0.0079	35.9	0.0373	0.0055
27.9	0.0819	0.0082	36.9	0.0504	0.0087
28.4	0.0969	0.0072	37.9	0.0567	0.0122
28.9	0.1094	0.0087	38.9	0.0500	0.0093
29.4	0.1183	0.0095	39.9	0.0488	0.0061
29.9	0.1151	0.0001	40.9	0.0458	0.0083

Table 2.6 Angular distribution of the scattered intensity I(θ) as a function of the laboratory angle θ for He (30 K) scattered by Kr.

θ	$I(\theta)$	ΔI	θ	$I(\theta)$	ΔI
3.22	6.0130	0.3890	12.72	0.9860	0.0160
3.72	3.9690	0.5500	13.22	0.9150	0.0200
4.22	1.9150	0.7660	13.72	0.8270	0.0320
4.72	9.4910	0.6720	14.22	0.7010	0.0190
5.22	6.9970	0.4910	14.72	0.5630	0.0040
5.72	5.4240	0.1370	15.22	0.4120	0.0120
6.22	4.0310	0.2260	15.72	0.2890	0.0100
6.72	2.8650	0.0600	16.22	0.1940	0.0090
7.22	1.8860	0.0280	16.72	0.1320	0.0140
7.72	1.2290	0.0360	17.22	0.1100	0.0100
8.22	0.8930	0.0510	17.72	0.0730	0.0150
8.72	0.6440	0.0100	18.22	0.1070	0.0110
9.22	0.6070	0.0440	18.72	0.1370	0.0140
9.72	0.6180	0.0060	19.22	0.1690	0.0200
10.22	0.7080	0.0010	19.72	0.2140	0.0110
10.72	0.8370	0.0220	20.22	0.2640	0.0080
11.22	0.9050	0.0210	20.72	0.2770	0.0090
11.72	1.0250	0.0020	21.22	0.3010	0.0090
12.22	1.0000	0.0001	21.72	0.2940	0.0140

Table 2.6 (continue)

θ	$I(\theta)$	$\triangle I$	θ	$I(\theta)$	$\triangle I$
22.22	0.2700	0.0070	32.22	0.0870	0.0110
22.72	0.2340	0.0070	32.72	0.0640	0.0080
23.22	0.2190	0.0100	33.22	0.0550	0.0070
23.72	0.1720	0.0130	33.72	0.0260	0.0070
24.22	0.1060	0.0110	34.22	0.0140	0.0040
24.72	0.0710	0.0180	34.72	0.0130	0.0060
25.22	0.0390	0.0070	35.22	0.0130	0.0030
25.72	0.0300	0.0040	35.72	0.0210	0.0080
26.22	0.0050	0.0040	36.22	0.0210	0.0080
26.72	0.0330	0.0090	36.72	0.0320	0.0080
27.22	0.0240	0.0060	37.22	0.0540	0.0010
27.72	0.0590	0.0070	37.72	0.0550	0.0020
28.22	0.0640	0.0030	38.22	0.0510	0.0040
28.72	0.0860	0.0140	38.72	0.0540	0.0040
29.22	0.1090	0.0090	39.22	0.0510	0.0020
29.72	0.1240	0.0140	39.72	0.0650	0.0060
30.22	0.1220	0.0030	40.22	0.0560	0.0030
30.72	0.1150	0.0090	40.72	0.0500	0.0080
31.22	0.1150	0.0090	41.22	0.0400	0.0090
31.72	0.0880	0.0070	41.72	0.0220	0.0050

Table 2.6 (continue)

θ	$I(\theta)$	ΔI	θ	$I(\theta)$	ΔI
42.22	0.0200	0.0050	45.22	0.0210	0.0080
42.72	0.0190	0.0030	45.72	0.0320	0.0090
43.22	0.0150	0.0060	46.22	0.0460	0.0060
43.72	0.0260	0.0080	46.72	0.0430	0.0070
44.22	0.0310	0.0100	47.22	0.0450	0.0040
44.72	0.0190	0.0080	47.72	0.0450	0.0100

Table 2.7 Angular distribution of the scattered intensity I(θ) as a function of the laboratory angle θ for He (20 K) scattered by Xe.

θ	$I(\theta)$	ΔI	θ	$I(\theta)$	ΔI
3.43	16.8130	0.0650	12.93	0.8220	0.0200
3.93	15.2010	0.6250	13.43	0.8880	0.0150
4.43	13.4060	0.3290	13.93	0.9840	0.0520
4.93	11.5560	0.2480	14.43	1.0000	0.0010
5.43	9.8650	0.7580	14.93	0.9960	0.0330
5.93	7.9920	0.4190	15.43	0.9660	0.0260
6.43	6.4380	0.2330	15.93	0.8880	0.0210
6.93	4.9950	0.0840	16.43	0.7820	0.0110
7.43	3.8850	0.1650	16.93	0.6560	0.0080
7.93	2.7090	0.1160	17.43	0.5340	0.0090
8.43	1.9700	0.0110	17.93	0.4520	0.0130
8.93	1.3110	0.0320	18.43	0.3140	0.0130
9.43	0.8890	0.0060	18.93	0.2370	0.0100
9.93	0.6140	0.0240	19.43	0.1550	0.0160
10.43	0.4450	0.0180	19.93	0.1110	0.0050
10.93	0.4430	0.0240	20.43	0.1010	0.0080
11.43	0.4720	0.0110	20.93	0.1200	0.0060
11.93	0.5790	0.0150	21.43	0.1230	0.0060
12.43	0.6930	0.0080	21.93	0.1670	0.0060

Table 2.7 (continue)

θ	$I(\theta)$	ΔI	θ	$I(\theta)$	ΔI
22.43	0.2120	0.0050	32.43	0.1190	0.0080
22.93	0.2610	0.0040	32.93	0.1200	0.0040
23.43	0.2940	0.0050	33.43	0.1450	0.0150
23.93	0.3240	0.0080	33.93	0.1600	0.0080
24.43	0.3570	0.0150	34.43	0.1650	0.0110
24.93	0.3390	0.0110	34.93	0.1590	0.0060
25.43	0.3460	0.0040	35.43	0.1640	0.0110
25.93	0.3150	0.0050	35.93	0.1490	0.0080
26.43	0.2930	0.0110	36.43	0.1150	0.0070
26.93	0.2520	0.0080	36.93	0.0960	0.0100
27.43	0.1870	0.0090	37.43	0.0710	0.0050
27.93	0.1400	0.0110	37.93	0.0610	0.0040
28.43	0.1110	0.0070	38.43	0.0320	0.0100
28.93	0.0670	0.0070	38.93	0.0210	0.0060
29.43	0.0440	0.0100	39.43	0.0220	0.0060
29.93	0.0430	0.0070	39.93	0.0270	0.0090
30.43	0.0460	0.0050	40.43	0.0280	0.0070
30.93	0.0420	0.0060	40.93	0.0330	0.0080
31.43	0.0600	0.0080	41.43	0.0420	0.0070
31.93	0.0710	0.0060	41.93	0.0480	0.0070

Table 2.7 (continue)

θ	$I(\theta)$	$\triangle I$	θ	$I(\theta)$	$\triangle I$
42.43	0.0740	0.0080	46.93	0.0540	0.0090
42.93	0.0820	0.0040	47.43	0.0350	0.0030
43.43	0.0920	0.0070	47.93	0.0410	0.0090
43.93	0.0880	0.0040	48.43	0.0200	0.0070
44.43	0.0700	0.0100	48.93	0.0170	0.0050
44.93	0.0900	0.0080	49.43	0.0170	0.0050
45.43	0.0780	0.0060	49.93	0.0240	0.0070
45.93	0.0580	0.0090	50.43	0.0270	0.0140
46.43	0.0690	0.0060			

Table 2.8 Angular distribution of the scattered intensity I(θ) as a function of the laboratory angle θ for He (40 K) scattered by Xe.

θ	$I(\theta)$	ΔI	θ	$I(\theta)$	ΔI
3.65	4.2627	0.0437	13.15	0.6701	0.0090
3.15	1.2718	0.0506	13.65	0.5279	0.0110
4.65	8.4911	0.0261	14.15	0.3786	0.0121
4.15	6.3674	0.0471	14.65	0.2920	0.0224
5.65	4.5370	0.1005	15.15	0.1824	0.0099
5.15	3.1197	0.0339	15.65	0.1173	0.0044
6.65	2.1319	0.0199	16.15	0.0943	0.0119
6.15	1.2902	0.0386	16.65	0.0962	0.0077
7.65	0.9022	0.0232	17.15	0.1410	0.0025
7.15	0.6905	0.0168	17.65	0.1564	0.0058
8.65	0.6685	0.0170	18.15	0.1893	0.0089
8.15	0.7153	0.0383	18.65	0.2440	0.0060
9.65	0.8445	0.0459	19.15	0.2529	0.0163
9.15	0.9347	0.0382	19.65	0.2778	0.0077
10.65	0.9609	0.0302	20.15	0.2733	0.0091
10.15	1.0000	0.0010	20.65	0.2684	0.0098
11.65	0.9708	0.0256	21.15	0.2206	0.0132
12.15	0.8924	0.0278	21.65	0.1931	0.0120
12.65	0.7692	0.0083	22.15	0.1366	0.0058

Table 2.8 (continue)

θ	$I(\theta)$	ΔI	θ	$I(\theta)$	ΔI
22.65	0.1037	0.0110	32.65	0.0091	0.0075
23.15	0.0697	0.0057	33.15	0.0110	0.0032
23.65	0.0377	0.0097	33.65	0.0161	0.0029
24.15	0.0329	0.0095	34.15	0.0315	0.0055
24.65	0.0209	0.0069	34.65	0.0405	0.0073
25.15	0.0320	0.0037	35.15	0.0394	0.0077
25.65	0.0501	0.0061	35.65	0.0454	0.0042
26.15	0.0552	0.0068	36.15	0.0526	0.0055
26.65	0.0824	0.0053	36.65	0.0512	0.0025
27.15	0.0957	0.0084	37.15	0.0622	0.0038
27.65	0.1060	0.0092	37.65	0.0467	0.0060
28.15	0.1112	0.0033	38.15	0.0432	0.0025
28.65	0.1146	0.0095	38.65	0.0308	0.0111
29.15	0.1136	0.0083	39.15	0.0269	0.0053
29.65	0.0877	0.0058	39.65	0.0220	0.0080
30.15	0.0640	0.0040	40.15	0.0172	0.0042
30.65	0.0581	0.0078	40.65	0.0032	0.0027
31.15	0.0338	0.0087	41.15	0.0101	0.0109
31.65	0.0181	0.0050	41.65	0.0116	0.0093
32.15	0.0166	0.0085	42.15	0.0199	0.0051

Table 2.8 (continue)

θ	$I(\theta)$	ΔI	θ	$I(\theta)$	ΔI
42.65	0.0227	0.0041	45.65	0.0319	0.0041
43.15	0.0323	0.0088	46.15	0.0391	0.0074
43.65	0.0250	0.0073	46.65	0.0285	0.0047
44.15	0.0252	0.0064	47.15	0.0275	0.0053
44.65	0.0286	0.0049	47.65	0.0268	0.0043
45.15	0.0459	0.0034	48.15	0.0194	0.0044

Table 2.9 Zero degree angle offsets for five experiments.

expts.	Ar20	Ar40	Kr30	Xe20	Xe40
offsets(deg.)	0.062	0.40	0.22	0.43	0.65

Table 2.10 Bounds to van der Waals coefficients for dipole-dipole (DD), dipole-quadrupole (DQ), quadupole-dipole (QD), quadrupole-quadrupole (QQ), dipole-octupole (DO), and octupole-dipole (OD) interactions (in atomic units).*

pairs	DD	DQ	QD	QQ	DO	OD
He-Ar	9.82±0.35	107±25	46.5±2.1	949±244	1940±450	358±58
He+Kr	13.6±0.6	162±40	64.4±3.7	1430±380	2670±620	498±83
He-Xe	18.3±0.6	251±75	85.6±3.4	2210±700	4210±1290	659±86

* K. T. Tang, J. M. Norbeck, and P. R. Certain, J. Chem. Phys., **64**, 3063 (1976).

Table 2.10 (continue) Calculated van der Waals coefficients.

paies	C_6	C_8	C_{10}
He+Ar	9.82	153.5	3247 (a.u.)
	134.98	590.4	3495 (kcal/mole/Å^i)
He+Kr	13.6	226.4	4598 (a.u.)
	186.9	870.9	4949 (kcal/mole/Å^i)
He+Xe	18.3	336.6	7079 (a.u.)
	251.5	1294.8	7620 (kcal/mole/Å^i)

Table 2.11 Optimized potential parameters for He-Ar, He-Kr, He-Xe from five experiments.*

SPFD

expt.	ϵ	r_m	A	α	b_0	b_1	b_2
Ar20	0.0711	3.461	595873	4.791	52.536	-4.456	5.276
Ar40	0.0653	3.469	489478	5.285	47.538	-4.509	6.826
Kr30	0.0685	3.671	486005	5.415	46.434	-4.565	7.289
Xe20	0.0700	3.917	21654940	4.590	60.049	-3.920	-4.034
Xe40	0.0722	3.878	25945058	4.570	54.758	-0.749	-32.37
expt.	b_3	x_f	τ	x_0	c_6	c_8	c_{10}
Ar20	1.466	1.438	88.077	0.861	135.5	593.1	3514
Ar40	-2.423	1.506	26.641	0.853	135.5	593.1	3514
Kr30	-3.142	1.467	18.205	0.822	186.9	870.9	4949
Xe20	28.667	1.291	50.757	0.794	251.5	1294.8	7620
Xe40	93.867	1.278	62.911	0.833	251.5	1294.8	7620

ESMMSV

expt.	ϵ	r_m	A	α	r_1	r_2
Ar40	0.0668	3.356	0.464	20.89	0.819	0.910
Kr30	0.0675	3.598	3.271	16.02	0.595	0.800
expt.	r_3	r_4	β_1	β_2	c_6	c_8
Ar40	1.140	2.056	8.644	5.587	144.4	1503
kr30	1.437	1.893	8.001	5.576	198.2	2500

* See Sec. IV(A) for potential form expressions and III(B) for experimental conditions.

Caption

Figure 2.1. Classical trajectories of He scattered by Ar.

Figure 2.2. Classical trajectories of He scattered by Ar with several collision energies.

Figure 2.3. Deflection function vs impact parameter; The signal contribution at certain angle.

Figure 2.4. Deflection function at with several collision energies.

Figure 2.5. JWKB phase shift function with several collision energies.

Figure 2.6. B(r) function (see text).

Figure 2.7. The momentum vects of incident and outgoing particles.

Figure 2.8. Calculated DFCS by a perturbation model. Comparision of the parameter effects of a simple square well potential.

Figure 2.9. Schematic diagram of a low-temperature He-beam source.

Figure 2.10. Drawing plot of He-beam source chamber.

Figure 2.11. Plot of Ar-beam source.

Figure 2.12. Newton diagram shows the relation between the positive and negative angle in both center-of-mass and laboratory coordinate system.

Figure 2.13. Determination zero degree offset by fitting reduced negative angle data. The offset $\delta = 0.4°$ is found by this fitting.

Figure 2.14. He (20 K) + Ar elastic scattering data and fitting by prenouced potential forms.

Figure 2.15. He (40 K) + Ar elastic scattering data and fitting by prenouced potential forms.

Figure 2.16. He (30 K) + Kr elastic scattering data and fitting by prenouced potential forms.

Figure 2.17. He (20 K) + Xe elastic scattering data and fitting by prenouced potential forms.

Figure 2.18. He (40 K) + Xe elastic scattering data and fitting by prenouced potential forms.

Figure 2.19. Optimized He-Ar interatomic potentials.

Figure 2.20. Optimized He-Kr interatomic potentials.

Figure 2.21. Optimized He-Xe interatomic potentials.

Figure 2.22. He (40 K) + Ar elastic scattering data fitted by the parameters obtained by Aziz *et al.*

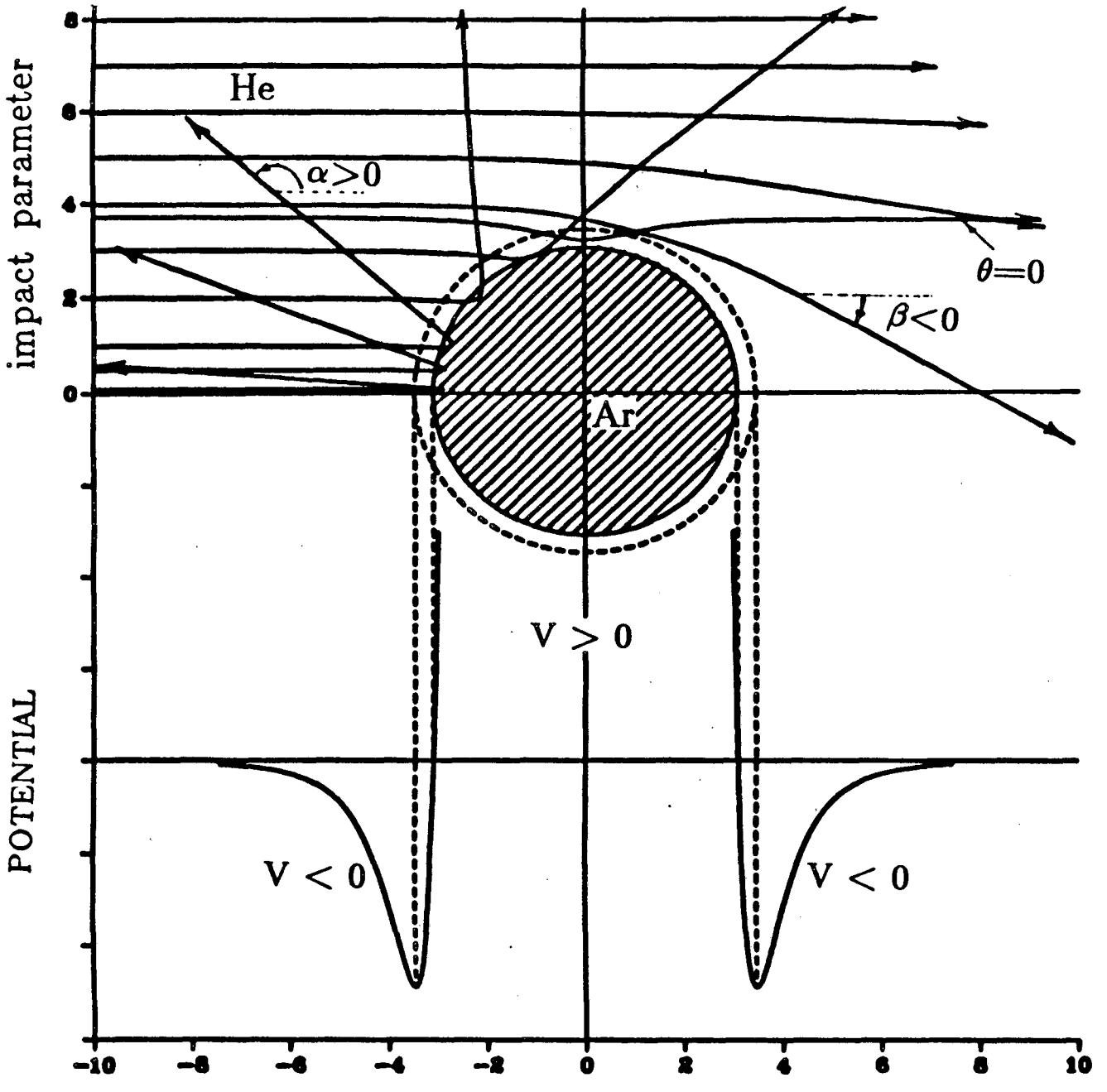
impact parameter
He
α>0
θ=0
β<0
Ar
V > 0
POTENTIAL
V < 0
V < 0
8
6
4
2
0
-10
-8
-6
-4
-2
0
2
4
6
8
10

Fig. 2.1

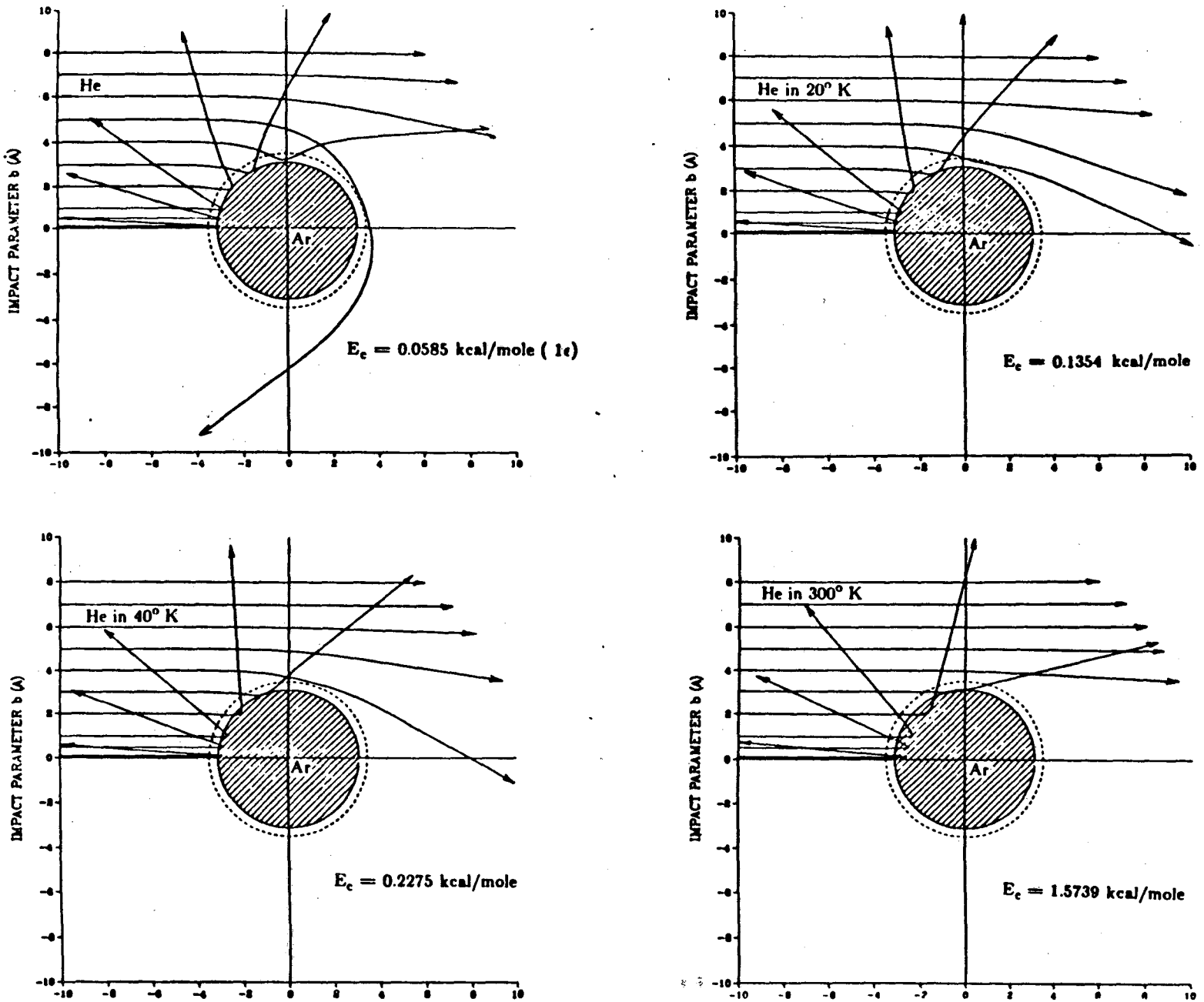
He
Ar
E_c = 0.0585 kcal/mole (1ε)
He in 20° K
Ar
E_c = 0.1354 kcal/mole
He in 40° K
Ar
E_c = 0.2275 kcal/mole
He in 300° K
Ar
E_c = 1.5739 kcal/mole
IMPACT PARAMETER b (Å)

Fig. 2.2

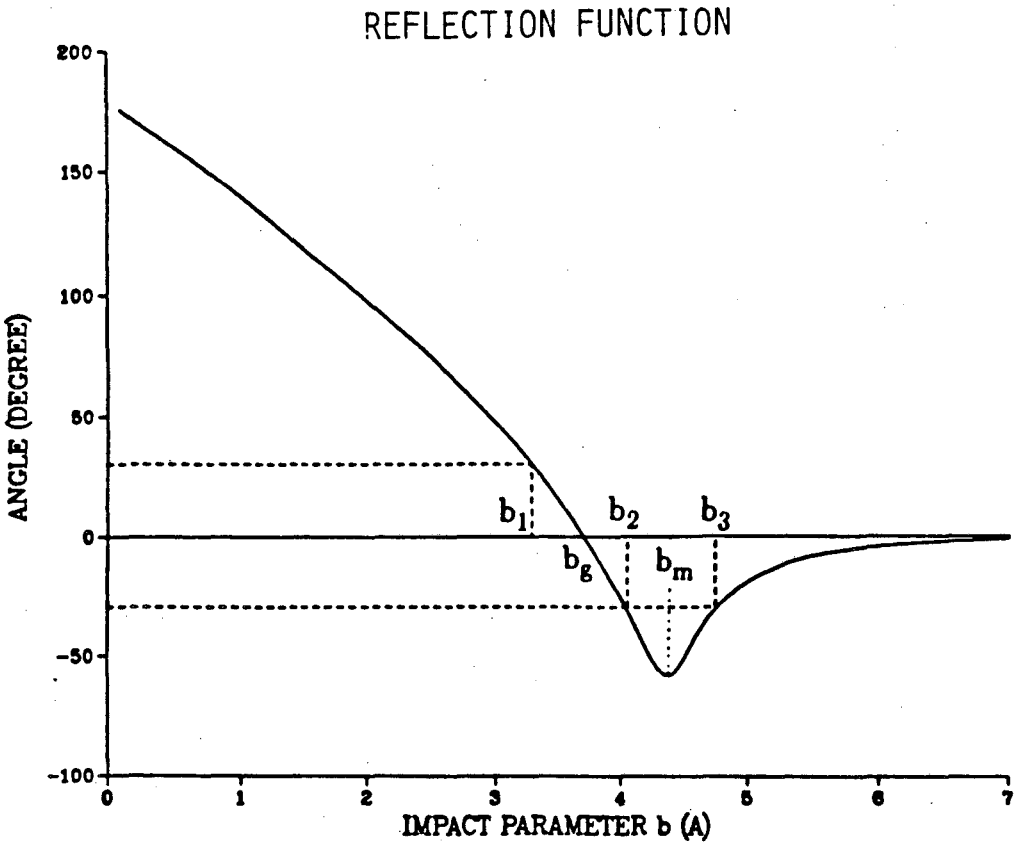
REFLECTION FUNCTION
ANGLE (DEGREE)
IMPACT PARAMETER b (A)
200
150
100
50
0
-50
-100
0
1
2
3
4
5
6
7
b_1
b_2
b_3
b_g
b_m

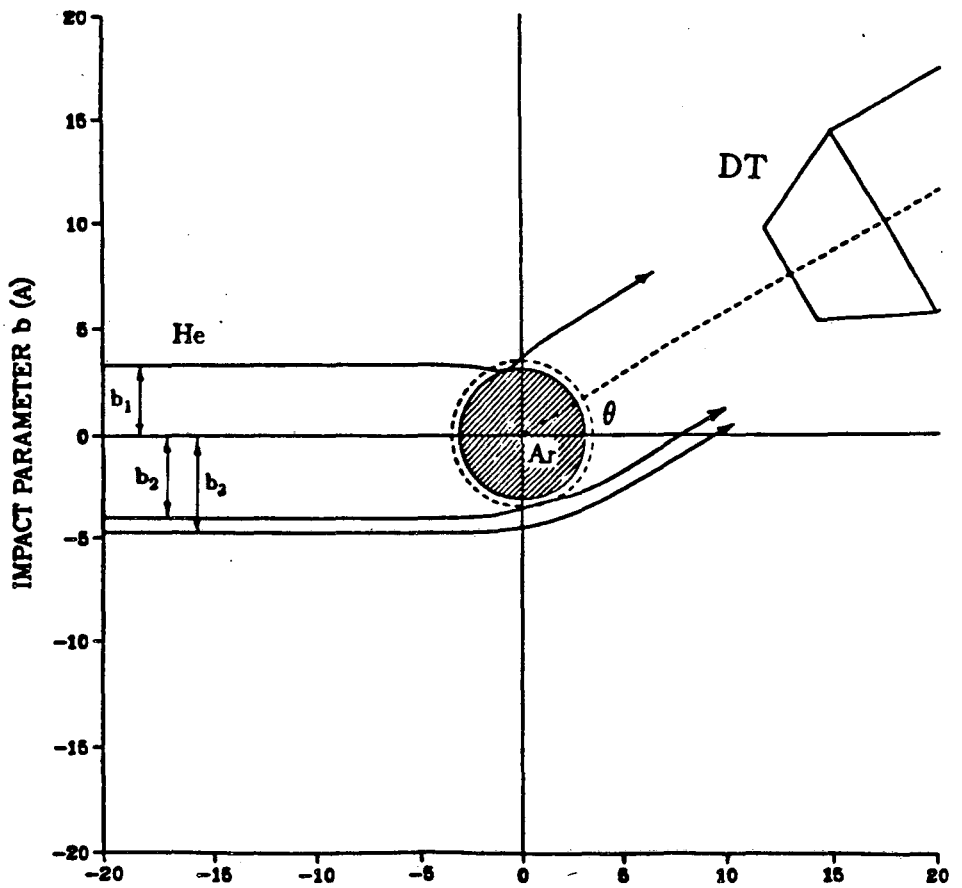
IMPACT PARAMETER b (A)
20
15
10
5
0
-5
-10
-15
-20
-20
-15
-10
-5
0
5
10
15
20
He
DT
Ar
θ
b_1
b_2
b_3

Fig. 2.3

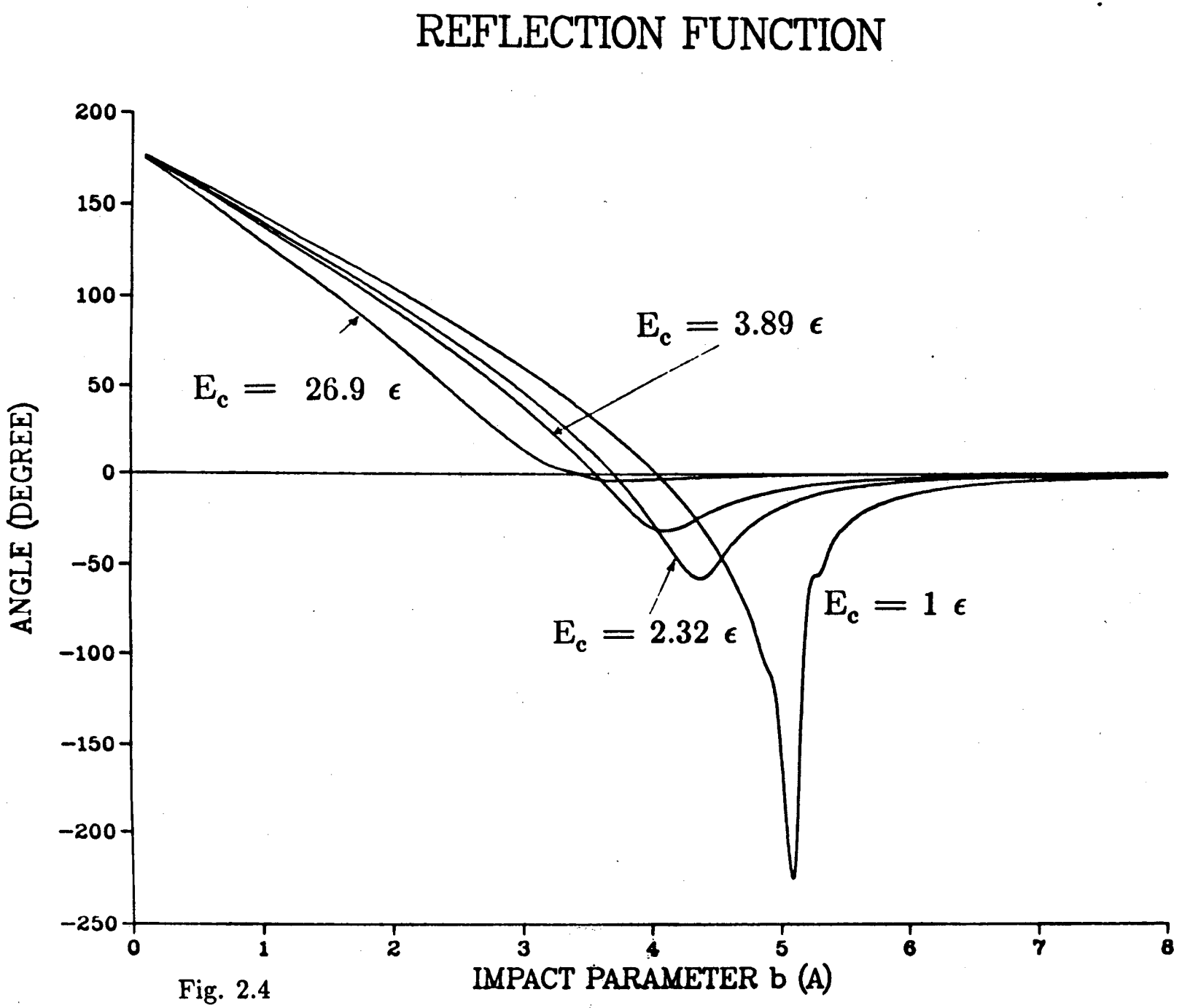
REFLECTION FUNCTION
ANGLE (DEGREE)
200
150
100
50
0
-50
-100
-150
-200
-250
0
1
2
3
4
5
6
7
8
IMPACT PARAMETER b (A)
$E_c = 26.9\ \epsilon$
$E_c = 3.89\ \epsilon$
$E_c = 2.32\ \epsilon$
$E_c = 1\ \epsilon$

Fig. 2.4

JWKB PHASE SHIFT FUNCTION

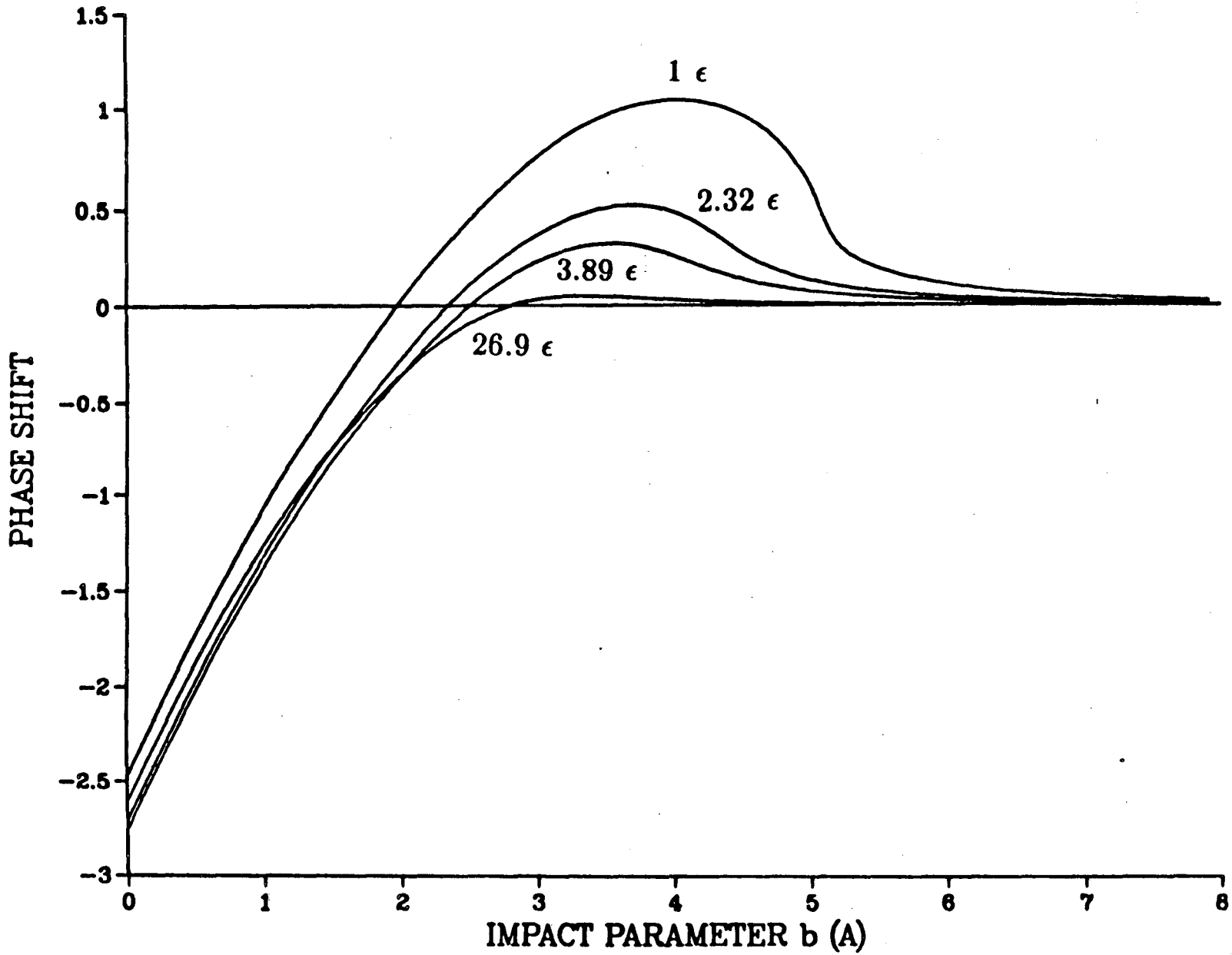

Fig. 2.5

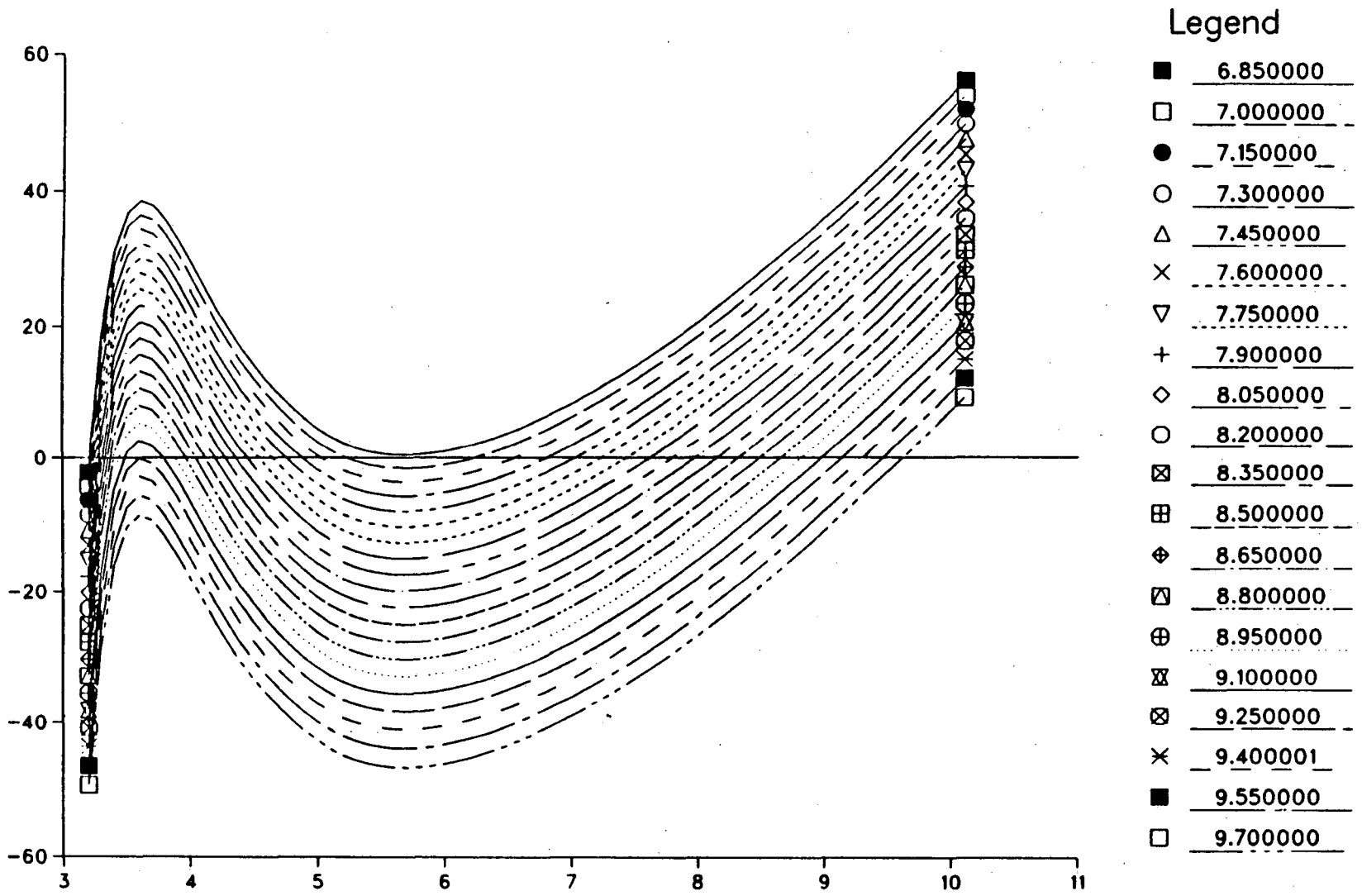
60
40
20
0
-20
-40
-60
3
4
5
6
7
8
9
10
11
Legend
6.850000
7.000000
7.150000
7.300000
7.450000
7.600000
7.750000
7.900000
8.050000
8.200000
8.350000
8.500000
8.650000
8.800000
8.950000
9.100000
9.250000
9.400001
9.550000
9.700000

Fig. 2.6

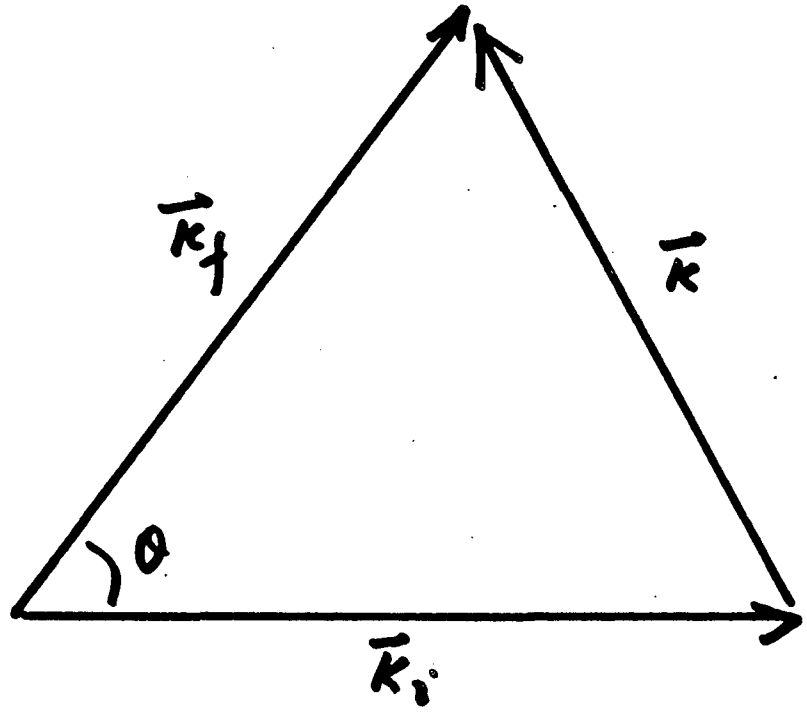

Fig. 2.7

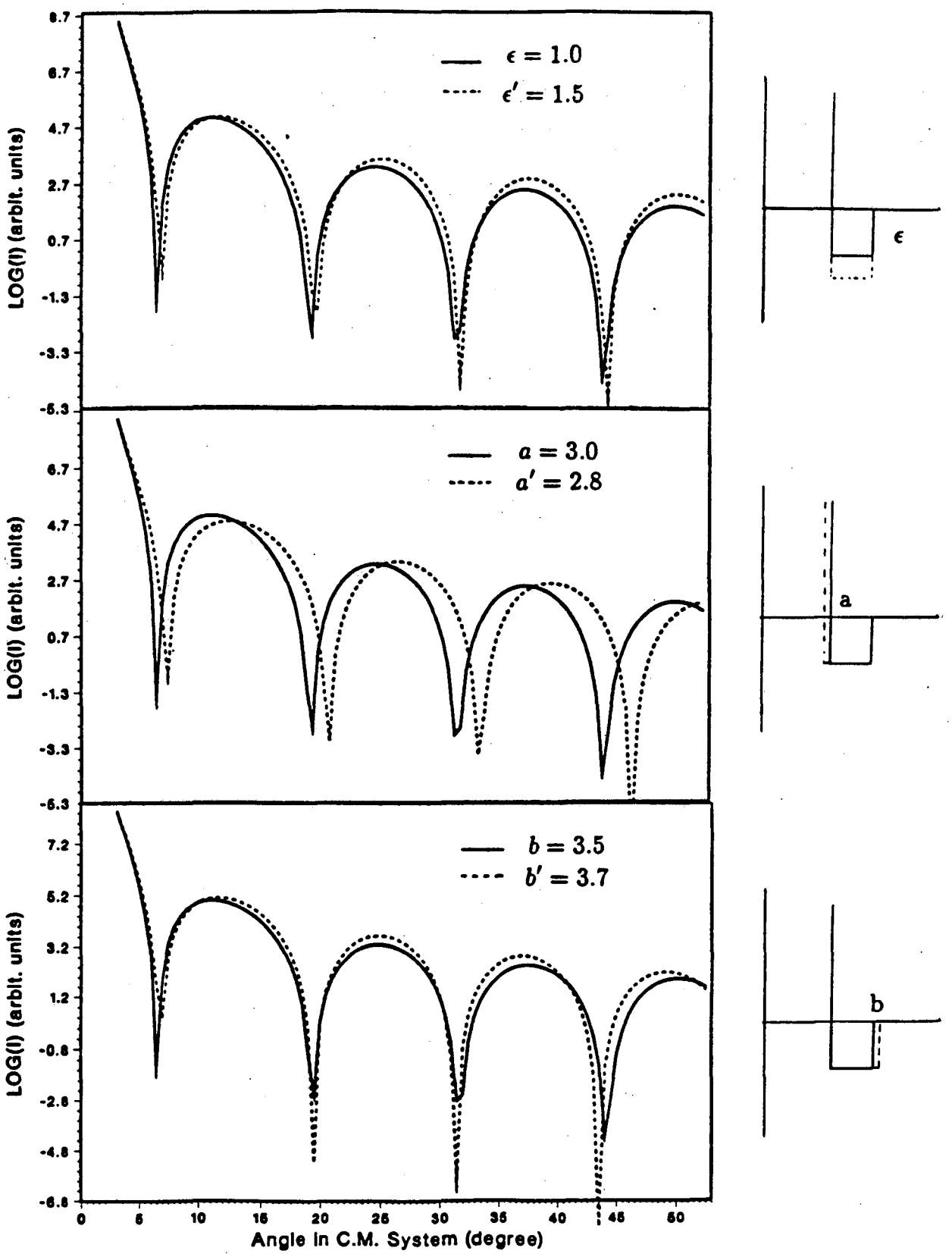
$\epsilon = 1.0$
$\epsilon' = 1.5$
$a = 3.0$
$a' = 2.8$
$b = 3.5$
$b' = 3.7$
LOG(I) (arbit. units)
Angle in C.M. System (degree)
ϵ
a
b

Fig. 2.8

Cold He Beam Source

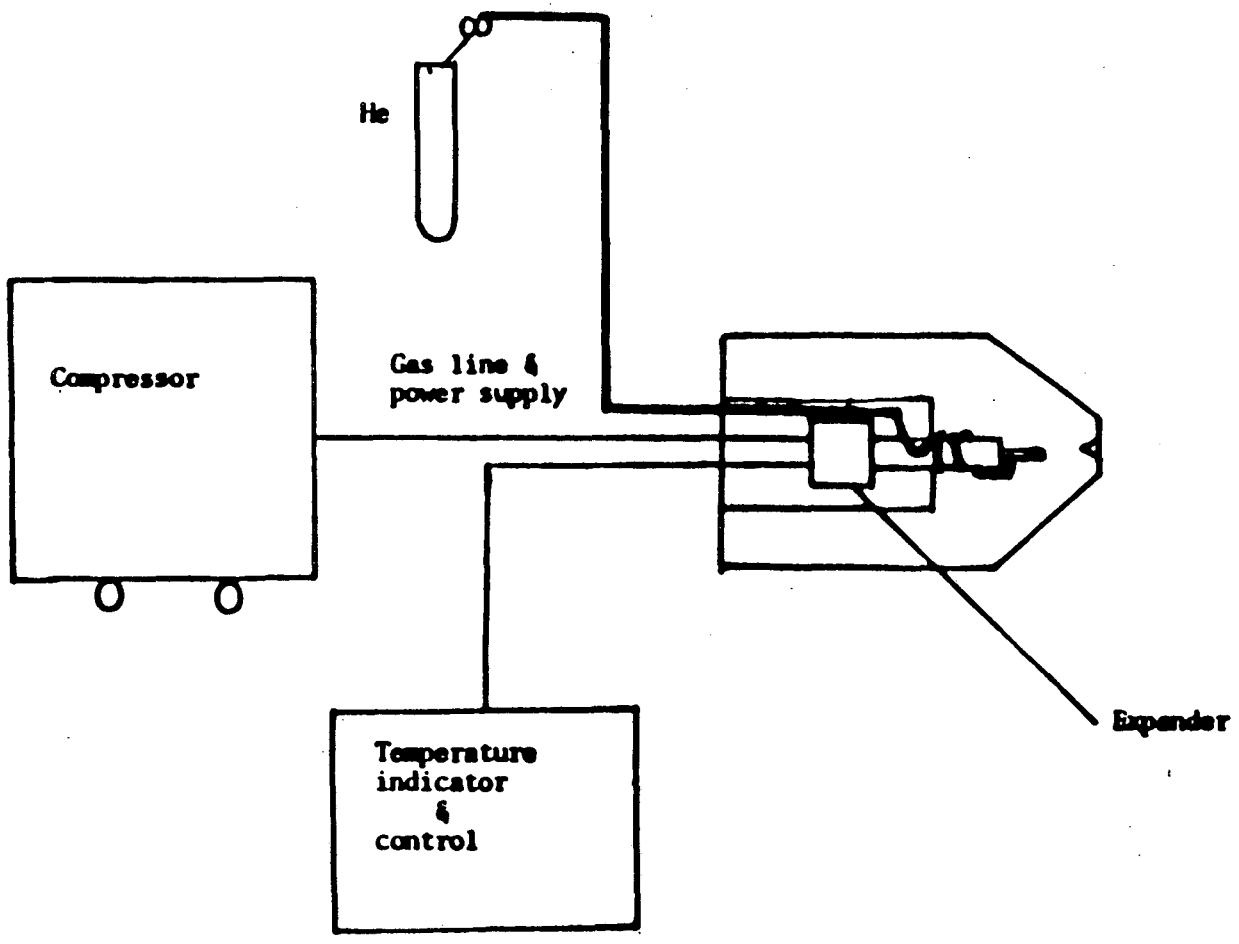

Fig. 2.9

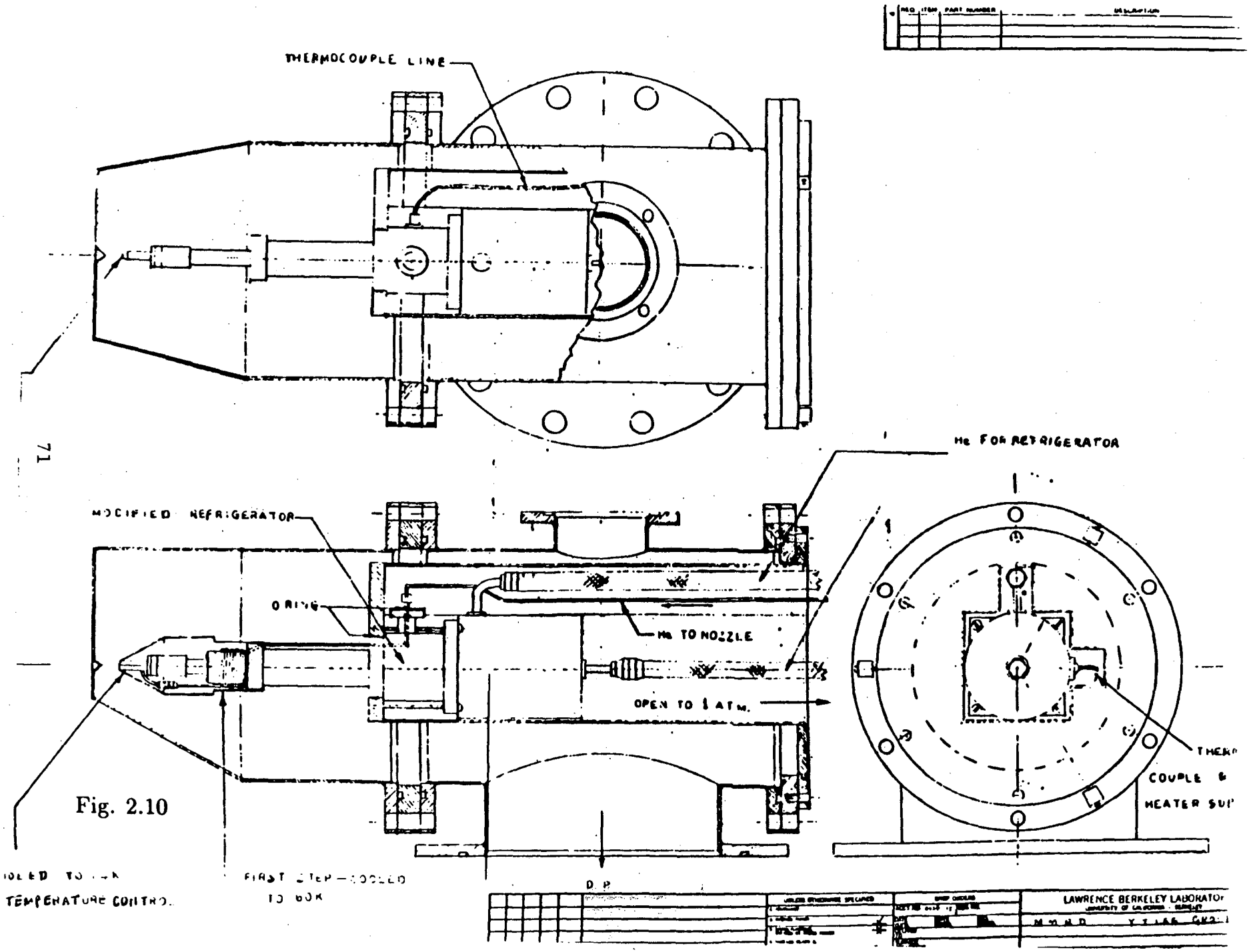
THERMOCOUPLE LINE
He FOR REFRIGERATOR
MODIFIED REFRIGERATOR
O RING
He TO NOZZLE
OPEN TO 1 ATM.
COUPLE &
HEATER SUP
TEMPERATURE CONTRO.
D.P.
LAWRENCE BERKELEY LABORATOR

Fig. 2.10

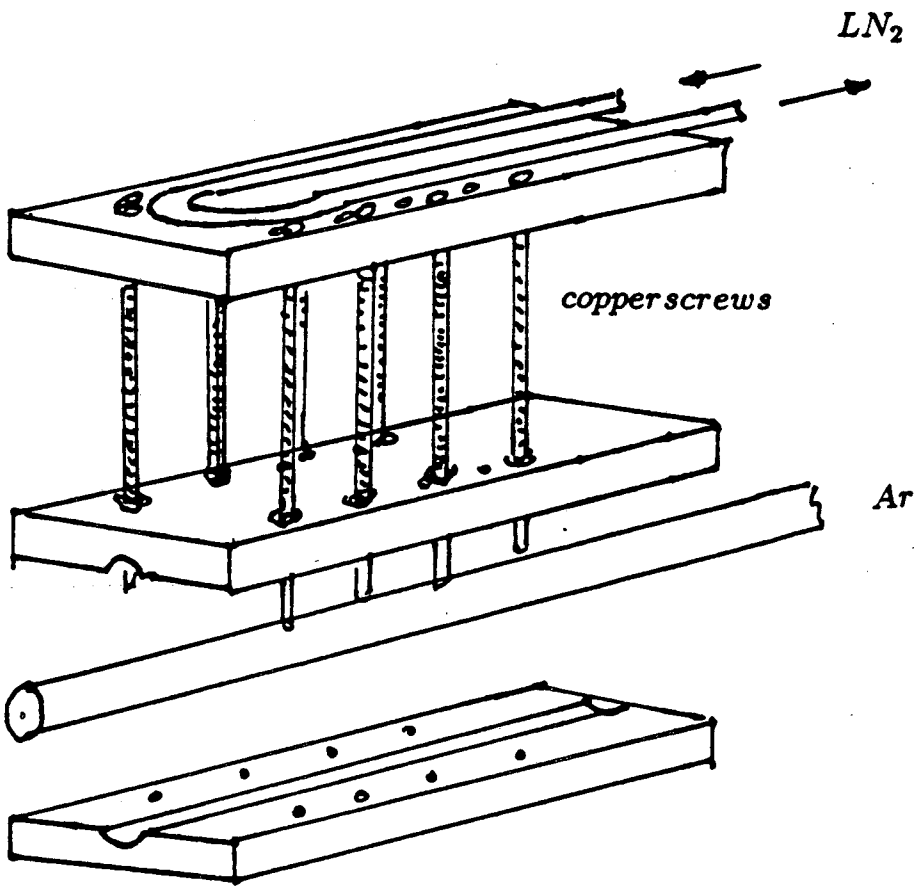

Fig. 2.11

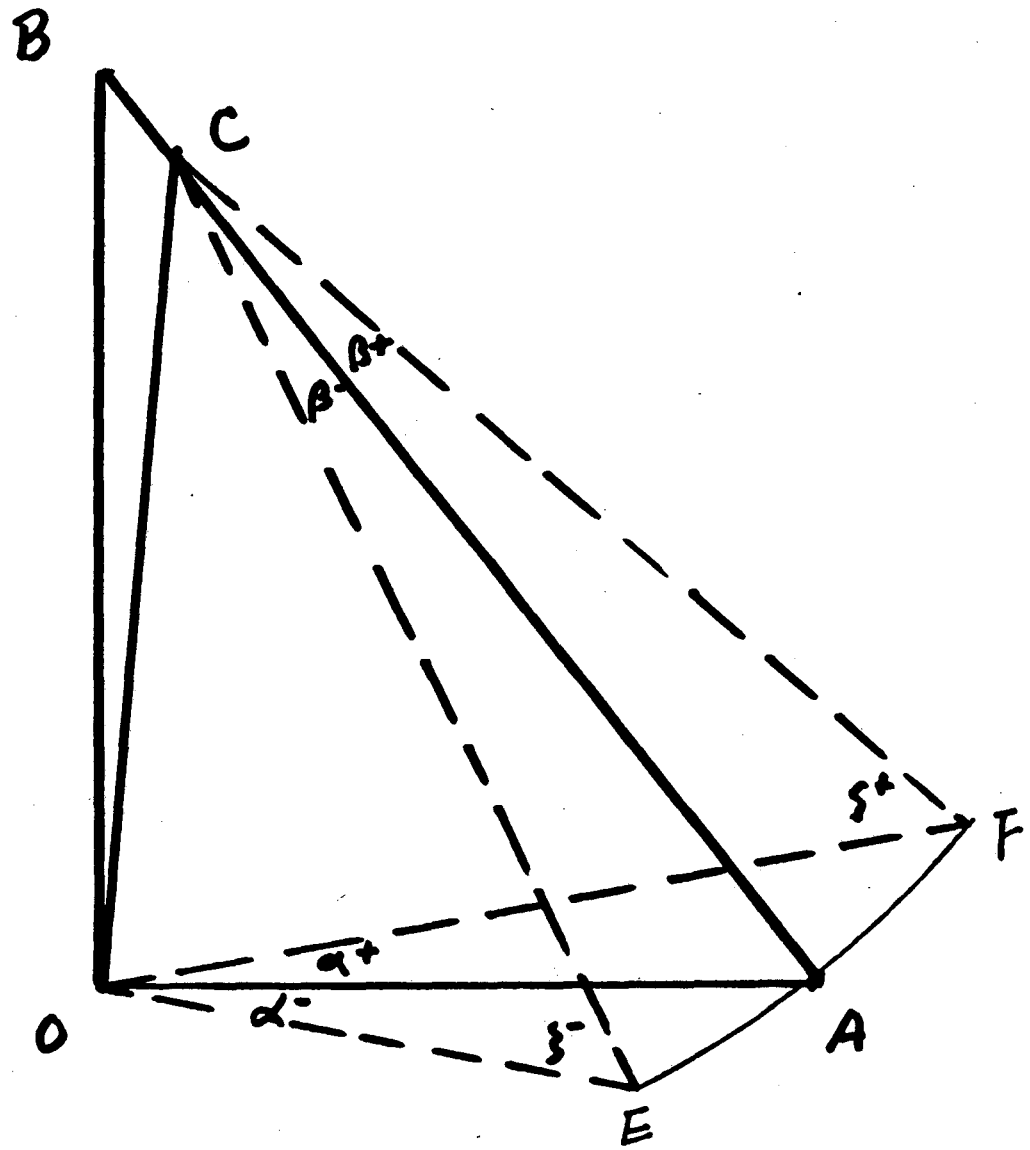

Fig. 2.12

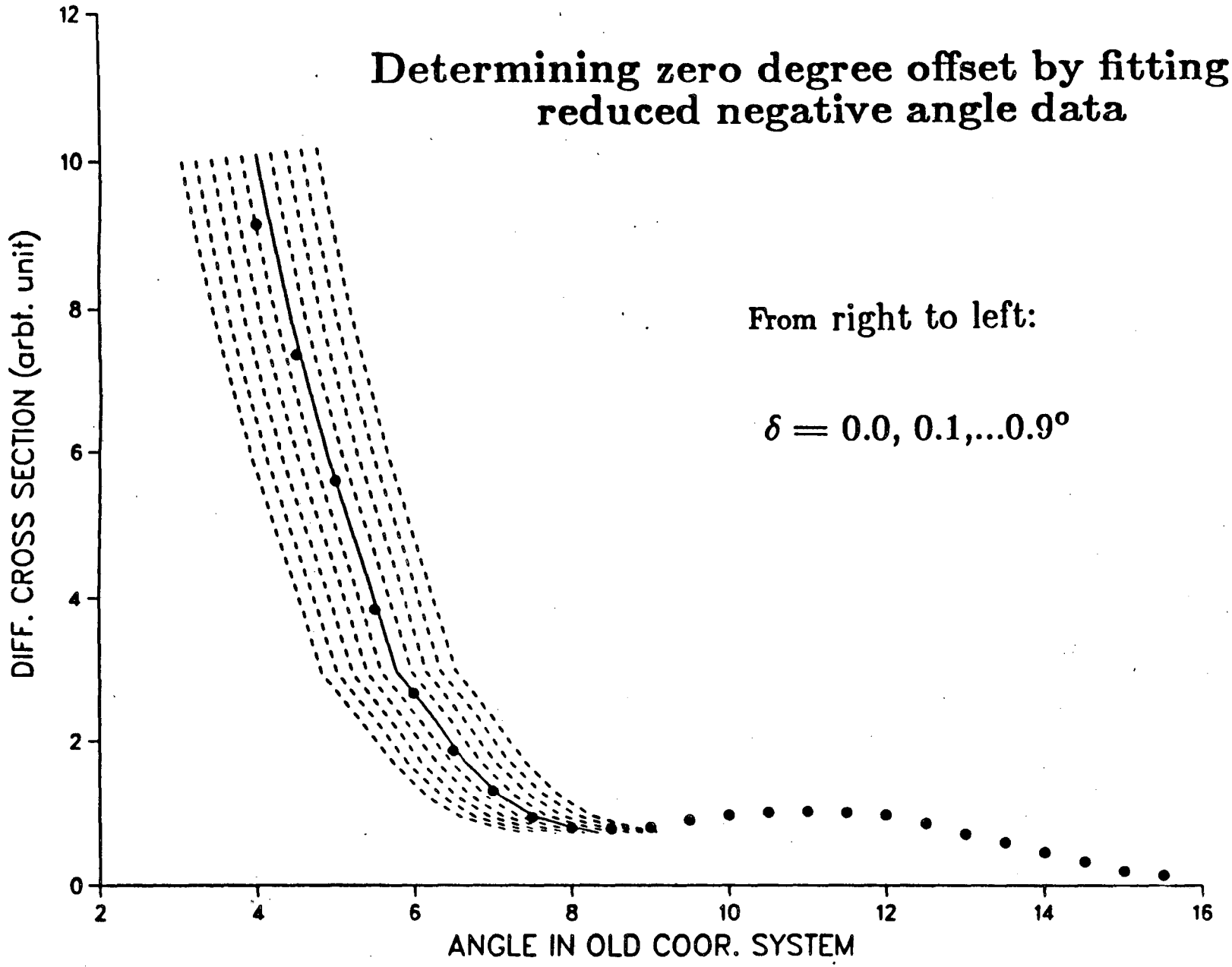
Determining zero degree offset by fitting reduced negative angle data
From right to left:
$\delta = 0.0, 0.1, \ldots 0.9^{o}$
DIFF. CROSS SECTION (arbt. unit)
ANGLE IN OLD COOR. SYSTEM
0
2
4
6
8
10
12
14
16

Fig. 2.13

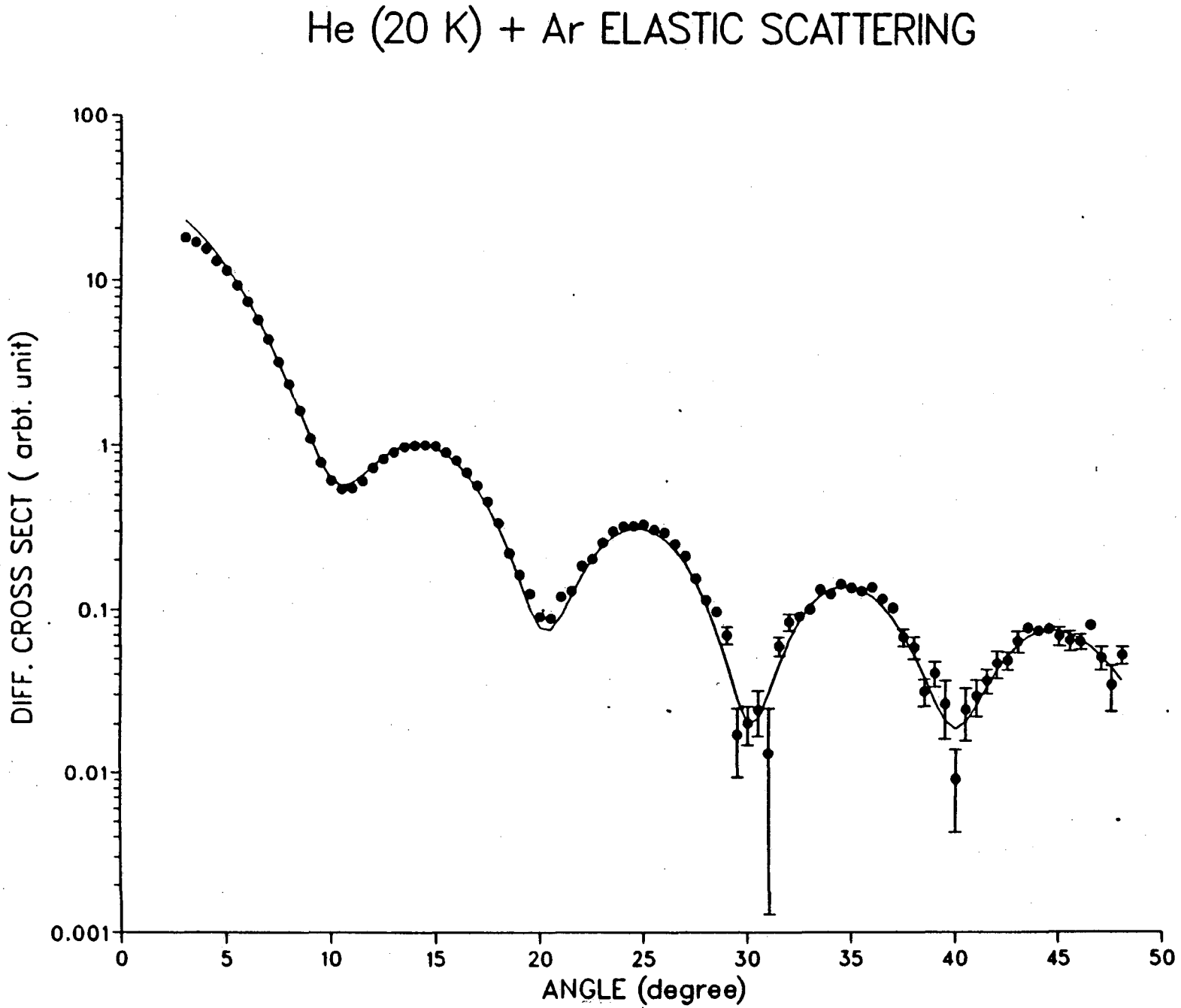
He (20 K) + Ar ELASTIC SCATTERING
DIFF. CROSS SECT (arbt. unit)
100
10
1
0.1
0.01
0.001
0
5
10
15
20
25
30
35
40
45
50
ANGLE (degree)

Fig. 2.14

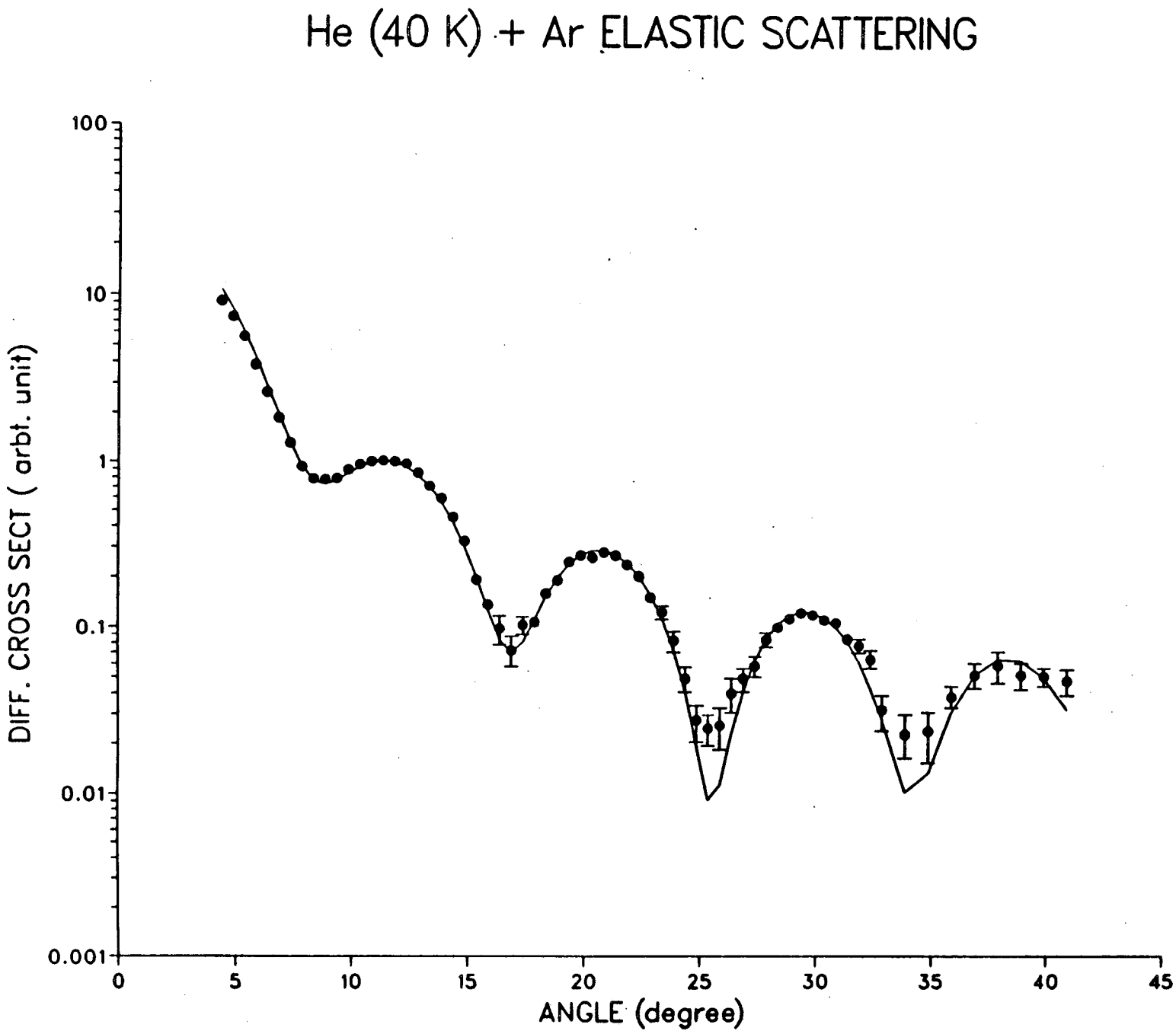
He (40 K) + Ar ELASTIC SCATTERING
DIFF. CROSS SECT (arbt. unit)
100
10
1
0.1
0.01
0.001
0
5
10
15
20
25
30
35
40
45
ANGLE (degree)

Fig. 2.15

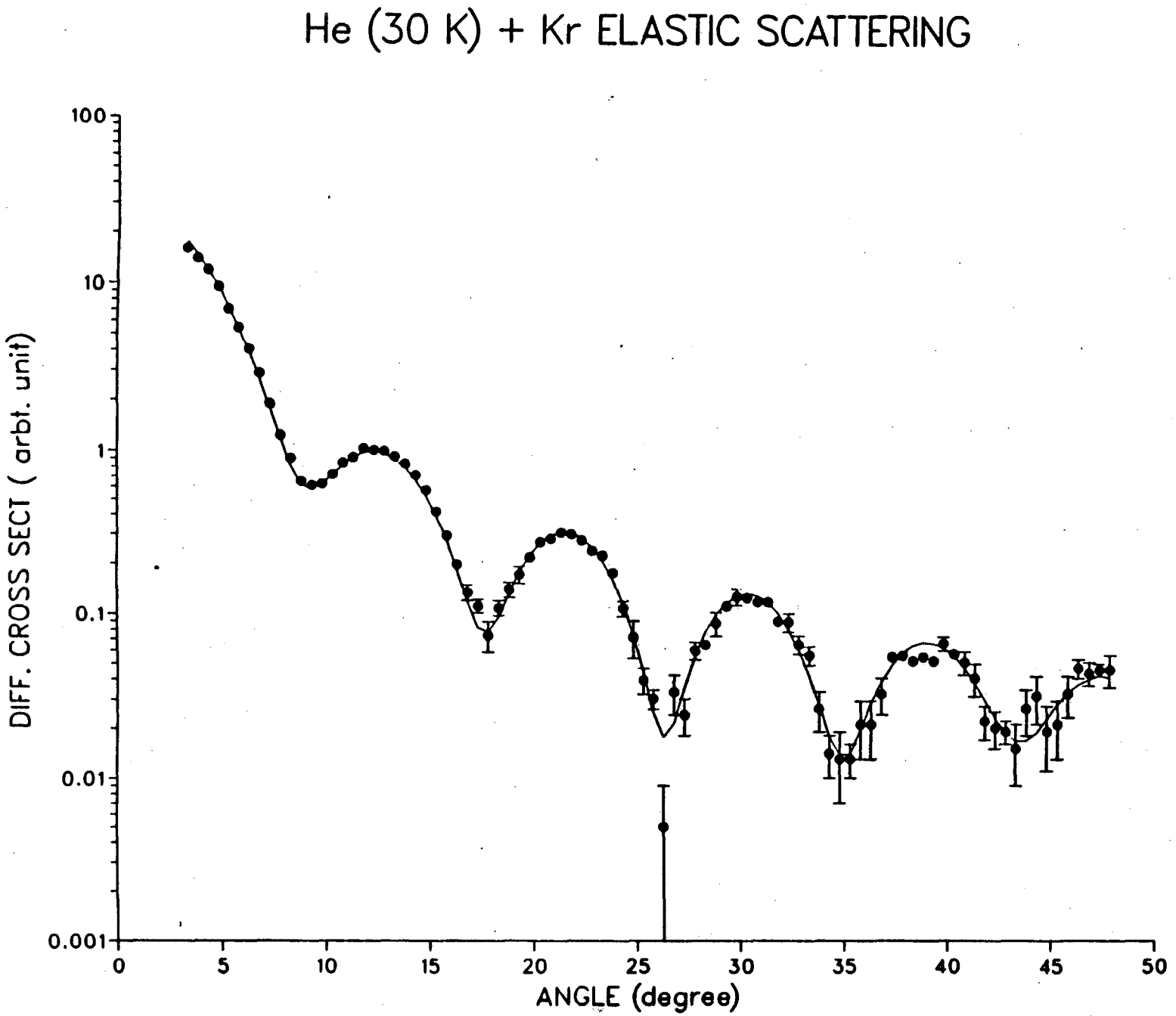
He (30 K) + Kr ELASTIC SCATTERING
DIFF. CROSS SECT (arbt. unit)
100
10
1
0.1
0.01
0.001
0
5
10
15
20
25
30
35
40
45
50
ANGLE (degree)

Fig. 2.16

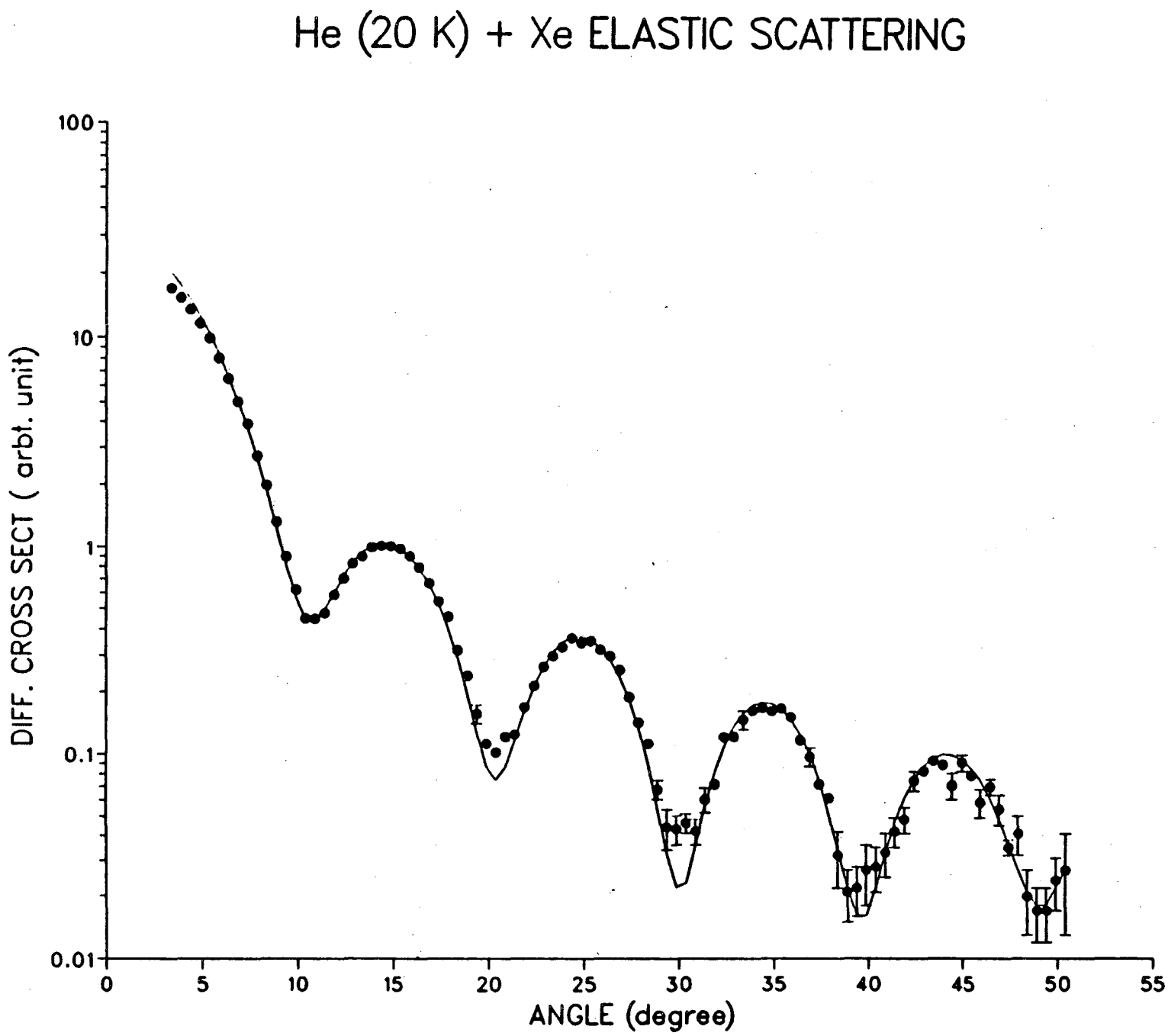
He (20 K) + Xe ELASTIC SCATTERING
DIFF. CROSS SECT (arbt. unit)
100
10
1
0.1
0.01
0
5
10
15
20
25
30
35
40
45
50
55
ANGLE (degree)

Fig. 2.17

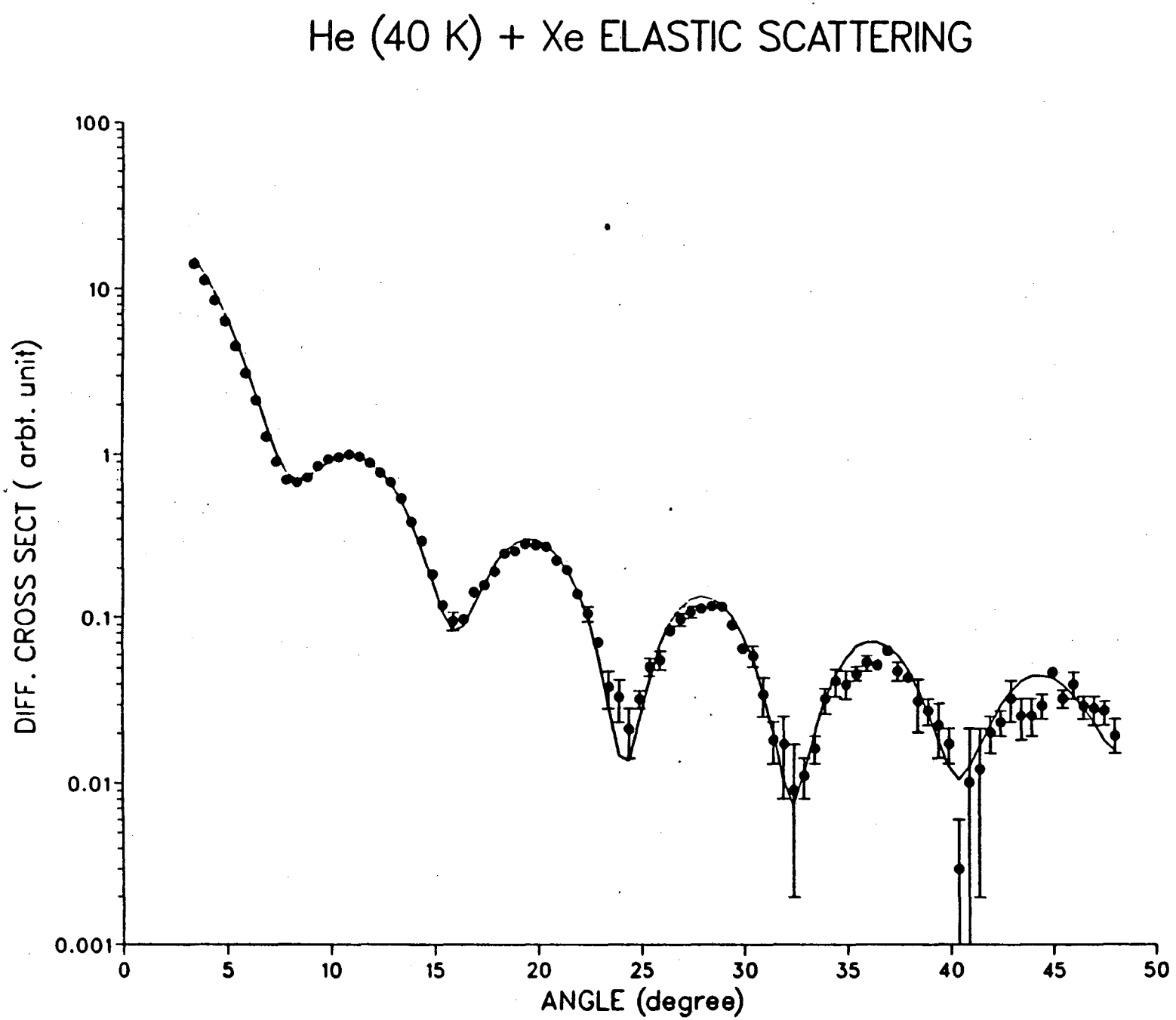
He (40 K) + Xe ELASTIC SCATTERING
DIFF. CROSS SECT (arbt. unit)
100
10
1
0.1
0.01
0.001
0
5
10
15
20
25
30
35
40
45
50
ANGLE (degree)

Fig. 2.18

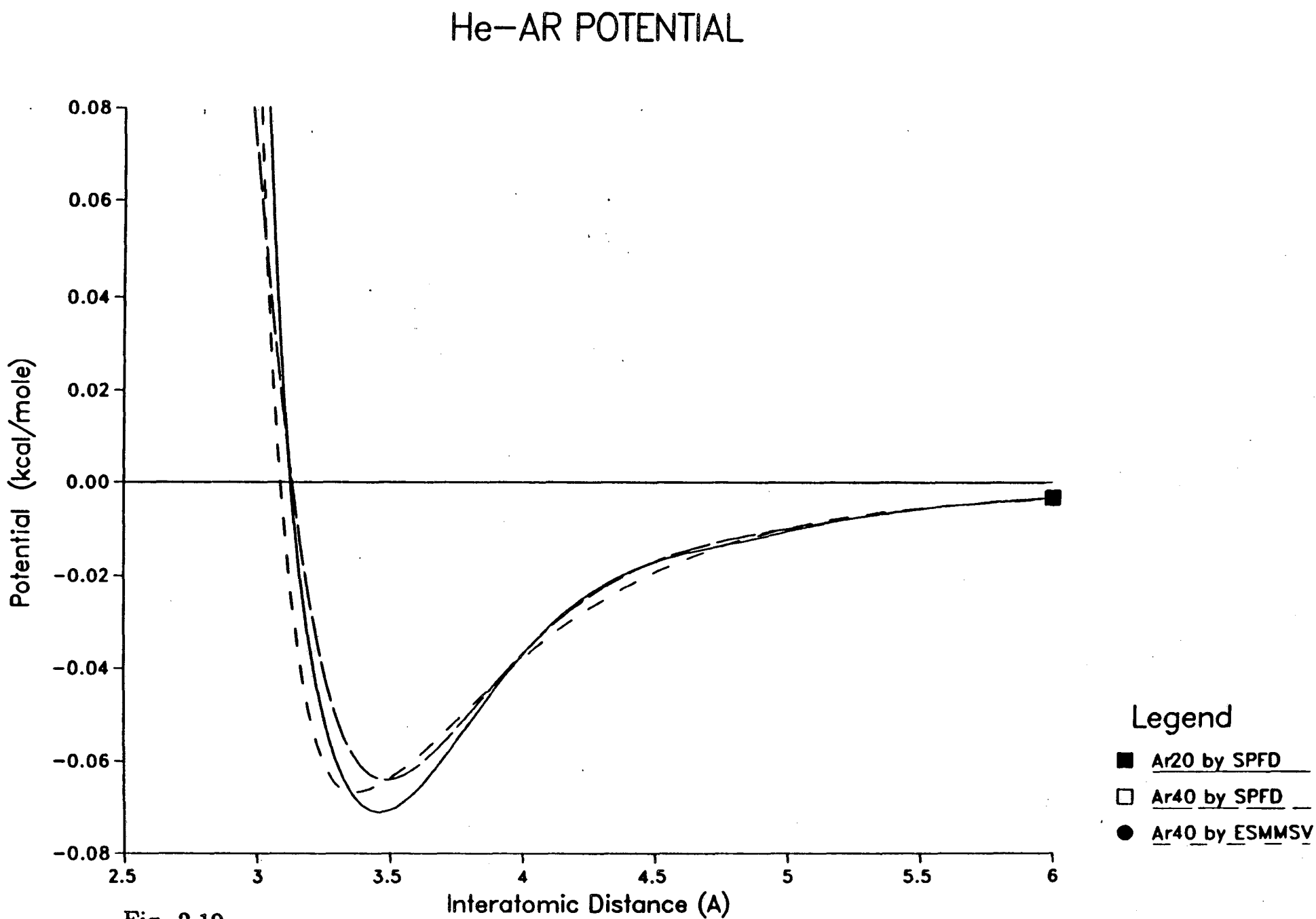
He–AR POTENTIAL
Potential (kcal/mole)
0.08
0.06
0.04
0.02
0.00
−0.02
−0.04
−0.06
−0.08
2.5
3
3.5
4
4.5
5
5.5
6
Interatomic Distance (A)
Legend
Ar20 by SPFD
Ar40 by SPFD
Ar40 by ESMMSV

Fig. 2.19

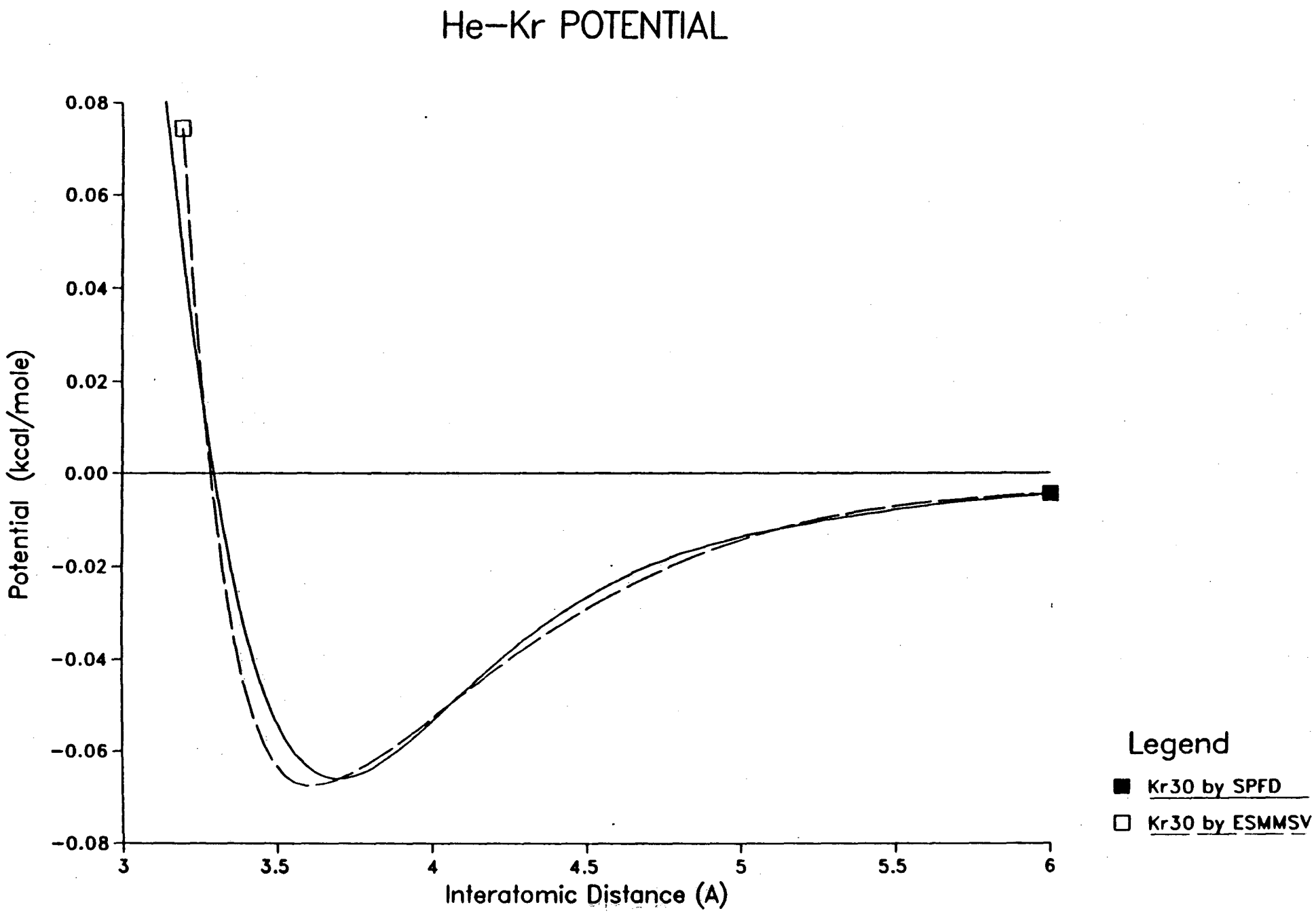
He–Kr POTENTIAL
Potential (kcal/mole)
0.08
0.06
0.04
0.02
0.00
−0.02
−0.04
−0.06
−0.08
3
3.5
4
4.5
5
5.5
6
Interatomic Distance (A)
Legend
Kr30 by SPFD
Kr30 by ESMMSV

Fig. 2.20

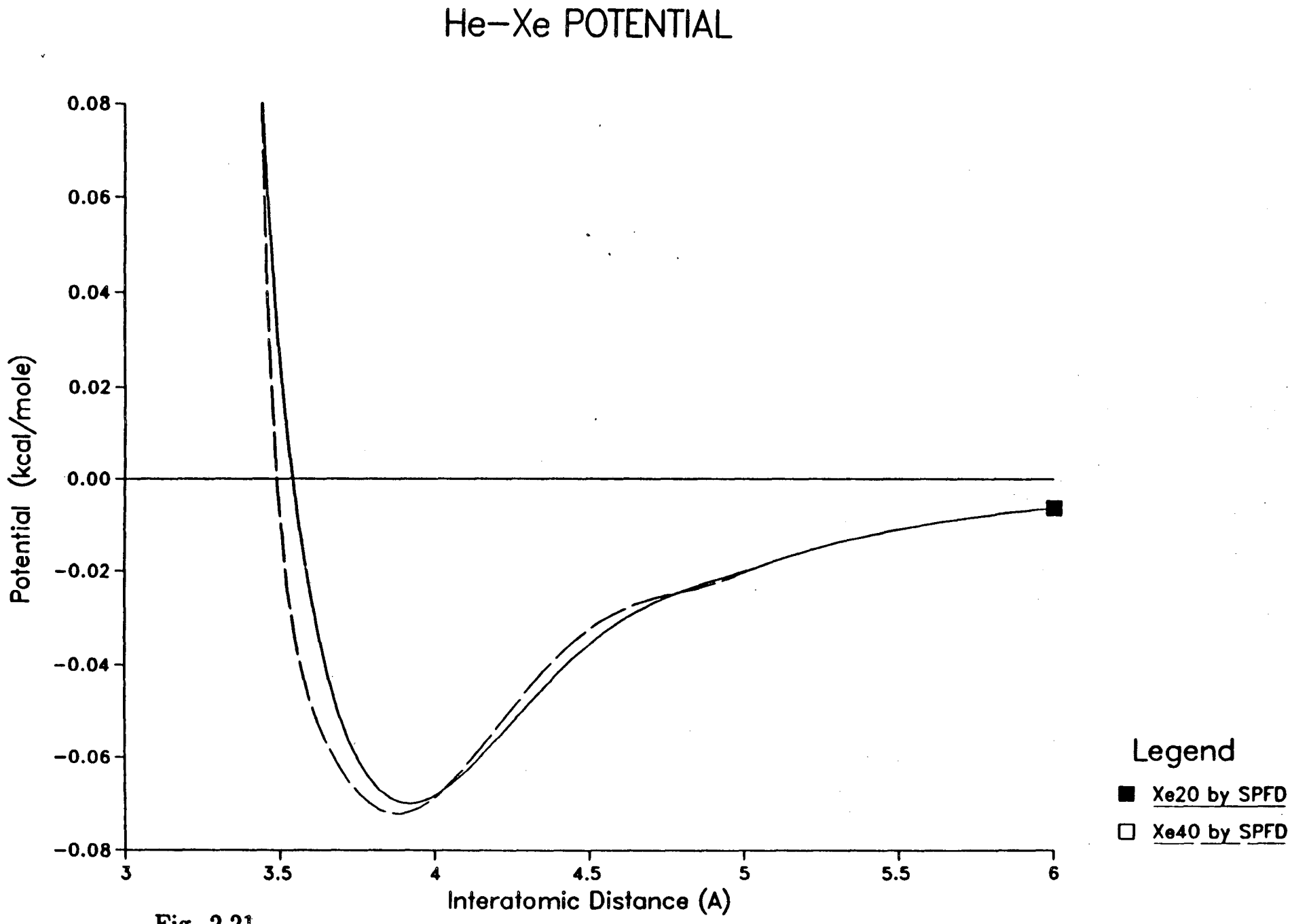
He–Xe POTENTIAL
Potential (kcal/mole)
0.08
0.06
0.04
0.02
0.00
-0.02
-0.04
-0.06
-0.08
3
3.5
4
4.5
5
5.5
6
Interatomic Distance (A)
Legend
Xe20 by SPFD
Xe40 by SPFD

Fig. 2.21

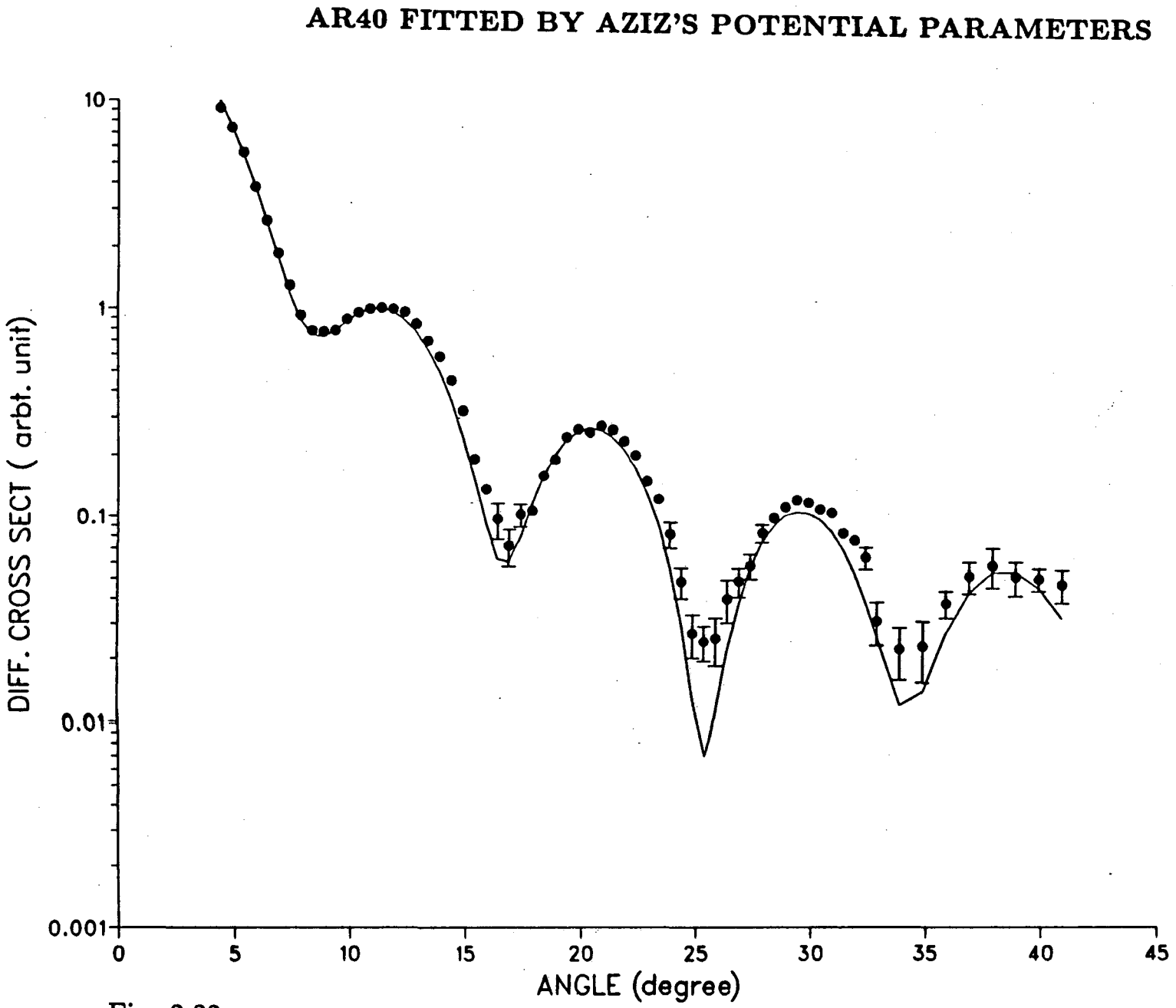
AR40 FITTED BY AZIZ'S POTENTIAL PARAMETERS
DIFF. CROSS SECT (arbt. unit)
10
1
0.1
0.01
0.001
0
5
10
15
20
25
30
35
40
45
ANGLE (degree)

Fig. 2.22

Chapter III. Reactive Scattering

Study of $O(^3P) + C_3H_4$

A. Introduction

Studies of combustion processes have always been of great interest since they are related to energy resources, industry, and environment science. An incompatible fact is that few combustion mechanisms are well known today although the history for humans utilizing combustion began more than ten thousand years ago. The difficulties existing in combustion studies are:

(1) Many products that result from a multi-channel reaction with many processes in each channel. For instance, the reaction of oxygen with ethylene was studied by Cvetanonic[1] in 1955. The final products he obtained were

$$\begin{aligned} O + 1.38C_2H_4 \rightarrow \quad & .5CO + .15CH_3CHO + .2C_2H_5CHO \\ & + .05C_3H_7CHO + .03C_2H_4O + .04CH_2CO \\ & + .09H_2 + .11CH_4 + .17C_2H_6 + .17C_3H_8 \\ & + p(C_2H_4O)_s \qquad ps = .03 \end{aligned}$$

To extract a mechanism from these products is really difficult. One can conceive of the difficulty when one attempts to figure out how the accident might have happened when merely seeing a bunch of debris in the junk yard.

(2) Usually not only the ground state but also the excited states are involved in an exothermic reaction. There might be energy transferred among different degrees

of freedom. Also, there might be internal conversion (IC), intersystem crossing (ISC), and some photochemical processes involved. Some of these processes might be carried out at a very high rate with energotic favourite. To separate these fast processes and know exactly what is going on at each step is the goal that people seek but for which most have not been successful.

However, much early work tried to reach this goal. In 1961, Jones and Cvetanovic studied[2] the reaction of $O(^3P)$ with benzene and toluene using mercury sensitized decomposition of NO_2 for the $O(^3P)$ source. Also, the technique of photolysis of N_2O for obtaining $O(^3P)$ is widely applied in many combustion studies. Havel *et al.* studied the reaction of $O(^3P)$ with allenes.[3] Hunziker *et al.* studied the photochemical modulation spectroscopy of $O(^3P)$ with olefins.[4] Hughes *et al.* studied[5] the reaction of $O(^3P)$ with condensed olefins below 100 K.

The other effective way to obtain oxygen atoms is by microwave discharge of O_2. Slagle *et al.* used this method[6] in the study of the reaction of oxygen atoms with vinylbromide. Andressen and Luntz studied[7] the reaction of $O(^3P)$ with saturated hydrocarbons. Replacing O_2 by NO + N, Lin *et al.* employed a microwave cavity to produce a oxygen beam in the study of reactions of $O(^3P)$ with allenes and methylacetylene.[8]

To overcome the difficulties of fast reaction rates, complicated multi-channel mechanisms, and identification of intermediates, many newly developed techniques have been applied. Crossed molecular beams is the most successful one. As we introduced in Chapters I and II, The elementary process can be well isolated in a

single-collision environment. Product identification can be done with high resolution detectors. Both angular distribution and velocity distribution measurements provide a lot of dynamic information such as the energy distribution among the different degree of freedoms, the entrance and exit barriers, the favored reaction orientation, relative intermediate lifetime, and so forth. In 1972 Kanofsky and Gutman[9] claimed direct observation of products produced by O-atom reactions with ethylene and propylidene using the technique although their beams were not perfectly secondary-collision proof. In the 80's many experimental studies of the reactions of oxygen atom with unsaturated as well as saturated hydrocarbons have been carried in the Lee group.[10-18] Oxygen-atom insertion and hydrogen-atom substitution mechanisms are suggested in many reactions involving unsaturated hydrocarbons,[10-15] and the abstraction of H-atom in reactions of oxygen with H_2 and saturated hydrocarbons[16-18] have been found.

Among the unsaturated hydrocarbons, allene came to be regarded as a chemical curiosity, mainly of interest for its unusual stereo-chemistry. Unlike the conjugated dienes, allene has a cumunulative bond system. The two π-orbitals are perpendicular to each other, and so are the two terminal CH_2 groups. Based on previous studies[3,8], the reaction of allene with oxygen is known to be exothermic with $\Delta H°$=-119.4 kcal/mole and $E_a = 1.6 \pm 0.5$ kcal/mole. The final products are carbon monoxide and ethylene which result from oxygen atom attacking the central carbon of allene to form a ring intermediate, cyclopropanone, followed by dissociation of this intermediate. To confirm this mechanism, and to look for other possible

reaction channels are the motivation of this study. A preliminary experiment has been done, and a new channel which is different from the central-carbon-attack channel was found. A theoretical study focusing on the two channels has also been done. In Part II (theoretical study) of this thesis, there is a more detailed systematic study on the reaction. In the experimental part, besides the details and results, I pay particular attention to the technique necessary to obtain the oxygen beam which is essential for the experiment.

B. Oxygen beam source

1. Radio Frequency Discharge

As introduced in last section, there are various techniques to obtain oxygen atoms. The one we employed is the radio-frequency (RF) discharge. In the molecular beam experiment a hot (v = 1000 - 2000 m/s), intense ($> 10^{18}$ atoms/sr/s), and stable oxygen beam source is needed. Compared with the microwave discharge, both produce hot plasmas in which oxygen atoms are produced from dissociation of O_2 or NO + O, but the RF discharge is better for obtaining a more stable high intensity beam. Because of the longer wave length of RF, the discharge conditions are insensitive to the geometric parameters and the change of media density during the ignition of discharge.

In 1979 Sibener *et al.* developed a oxygen beam source based on RF discharge in the Lee group. One may find a detailed description in their publication.[22] The major working part is a quartz nozzle with coolant jacket surrounded by a copper coil which, as a terminal of the RF output, provides an intense electromagnetic field to induce the discharge in the nozzle. The block diagram is shown in Fig. 3.1. where the RF wave is initially generated by a oscillator and amplified by a linear amplifier then, via a matching network, the power is transmmited to the working part which we have been described.

The working conditions of our experiment are listed in Tab. 3.1. In such a hot plasma generator and power transfer (120 - 300 W) system, the discharge must be carried out under optimal conditions. Any mistuning, ill-matching, and inefficient

transfer may cause discharge failure, low plasma temerature, or equipment damage.

In such a RF range (14 Mc), the physical and geometric factors such as the dimension of the coil and wires, composition and pressure of the gas, nozzle aperture diameter, and even the coolant property can considerably affect the discharge. Thus, for any new set of parameters the system needs to be carefully re-adjusted. Since the main part is installed in the high vaccum chamber of the molecular beam machine, a good knowledge of the plasma mechanism and network should help one to work effectively on this aparatus and to obtain a better quality oxygen beam.

2. Plasma Mechanism

From glow discharge (low pressure and low temperature) to arc discharge (normal pressure and high temperature), plasmas have been utilized for more than 100 years. The mechanism of glow discharge has been well studied.[20,21,23–26] However, the mechanism of arc ignition is not known as well. In our plasma generator, the discharge is similar to a glow discharge but at higher pressure. An interesting phenomenon of the cool plasma to hot plasma transition at a critical point has been observed. I intend to apply gas molecular collision theory[19] to describe the whole process which includes (1) low pressure ignition and (2) high pressure hot plasma production. I will also analyze the the energy transfer from the LC tank circuit to the discharge medium via (1) capacity discharge and (2) inductive discharge.

a. Low pressure ignition

The acceleration of electrons in an external electromagnetic field and the collision between electrons and molecules are the two major processes which dominate the ignition process. Before ignition energy is accumulated in the acceleration of electrons and the collisions are *elastic*. When the energy of the electrons is above a certain threshold, bombardment will cause ionization, excitation, and dissociation. These collisions are *inelastic*.

The following are necessary conditions for ignition:

(1) *seeds*. They actually exist everywhere. For instance, due to cosmic rays and the earth's radiation there are always 5 pairs of ions produced in 1 cm^3 atmosphere per second.[5] Even in a chamber separated by a thick wall or an underground cave

the air is still filled with some residual free electrons. During experiments we found it hard to ignite when the apparatus was not used for a long time but easier to use after the first time, because residual ions could stick to the walls of quartz nozzle for a while and the seeds might help the ignition.

(2) *the electromagnetic field.* It is the driving energy resource. It initially accelerates the electrons and compensates the energy loss caused by collisions.

(3) *enough mean free path.* This provides enough space for electron acceleration, and lets the electrons gain enough velocity before colliding with other particles.

In Fig. 3.2 is a diagram of a collision between an electron and a molecule. The large arrow points in the direction of the external electric field E. An electron e collides with a molecule M at A and subsequently collides with another molecule at B. The interval AB is the mean free path λ. The energy and momentum conservation laws require

$$\frac{1}{2}mv^2 = \frac{1}{2}mv'^2 + \frac{1}{2}MV^2 \tag{3.1}$$

$$mv = MV - mv' \tag{3.2}$$

where m and M are the masses of the electron and molecule, respectively, and v and v' are the velocities of the electron before and after the collision respectively; V is the velocity of the molecule.

Canceling V from (3.1) and (3.2), we get

$$v' = (\frac{M-m}{M+m})v$$

and

$$E' = \frac{1}{2}mv'^2 = \left(\frac{M-m}{M+m}\right)^2 E$$

The energy loss is

$$\Delta E = E - E' = \frac{4Mm}{(M+m)^2}E$$

When $m << M$

$$\Delta E = \frac{4m}{M}E \qquad or \qquad \Delta E = \chi E \tag{3.3}$$

Since the collision is not always collinear we may take the average $\chi = 2m/M$. When an electron collides with Ne, $\chi = 5.4 \times 10^{-5}$. When an electron collides with O_2, $\chi = 3.6 \times 10^{-5}$. One can see that the energy loss is really small.

If the energy loss could be compensated by the external electric field the process would reach equilibrium

$$eE\lambda cos\theta = \frac{1}{2}\chi m v^2 \tag{3.4}$$

Taking the statistical average over the individual collision leads to

$$eE\lambda < cos\theta > = \frac{1}{2}\chi m < v^2 > \tag{3.5}$$

From Fig. 3.2, $cos\theta = AD/\lambda$, and AD = AE + ED, where AE is the thermal random walk length and ED is the draft motion interval.

$$AE = vtcos\beta \tag{3.6.1}$$

$$ED = \frac{1}{2}\left(\frac{eE}{m}\right)t^2 \tag{3.6.2}$$

Since $< cos\beta > = 0$ the thermal random walk term vanishes. Substituting $t = \lambda/v$ into (3.6.2), then into (3.4) we get

$$\bar{v}^4 = \frac{e^2E^2\lambda^2}{m^2\chi} \tag{3.7}$$

ignoring the difference between $< v^2 >$ and $< v >^2$ since it doesn't make a significant difference for our qualitative analysis. Finally we get the formula

$$\bar{v} = \sqrt{\frac{eE\lambda}{m\sqrt{\chi}}} \quad . \tag{3.8}$$

Now let us calculate the translational temperature of electrons under our experimental conditions. At 0° C and P = 1τ the mean free paths for Ne and O_2 are 6.6 $\times 10^{-2}$ and 4.1 $\times 10^{-2}$. At P = 5τ we take $\lambda \approx 1.0 \times 10^{-2}$ and the electric field intensity $E \approx 60$ v/cm. By using (3.8)

$$\begin{aligned} \bar{v} &= \sqrt{\frac{60 \times 4.8 \times 10^{-10} \times 10^{-2}}{9.1 \times 10^{-28}\sqrt{4 \times 10^{-5}} \times 300}} \\ &= 4.07 \times 10^{8} cm/s \end{aligned}$$

Compared with the mean velocity of electrons at room temperature

$$v_0 = \sqrt{\frac{3KT}{m}} = 1.16 \times 10^{7} cm/s$$

By using the relation

$$T_e = \left(\frac{\bar{v}}{v_0}\right)^2 T$$

and T= 300 K we get

$$T_e \approx 369,313K$$

The equivalent energy of electron is about 31 eV. Compared with the ionization potentials and dissociation energies which are listed in Tab. 3.2, we can see that when the output voltage reaches E = 30-100 V/cm it should be easy to ignite the mixture of O and Ne (or He) at P = 1-5τ. The ionization potential of He is 3 eV higher than that of Ne. According to Eq. (3.8) E should be increased by 13.5%

when seeding in He. Since E $\propto$ V and the output voltage is proportional to the ratio of n_2/n_1, we should increase the ratio by 13.5% by moving the tap position lower.

When we use a small nozzle aperture and 500 τ instead of 300 τ the mean free path will be reduced by 60%. Accordingly we should increase E by 60% by lowering the tap position.

Under this low pressure the features of the discharge are:

(1) The temperature of electrons is high; and molecules is large (more than 3 orders of magnititude). This is a low-entropy system where the energy randomizing between electrons and ions is unlikely although both exist in the same nozzle. It is caused by the long mean free path and the poor transfer efficiency (see Eq. (3.3)). But under high pressure collisions will be increased as well and the energy transfer becomes more important. We are going to discuss it for hot plasma case.

b. Hot Plasma and Critical Phenomena

At the beginning of the ignition the high pressure makes a short mean free path and kills the accumulation of the translation energy of the electrons. But as soon as the ignition starts the increasing pressure becomes helpful. Because electrons have been speeded up, there is no need to worry about collision any more since the bombardment produces more free electrons and the energy loss can be compensated by absorbing more energy from the external field. The discharge process can be maintained by itself. One should gradually increase the gas pressure at that time to obtain a hot and intense plasma.

The absorption of energy can be understood by the following analysis. Taking a one-dimensional collision as an example, the electionic motion satisfys

$$m\dot{v} + \nu m v = eEe^{i\omega t} \tag{3.9}$$

where the second term is the momentum change in the collision, and ν is the collision frequency. Solving Eq.(3.9) we get

$$v = \frac{e^{i\omega t}}{\nu + i\omega} \tag{3.10}$$

Multipling by e we get the current

$$I = \frac{ee^{i\omega t}}{\nu + i\omega} \tag{3.11}$$

The energy is

$$P = Re(I\bar{U}) = \frac{\nu E e^2}{\nu^2 + \omega^2} \tag{3.12}$$

One can see that if $\nu = 0$ the electric field does not do work. Without collisions (no second term in (3.9)), the electrons would move according to the frequency of the external field. But there is a 90° phase difference between the electronic current and the external E. No work is actually done. We have also shown that the working impedance has the property of *pure resistance*. In short, if no collision, there will be no energy transfer and discharge ! The electron, as a medium of energy transfer, plays a central role here.

The experimental observation is that the transition from a cool plasma to a hot plasma does not occur gradually. Fig. 3.3 shows that there is a critical point (p $\approx 330\tau$) where the beam source chamber pressure shows a sudden drop. Before the

critical point the ratio of off/on (RF power turned off and on) pressure is about 1.6 which indicates the plasma is cool. But when pressure is increased higher than the critical pressure the ratio suddenly jumps to 2.6.

The critical phenomena can be understood as following: At low pressure the collisions between electrons and molecules are not important, but when the pressure reaches a certain level the velocity of the molecules is increased by a high frequency collisions. Notice that the frequency is proportional to the velocity

$$\nu = \sqrt{2}\pi n \sigma^2 \bar{v} \tag{3.13}$$

For O_2 , $\sigma = 3.62 \times 10^{-8}$ cm. At T = 273 K and p = 330 τ the frequency of one O_2 molecule colliding with electrons is 7.22×10^8 /sec. The increased velocity positively feedsback to increase the collision frequency, more frequent collisions provide more chances to gain energy....., and the temperature will suddenly go up. The plasma becomes hot from there on.

The above analysis is based on the assumption that there exists only an electric field. But actually besides the electric field there is an intense magnetic field as well. We should also notice that in the LC tank circuit the coil is mainly for storage of magnetic field energy rather than electric field energy.

c. Inductive discharge

Along the axial direction of the coil there is an intense magnetic field. The electron moving in the quartz nozzle will follow a path bent by the Lorentz force

$$\vec{f} = e\vec{v} \times \vec{B} \tag{3.14}$$

But this force does not do work on the electrons since the direction of the force is perpendicular to the direction of motion. Taking $\vec{B}$ = constant and solving the following equation

$$m\dot{\vec{v}} = e\vec{v} \times \vec{B} \tag{3.15}$$

the electron trajectories can form a circle with radius r (Larmov radius) and the plane is perpendicular to the direction of the magnetic field. The stronger the field strength and the smaller the mass, the smaller r. We see again that electrons play a more important role than ions. With enough mean free path one may expect that all the electrons rotate to form a magnetic dipole moment which is parallel to the magnetic field direction in order to lower the energy.

Establishing an *order* motion of particles always requires the consumption of energy, but in this case the energy is stored in the form of rotational energy and is not released.

In an alternating magnetic field $\vec{B} = \vec{B}_0 e^{i\omega t}$ the electron trajectories could be obtained by solving the following equations:

$$\begin{aligned} m\dot{v}_x &= ev_y B_z e^{i\omega t} \\ m\dot{v}_y &= -ev_x B_z e^{i\omega t} \end{aligned} \tag{3.16}$$

The detailed mathematical derivation will not be presented here, only a brief description instead:

The trajectory is a combination of two motions:[20] (1) electrons rotate about a certain axis; (2) the axis varies periodically under the influence of the alternating external magnetic field. The motion of the axis direction might be either vibration, rotation, or a combination of these.

In general, the above two motions do not do any work since (1) the rotational plane of the electron is perpendicular to the Lorentz force; (2) If there is no phase lag between the axis of rotation and the direction of the alternating external field there is no angular difference between the magnetic dipole moment and the external field at each moment. Therefore the torque vanishes.

To illustrate the second point we may think of an asynchronous motor with no load. The current is zero unless the rotor rotates slower than the magnetic field.

However, under the following conditions the energy consumption and energy transfer may happen:

(1) When electron collides with a molecule it destroys the *order* motion (electrons rotate around the axis which exactly follow the alternative direction of external field) of the electron. The external magnetic field will provide the energy to recover the *order* motion in order to lower the energy of the system. During this process an angular difference between the external field and the magnetic dipole moment exists. The work done by the non-zero torque will require the external field to provide the same amount of energy.

(2) When the average magnetic field strength changes, say, becomes weaker, the Lorentz force is not strong enough to bind the rotation of the electrons and the energy stored in rotational motion will be transferred to translational energy. Then the electrons will behave similarly as in the other case, that is, the electron will collide with molecules in the way analyzed in the last section.

This second case can be utilized to form a supersonic beam and to keep the

hot plasma concentrated at the tip of nozzle. This phenomenon has been applied in plasma physics and the term "magnetic nozzle" of supersonic beam has been used.[21] Inside a coil the strength and the direction of a magnetic field is constant, but at the tip of the coil the magnetic field lines diverge. There is a rapid change of field strength. The stored rotational energy is released suddenly. It happens just like a stone fasten to one's hand by a thread that is whirled with a high rotational speed and the thread suddenly breaks.....

Finally the effect of the coil dimension will be discussed. Fig. 3.4 is the calculated magnetic field distributed along the Z-axis with four geometries. The different geometries are listed in Tab. 3.3. From the plot we see that the field can be concentrated in the front part of quartz nozzle by choosing $r_1 < r_2$ and $l_1 < l_2$.

3. Operation of Apparatus

a. Matching

Matching is the key to success. As well-known, between source circuit and load circuit when $R_{out} = R_{in}$ the energy transfer reaches a maximum. But since we work in a RF system where many non-resistive elements exists as well, the matching problem turns little bit complicated. It includes : (1) non-resistance matching and (2) resistance matching. Basically these two matching are independent, but under certain condition there exists an interaction between them. These will be analyzed in the following.

We denote the impedance of the source circuit by Z_1 and the load circuit by Z_2, and write

$$Z_j = R_j + i\rho_j \quad (j = 1, 2) \tag{3.17}$$

where R is the pure resistance and ρ is the imaginary component which has a 90° phase difference from the pure resistance. R_1 mainly results from the inner-resistance of the vacuum tube of the linear amplifier(LA). R_2 is the discharge resistance. (we will show why the character of gas discharge is purely resistive). The imaginary component ρ results from various capacitances, coils, and distributed inductances of the wires.

Fig. 3.5 shows the circuit diagram. Assuming that the source S generates a potential U_1, the total current is

$$I = \frac{U_1}{Z_1 + Z_2} \tag{3.18}$$

The voltage drop across Z_2 is

$$U_2 = I \cdot Z_2 = \frac{U_1 Z_2}{Z_1 + Z_2} \tag{3.19}$$

In a complex circuit the power is defined as

$$P = Re(I \cdot \bar{U}) \quad or \quad Re(\bar{I} \cdot U) \tag{3.20}$$

where the upper bar represents "complex conjugation". The power obtained in Z_2 is

$$P_2 = \frac{\mid U_1 \mid^2 Re(Z_2)}{\mid Z \mid^2} = \frac{\mid U_1 \mid^2 R_2}{\mid Z \mid^2} \tag{3.21}$$

By using expression (3.1) we get

$$P_2 = \frac{\mid U_1 \mid^2 R_2}{(R_1 + R_2)^2 + (\rho_1 + \rho_2)^2} \tag{3.22}$$

Assume R_2 and ρ_2 are adjustable. In order to obtain optimal energy transfer the following conditions should be satisfied

$$\frac{\partial P_2}{\partial \rho_2} = 0 \quad and \quad \frac{\partial P_2}{\partial R_2} = 0 \tag{3.23}$$

Substituting P_2 from Eq. (3.22) into (3.23) we obtain

$$\rho_1 + \rho_2 = 0 \tag{3.24.1}$$

$$R_1 = R_2 \tag{3.24.2}$$

The meaning of (3.24.1) and (3.24.2) is simple and clear: besides the general requirement that $R_1 = R_2$, the imaginary components in the circuit should cancel each other.

However, our system is set up such that the design attempts to achieve a stronger condition than Eq. (3.24). The design demands both $\rho_1 = 0$ and $\rho_2 = 0$ instead of canceling each other. The adjustment procedure to obtain these conditions is: (1) Set the working frequency of generator to be ω; (2) Adjust the capacity of the LA to be resonant with ω. (3) Adjust the capacity of the LC tank circuit to be resonant with ω. Obviously steps (2) and (3) make $\rho_1 = 0$ and $\rho_2 = 0$. This adjusts the "local resonance" rather than the "total resonance". The advantage is that the total system is more stable whenever disturbances arise from either the source or the working part. It is also easier that way to adjust and re-adjust when mistuning is caused by condition changes.

b. Non-resistive matching

The difficulties of matching perfectly come from:

(1) distributed parameters: The coupling between the wires, coil, capacitor plates, and chassis will induce additional capacitance or inductance. For example, putting on a reducer flange to the beam source will cause about a 10 pf capacity increase. This would have little effect on a low frequency circuit, but has a great effect on a RF circuit since the total capacity of LC tank circuit is only 75 pf ! Eventually the distributed parameter will destroy the resonant condition.

(2) changes in working conditions: Fig. 3.6 shows the effective circuit diagram of the discharge. The solid line represents the LC tank circuit. The energy is coupled in across a few turns ($n_1 \approx 2\frac{1}{4} - 2\frac{1}{2}$). The ground connection is provided by a tap whose position on the coil is removable, and thus to form a self-boost transformer

with variable turn ratio (equivalently drawn by a primary coil input transformer). The dotted line in the drawing represents the coupling between the secondary coil and the discharge medium where R_d is the working resistance of the discharge, C_d is the coupling capacity and L_d is the coupling inductance. Before ignition, because $R_d = \infty$, the coupling circuit (dotted line) actually dose not exist. But as soon as the discharge starts the energy will be transferred to the medium via both (1) capacitive coupling and (2) inductive coupling. As these two branch circuits are connected with LC tank circuit, the resonance will be destroyed.

Therefore, an impedance matching network is necessary to perform a complementary adjustment. It provides a positive or negative ρ to cancel the residual $\rho_1 + \rho_2$ components.

$$\rho_1 + \rho_2 + \rho = 0 \tag{3.25}$$

Fig. 3.7 is a matching network circuit diagram where L and C_2 make possible $\rho > 0$, and C_1 enable $\rho < 0$.

When the discharge starts, R_d will change according to the pressure and temperature of the gas. In general, a larger discharge current will induce a smaller R_d, and a smaller R_d will increase the effect of coupling capacitance and coupling inductance. This is what could be called the interaction between resistance matching and non-resistance matching. Thus , while increasing the pressure of the working medium one must carefully hold the resonance condition by finely adjusting C_1 and the C_2 to keep the SWR values as close to one as possible.

Sibener *et al.* observed[22] that at different pressures one should apply different

working frequencies. It is not hard to interpret this observation, since ρ_1 and ρ_2 relate to ω as

$$\rho = \omega L \left(1 - \frac{1}{\omega^2 LC}\right) \tag{2.26}$$

Changing ω will allow one to satisfy the resonance condition, The adjustment procedure is $\omega \rightarrow \rho_2 \rightarrow \rho_1$.

Here I suggest a new way to satisfy the resonant condition. The order is $\rho_2 \rightarrow \omega \rightarrow \rho_1$. The usual way is to set up ω first, then according to ω adjust the LC tank circuit. My suggestion is to fix the LC tank circuit and vary ω to satisfy the resonance conditions followed by optimizing the LA parameter. Fig. 3.8 shows a comparison between the present design and my suggestion. The big advantage is that the variable capacity can be replaced by a small size fixed capacity. We can get rid of all the items above the beam source by placing a small fixed-capacity (30-75 pf) into the source. We can save two long copper wires plus a ground connection wire. The input junction is moved to the coil tap position (TP) and the coaxial shield of the cable can be used as a ground. Thus we can (1) reduce all the energy loss which was caused by a) skin effects, b) radiation, and c) eddy current in the connection path; (2) improve the Q-factor ($Q = \sqrt{\rho/R}$) and resonance; (3) eliminate many possible sources of problems (feedthrough, junctions); (4) reduce the unexpected and unpredictable distributed parameters. I'd like to estimate several examples of these losses:

(1) The resistance of bare copper wire for 14 MC AC is relatively large due to the skin effect. The energy cosumed in the wire may cause the solder to melt at the

junction of the feedthrough or the tap if the cyclicing water is not on.

(2) The eddy current induced by electronic and magnetic field coupling between wires and sharp edges of metal could cause the plastic support burning to dark.

(3) The power output impedance is designed to be 50 Ω. Several Ω induced by the skin effect and junctions will worsen the resonance curve.

(4) The power used in the discharge is believed to be less than 50 W.[8] The power supply provides 250-300 W power. That is a 200-250 W loss! The one major loss is the plate dissipation of the LA. The other is the long distance connection between the capacity outside and the coil inside. The elimination of three long connection wires is a big improvement, because in a RF circuit even inch shorten always has a great effect.

c. Resistive matching

In general, the resistance matching problem is independent of non-resistance matching (see Eqs. (2.25) and (2.26)). In other words, it is not guaranteed that a hot plasma can be achieved even though non-resistance matching is perfect.

Since R_1 to R_2 are not adjustable, the only way left to change the ratio of n_1 and n_2 is by moving the tap position.

$$\frac{R_1}{R_2} = \left(\frac{n_1}{n_2}\right)^2 \tag{2.27}$$

Notice the square dependence in the formula. It is easy to understand why the ratio of turns dramatically changes the matching. Even a 1/12 turn will make an enormous differece.

How to find the right tap position ? This is certainly a trial-and-error process. But from observing the working condition we can make comparison and decide how to make adjustments. Since the pure resistance is induced by the draft current during the discharge of the gas, a larger draft current causes a smaller resistance. In plasmas electrons are the major charge carriers. The motion of electrons under the external field forms the draft current. The motion of ions also forms a current but it is less important since ions move much slower. The intensity of the current is determined by the density and the velocity of electrons, and the velocity is determined by the intensity of the external electric field and the length of the mean free path. The intensity of the electric field is determined by the power supply and geometry, and the mean free path is determined by the pressure and type of molecule. After ignition, the yield of electrons by bombardment ionization will be competitive with the recombination of ions and the equilibrium density will dominate the amplitude of the drift current.

The following are several examples:

(i) Seeding the gas in Ne will cause a larger draft current than seeding in He. The tap position should be moved up (to reduce the ratio by increasing n_1) when using Ne.

(ii) When using a smaller nozzle aperture the tap position should be moved down since the smaller aperture induces a smaller draft current.

(iii) When using higher pressure, the tap position should be moved down since the high pressure reduces the mean free path and that makes it harder for the

electrons to move.

d. Trouble-shooting

a) *Tap position too low*: The coil, as a secondary part of the transformer, is supposed to produce a higher voltage. But the output impedance does not match the heavy load. The phenomenon is : The discharge is easy to ignite at a low pressure, but as the pressure increases, the brightness of the glow dims and dies off easily before reaching the working pressure. Sometimes it reaches the working pressure, but still dies off after few minutes. The plate current of the LA reads too high (> 300 ma). The LA, cable, especially the junction feels very hot. The output is very sensitive to change in the oscillator drive setting. But when the working pressure is reached, the output can not be increased further.

b) *Tap position too high*: This causes a low output voltage. The phenomenon is that the discharge is difficult to ignite. But as soon as it does, it won't die off when the pressure is inceased. There is no observable change in the brightness of the discharge glow before and after increasing the pressure. A really hot plasma can not be achieved. The plate current of the LA reads too low. It can not be raised to more than 200 ma.

During the pressure increase we observed a transition point at about 330 τ. It is a critical point where the cool plasma turns to hot plasma. One can observe both that the color turns brighter and the beam source chamber pressure suddenly drops down. But if the tap position is too high, this transition can not be seen, similarly if the tap position is too low. The critical point will be replaced by an unstable

region. In this region the glow flashes between bright and dull continuously, and the beam source chamber ion gauge and SWR reading oscillate accordingly.

In summary, we have seen that both the non-resistance matching and the resistance matching are independent. But the distributed parameters will cause the pure resistance to be impure, also the working resistance causes two branch of non-resistive elements to be added in. Thus any resistance adjustment will affect the non-resistive resonance and in turn be affected by it.

C. Preliminary Experiment

This experiment was carried out in the B-machine of the Lee group. The general operation has been described in Chapt. II. The major difference from that description is in the beam sources. The 2° beam was replaced by allene gas which is seeded in He, and oxygen atoms were produced by RF discharge with 95 % of Ne. The major condition for each beam is listed in Tab. 3.4. We had tried both Ar and Ne as seeding gases. As shown in Tab. 3.2, Ar has a lower ionization potential (15.76 vs 21.56 eV of Ne) and is easier to ignite, but seeding in Ne may obtain higher temperature beam. The performance was started by turning on the discharge when the vacuum pumping was ready. A few τs of oxygen stagnation pressure is good for ignition since the electrons need a longer mean free path to accelerate (see Sec III(B)). As soon as one sees the glow in the quartz nozzle through an observing window, one should carefully adjust the regulator to increase the oxygen mixture gas pressure. At the same time the adjustment on the matching network is necessary to be well accomodated with the change of pressure. Too fast in increasing pressure or inadequate adjustment in matching may cause the ignition failure. On the other hand, leaving the discharge running in few τs without increasing pressure may cause quartz melting and expansion of the nozzle aperture. During the discharge, it is dangererous to run the machine without water cyclicing. It may cause the solder at the junction to feedthrough and tap melting. In a worse case, it may damage the expensive quartz nozzle. An interlock is necessary for protection.

The angular distribution and velocity distribution of the reactive products were

measured. Plots of these quantities are shown in Figs. 3.9 and 3.10, respectively. In a scanned mass number search with the mass spectrometer, the most intense signal occured at m = 54 and 53. Due to the similar shape to the angular distribution at m = 55, it is believed that these are the fragments of the product C_3H_3O (m = 55). The other evidence is that the peak of the data curve occurs at 65° which is in good agreement with the calculated center of mass laboratory angle (60.9°).

This allenyloxy radical, C_3H_3O resulted from the oxygen atom attacking one of the terminal carbon atoms of allene molecule followed by kicking out a hydrogen atom. The reaction is

$$O(^3P) + CH_2CCH_2 \;=\; CH_2CCHO + H \tag{3.28}$$

which is a new reaction channel for $O(^3P)$ + allene. In contrast with the widely accepted $CO + C_2H_4$ product channel, this channel does not have a ring structure intermediate. A detailed comparison between these two channels will be made in Part II (theoretical studies).

In this channel, allene shows general unsaturated hydrocarbon behavior, that is: (1) The insertion of oxygen atom ($O(^3P)$) to a double bond makes a 1,3 triplet diradical; (2) The crowd sp^3 hybridation in oxygen attacked carbon becomes sp^2 after a hydrogen leaves. This behavior is consistent with previous crossed molecular beam studies of oxygen reaction with unsaturated hydrocarbons. The molecular beam technique is good for the detection of radical products since the active species won't exist long in collision environment. But the scattering detection needs enough intensity at each solid angle that cause difficulty in the study where products dis-

tributes in a wide range angle. It might be one of the reasons for failure to obtain signal at m = 28, because both products the carbon monoxide and the ethylene have the same mass in the other channel, and the equal masses makes both species move fast and result in a wide angular distribution. The other reasons will be discussed further in the theoretical part of this thesis.

Appendix: Butch's Theorem

The Butch's theorem is:

$$\frac{dA}{dt} = \frac{er}{4\pi m}\frac{d\Phi}{dt} \qquad (B1.1)$$

where A is the area scanned by trajectory *rvec*, m is the mass of electron, and Φ is the amount of magnetic flux. A cylindrical coordinate system is assumed with the z-axis coinciding with the axis of the coil. Since the magnetic field has cylindrial symmetry $B_\theta = 0$.

In a polar coordinate system

$$\ddot{\vec{r}} = (\ddot{r} - r(\dot{\theta})^2)\hat{i} + (r\ddot{\theta} + 2\dot{r}\dot{\theta})\hat{j} \qquad (B1.2)$$

where $\hat{i}$ and $\hat{j}$ are unit vectors in the radial and tangential directions, respectively. The trajectories of the electrons satisfy the relations

$$m(\ddot{r} - r(\ddot{\theta})^2) = ev_\theta B_z \qquad (B1.3.1)$$

$$m(r\ddot{\theta} + 2\dot{r}\dot{\theta}) = -e(v_r B_z - v_z B_r) \qquad (B1.3.2)$$

Eq.(B1.3.1) is related to the *radial* motion and Eq.(B1.3.2) is related to the *tangential* motion.

Notice that

$$\frac{d(r^2\dot{\theta})}{dt} = r(r\ddot{\theta} + 2\dot{r}\dot{\theta})$$

and

$$r^2\dot{\theta} = 2\frac{dA}{dt},$$

which when combined with (3.30.2) lead to

$$\frac{2m}{r}\frac{dA}{dt} = -e(v_r B_z - v_z B_r) \qquad (B1.4)$$

In Figure 3.7 we describe a small cubic element formed by $dz \times d\theta \times dr$. $d\theta dr B_z$ is the amount of magnetic flux which passes through the unit surface perpendicular to Z-axis, and $-d\theta dz B_r$ is the amount of magnetic flux which passes through the unit surface perpendicular to the radial direction. Since $B_\theta = 0$ there is no magnetic flux passing the tangential direction. Therefore

$$-\left(\frac{dr}{dt}B_z - \frac{dz}{dt}B_r\right) = \frac{1}{\theta}\frac{d\Phi}{dt} \qquad (B1.5)$$

Integrating with respect to θ

$$\frac{4\pi m}{r}\frac{dA}{dt} = e\frac{d\Phi}{dt} \qquad (B1.6)$$

Thus Eq. (B1.1) has been proven.

References

(1) R. J. Cvetanovic, J. Chem. Phys., **23**, 1375 (1955).

(2) G. R. H. Jones and R. J. Cvetanovic, Can. J. Chem., **39**, 2444 (1961).

(3) J. J. Havel, J. Am. Chem. Soc., **96**, 530 (1974).

(4) H. E. Hunziker, H. Kneppe, and H. R. Wendt, J. of Photochemistry, **17**, 377 (1981).

(5) A. N. Hughes, M. D. Scheer, and R. Klein, J. Phys. Chem., **70**, 789 (1966).

(6) I. R. Slagle, D. Gutman, and J. R. Gilbert, Chem. Phys. Lett., **26**, 111 (1974).

(7) P. Andresen and A. C. Luntz, J. Chem. Phys., **72**, 5842 (1980).

(8) M. C. Lin, R. G. Shortridge and M. E. Umstead, Chem. Phys. Lett., **37**, 279 (1976).

(9) J. R. Kanofsky, and D. Gutman, Chem. Phys. Lett., **15**, 236 (1972).

(10) S. J. Sibener, R. J. Buss, P. Casavecchia, T. Hirooda, and Y. T. Lee, J. Chem. Phys., **72**, 4341 (1980).

(11) R. J. Buss, R. J. Baseman, G. Z. He, and Y. T. Lee, J. Photochem. **17**, 389 (1981).

(12) G. Z. He, R. J. Buss, R. J. Baseman, R. Tse, and Y. T. Lee, J. Phys. Chem., **86**, 3547 (1982).

(13) R. J. Baseman, R. J. Buss, P. Casavecchia, and Y. T. Lee, J. Am. Chem. Soc., **106**, 4108 (1984).

(14) R. J. Baseman, Ph. D. thesis, U. C. Berkeley (1982).

(15) R. J. Baseman, *Report 1982*, LBL-15259; Order No. DE83004296, 249 pp.

(Eng).

(17) P. Casavecchia, R. J. Buss, S. J. Sibener, and Y. T. Lee (1979).

(18) P. Casavecchia, R. J. Buss, S. J. Sibener, and Y. T. Lee (1980).

(19) C. E. Frish and A. V. Timoreva, "*General Physics*", (Russian) National Publish House for Technical-Science Literature, 1953.

(20) F. H. Field and J. L. Franklin, "*Electron Impact Phenomena*", pp244-279 (1957).

(21) J. L. Delgroix, "*Plasma Physics*" (1965).

(22) S. J. Sibener, R. J. Buss, C. Y. Ng, and Y. T. Lee, Rev. Sci. Instrum. **51**, 167 (1980).

(23) Edited by R. H. Huddlestone and S. L. Leonard, "*Plasma Diagnostic Techniques*" (1965).

(24) R. C. Davidson, "*Method in Nonlinear Plasma Theory*" (1972).

(25) *Symposium on Computer Simulation of Plasma and Many-Body Problem*, cosponsored by NASA LRC and The College of William Mary, (1967).

Table 3.1 Hot plasma conditions

frequency	$14 \pm 2MC$
terminal power	120 - 300 watt
working medium	O_2 seeding in Ne (or Ar)
ignition pressure	1-3 τ
working pressure	200-600 τ
aperture diameter	5-10 mil
dissociation percentage	60-90%
atomic O velocity	1100-2100 m/s

Table 3.2 Ionization potentials and dissociation energies for several molecules

mol.	He	Ne	Ar	O
pot. (eV)	24.48	21.56	15.76	13.61

mol.	$O_2 \rightarrow O^-$	$O_2 \rightarrow O(^3P)$	$O_2 \rightarrow O(^1D)$	$O_2 \rightarrow O^+(^2D)$
pot. (eV)	16.9 ± 0.2	$18.9 - 19.2$	20.8 ± 0.2	20.5 ± 0.2

Table 3.3 Coil dimension (see parameter definition in Fig. 3.4)

#	n_1	n_2	l_1	l_2	r_1	r_2 (cm)
1	6.5	5	6	6.5	2.58	2.58
2	6.5	5	6	6.5	0.685	0.685
3	6.5	5	6	6.5	0.685	2.58
4	6.5	5	4	8.5	0.685	2.58

Table 3.4 Expeimental conditions for $O(^3P)$ reacting with allene.

O_2 in Ne (%)	5
O_2 pressure (τ)	550
$O(^3P)$ velocity (m/s)	1616
O_2 speed ratio	6.7
allene in He (%)	20
allene pressure (τ)	350
allene velocity (m/s)	1162
allene speed ratio	9.77
collision energy (kcal/mole)	5.41
calculated center of mass	60.9° (from O beam)
signal at peak (cps)	8.6

Caption

Figure 3.1. Block diagram of radio frequency discharge aparatus.

Figure 3.2. An electron collides with the molecules in the external electric field. The mean free path is AB between the two collisions, and the trajectory is represented by a curve.

Figure 3.3. Source pressure of hot/cold plasma as a function of nozzle pressure. There is a critical jumping point at p = 330τ. The lower panel is the ratio.

Figure 3.4. The effects of coil geometry to the magnetic intensity distribution along the axis of coil.

Figure 3.5. The circuit diagram of radio frequency discharge with power supply. Z_1 is the output impedence of RF generator, Z_2 is the working impedance of discharge.

Figure 3.6. Equivalent circuit diagram of LC tank which induces the discharge in the quartz nozzle inside the coil.

Figure 3.7. Matching network circuit diagram.

Figure 3.8. Comparison between the oxygen beam source of present one (above) and the suggested one (below).

Figure 3.9. Plot for illustrating *Butch's theorem.* The rotational energy of a particle with charge can be transfered to translational energy in a divergent magnetic field.

Figure 3.10. Angular distribution of mass 53 product in the reactive scattering of $O(^3P)$ with allene.

Figure 3.11. Velocity distribution of mass 55 product in the reactive scattering of $O(^3P)$

with allene.

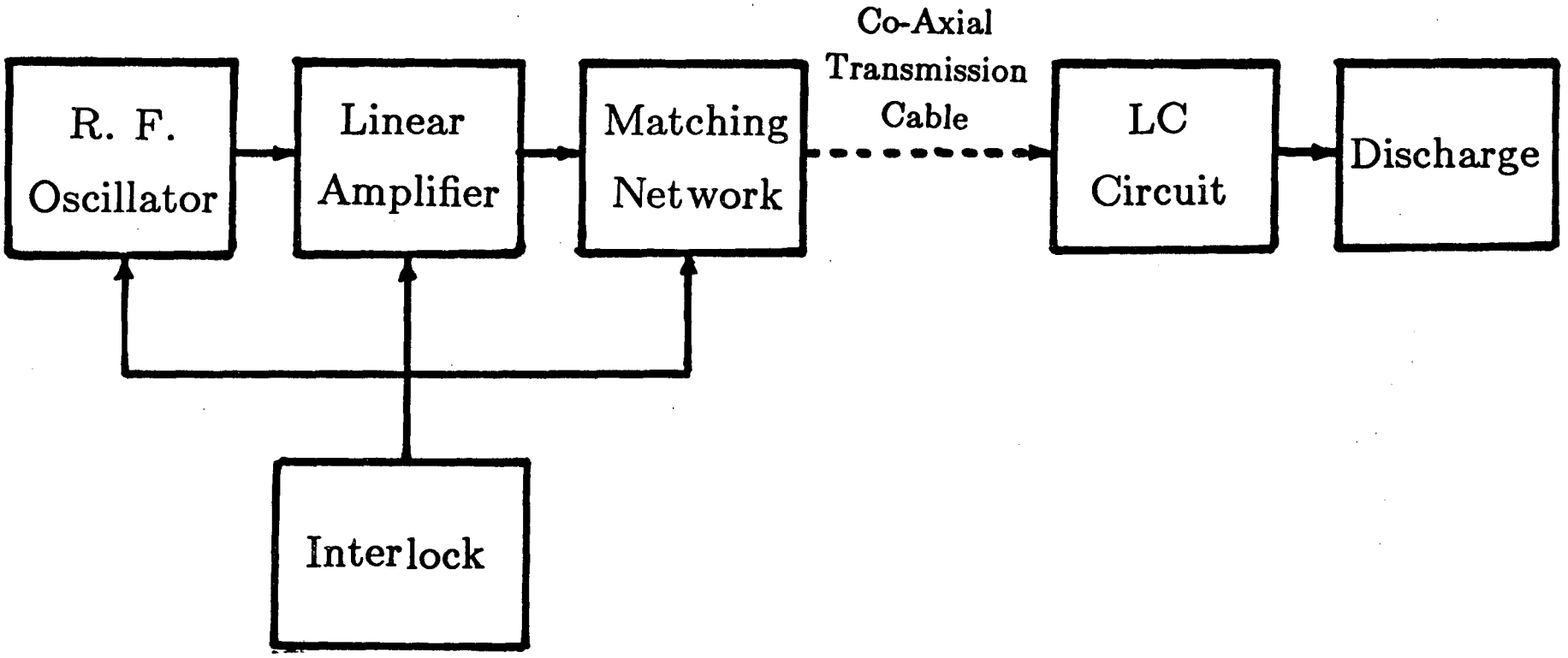
R. F.
Oscillator
Linear
Amplifier
Matching
Network
Co-Axial
Transmission
Cable
LC
Circuit
Discharge
Interlock

*Fig.*3.1

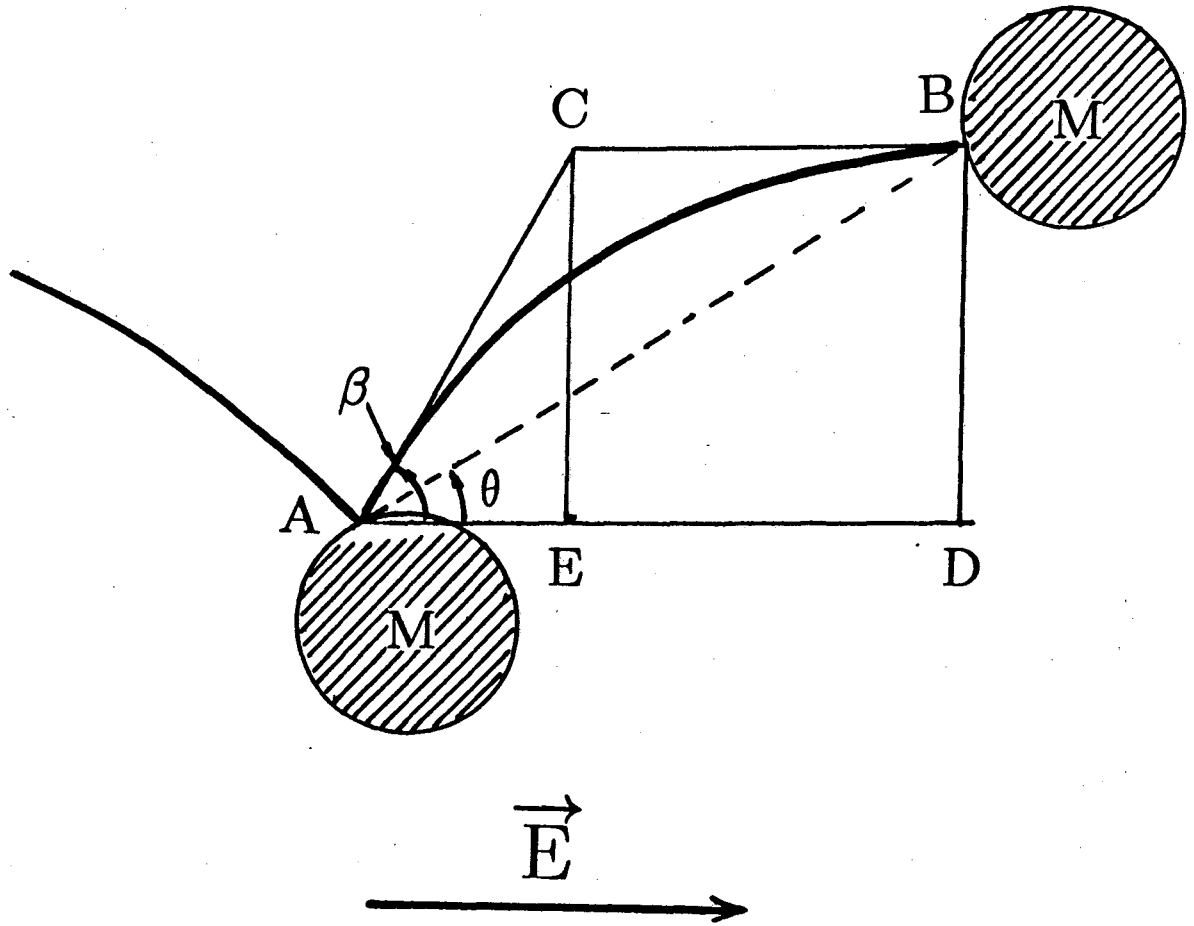

Fig.3.2

SOURCE PRESSURE OF HOT/COLD PLASMS

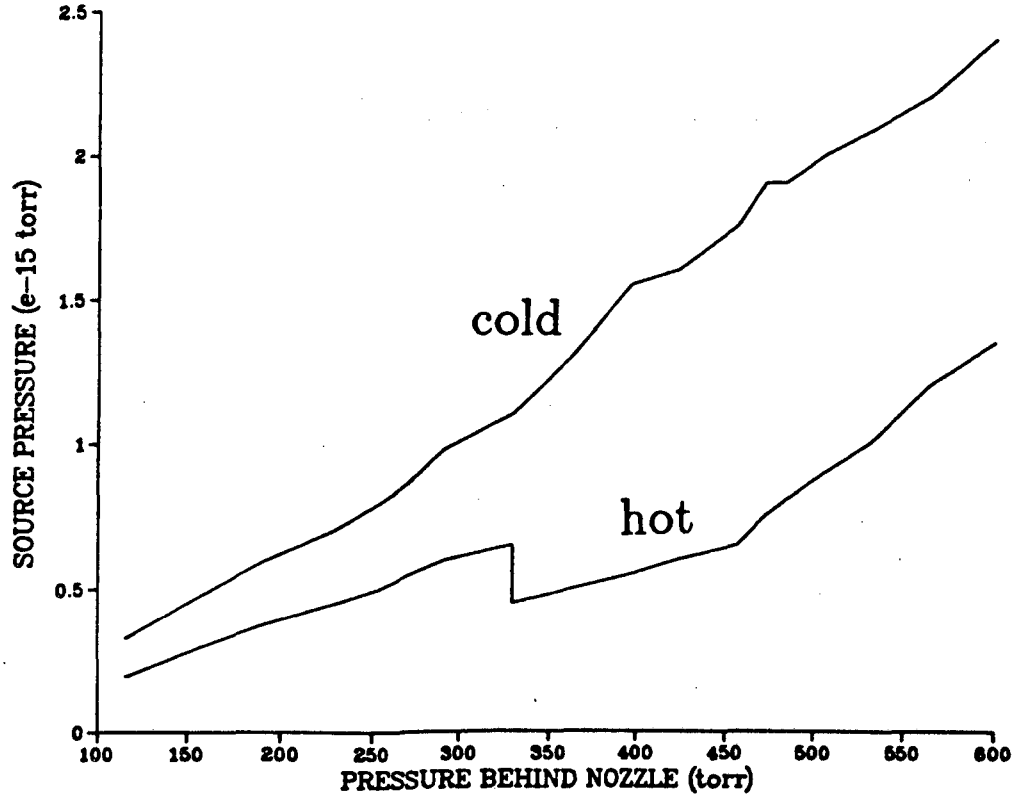

RATIO OF HOT/COLD PLASMS PRESSURES

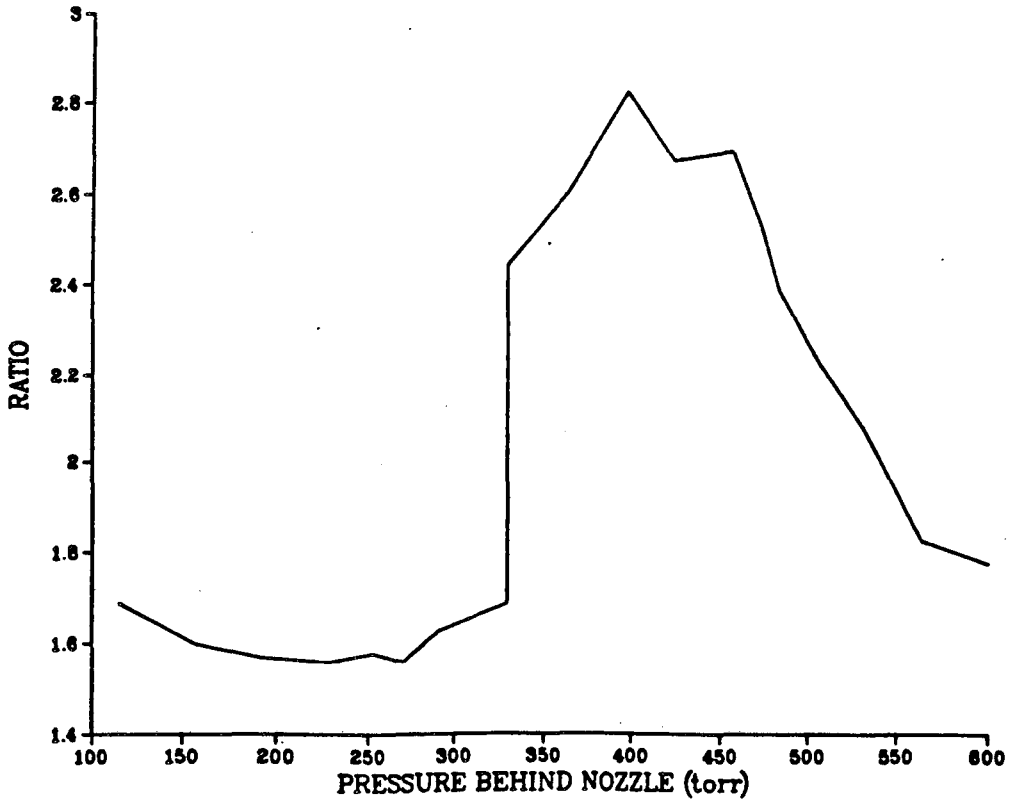

Fig.3.3

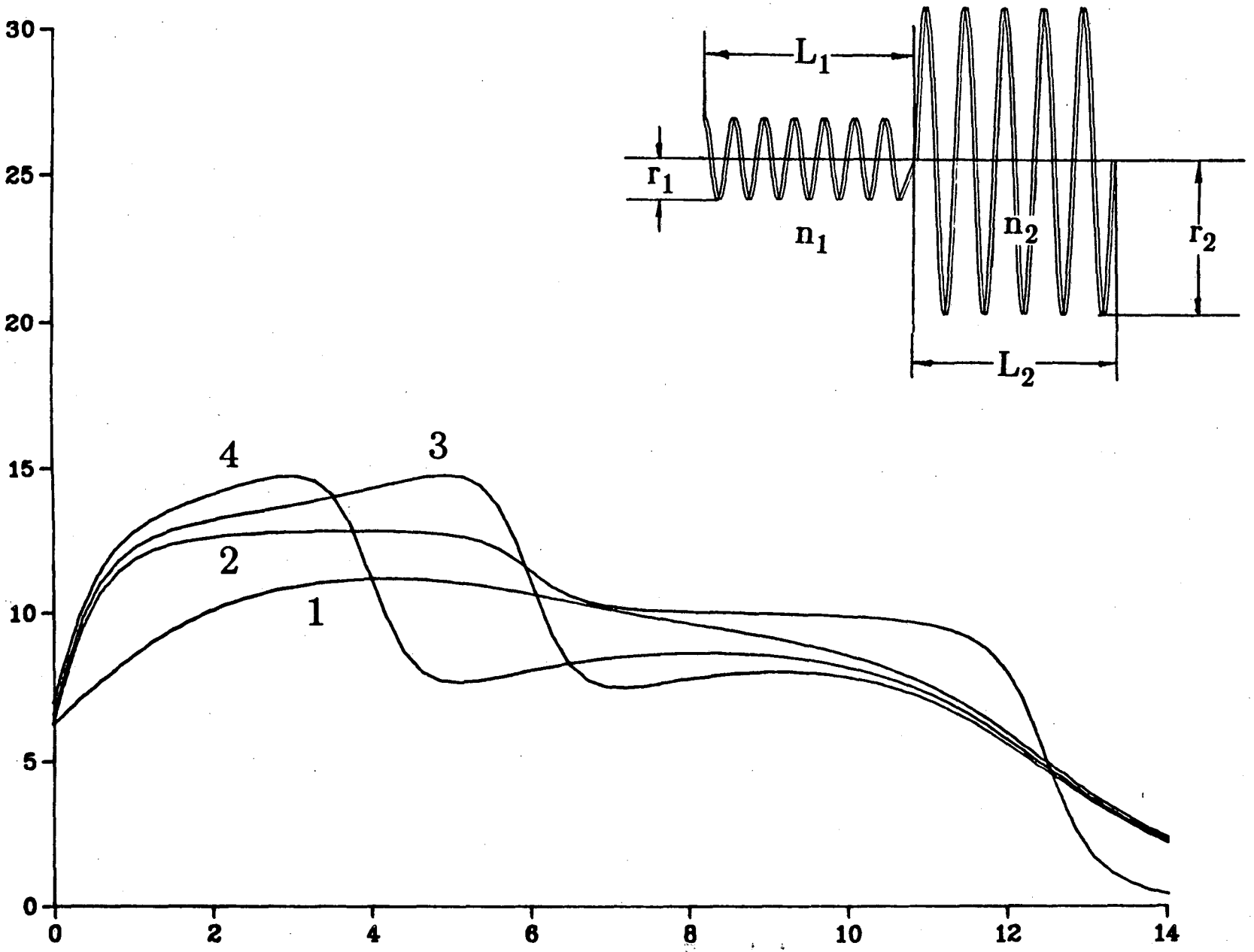

*Fig.*3.4

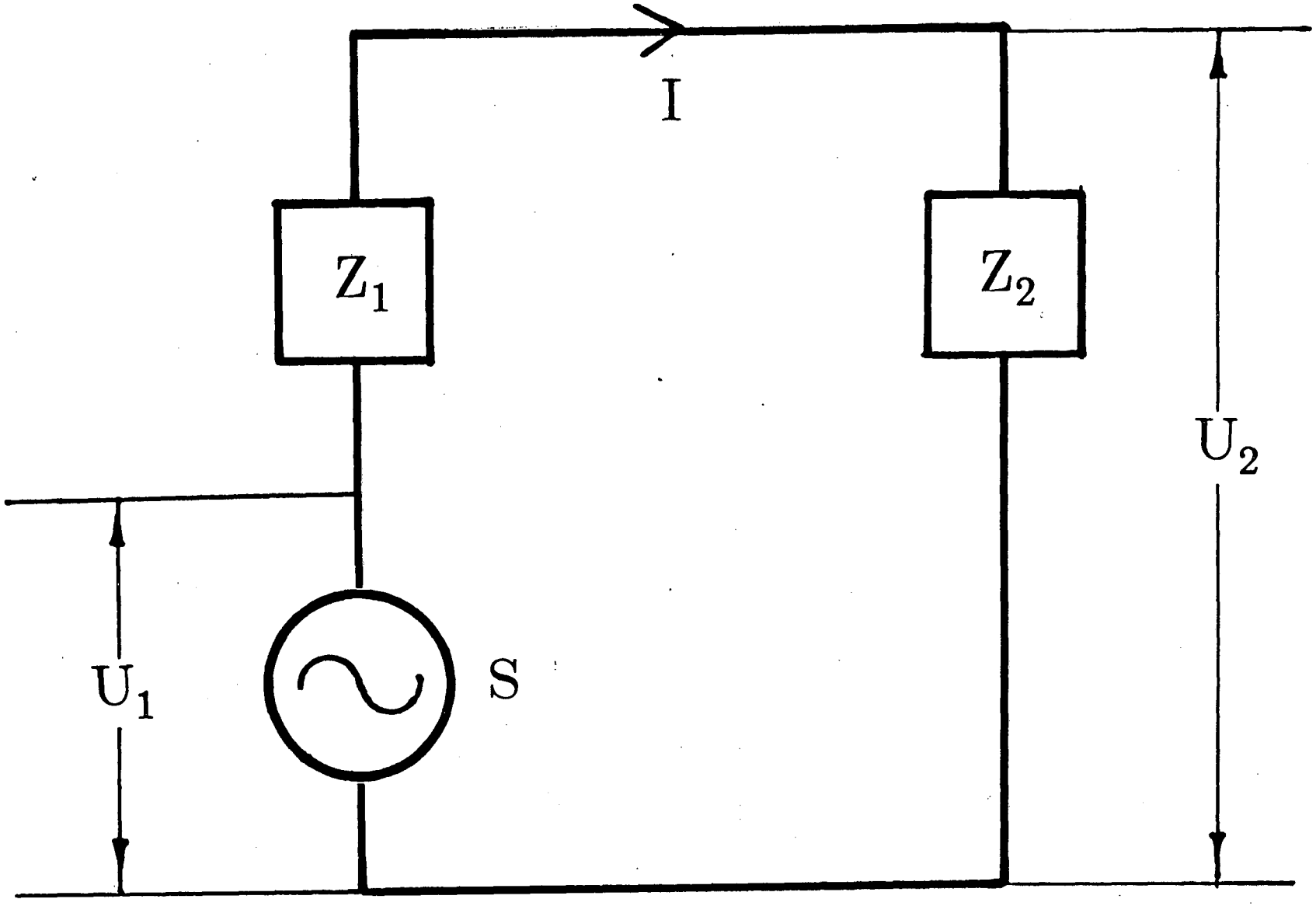

*Fig.*3.5

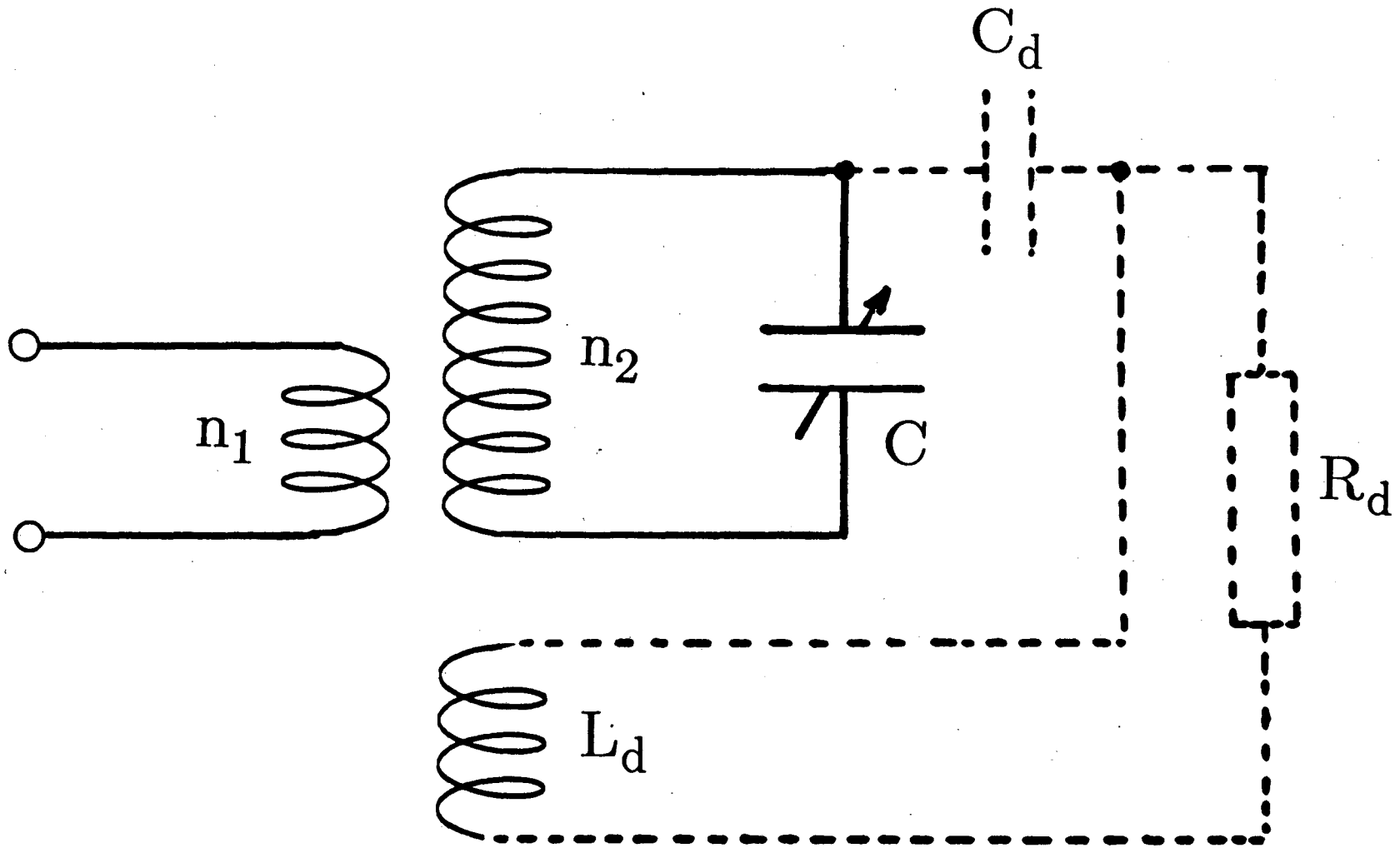

*Fig.*3.6

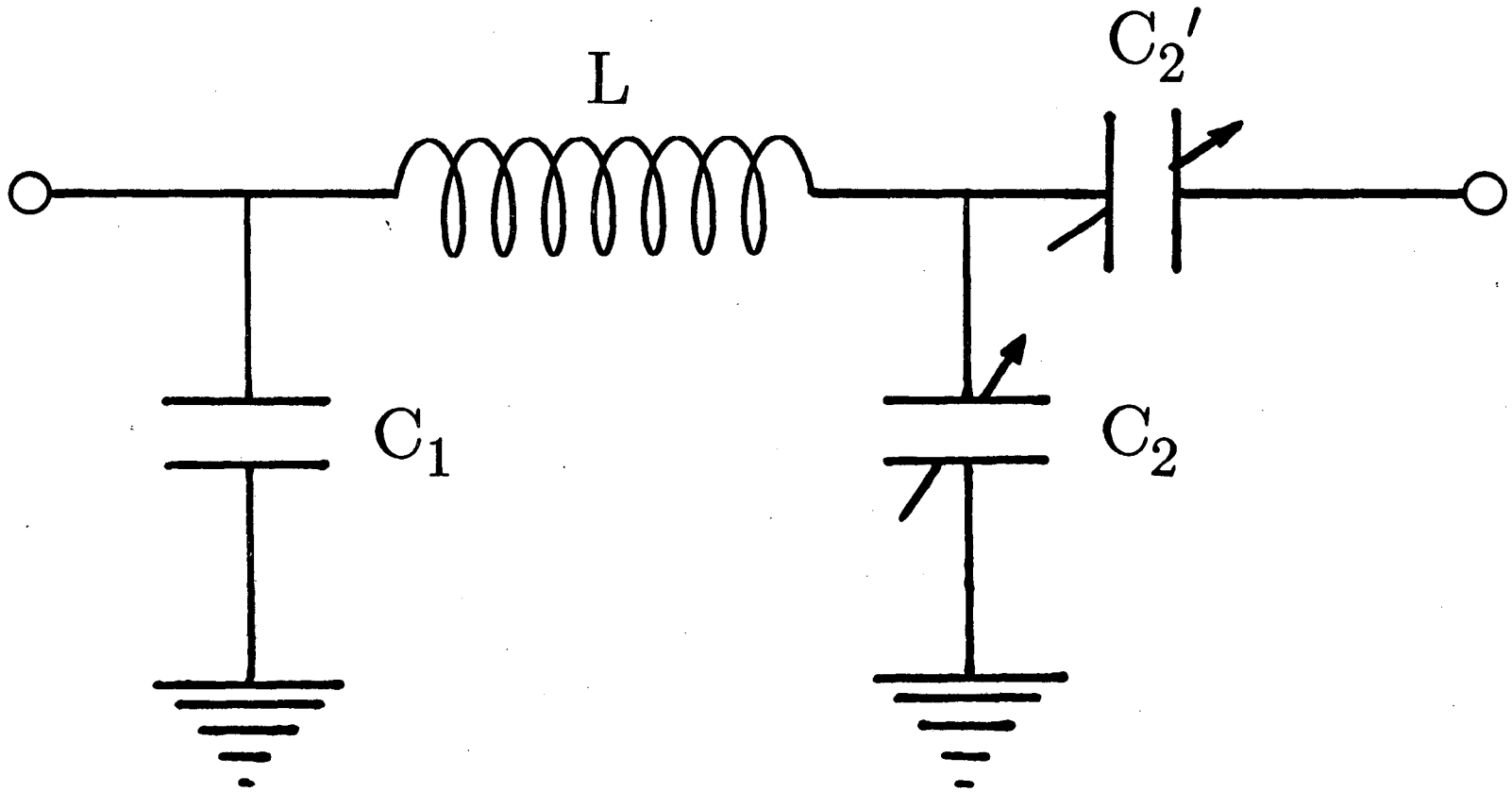

*Fig.*3.7

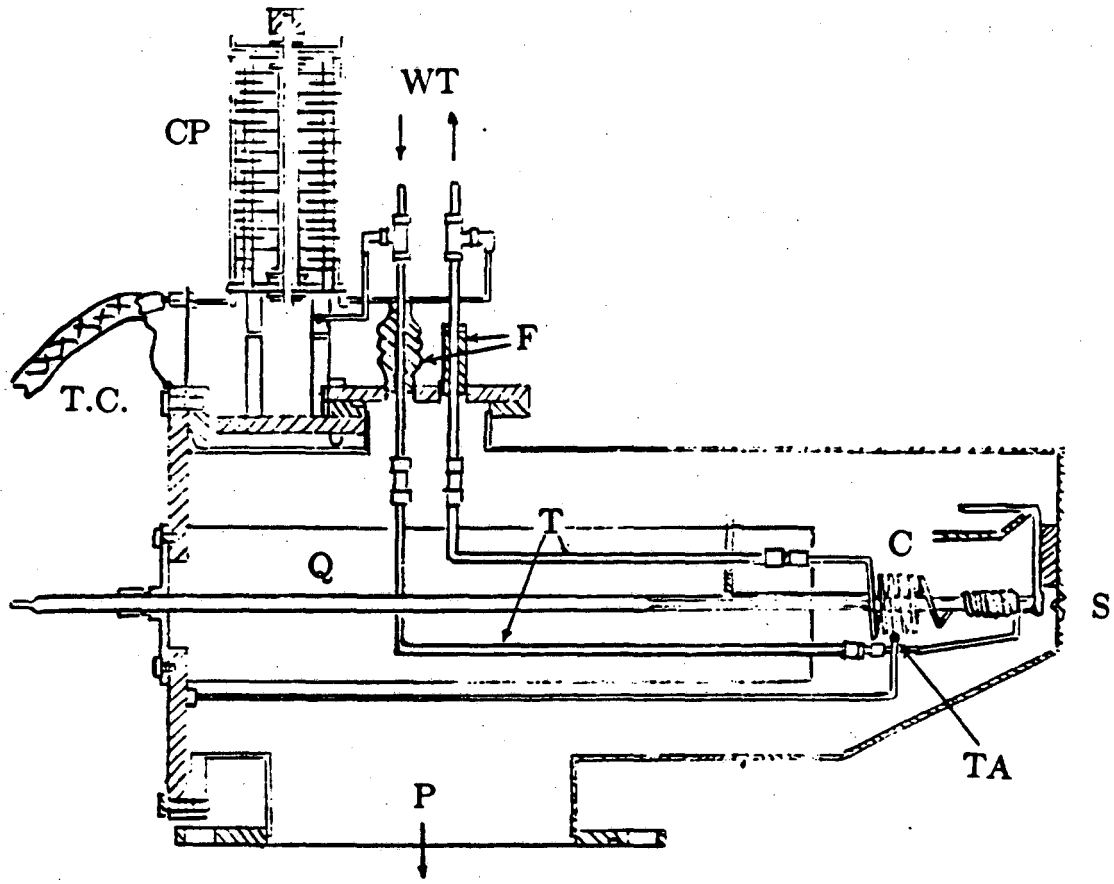

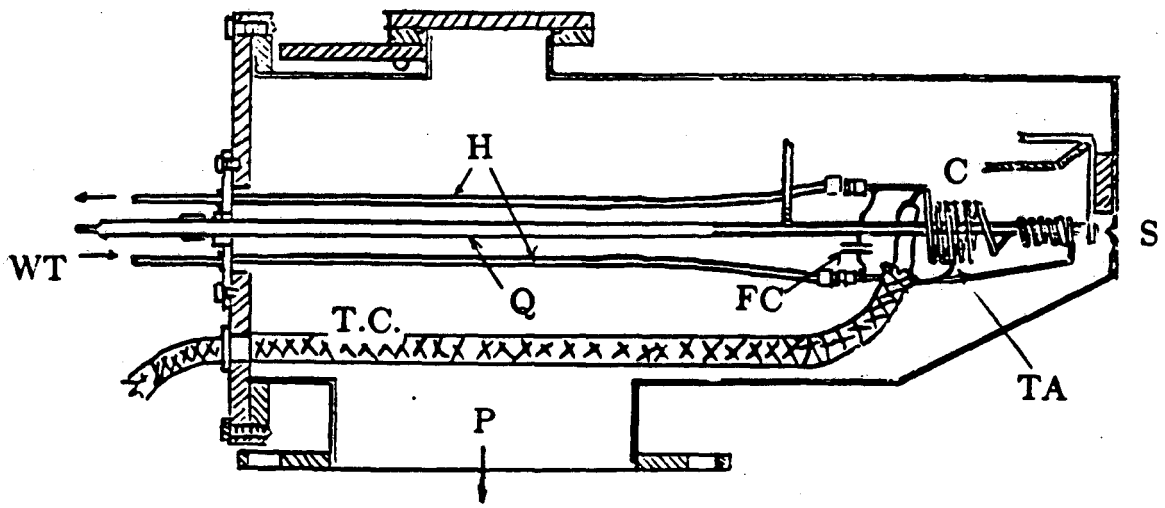

*Fig.*3.8

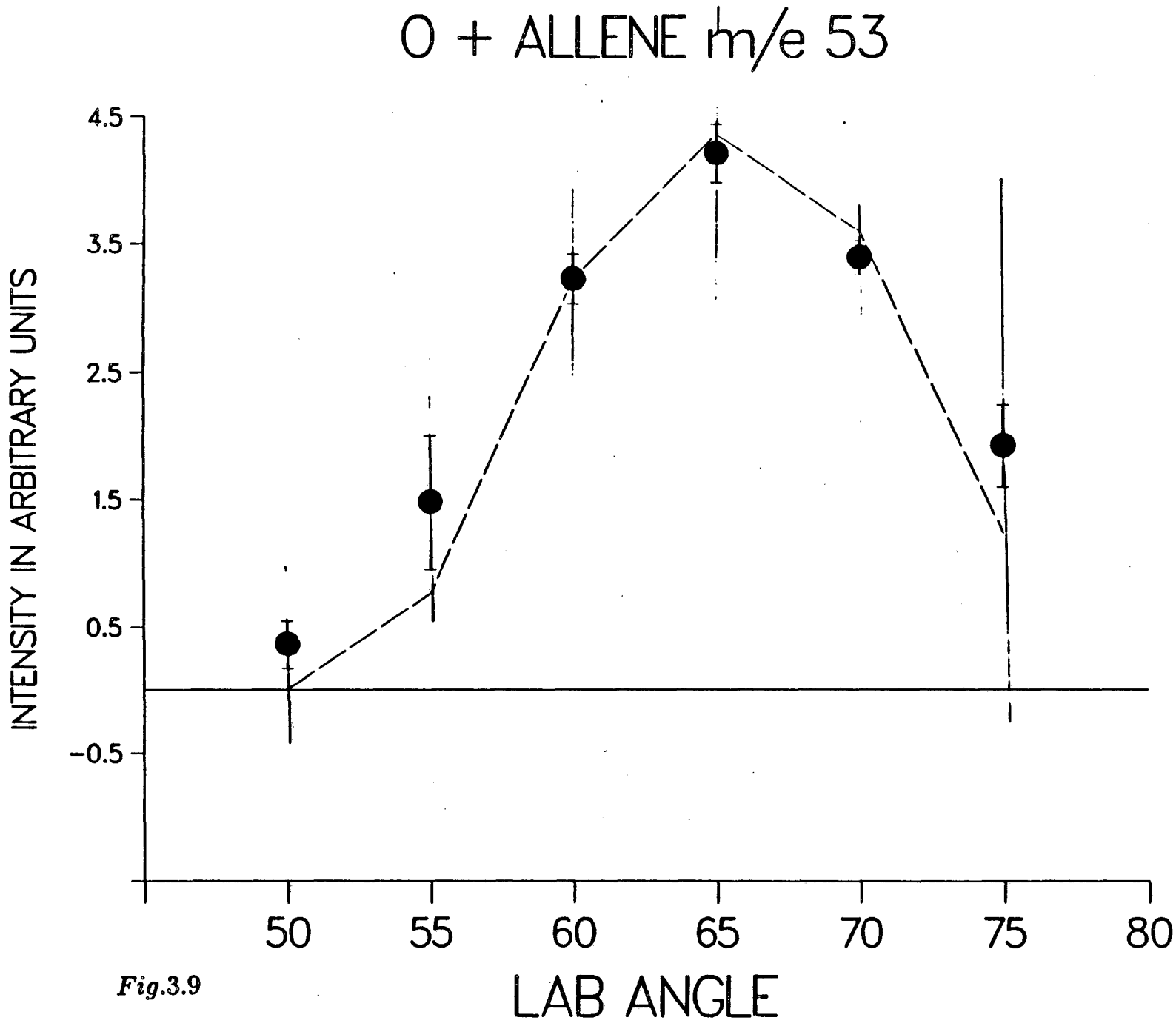
O + ALLENE m/e 53
INTENSITY IN ARBITRARY UNITS
4.5
3.5
2.5
1.5
0.5
-0.5
50
55
60
65
70
75
80
LAB ANGLE

Fig.3.9

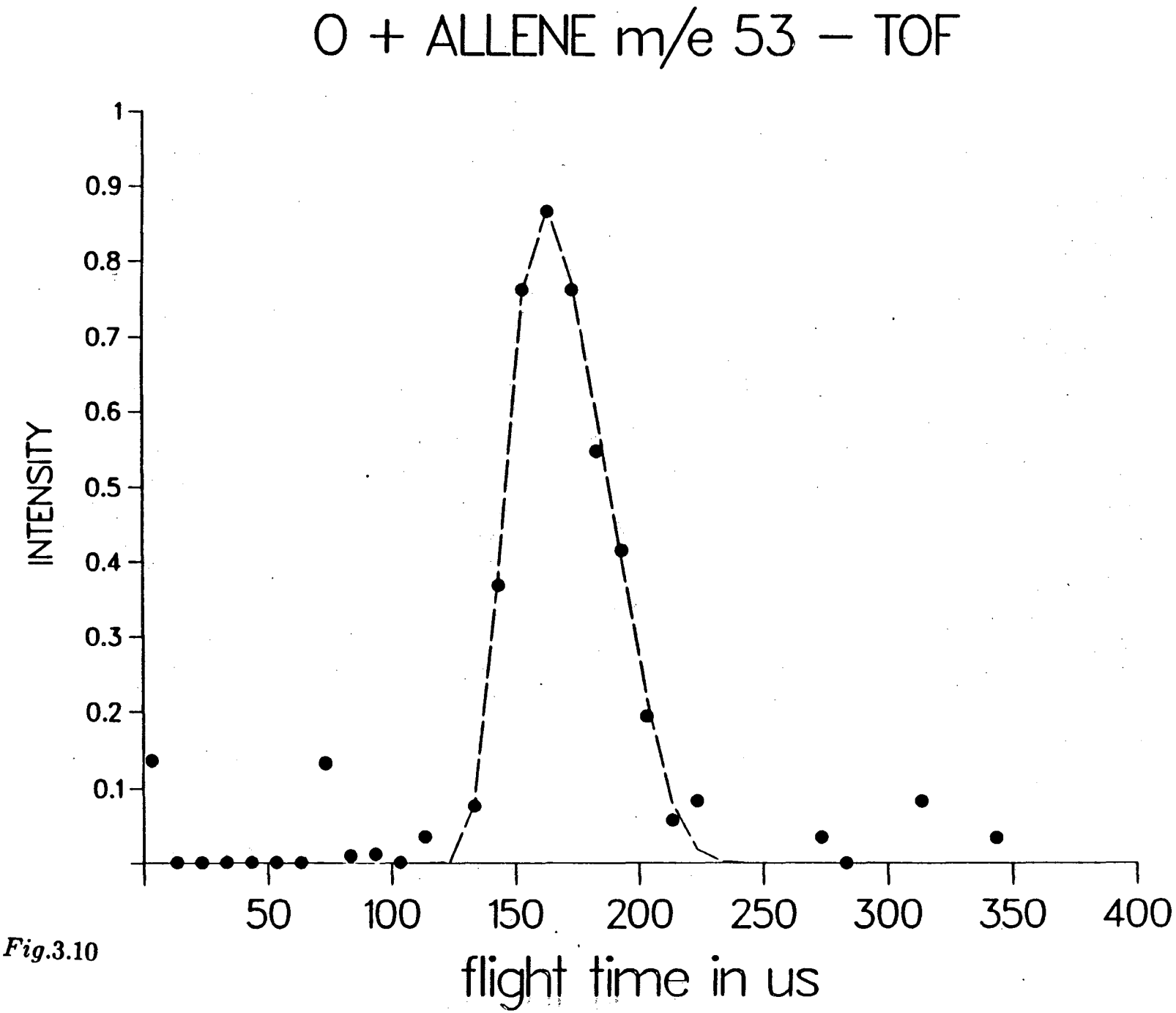
O + ALLENE m/e 53 – TOF
INTENSITY
1
0.9
0.8
0.7
0.6
0.5
0.4
0.3
0.2
0.1
50
100
150
200
250
300
350
400
flight time in us

*Fig.*3.10

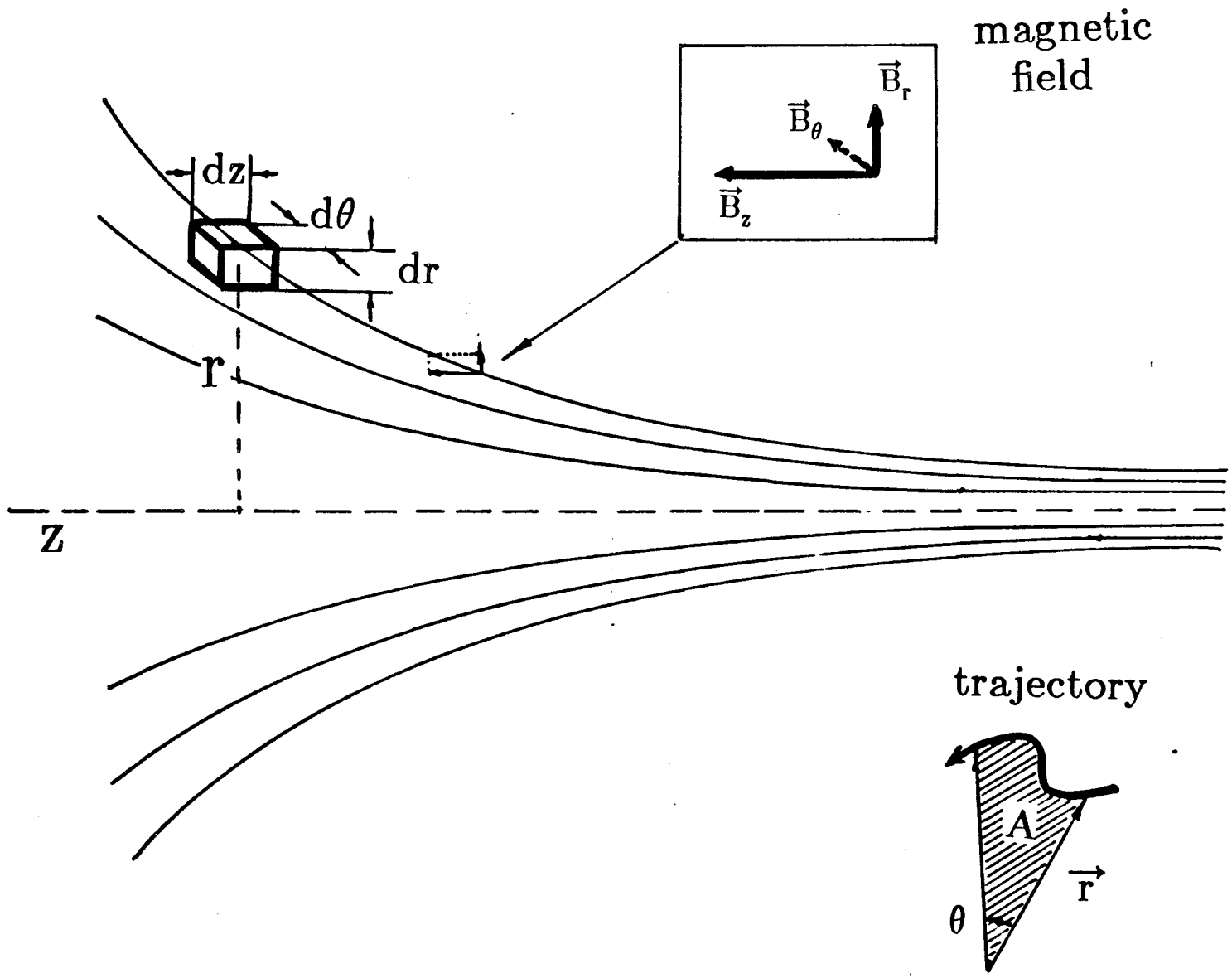
magnetic field
$\vec{B}_r$
$\vec{B}_\theta$
$\vec{B}_z$
dz
$d\theta$
dr
r
z
trajectory
A
$\vec{r}$
θ

*Fig.*3.11

PART TWO:

Theoretical Study

Chapter IV MCSCF Study of $O(^3P)$ + Allene

A. Introduction

The reaction of $O(^3P)$ atoms with allene molecule has received much attention for more than fifteen years.[1-4] The widely accepted mechanism is that the major reaction products, carbon monoxide and ethylene are obtained via a ring intermediate, cyclopropanone.

$$O(^3P) + C_3H_4 \rightarrow$$

$$\rightarrow CO + C_2H_4 \tag{4.1}$$

It starts with the central carbon atom attacked by oxygen atom followed by ring closure to form a stable intermediate, cyclopropanone. By a concerted cheletropic dissociation the ring is broken to form products. Lin and co-worker[3] studied the product CO vibrational energy distribution by a resonant absorption method, and found a hot vibrational temperature, favoring a concerted cheletropic dissociation afterward. The structure of cyclopropanone has been reported both experimentally and theoretically[5-7]. Using the geometry obtained by spectrum analysis[5], an INDO and an *ab initio* Hartree-Fock (HF) calculation[6] shows that the highly strained ring structure has a fairly stable energy. But little information was known about the reaction path either between reagents and intermediates, or between intermediates and products. A theory of the conservation of angular momentum by

spin-flipping and electron jumping simultaneously between two perpendicular orbitals was suggested[4] to interpret the possibility of the spin-forbidden reaction. But both the initial triplet and the final singlet potential energy surfaces remained to be detailed.

Besides the above well-known mechanism another mechanism has been proposed recently based on a molecular beam experiment[8] which involves oxygen atom attack on a terminal carbon. By taking advantage of unambiguous identification of collision products, Lee and co-workers reported a series of results of for $O(^3P)$ reacting with unsaturated hydrocarbons, indicating that insertion of oxygen atom into a double bond to form a diradical, followed by loss of a hydrogen is a favorable mechanism for many olefin combustion systems.[9-14] When $O(^3P)$ atoms attack terminal carbons of allene, the mechanism can be an addition followed by a hydrogen leaving

$$O(^3P) + C_3H_4 \rightarrow CH_2CCH_2O$$

$$\rightarrow CH_2CCHO + H \tag{4.2}$$

The interesting points that lead us to study this system are:

(1) Allene is the simplest unsaturated hydrocarbons that has perpendiculer π bonds. The rich and active valence π electrons make it easy to react with oxygen atoms.

(2) As a three carbon-atom system for allene there can be a competition between different reaction channels depending on which of the carbons is attacked by oxygen.

(3) The formation of a diradical is an important step in the reaction of unsaturated hydrocarbon with oxygen. It is interesting to study the electronic structure , molecular geometry, and formation mechanism of this system to learn more about the diradical behavier.

(4) One of the reaction channels (Eq. 3.1) is spin-forbidden. Probably, the other channel also involves intersystem crossing. The discussion about why and how it might happen may be interesting and absorbing.

The present study focuses on these two reaction channels: central carbon attack (CCA) and terminal carbon attack (TCA). We intend to characterize the key features along the reaction paths, i.e., the energies and geometries of all possible intermediates, the transition states, and consequent products. The HONDO code[48] has been employed for geometry optimizations and energy calculations. As a probe study we did a MCSCF study with a single-zeta (SZ) basis set. The major study is done with a double-zeta (DZ) basis set. We also carried out a study with a double-zeta plus polarization (DZP) basis set. Sec. B is a study of allene. The CCA and TCA channel calculations are presented in Sec. C and E respectively. Our calculation in Sec. D makes a comparison between the triplet intermediate, oxyallyl and the singlet intermediate, cyclopropanone. In Sec. F we present the vinoxyl radical study. Sec. G is a discussion about intersystem crossing. Sec. H is a brief summary.

B. Allene

Allene molecule is well known as having a linear c=c=c chain, but the two CH_2 groups lie in planes at right angles to each other and passing through the c=c=c axis. (Fig. 3.1) The calculated geometries with three different basis sets are shown in Table 3.1. It agrees with the parameters obtained by Raman spectroscopy.[15] The finding of zero dipole moment[16] confirms its high symmetry (D_{2d}). Several allene property studies show that allene has very small exaltation of molar refraction[17,18] and slight exaltation of diamagnetic susceptibility.[19-21] This means that there is no conjugation or delocalization of electrons occuring between the two π bonds. But the existence of partial triple-bond character[22-25] in allene indicates that there is hyperconjugation occuring between the CC π orbital and the σ orbitals of the CH_2 groups which is located in the other side of molecule but in the same plane with the π orbital.

Spectroscopic studies[26-30] show that all eleven normal modes ($3A_1$, $1B_1$, $3B_2$, $4E$, see Fig. 3.2) are Raman active and seven of them ($3B_2$, $4E$) are infrared active. The torsional mode frequency obtained by Raman spectroscopy[3] is $\nu_4 =$ 820 cm^{-1}. The frequency of the anti-symmetric stretching mode of C=C=C chain (B_2) is obtained by both Raman and infrared spectroscopy as $\nu_2 = 1980$ cm^{-1}.

We carried out a MCSCF calculation with a DZ basis set to study the potential energy as function of the twist angle of one CH_2 group with respect to each other. (Fig. 3.3) At $\phi = 90°$ the ground state ($1A_1$) has a minimum. The well depth is 2.32 ev as measured from the minimum to the energy for $\phi = 0°$. The excited state

is more stable at $\phi = 0°$ than at right angle (D_{2d} symmetry) where the doubly degenerate E state splits into two branches B_1 and B_2, when the D_{2d} symmetry is broken by the twisting motion. The high barrier (2.32 ev) prevents the two CH_2 groups from rotating freely.

Before discussing the change of the perpendicular π system when allene is attacked by oxygen atom, it is interesting to look at the situation when one of the four π-electrons is taken away (either by reaction or by ionization) from the π bond. Recently the photoelectron spectrum of ionic allene was carried out by Yang *et al.* group.[31] The spectrum associated with the transition from the ground-state of C_3H_4 to the doubly degenerate ground state 1^2E and excited state 2^2E of allene cation (see Fig. 3.5) is shown in Figs. 3.4 and 3.6, respectively. The high resolution spectrum shows that four or five very sharp torsional vibration peaks occur at a transition energy of 10 eV. (Fig. 3.4.) This means that there is a ground state potential well which is able to hold four or five torsional vibration states. From the spectroscopy the frequency is obtained as $\nu_4 = 751$ cm^{-1} which is less than that of allene. It reflects the fact that the C-C-C bonding weakens. The analysis of the spectrum of the excited state transition (also doubly degenerate E at D_{2d} symmetry) indicates that there are many fine-structure peaks that are induced by three symmetric modes (A_1) and their overtone combinations. Table 3.2 is the comparison of frequencies between C_3H_4 and its cation. The relaxed frequencies of the cation provide further evidence for the weakening of C-C bonding. Our MCSCF calculation of $C_3H_4{}^+$ show a double well with minimum at $\phi = 52.2°$ and well

depth 0.8 eV relative to the energy at $\phi = 0°$. (Fig. 3.7) The optimized ion geometry shows that the C-C bond length is 1.346 a.u. (vs. 1.32 a.u. of the neutral molecule), with no change of C-H bond length.

From this study we conclude:

(1) When one of the electrons is taken away from the π-system the C-C bonds become weaker. The C-C bond length is enlarged by 2%, The stable geometry will be the two CH_2 groups at a angle of 52.2°, instead of at a right angle with respect to each other. There is almost no change of C-H bond length.

(2) The torsional motion barrier is reduced by 60% compared with allene molecule, and the vibrational frequency is reduced by 13%, but the rotation is still not free. The several sharp and non-split torsional mode peaks provide the evidence of a deep potential well.

(3) From our property calulation we learned that the charge distribution between the C=C=C charge and four terminal hydrogens are 18.7 : 3.3 for C_3H_4 molecule, and 18.2 : 2.8 for $C_3H_4{}^+$ cation. This means that during ionization one electron is not taken solely from C=C π-bond orbital but also from the hydrogens. The C-C bond is weakened but not as much as we expected. For instance, we thought that the leaving of one electron might cause the two CH_2 groups rotating freely. In fact, the electrophilic C=C=C chain attracts the electron from terminal hydrogen to keep the C-C bonding.

C. CCA Channel

The perpendicular π-system provides a wide acceptance angle for oxygen atoms

to attack the central carbon atom. The most favorable electronic occupation of oxygen p-orbitals for reaction is $| 2p_x^1 2p_y^2 2p_z^1 |$ (Fig. 3.8). The unpaired $2p_x$ electron is ready to form a σ bond with the central carbon of allene molecule and the unpaired $2p_z$ electron to form a C-O π bond. As soon as the σ- and π-bonds are formed, the two CH_2 groups are free to rotate while the two C-C bonds bend backwards with respect to the oxygen direction. Assuming the process is carried out without intersystem crossing, a triplet intermediate, oxyallyl, with 23.52 kcal/mole lower energy than reactants will eventually be formed. The barrier to the transition state for this process is 16.68 kcal/mole. The other singlet intermediate, cyclopropanone which is believed to lead to final products has more stable energy (44.7 kcal/mole lower than reactants). A detailed comparison of the two intermediates will be given in Sec. D. One major feature I'd like to point out here is that the triplet intermediate does not have ring structure but is a planar molecule with C_{2v} symmetry.

The calculated total energies at three critical positions: (1) asymptotic reactants, (2) transition state, (3) triplet intermediate along CCA path are shown in Table 3.3. Table 3.4 lists the interaction energies. The optimized geometries for all the species (reactants, transition state, intermediates) are summarized in Table 3.5 where the singlet intermediate, cyclopropanone is also involved. Notice there are two resonance structures (A' and A'') for the triplet intermediate.

Taking C-O distance as the reaction coordinate and using a SZ basis set, I did a MCSCF calculation geometry optimized at each of the 12 points along CCA path. Fig. 3.9 plots the PES as function of C-O distance, and the Fig. 3.10 is

the C-C bond lengths and the C-C-C bending angles vs C-O distance. From these calculations the key feature of the CCA reaction process can be described as follows:

(1) There is no observable interaction for C-O distances greater than 3Å.

(2) When C-O distance is less than 3Å the energy increases while the C-C-C chain bends backward and the two C-C bonds stretch little bit. Also, the two CH_2 groups twist from the position perpendicular to each other (as seen in Sec. B when one electron is ionized).

(3) Before the saddle point (S) is reached there is a 45° bending of the C-C-C bond. The bending continues beyond the saddle point but is not as rapid as before. In contrast to the slower geometry change, the energy decreases more rapidly than before until a stablized intermediate are reached.

(4) During the approach of oxygen atom the perpendicular π bonds of allene is destroyed by the formation of the C-O bond. There can be a disrotatory or a mixture of disrotatory and conrotatory motions of the two CH_2 groups that lead the whole molecule to a planar structure.

D. Singlet Cyclopropanone and Triplet Oxyallyl

There is no doubt about the existance of the cyclopropanone (CP) molecule. But 20 years ago, an extended Hückel calculation[32] indicated that the highly constrained ring structure should be less stable than the singlet oxyallyl (OX) radical which is geometrically similar to the triplet intermediate which is obtained in the CCA channel calculation of this study (see Sec. B). In a later INDO study[33] the order of stability was reversed in favor of the ring structure. Many calculations

carried out recently[6] confirm these findings, but no comparision was made between the singlet and triplet intermediates. The results of this study that I showed in Sec. C indicate that the triplet oxyallyl is 21.2 kcal/mole less stable than singlet cyclopropanone. It is interesting to look at the differences of geometry and electronic structure between the two molecules.

The structral parameters of cyclopropanone were experimentally determined by microwave spectroscopy[5] and electron differaction[34]. Those results are compared with the computed results of this study for both singlet cyclopropanone and triplet oxyallyl and are listed in Table 3.6. My optimized C-O bond length is slightly longer than experiment, but the other parameters are in good agreement with the parameters deduced from experiment. The basic differences are:

(1) CP is a ring molecule. The smaller C-C-C angle (67.4°) and smaller C_2-C_3 bond length indicate that there is bonding between C_2 and C_3. Triplet OX is an open ring molecule. The C-C-C bending angle (125.8°) of OX and the two C-C-H angles (120.2°) indicate that each of the carbon atoms is sp^2 hybridized.

(2) The two CH_2 groups of CP are perpendicular to the ring plane. The triplet OX has a planar structure with its two CH_2 groups lying in the plane.

(3) CP has a regular C=O double bond length (1.20 Å) and C-C single bond length (1.50 Å). All the C-O and C-C bond length of triplet OX lie between regular single and double bonds.

To better understand the causes of the features of OX in (2) and (3), let us look at the electronic structure of triplet OX. There are 3 in-plane electrons (represented

by open circles in Fig. 3.8) and 5 out-of-plane electrons (represented by dark solid circles) that are correlated during the CCA channel reaction. One p_x electron of oxygen and one of the π_x electrons of allene form a C-O σ bond of OX. The other in-plane electron remains in the in-plane lone-pair orbital on the oxygen side to become one of the radical electrons. The 5 out-of-plane electrons (two in π_z, two in CH σ bonds and one in p_z of oxygen originally) form a delocalized π-system among the three carbon and one oxygen atoms. A planar structure, therefore, favors stabilizes the total energy. Since there is one electron less than that needed for three π bonds formed from two C-C bonds and one C-O bond, the three bond length are slightly larger than that of a regular double bond , but shorter than a single bond.

The remaining problems are: (1) How does CP dissociate to CO + C_2H_4 ? and (2) How does the CCA channel on the triplet pes correlate with the singlet intermediate CP ? In reply to the first question, Yamabe *et al.* have explored[7] the possible paths of photodissociation. That study showed that there is no easy pathway connecting ground-state CP to the products ground-state. By examing the state correlation diagram, the authors showed that there is no simple concerted C-C bond cleavage process in the reaction. The most favorable path that they found is accompanied by a "bent-in-plane" motion, i.e., one initiated by scission of the C_1-C_2 bond to the carbonyl with subsequent formation of a "*zwitterionic* intermediate," followed by internal conversion (IC) or intersystem crossing (ISC) ($^{1,3}A \rightarrow ^1 S_0$) to the ground-state pes leading to ground-state products.

ISC is also relevant to the second question. There will be a discussion of ISC

in Sec. G. Before going to that discussion, the planar diradical with its resonance structures ($^{1,3}A'$ and $^{1,3}A''$) and the relation between the existance of resonance structures and ISC will be discussed in Sec. F.

E. TCA Channel

As shown in Chapt. III, first part (experimental study) of this thesis, the TCA channel has been observed in molecular beam experiments at relatively small collision energies (5-8 kcal/mole). There are several reasons that favor of this channel over the CCA channel: (1) The products are composed of a light species (H) and a heavy species (C_3H_3O). In the center-of-mass coordinate system both species share the total translational energy of the products. The large mass ratio (55:1) of C_3H_3O to H results in C_3H_3O move very slowly relative to H. In the laboratory coordinate system the heavy species is distributed over a small angle range leading to an easily detectable signal. In contrast, the mass ratio of the CCA channel is 1:1. Both species spread over a wide angle range that makes products difficult to detect. (2) The masses of both CO and ethylene (CCA products) are 28. It is close to the high noise background (caused by CO or N_2 residues) range of masspectrometer. C_3H_3O does not have this problem. (3) As shown in Sec. D, the CCA reaction does not have a staightforward path to final products. This might dramatically reduce the possibility of reaction under single-collision conditions.

Many reactions of oxygen with olefins, similar to the TCA channel have been studied.[9-14] The usual process is initiated by the addition of an oxygen to a double bond to form a diradical followed by elimination of a hydrogen atom. One example is the reaction of oxygen with ethylene. Baseman *et al.*[10,13-14] showed that this channel is the dominate one in molecular beam experiments. Both the addition intermediate and vinoxy radical product have been studied theoretically by Dupuis

et al.[35,36]. However, it would be interesting to learn the following questions: Is there a stable addition intermediate for the allene reaction case? How does the magnitude of the transition-state barrier compare with that for the CCA channel. What is the mechanism of reaction?

The MCSCF total energies at (1) reactant; (2) transition state; and (3) addition intermediate are shown in Tab. 3.7. The reaction energies are listed in Tab. 3.8. It is interesting to note that the addition intermediate is more stable (-8.15 kcal/mole) than $C_3H_4 + O$ with a SZ basis set, but less stable with both DZ and DZP basis sets (7.90 and 7.21 kcal/mole, respectively). The problem was encountered in the calculation of oxygen reacting with ethylene.[35] In that paper the addition intermediate energy has a negative sign (-7.7—-11.4 kcal/mole) relative to C_2H_4+O with a STO-3G (equivalent to our SZ) basis set, but positive (8.5−13.2 kcal/mole) with a 3-21G (equivalent to our DZ) basis set. The only difference in the two sets of calculations is that the result using the DZP basis set is negative in the ethylene reaction but positive in the allene reaction. From CI calculations Dupuis *et al.* estimate the stabilization energy to be about 15 kcal/mole for the ethylene reaction. This is also a reasonable value for the allene reaction.

Compared with the CCA intermediate the TCA intermediate has a smaller stabilization energy. The existence of the planar structure and delocalized π-system of the CCA intermediate may account for the difference. This diradical molecule has a symmetry plane (CCCO) but does not have planar structure. The terminal CH_2 group is in the plane but the oxygen linked CH_2 group is out of plane but

symmetric with respect to the plane (see Tab. 3.9). A more crowd sp^3 hybridazation in oxygen-linked carbon reduces the π-type CO bonding. A largerbond CO bond length (1.40-1.50 Å) provides the evidence for this view. Both the geometry and electronic structure analysis shows that the $C_1 - C_2$ double bond remain intact during the reaction. The two CH bonds lengthen for the oxygen-linked carbon (1.087 Å) and are slightly longer than the two terminal CH groups (1.078 Å).

The reaction may proceed when oxygen attacks the terminal carbon with a π orbital in the CCCO plane and CH_2 out of the plane. Dupuis *et al.* thought an asymmetric approach, i.e., the oxygen comes in along the ethylene plane that has a π orbital perpendicular to the plane. The reason I believe this is the preferred approach direction is that for the allene TCA reaction the formation of the CO σ bond is more important than formation of the π bond, since the out-of-plane CH_2 group eliminates π-type bonding between CO or CC. In contrast to the CCA channel (Sec. C), the electronic configuration of the attacking oxygen that favors reaction can be either $\mid 2P_x^1 2P_y^2 2P_z^1 \mid$ or $\mid 2P_x^1 2P_y^1 2P_z^2 \mid$. The former configuration leads to a $^{1,3}A''$ product with a longer CO bond length (1.5 Å), whereas the latter leads to a $^{1,3}A'$ product that has a shorter bond length (1.4 Å). (see Tab. 3.9) The reaction process can be described as an uncoupling of C=C bonding and the formation of a CO σ bond. The repulsion pushes the two hydrogens back, and the other C=C bond together with the terminal CH_2 group remain unchanged. The replacement of one allene π bond by a CO σ bond should lower the energy but not as much as for the CCA channel. This analysis of the mechanism also provides the

explanation for the higher transition-state barrier.

The lone-pair orbitals of $^{1,3}A'$ and $^{1,3}A''$ are shown in Fig. 3.12 where the $^{1,3}A''$ state is a $\pi\sigma$ type diradical with one radical electron in plane and the other out of plane, and the $^{1,3}A'$ is a $\sigma\sigma$ type radical with both radical electrons in the plane.

Compared with the CCA channel, the TCA channel has a higher (also, not adequate to molecule beam experiment with less collision energy) barrier and a less stable intermediate. The question that arises is what mechanism dominates this channel: addition or substitution? The well-known addition mechanism was originally suggested by Cvetanovic,[45] and confirmed by several authors[38,39] for the reaction of oxygen with olefins. As we discussed in Secs. C and E, there should be no doubt about electronphilic addition of $O(^3P)$ to central carbon. An interesting test can be made for $O(^3P) + C_3O_2$ where only the central carbon is available to be attacked. An investigation using a CO laser resonance absorption technique[46] found a near-statistical CO vibrational energy distribution in the $O(^3P) + C_3O_2$ reaction. It provides evidence for the existence of a C_3O_3 intermediate. In contrast, a laser-induced fluorescence (LIF) study of CH_2CHO produced in a crossed molecular beam reaction found[43,44] a nonstatistical nascent vibrational state distribution. It demonstrats that CH_2CHO is formed through a direct scattering process rather than from decay of a long-lived complex. This is also consistent with the non-symmetric angular distribution found in the molecular beam experiment.[10,13,14] and the absence of quenching of the CH_2CHO product at high gas pressure in the

LIF study.[42] The reaction of oxygen with ethylene is similar to the TCA channel of oxygen with allene. The overly high entrance and exit barrier obtained by this calculation can be reduced by consider such a reaction pathway: As oxygen approachs the terminal carbon while the hydrogen attached to this carbon starts to leave. As I analyzed early in this section, this substitution mechanism may involve a symmetric approach, i.e., oxygen attack along the π orbital plane, instead of asymmetric approach.

F. Allenyloxy Radicals

The *trans* and *cis* allenyloxy radicals are the products of the TCA channel, resulted from the addition intermediates when one of the hydrogens of the central carbon is kicked out. The sp^3 hybridization becomes sp^2 and a planar geometry (see Fig. 3.10) can be achieved in this way. The optimized geometric parameters for various wavefunction are listed in Tab. 3.10.

In the study of the electronic structure of vinoxy radical CH_2CHO^{35} there are three structures formed: a $^2A''$ ethenyloxy radical with a C=C double bond, a $^{1,3}A''2$ formyl methyl radical with C=O double bond, and a $^2A'$ ethenyloxy radical with unpaired electron located in the plane at oxygen. The question that arises is: should the similar structures exist for allenyloxy radical? The answer is no. The explanation is as follows: (1) There is a lone-pair orbital in hydrogenless C_1 atom which is in a good position to accept an unpaired electron. The 135° bending reflects a deformed sp^2 hybridization with a lone-pair tail. Therefore, any $^{1,3}A''2$ state would seem not to favor this radical. (2) The C-C-C-O chain favors forming a conjugate π-system which is similar to butadiene. That is, there should be a C=O double bond and a C=C double bond with the terminal carbon. Such evidence is provided by the shorter C=O, $C_1 - C_2$ bond lengths (1.27 Å and 1.348 Å , respectively) and the longer $C_1 - C_3$ bond length (1.47 Å).

The stability of the 4 electron π-system structure can also be obtained by symmetry analysis. Let us compare the symmetry of this structure with that of the CCA intermediate. This geometry (*trans* or *cis*) has C_s symmetry, and the CCA

intermediate has C_{2v} symmetry. Further analysis indicates that the higher C_{3v} symmetry can be achieved for identical atoms system. In other words, C_{2v} symmetry can be treated as a reduction from C_{3v} obtained by replacing a terminal carbon by oxygen. Fig. 3.12 shows the energy correlation of molecular orbital. The doubly degenerate E orbital of C_{3v} splits into non-bonding and weakly bonding orbitals (b_2) (see Fig. 3.11) by the perturbation of oxygen substitution. The C_{2v} symmetry structure provides the stability for either 4 or 5 electrons in this π orbitals. Differing from CCA intermediate these chain structure allenyoxy radicals does not contain a non-bonding orbital. Instead, there are two bonding and two anti-bonding orbitals (see Fig. 3.12) in C_s symmetry. Therefore only a π-electron system containing 4 electrons ($^2A'$) can be stable.

G. Intersystem Crossing

1. Spin-Orbit Interaction

Intersystem crossing (ISC) plays a significant role in many reactions of $O(^3P)$ with unsaturated hydrocarbons. $O(^3P)+C_3H_4$ is one of the examples in which reaction is initiated by a triplet reactant and concluded with singlet products. Recently, efforts have been made to explore the C-C bond rupture channel in $O(^3P) + C_2H_4$ in a molecular beam experiment. The barrier (about 50 kcal/mole higher than the stablized intermediates and more than 20 kcal/mole higher than reactants) had been a difficulty for a hydrogen atom migration followed by a C-C bond rupture along the triplet potential energy surface. In other words, the C-C bond rupture channel would not be proceeded on the triplet pes, and it might be easier when the reaction takes place on the singlet pes. This would require an ISC along the reaction pathway.

As discussed in previous sections (3, 4, 5) there is always diradical formation when the oxygen-atom insertion causes the opening of a C=C double bond. The vertical energy splitting between the singlet and triplet diradical can be estimated by counting the different electron-electron interactions of the two cases: parallel spins and one of them flipped. There are two terms that may change during the spin flip: one arises from the interaction between the flipped electron with the closed-shell electrons, the other occurs because of the interaction between the two radical electrons. It seems unlikely that there is any difference from the first term since the direction of the spin does not affect the interaction of a single electron with

paired electrons. The only difference arises from the interactions between unpaired electrons with same and opposite spin. The overall singlet-triplet energy gap can be written as

$$\Delta E = < i \mid V \mid j >_t - < \bar{i} \mid V \mid j >_s \tag{4.3}$$

where the bar denotes a spin down electron (β) and the absence of a bar denotes spin up (α). If the interactions in both cases are small (it might be the case when the two radical electrons are geometrically apart or have different symmetries), the singlet-triplet energy gap will be small. The 9.023 kcal/mole energy gap[2] between $^1B_1$ and $^3B_1$ states of CH_2 may be the maximum one since the two radical electrons interacting with each other belong to the same carbon atom. For another example, among the four resonance structures of C_2H_4O diradicals ($\sigma\sigma$, $\sigma\pi$, $\pi\sigma$, $\pi\pi$, see Ref. 34) each has a singlet-triplet energy gap that is less than 3 kcal/mole. (see Tab. 3.11)

However, a small singlet-triplet energy gap does not provide a sufficient condition for a spin-forbidden transition. The possibility exists becauses of the spin-orbit interaction. The spin-orbit coupling operator is defined as

$$\hat{H}_{so} = \frac{e^2}{2m^2c^2} \sum_{K,p} (\frac{Z_K}{r_{pK}^3} \hat{L}_p \cdot \hat{S}_p)$$

$$= \sum_{K,p} A_{Kp}(\hat{L}_{xp} \cdot \hat{S}_{xp} + \hat{L}_{yp} \cdot \hat{S}_{yp} + \hat{L}_{zp} \cdot \hat{S}_{zp}) \tag{4.4}$$

where $\hat{L}_p$ and $\hat{S}_p$ are the orbital angular and spin angular momentum operators for electron p, Z_K/r_{pK}^3 represents the effective electric field acting on electron p at a distance r_{pK} from nucleus K. Tab. 3.12 shows the effect of the spin and orbital

angular momentum operator. From the definition one finds that non-vanishing coupling matrix elements can be obtained by acomplishing a spin flip with an electron jump between two perpendicular p-orbitals.

For an atom-centered basis set, the following matrix element relation holds,

$$< \bar{\psi}_\mu \mid \xi \hat{L}_y \cdot \hat{S}_y \mid \psi_\nu > \neq 0 \tag{4.5}$$

$$when \quad \psi_\mu = 2p_z, \quad \psi_\nu = 2p_y$$

We now discuss the molecular orbital. The singlet and triplet MO wavefunction can be expressed as

$$\begin{aligned} {}^1\psi_k &= \sum_a C_{ak} V_a(ij') \\ {}^3\psi_m &= \sum_b C_{bm} T_b(lk') \end{aligned} \tag{4.6}$$

Ignoring the closed shells, the singly occupied MOs are

$$\begin{aligned} V_a(ij') &= \frac{1}{2}[\varphi_i(p)\varphi_{j'}(q) + \varphi_i(q) + \varphi_{j'}(p)] \\ &\quad \times[\alpha(p)\beta(q) - \alpha(q)\beta(p)] \\ T_b(lk') &= \frac{1}{2}[\varphi_l(p)\varphi_{k'}(q) + \varphi_l(q) + \varphi_{k'}(p)] \\ &\times \left\{ \begin{array}{lcl} [\alpha(p)\alpha(q) - \beta(p)\beta(q)] & : & \Gamma_- \\ [\alpha(p)\beta(q) + \alpha(q)\beta(p)] & : & \Gamma_z \\ i[\alpha(p)\alpha(q) + \beta(q)\beta(p)] & : & \Gamma_+ \end{array} \right\} \end{aligned} \tag{4.7}$$

Finally,

$$<^1 \psi_k \mid \hat{H}_{so} \mid^3 \psi_m >$$

$$= \sum_{a,b} C^*_{ak} C_{bm} < V_a(ij') \mid \hat{H}_{so} \mid T_b(lk') > \tag{4.8}$$

Non-vanishing matrix elements exist only with the V's and T's that contain the non-vanishing matrix element of atomic-centered basis set (4.5). From (4.6) It may happen when $\bar{\psi}_\mu$ and ψ_ν are different p-type orbitals (i.e., one p_x and the other p_y). In other words, intersystem crossing may happen when the electron jumps between two molecular orbitals perpendicular to each other. During the transition the change of orbital angular momentum is compensated by the spin angular momentum. Total angular momentum is conserved.

2. Resonance Structures of Radicals

We have shown that there are always many resonance structures of radicals. Take the planar molecules (CCA intermediate, TCA allenyloxy radical, or ethyloxy radical) as examples, the reason there have been so many resonance structures is the existence of more than two molecular orbitals for radical electrons. Especially, there are several in-plane orbitals (a') and out-of-plane orbitals (a'') with nearly degenerate energies. The lone-pair orbitals at oxygen sites or hydrogenless carbon sites are good a' orbitals for radical electrons. The non-bonding a'' orbitals are the other candidates favoring the occupying of π-type radical electrons. The different occupations among these orbitals ($\sigma\sigma$, $\sigma\pi$, $\pi\sigma$, $\pi\pi$ etc.) lead to various resonance structures.

For instance, the 4-electron π-system ($^{1,3}A''$) CCA intermediate can be formed from a 5-electron π-system ($^3A''$) in the following ways (see Fig. 3.12):

(1) move one electron from $2a_2$ to $7b_1$ without changing spin;

(2) move one electron from $1b_2$ to $7b_1$ with change of spin;

(3) move one electron from $2a_2$ to $7b_1$ with change of spin, then let the $1b_2$ electron jump to $2a_2$.

Here, I want stress that the jump might happen not only at intermediate state, but also at any moment of whole reaction process. The torsional motion of CH may facilitate the connection between the perpendicular orbitals. Since the singlet-triplet energies are small there should be a high probability for surface crossing between the singlet and triplet pes.

3. *Conclusion*

It is very likely that many reactions of oxygen with unsaturated hydrocarbons involve an ISC. A polyatomic system provides various orbitals for radical electrons. Although differing in the occupation of these orbitals the resonance structures have nearly degenerate energies. Since all the radical electrons are active valence electrons, and for planar geometry the out-of-plane orbitals are delocalized, an electron jump between these non-bonding orbitals accomplished with a spin-flip is easily associated with spin-orbit coupling. The spin-orbit coupling makes the ISC possible when the transition includes a p orbital having a 90° change, that is symmetry- forbidden and spin-forbidden but the angular momentum is conserved in the process. The ISC might happen along the reaction path with both singlet and triplet pes have crossing or near crossing. CH torsional motion may help the transition.

H. Summary

There are two reaction channels, CCA and TCA in the reaction of $O(^3P)$ with allene. For each channel, a MCSCF study of reactants, intermediates, and products has been carried out. Fig. 3.15 is a correlation diagram containing all the relevant molecules and radicals of this reaction. The major findings of this study are:

(1) For the CCA channel there is a 16.68 kcal/mole barrier to formation of the triplet intermediate oxyallyl which lies 23.52 kcal/mole below the reactants. Differing from singlet intermediate cyclopropanone the triplet has a planar structure with delocalized π electrons. Due to σ bonding, the ring molecule CP is 21.2 kcal/mole more stable than triplet oxyallyl. The fairly low barrier and the stability of the intermediate favors an insertion mechanism.

(2) A MCSCF calculation carried out at 12 different C-O separations shows that the CCA reaction mechanism includes the decoupling of two perpendicular π bond and the formation of CO σ and π bonds. The geometry changes include CH_2 group twisting, C-C-C chain bending, and C-C stretching when one reduces the CO distance. The perpendicular π system widely accepts oxygen atom attack along each of the two π orbital plane.

(3) For the TCA channel the barrier is higher (27 kcal/mole) than that of CCA channel and the intermediate is less stable (7-8 kcal/mole higher than reactant by this study) than that of CCA channel. This suggests a substitution mechanism rather than an unimolecular dissociation after a long-lived intermediate formation. One π-bond decoupling (there are two π bonds in all) is replaced by CO σ-bond

formation. This channel (TCA) favors oxygen attack along the plane containing π orbital.

(4) The TCA products, *trans* and *cis* allenyloxy radicals, also have planar structures and delocalized π electrons. They do not favor 5 out-of-plane electron configurations as the CCA intermediate does, but 4 conjugated π electrons.

(5) The diradicals has many resonance structures with various radical electron orbital occupancies (both in plane, both out of plane, or one in one out, etc.). A polyatomic molecule provides several lone-pair orbitals in the plane and also several non-bonding orbitals perpendicular to the plane, and all the orbitals are nearly degenerate. The pes curve-crossing facilitates electron transitions among these orbitals. Whenever an electron transition between two perpendicular p-type orbitals happens, this may cause intersystem crossing via the spin-orbit coupling, because the change of spin angular momentum can be compensated by the change of orbital angular momentum. For such a case, the non-vanishing matrix elements have contributions to the transition probability.

References

(1) P. Herbrechtsmeir and H. G. Wagner, Ber. Bunsenges, Physik. Chem. **76**, 517 (1972).

(2) J. J. Havel, J. Am. Chem. Soc., **96**, 530 (1974).

(3) M. C. Lin, R. G. Shortridge and M. E. Umstead, Chem. Phys. Lett., **37**, 279 (1976).

(4) Y. N. Chiu and M. S. F. A. Abidi, J. Phys. Chem. **86**, 3288 (1982).

(5) J. M. Pchan, J. E. Baldwin, and W. H. Flygare, J. Am. Chem. Soc., **91**, 1896 (1969).

(6) A. Liberles, A. Greenberg, and A. Lesk, J. Am. Chem. Soc., **94**, 8686 (1972).

(7) S. Yamabe, T. Minato, and Y. Osamura, J. Am. Chem. Soc., **2**, 4525 (1979).

(8) A. M. Schmoltner, S. Y. Huang, R. Bruzynski, and Y. T. Lee, private communication.

(9) S. J. Sibener, R. J. Buss, P. Casavecchia, T. Hirooda, and Y. T. Lee, J. Chem. Phys., **72**, 4341 (1980).

(10) R. J. Buss, R. J. Baseman, G. Z. He, and Y. T. Lee, J. Photochem. **17**, 389 (1981).

(11) G. Z. He, R. J. Buss, R. J. Baseman, R. Tse, and Y. T. Lee, J. Phys. Chem., **86**, 3547 (1982).

(12) R. J. Baseman, R. J. Buss, P. Casavecchia, and Y. T. Lee, J. Am. Chem. Soc., **106**, 4108 (1984).

(13) R. J. Baseman, Ph. D. thesis, U. C. Berkeley (1982).

(14) R. J. Baseman, *Report 1982*, LBL-15259; Order No. DE83004296, 249 pp. (Eng).

(15) B. P. Stoicheff, Can. J. Phys., **33**, 811 (1955).

(16) H. E. Watson, G. P. Kane and K. L. Ramaswany, Proc. Roy. Soc. **152**, 130 (1936).

(17) M. L. Huggins, J. Am. Chem. Soc., **61**, 916 (1941).

(18) A. A. Petrov and A. V. Federova, Russ. Chem. Rev. (Engl. Transl.), **33**, 1 (1964).

(19) C. Barter, R. G. Meisenheimer, and D. P. Stevenson, J. Phys. Chem., **64**, 1312 (1960).

(20) J. Guy, J. Tilleau, M. Gaudemar, and B. Gross, Comp. Rend., **243**, 34 (1956).

(21) J.-F. Labrre and F. Gallais, Compt. Rend., **253**, 1935 (1961).

(22) W. J. Jones and W. J. Orville-Thomas, "*Proceedings of the 4th International Meeting on Molecular Spectroscopy, Bologna, 1959*," p 305; Chem. Abstr., **59**, 4679 (1963).

(23) H. O. Pritchard and F. H. Sumner, Proc. Roy. Soc. (London), **A235**, 136 (1956).

(24) B. Pullman and G. Berthier, Bull. Soc. Chim. France, 145 (1949).

(25) J. Serre, J. Chem. Phys., **53**, 284 (1956).

(26) G. Herzberg, "*Molecular Spectra and Molecular Structure*", Vol. II, 1945.

(27) J. W. Linnett and W. H. Avery, J. Chem. Phys., **6**, 686 (1938).

(28) I. M. Mills and J. L. Duncan, J. Mol. Spectry., **9**, 244 (1962).

(29) J. Overend and B. Crawford, J. Chem. Phys., **29**, 1002 (1958).

(30) K. N. Rao, A. H. Nielsen, and W. H. Fletcher, J. Chem. Phys., **26**, 1572 (1957).

(31) Z. Z. Yang, L. S. Wang, and Shirley, private communication.

(32) R. Hoffman, J. Am. Chem. Soc., **90**, 1475 (1968).

(33) J. F. Olsen, S. Kang, and L. Burnelle, J. Mol. Struct., **9**, 305 (1971).

(34) J. Coetzer, Ph. D. thesis, Indiana University (1968).

(35) M. Dupuis, J. J. Wendoloski, T. Takada, and W. A. Lester, Jr., J. Chem. Phys., **76**, 481 (1982).

(36) M. Dupuis, J. J. Wendoloski, and W. A. Lester, Jr., J. Chem. Phys., **76**, 488 (1982).

(37) R. J. Cvetanovic, *Prog. React. Kinet.*, **2**, 39 (1964).

(38) R. E. Huil and J. T. Herron, *Prog. React. Kinet.*, **8**, 1 (1978).

(39) M. C. Lin, "*Potential Energy Surfaces*", K. P. Lawley, Ed. Wiley, New York, 1980, p136.

(40) N. Honjou, J. Pacansky, and M. Yoshimine, J. Am. Chem. Soc., **107**, 5332 (1985).

(41) J. R. Kanofsky, and D. Gutman, Chem. Phys. Lett., **15**, 236 (1972).

(42) H. E. Hunziker, H. Kneppe, and H. R. Wendt, J. of Photochemistry, **17**, 377 (1981).

(43) G. Inoue and H. Akimoto, J. Chem. Phys., **74**, 425 (1981).

(44) K. Kleinmanns and A. C. Luntz, J. Phys. Chem., **85**, 1966 (1981).

(45) R. J. Cvetanovic. "*Addition of Atom to Olefins in the Gas Phase*", pp.122.

(46) D. S. Y. Hsu and M. C. Lin, J. Chem. Phys., **68**, 4347 (1978).

(47) N. C. Baird, R. R. Gupta, and K. F. Taylor, J. Am. Chem. Soc., 4531 (1979).

(48) M. Dupuis, J. Rys, and H. F. King, J. Chem. Phys. **65**, 111 (1976).

Table 4.1 Optimized Allene Geometries

Wavefunction	C-C(a.u.)	C-H(a.u.)	$\angle CCH(deg.)$
SZ,MC	1.318	1.087	121.8
DZ,MC	1.330	1.077	121.2
DZP,MC	1.324	1.079	120.9

Table 4.2 Comparison of normal mode frequencies of C_3H_4 and $C_3H_4^+$.[a]

Mode		$\Delta f(cm^{-1})$	
symm.	$\Delta\nu$	C_3H_4	$C_3H_4^+$
b_2	0-1	820	750.6
	1-2	–	721.5
	2-3	–	676.3
	3-4	–	577.9
	4-5	–	468.1
$1a_1$	0-1	1071	1025
$2a_1$	0-1	1432	1331
$3a_1$	0-1	2993	2611

[a] Frequencies for C_3H_4 molecule are obtained from Raman spectrum (Herzberg).

Frequencies for $C_3H_4^+$ are obtained from photoelectron spectrum (Yang *et al.*).

Table 4.3 Total Energies (a.u.) along CCA Pathway*

Wavefunction	Reactant	Trans. State	Intermediate
SZ,MC	-188.3035	-188.2822[a]	-188.3629[c]
DZ,MC	-190.6887	-190.6621[b]	-190.7219[d]
DZP,MC	-190.7289	–	-190.7627[e]

Table 4.4 Interaction Energies† (kcal/mole) along CCA Pathway

Wavefunction	Barrier	Binding Energies
SZ,MC	13.36	-37.88
DZ,MC	16.68	-20.82
DZP,MC	–	-23.52

* R is the central carbon to oxygen atom distance.

[a] R = 1.985Å.

[b] R = 1.998Å.

[c] R = 1.385Å.

[d] R = 1.315Å.

[e] R = 1.362Å.

† The total energy of $C_3H_4 + O(^3P)$ is zero of energy.

Table 4.5 Molecular Geometries along CCA Pathway

Mols.*	W.F	C_1-C_2^a	C_1-C_3^a	C-O^a	C-H^a	$\angle CCC^b$	$\angle CCH^b$	$\angle CHP^c$
AL+O	SZ,MC	1.318	1.318	10	1.087	180	121.8	0
	DZ,MC	1.330	1.330	10	1.077	180	121.2	0
	DZP,MC	1.324	1.324	10	1.079	180	120.9	0
T. S.	DZ,MC	1.340	1.380	1.988	1.072	149.6	121.0	0
OX,$^3A'$	DZ,MC	1.430	1.430	1.315	1.070	123.2	121.5	0
$^3A''$	DZP,MC	1.429	1.429	1.362	1.074	125.8	120.2	0
CP,$^1A'$	DZ,MC	1.469	1.469	1.249	1.072	67.4	119.2	90

* AL-Allene, OX-Oxyallyl intermediate, CP-Cyclopropanone,

T. S.-Transition state.

[a] Bond lengths in Å.

[b] Angle in degree.

[c] Torsional angle of CH group to plane in degree.

Table 4.6 Geometries of Cyclopropanone and Oxyallyl

Mols.*	W.F	C_1-C_2^a	C_1-C_3^a	C_1-C_3^a	C-O^a	C_1-$H_{a,b,c,d}$
CP	expt.[d]	1.475(17)	1.475(17)	1.575(12)	1.191(20)	1.086(25)
	DZ,MC	1.469	1.469	1.630	1.249	1.072
OX,$^3A'$	DZ,MC	1.430	1.430	2.516	1.315	1.070
$^3A''$	DZP,MC	1.429	1.429	2.544	1.362	1.074

Mols.*	W.F	$\angle CCC^b$	$\angle CCH^b_{a,b,c,d}$	$\angle CH_2 - P^{c,d}$
CP	expt.[d]	57.7(4)	117.4(4)	90
	DZ,MC	67.4	119.2	90
OX,$^3A'$	DZ,MC	123.2	121.5	0
$^3A''$	DZP,MC	125.8	120.2	0

* CP-Cyclopropanone, OX-Oxyallyl intermediate.

[a] Bond lengths in Å.

[b] Angle in degree.

[c] The angle between CH_2 plane and CCC plane in degree.

[d] J. M. Pochan, J. E. Baldwin, and W. H. Flygare, J. Amer. Chem. Soc., **91**, 1896 (1969).

Table 4.7 Total Energies (a.u.) along TCA Pathway

Wavefunction	Reactant	Trans. State	Intermediate
SZ,MC	-188.3035	-188.2805	-188.3165
DZ,MC	-190.6887	-190.6595	-190.6772
DZP,MC	-190.7289	–	-190.7153

Table 4.8 Interaction Energies† (kcal/mole) along TCA Pathway

Wavefunction	Barrier	Binding Energies
SZ,MC	14.43	-8.15
DZ,MC	27.00	7.21
DZP,MC	–	8.50

† The total energy of $C_3H_4 + O(^3P)$ is zero of energy.

Table 4.9 Molecular Geometries along TCA Pathway

Mols.*	W.F	C_1-C_2^a	C_1-C_3^a	C-O^a	C_1-H_a	C_1-H_b	C_1-H_c^d
AL+O	SZ,MC	1.318	1.318	10	1.087	1.087	1.087
	DZ,MC	1.330	1.330	10	1.077	1.077	1.077
	DZP,MC	1.324	1.324	10	1.079	1.079	1.079
ADD	SZ,MC	1.336	1.515	1.503	1.083	1.082	1.094
	DZ,MC	1.342	1.487	1.503	1.075	1.073	1.081
	DZP,MC	1.332	1.494	1.402	1.079	1.076	1.087

Mols.*	W.F	$\angle CCC^b$	$\angle CCH_a^b$	CCH_b^b	$\angle CCH_c^{b,d}$	$\angle CCO^b$	$\angle CH_cP^{c,d}$
AL+O	SZ,MC	180	121.8	121.8	121.8	90	–
	DZ,MC	180	121.2	121.2	121.2	90	–
	DZP,MC	180	120.9	120.9	120.9	90	–
ADD	SZ,MC	132.8	122.1	121.3	111.0	112.9	120.0
	DZ,MC	136.4	121.2	120.9	112.0	112.2	118.7
	DZP,MC	136.4	121.2	121.2	108.8	111.2	120.1

* AL-Allene, OX-Oxyallyl intermediate, ADD.-TCA additional intermediate, T. S.-Transition state.

^{a,b} Bond lengths in Å. Angle in degree.

^{c} Torsional angle of CH group to plane in degree.

^{d} Taking CCCO as a plane of symmetry, H_a and H_b are in the plane, H_c and H_d are symmetric with regard to the plane.

Table 4.10 Molecular Geometries of Allenyloxy Radicals

Mols.*	W.F	C_1-C_2^a	C_1-C_3^a	C-O^a	C-H_1^a
cis	DZ,HF	1.370	1.430	1.277	1.073
	SZ,MC	1.390	1.440	1.330	1.083
	DZ,MC	1.348	1.470	1.273	1.073
trans	DZ,MC	1.347	1.475	1.218	1.078

Mols.*	W.F	C-H_2^a	C-H_3^a	$\angle CCC^b$	$\angle CCH^b$
cis	DZ,HF	1.077	1.076	134.0	122.0
	SZ,MC	1.085	1.095	135.0	123.8
	DZ,MC	1.075	1.077	135.0	122.0
trans	DZ,MC	1.072	1.087	130.5	122.0

* All the molecules have planar structure.

[a] Bond lengths in Å.

[b] Angle in degree.

Table 4.11 Singlet-Trplet Energy Gap of C_2H_2O.*

states[a]	STO-3G	3-21G	DZP
$^{1,3}A''\pi\sigma$	1.7	2.0	1.6
$^{1,3}A'\sigma\sigma$	2.6	2.7	2.6
$^{1,3}A'\pi\pi$	0.5	0.8	0.9
$^{1,3}A''\pi\sigma$	1.6	1.6	1.8

* Energies are in kcal/mole.

[a] See text for electronic configurations.

Table 4.12 The Effects of Spin and Angular Momentum Operator

	α	β		p_x	p_y	p_z
S_x	$\frac{\hbar}{2}\beta$	$\frac{\hbar}{2}\alpha$	L_x	0	$i\hbar p_z$	$-i\hbar p_y$
S_y	$i\frac{\hbar}{2}\beta$	$-i\frac{\hbar}{2}\alpha$	L_y	$-i\hbar p_z$	0	$-i\hbar p_x$
S_z	$\frac{\hbar}{2}\alpha$	$-\frac{\hbar}{2}\beta$	L_z	$i\hbar p_y$	$-i\hbar p_z$	0

Caption

Figure 3.1. Allene molecular structure.

Figure 3.2. Normal modes of allene molecules.

Figure 3.3. Two low-lying state potential energy of C_3H_4 as a function of CH_2 group twisting angle.

Figure 3.4. Correlation diagram of allene and cation.

Figure 3.5. Photoelectron spectrum of C_3H_4 molecule.(ground state, Z.Z. Yang *et al.*)

Figure 3.6. Photoelectron spectrum of C_3H_4 molecule.(excited state, Z. Z. Yang *et al.*)

Figure 3.7. Two low-lying state potential energy of $C_3H_4^+$ as a function of CH_2 group twisting angle.

Figure 3.8. CCA channel reaction electron correlation. During the decoupling of two perpendicular π bonds of allene and the formation of CO σ and C=O π bond, the 5 out-of-plane form a delocalized π system.

Figure 3.9. Potential energy curve along CCA pathway.

Figure 3.10. Geometry changes during CCA reaction.

Upper panel: C-C bond length vs CO distance.

Lower panel: C-C-C bending angle vs CO distance.

Figure 3.11. *trans* and *cis* allenyloxy radicals geometry.

Figure 3.12. Electron configureation of oxyallyl diradical. The weakly bonding orbital $2a_2$ and non-bonding orbital $1b_2$ can be thought as splited from the doubly degenerate E state of C_{3v} symmetry by the replacement of oxygen atom (see text of Sec. 7.2). 5 out-of-plane

and 1 in-plane ($7b_1$) electron occupation forms a $\pi\sigma$ diradical ($^3A''$). The other resonance states can be made by a re-arrangement of occupation from this configuration.

Figure 3.13. Four out-of-plane molecular orbitals of oxyallyl diradical.

Figure 3.14. Four out-of-plane molecular orbitals of allenyloxy radical. Differing from oxallyl diradical (C_{3v}) there are no non-bonding orbital but two bonding and two anti-bonding orbitals.

Figure 3.15. Correlation diagram of relevant molecules of $O(^3P) + C_3H_4$ reaction.

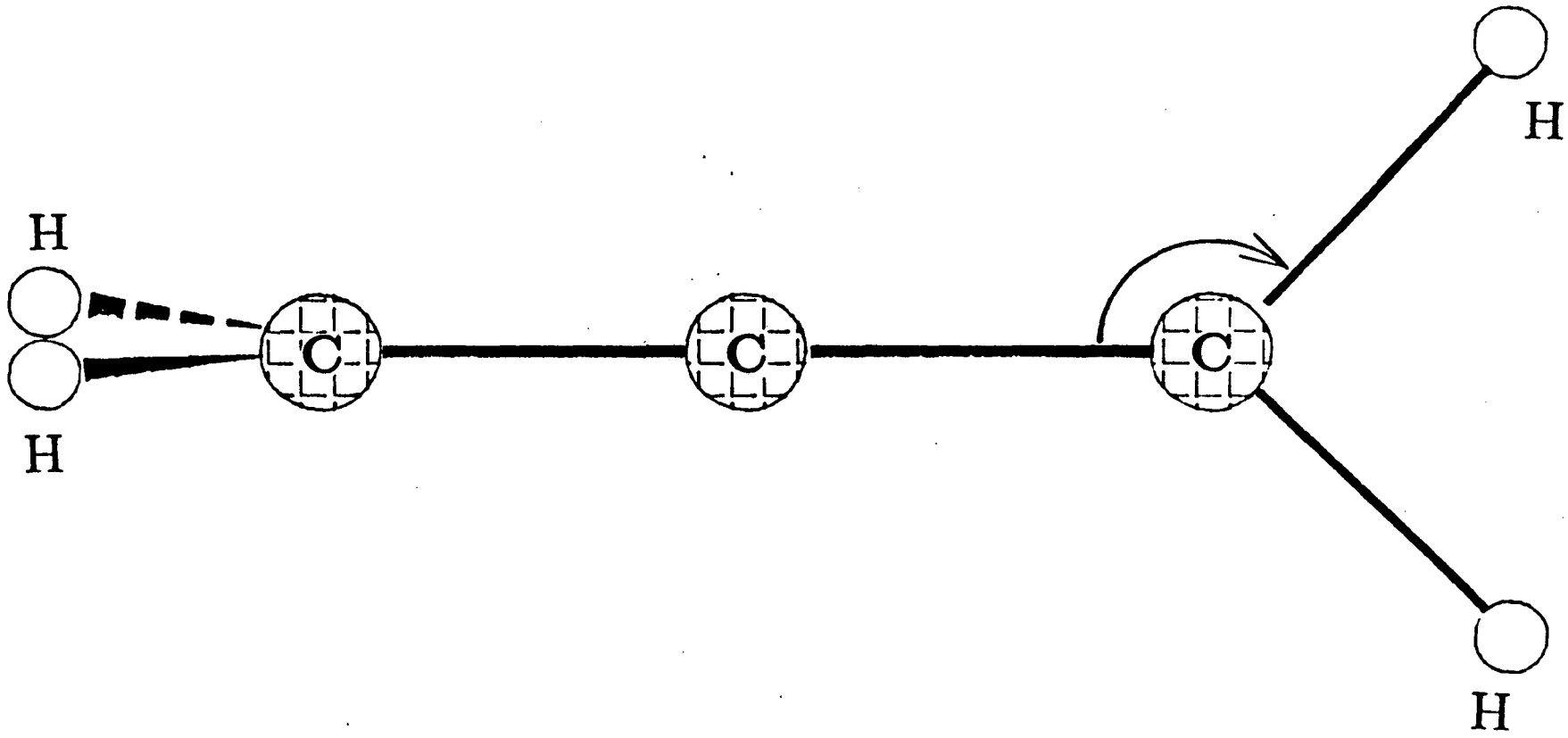

Figure 3.1

Normal Modes of Allene Molecule

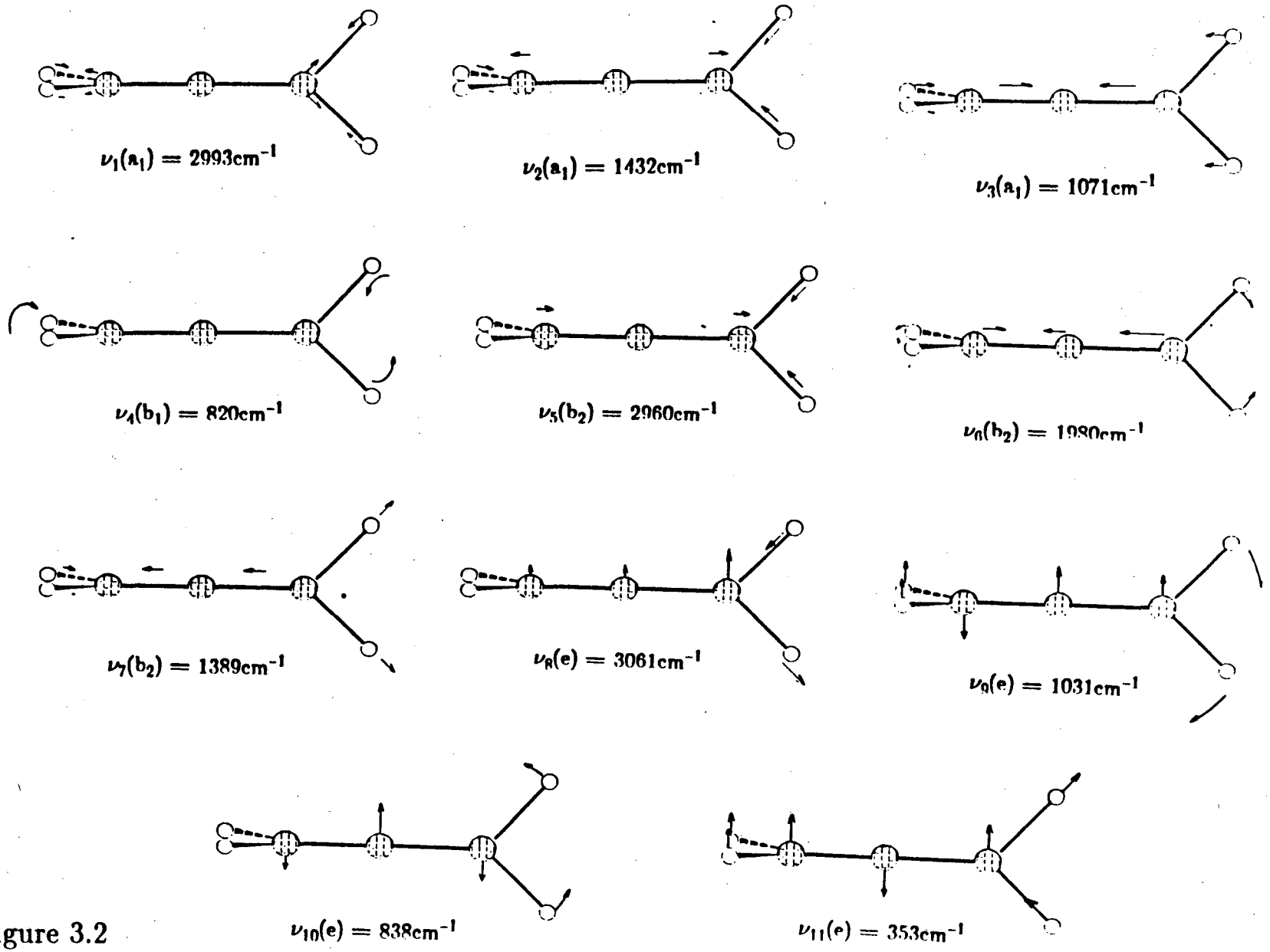

Figure 3.2

LOW-LYING STATES PES OF C3H4 VS TWISTING ANGLE

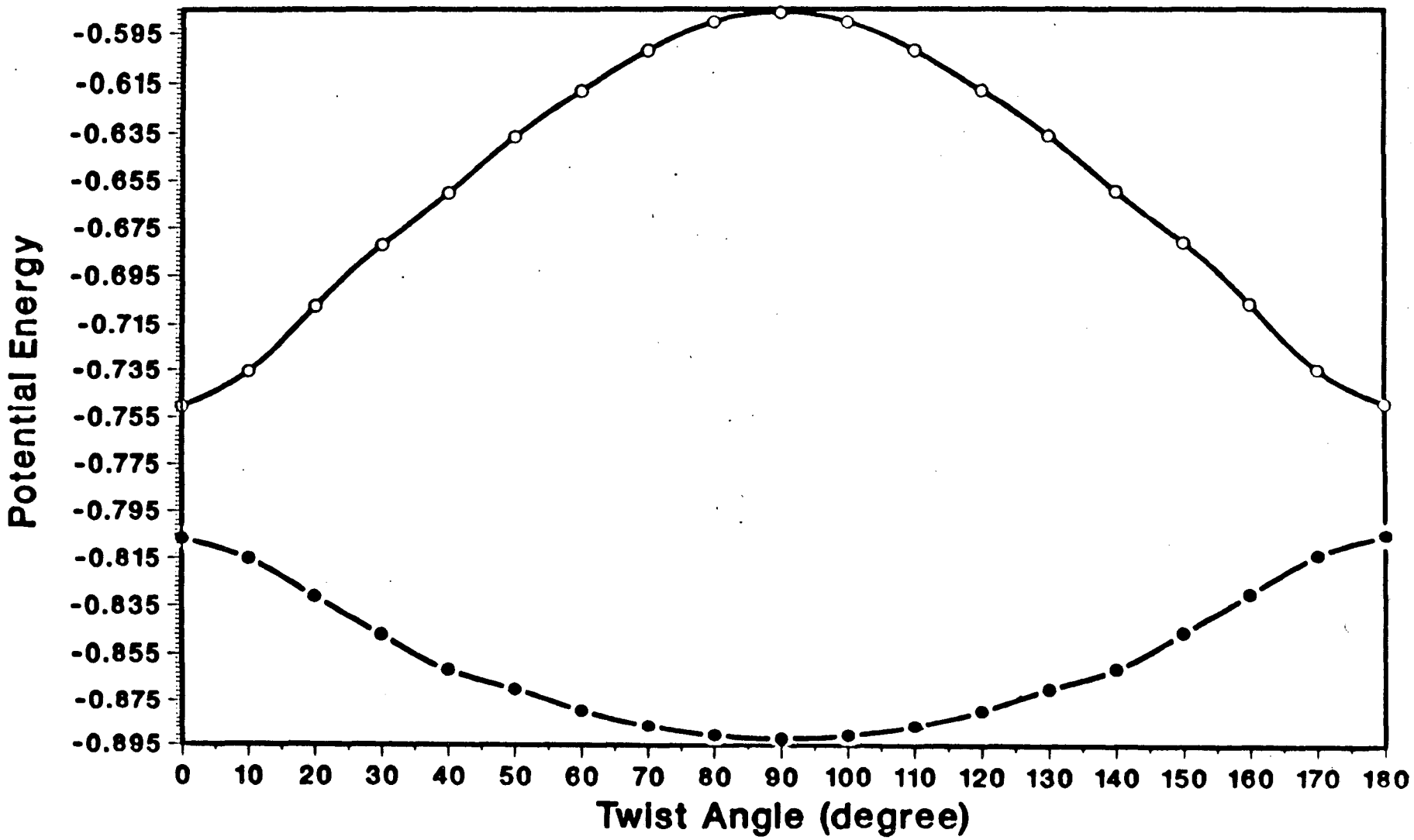

Figure 3.3

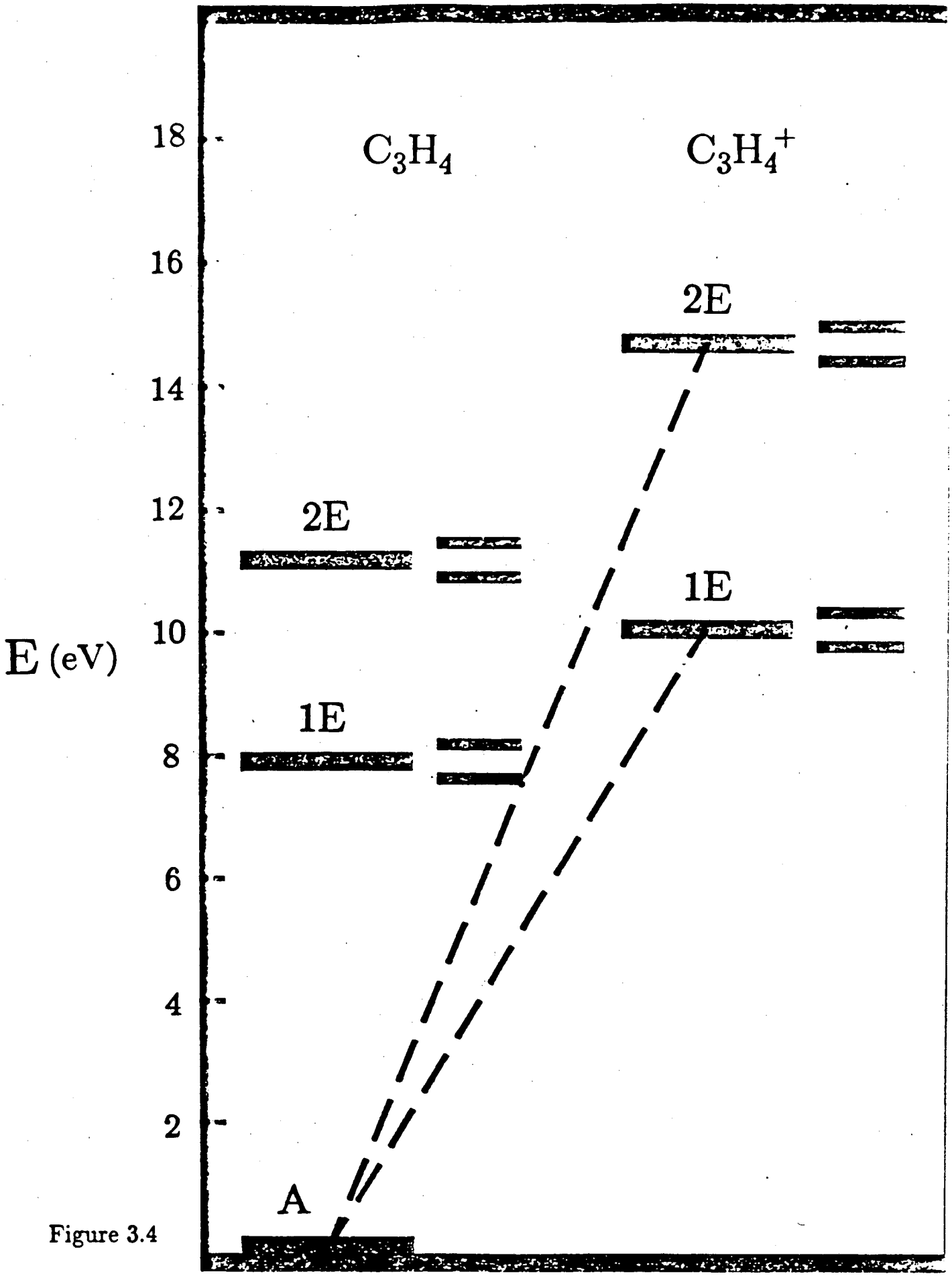

Figure 3.4

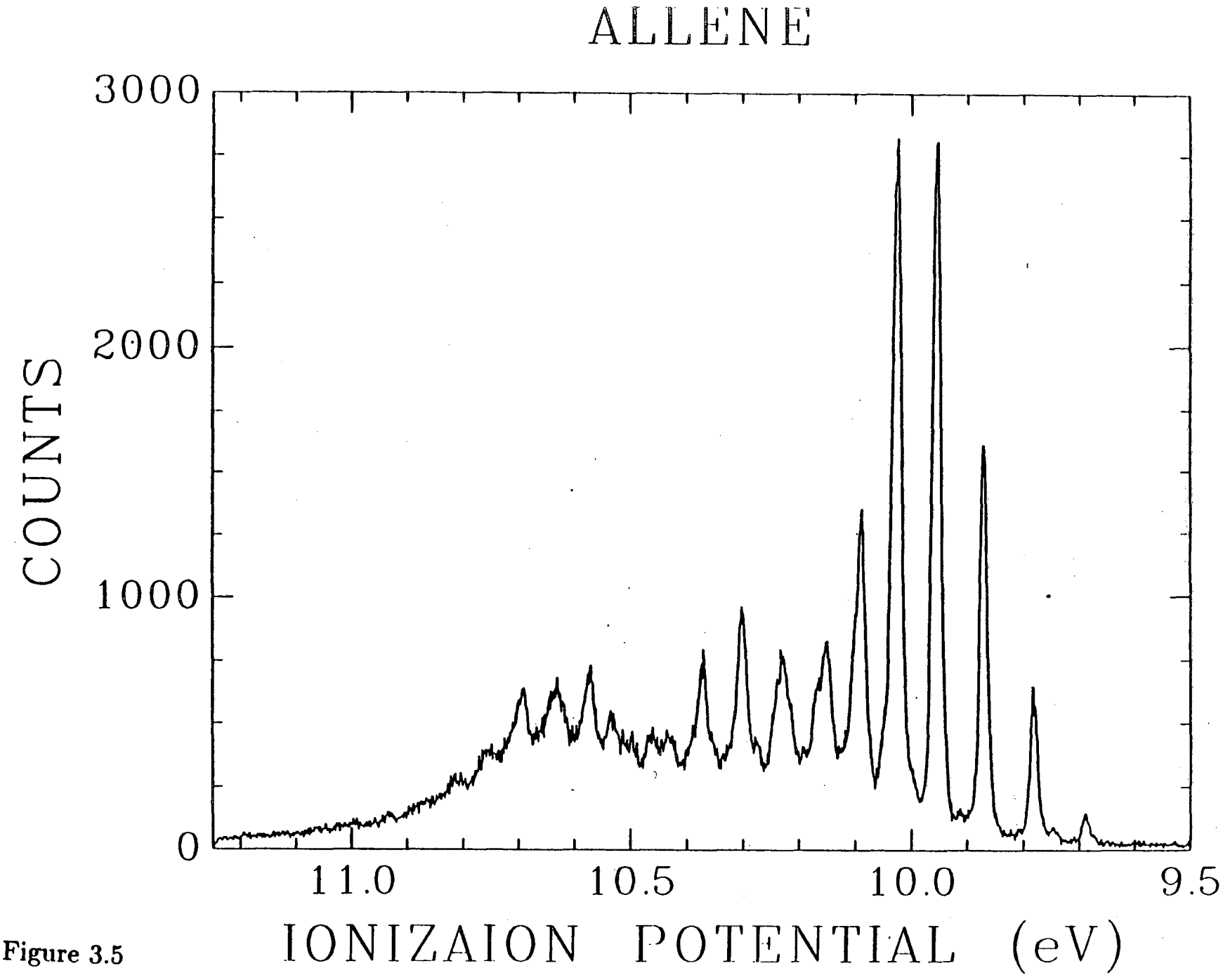
ALLENE
3000
2000
1000
0
COUNTS
11.0
10.5
10.0
9.5
IONIZAION POTENTIAL (eV)

Figure 3.5

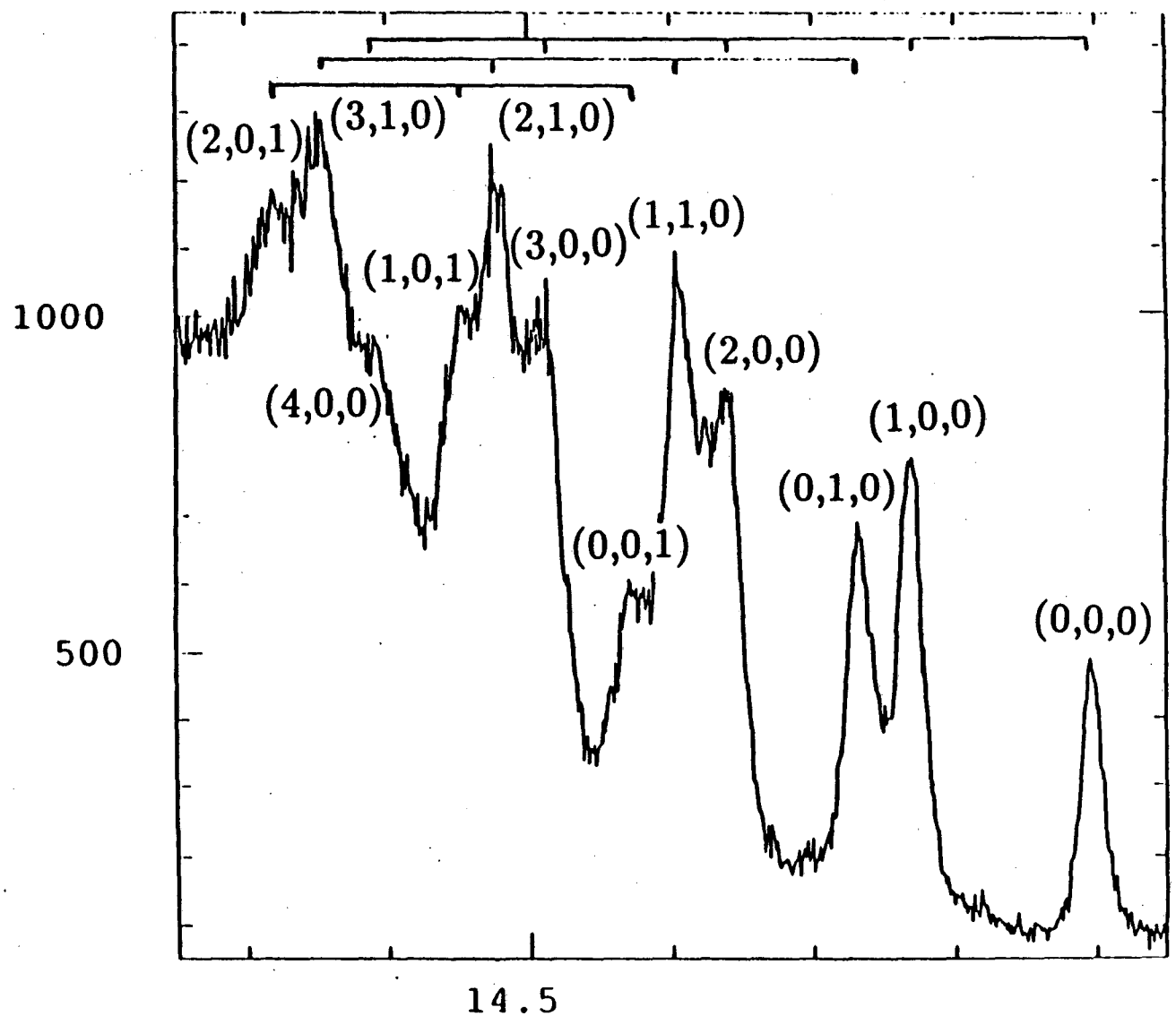

Figure 3.6

ALL: FB.DAT

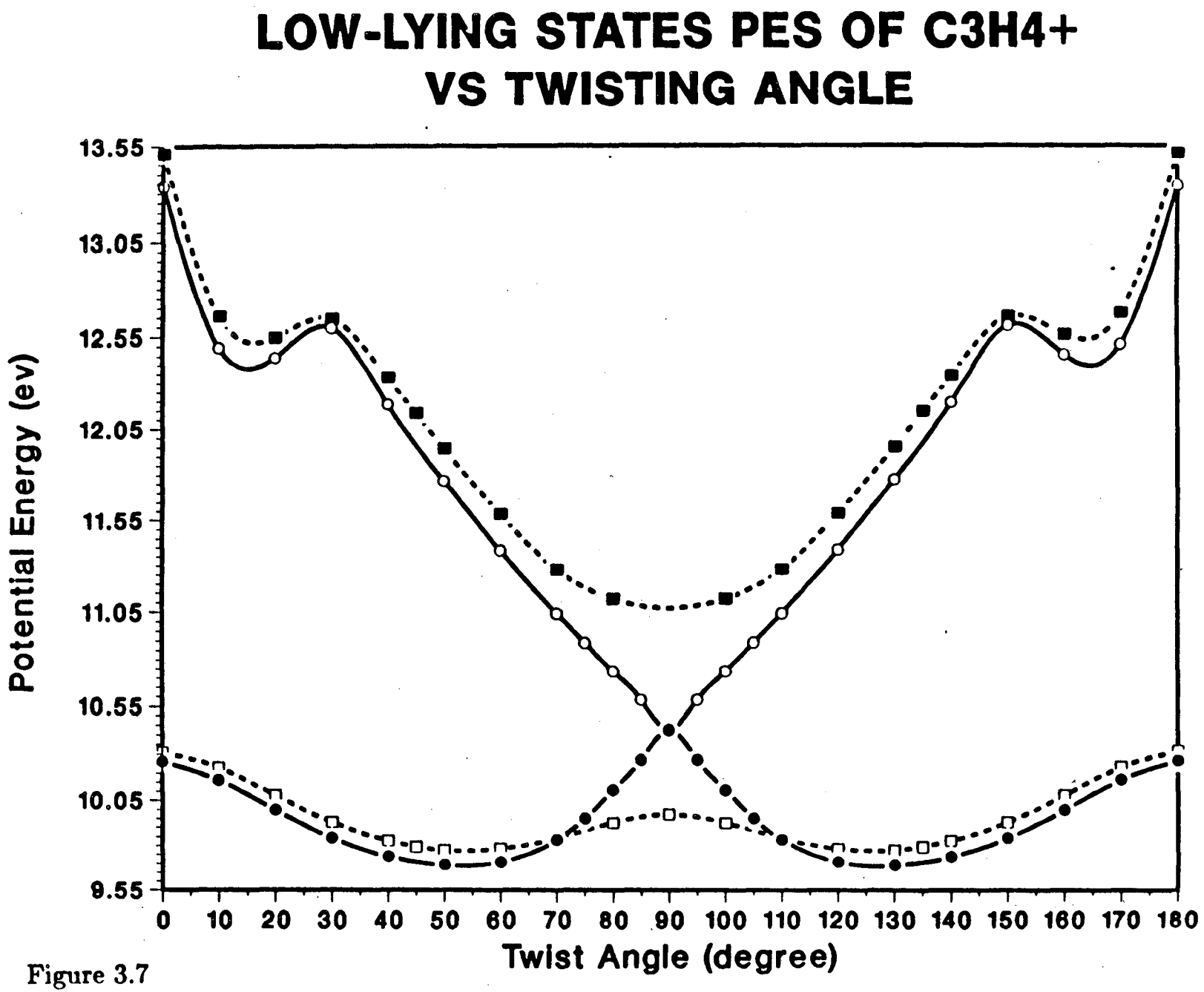
LOW-LYING STATES PES OF C3H4+
VS TWISTING ANGLE
Potential Energy (ev)
13.55
13.05
12.55
12.05
11.55
11.05
10.55
10.05
9.55
0
10
20
30
40
50
60
70
80
90
100
110
120
130
140
150
160
170
180
Twist Angle (degree)

Figure 3.7

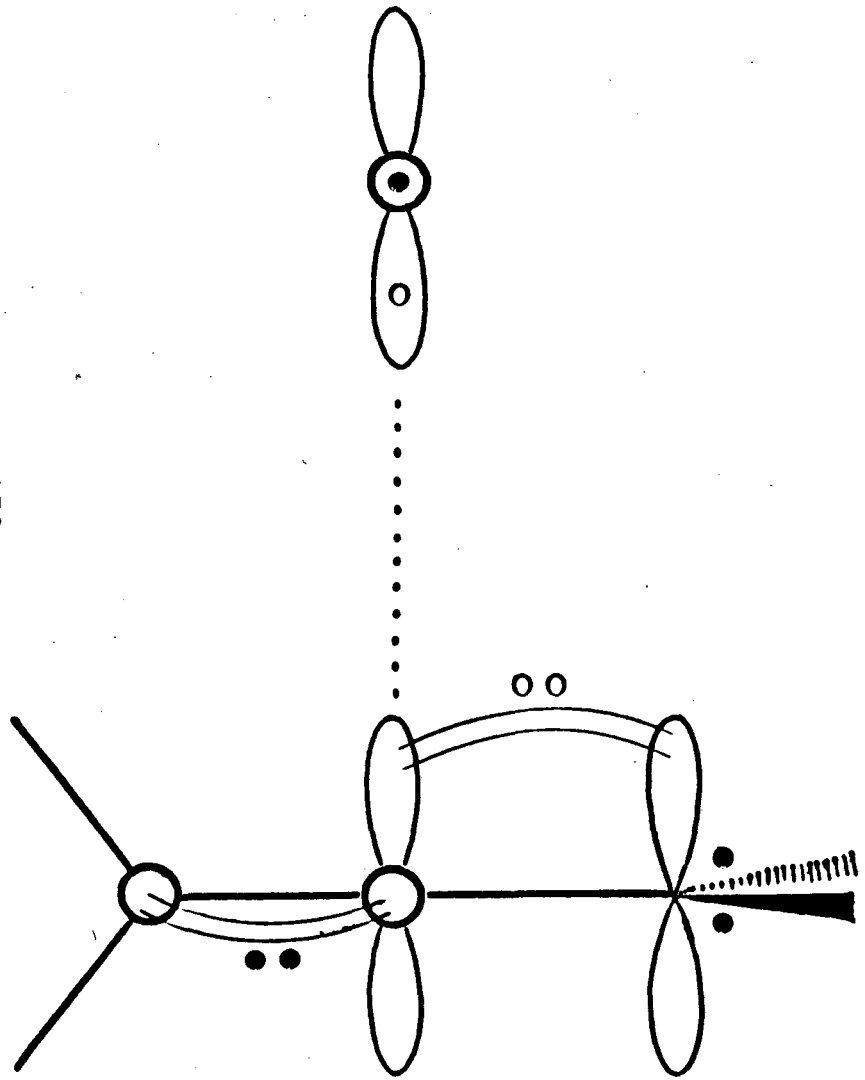

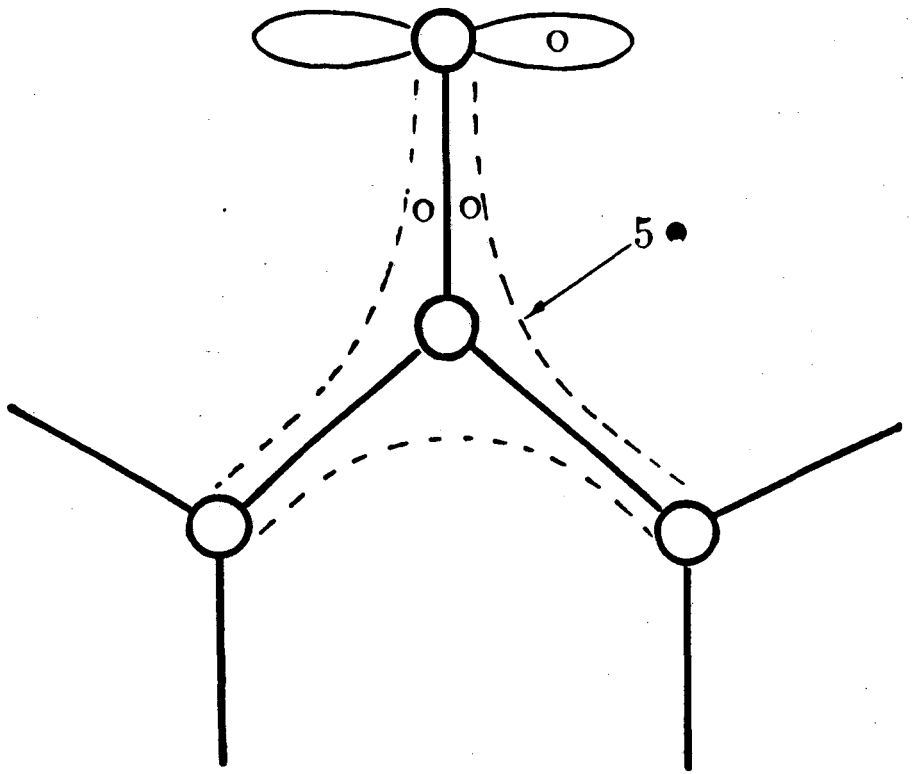

Figure 3.8

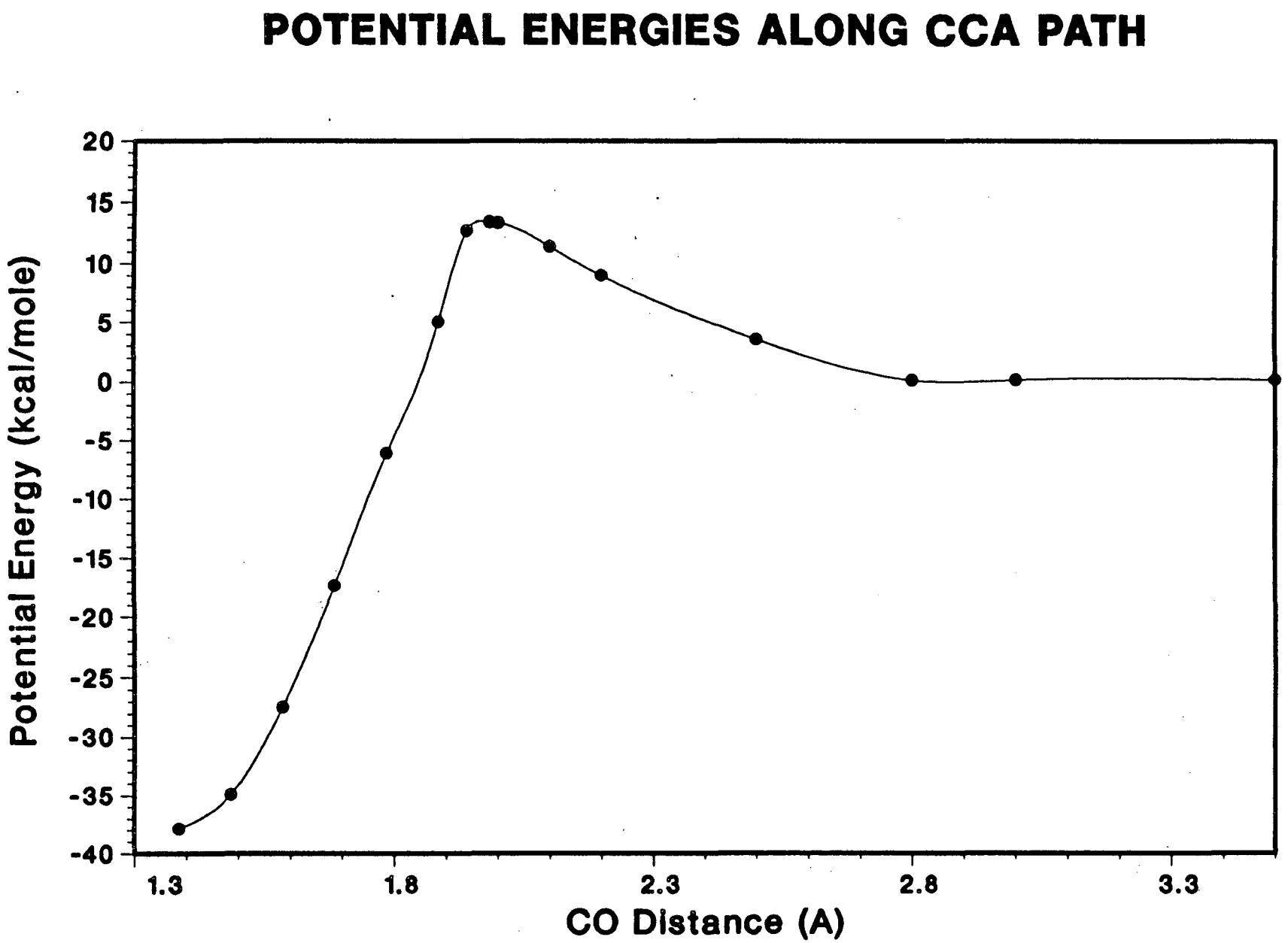
POTENTIAL ENERGIES ALONG CCA PATH
Potential Energy (kcal/mole)
20
15
10
5
0
-5
-10
-15
-20
-25
-30
-35
-40
1.3
1.8
2.3
2.8
3.3
CO Distance (A)

Figure 3.9

C-C BOND LENGTH VS CO DISTANCE

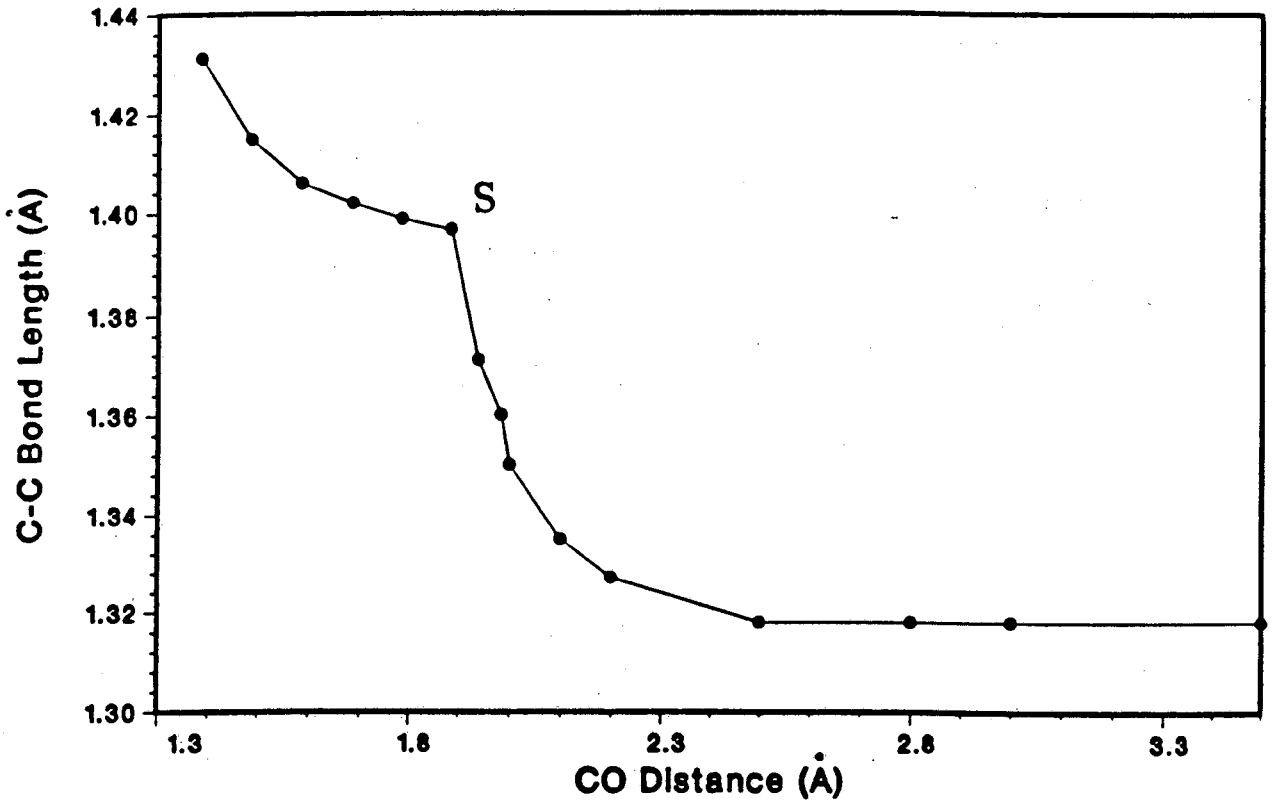

C-C-C BENDING ANGLE VS CO DISTANCE

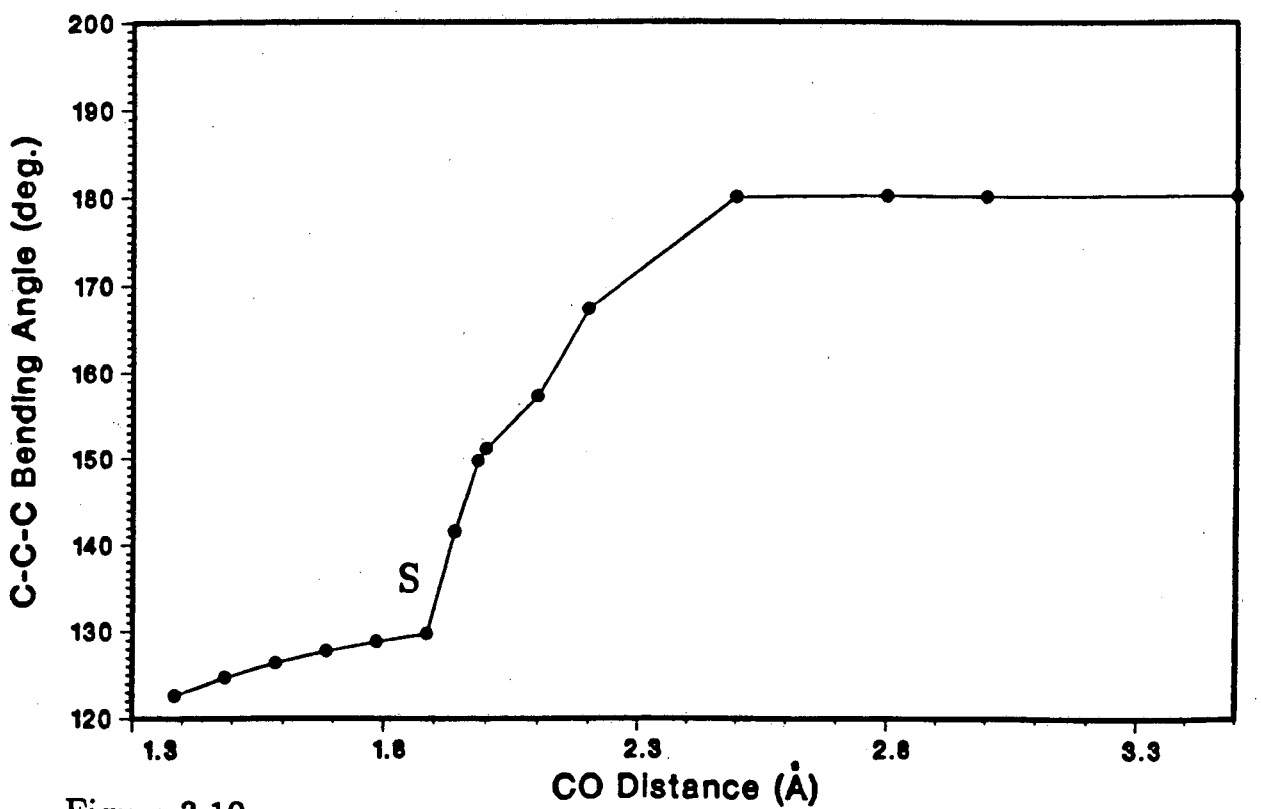

Figure 3.10

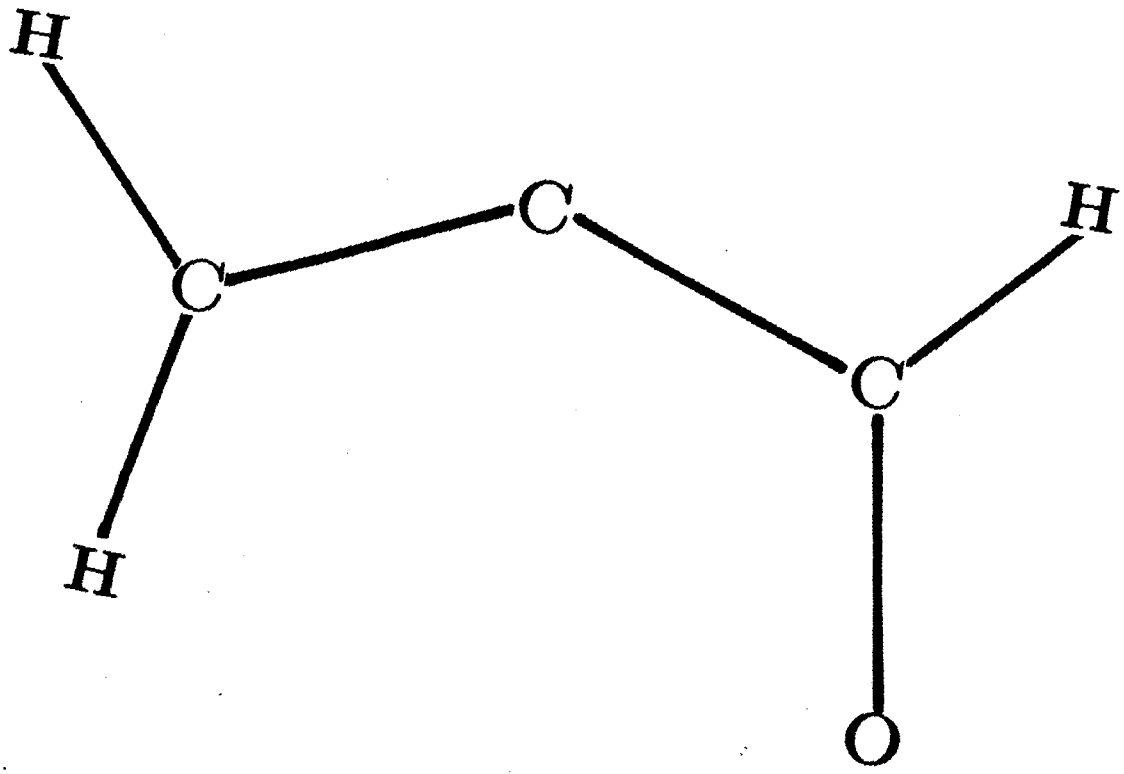

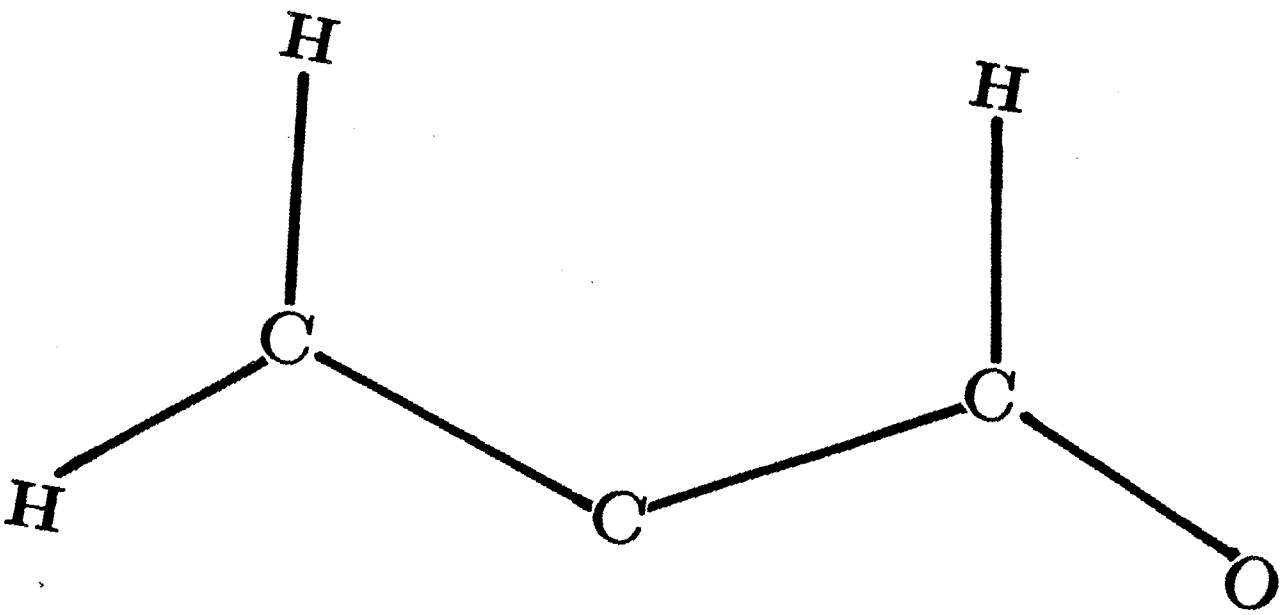

Figure 3.11

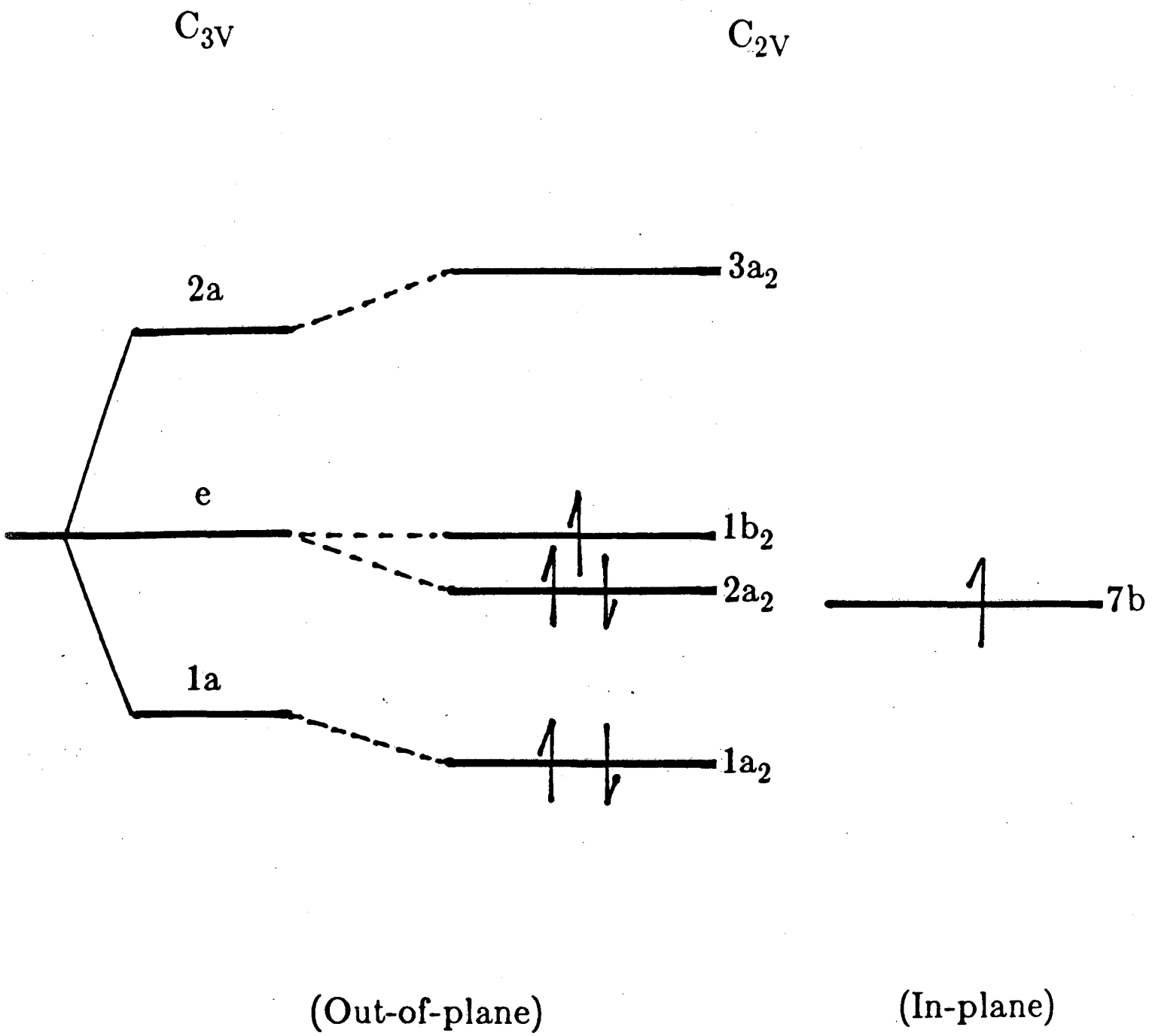

Figure 3.12

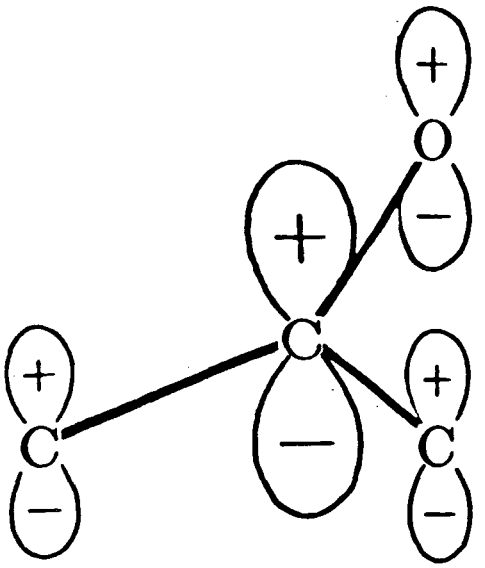

$1a_2$ Bonding orbital.

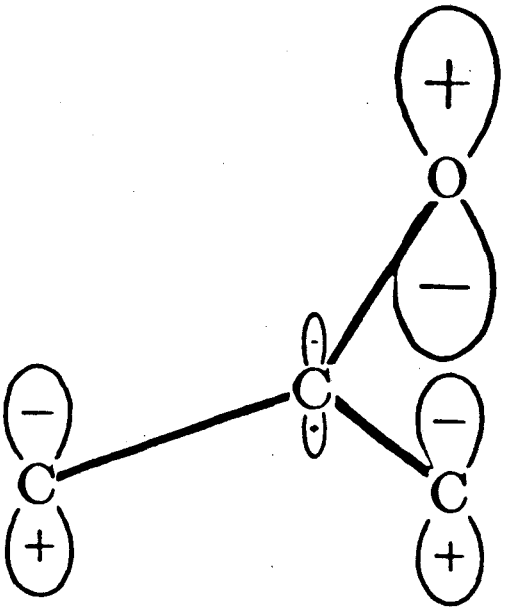

$2a_2$ Weakly bonding orbital.

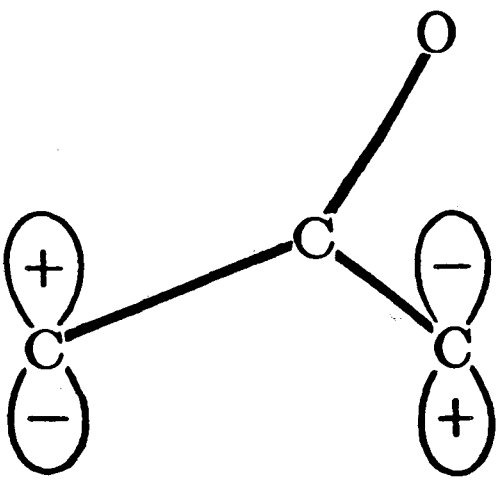

$1b_2$ Non-bonding orbital.

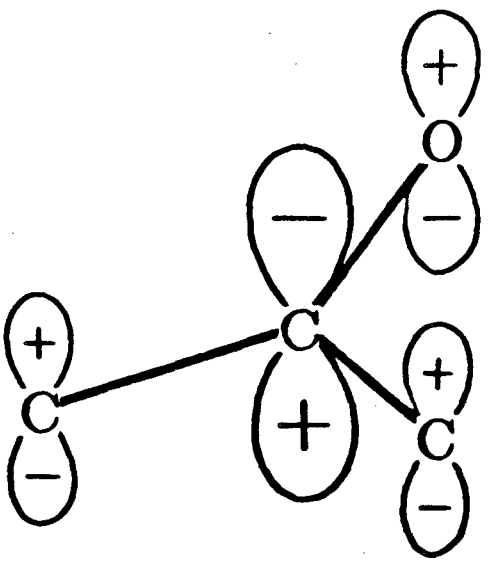

$3a_2$ Anti-bonding orbital.

Figure 3.13

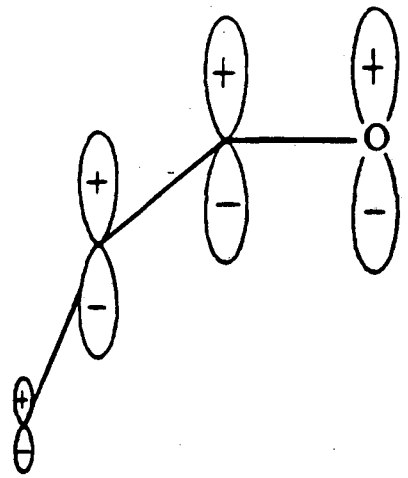

$1A''$ *Bonding orbital*

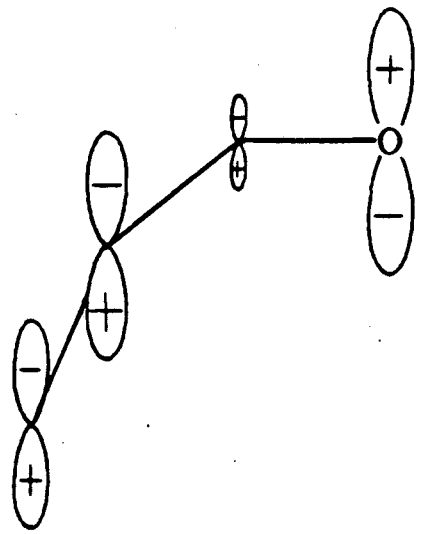

$2A''$ *Bonding orbital*

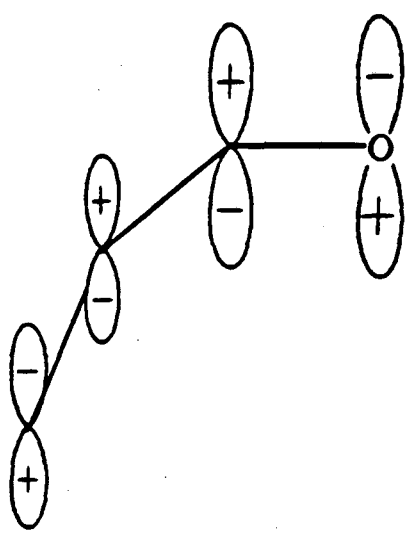

$3A''$ *Anti – bonding orbital*

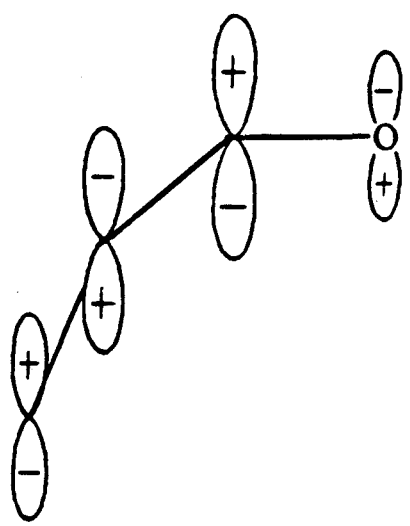

$4A''$ *Anti – bonding orbital*

Figure 3.14

Figure 3.15

Correlation Diagram of $O(^3P)$ + Allene

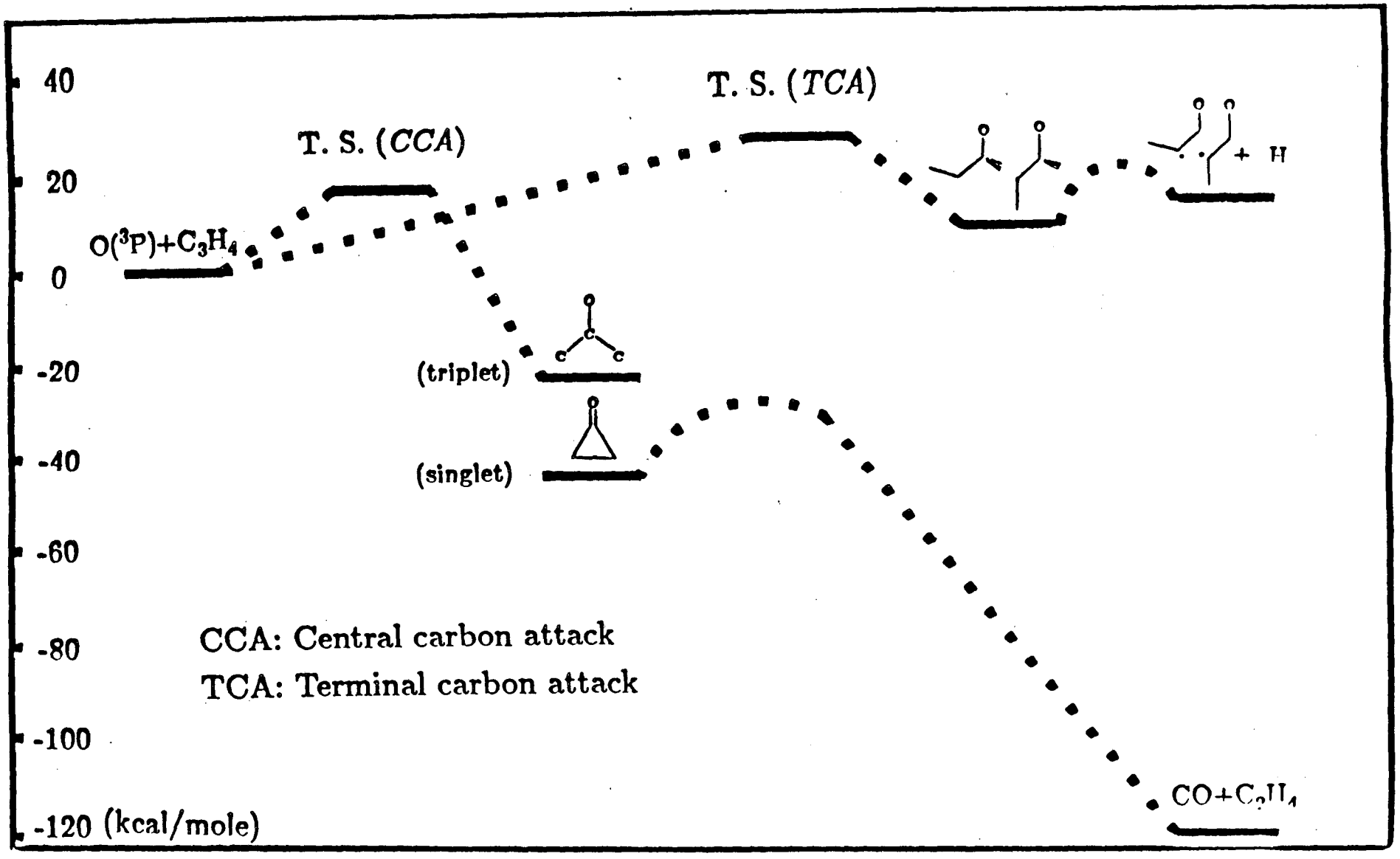

Chapter V. Optimized Trial Functions for Quantum Monte Carlo

A. Introduction

There is no doubt on the importance of the role played by computational chemistry. As I showed in Chapt. IV, an *ab initio* MCSCF study can provide many informations, such as electronic state energies, molecular geometries, potential energy surface which are all useful with comparing to the experimental results in order to understand both the molecular structure and the dynamic process. However, there is still a great descrepency in meeting the needs by the growth of demands in chemistry, material science, biochemistry, and solid-state physics. For instance, it is still expansive to handle the calculation on a small system, such as an oxygen atom reacting with allene molecule (9 atoms, 30 electrons) in update computer. A calculation[1] to obtain the mass of the proton based on quantum chromodynamics, the dominant theory that attempts to describe the ultimate structure of matter, requires about 10^{17} floating-point operations for an accuracy of 10 percent. That would occupy 15 years of a typical supercomputer's time!

The other problem is the computal accuracy. Compared with a typical elctronic energy scale, say several eV, an accuracy of 5 percent which is several kcal/mole of error would not fit the requirement of a chemical problem since several kcal/mole is critical in a chemical reaction with such amount of barrier.

One of the major error in an *ab initio* calculation is caused by miscounting the correlation energy which comes from the conflict where the Hartree-Fock (HF)

method[2] assumming the electrons are indepedent but in reality the electrons are correlated. According to Löwding's estimation,[3] the correlation between two electrons with unlike spin may cause about 1 eV correlation energy which has not been counted by HF method with a single-determinant wavefunction. Using the configuration interaction[4] (CI) or multi-configuration[5] (MC) method which has a multi-determinant wavefunction instead certainly improves the total energy, but the computal time inceases according to a $N^6 \sim N^7$ relation as increasing the number of elelctrons.

To fully utilize the quantum calculation to many fields this situation needs a breakthrough. As noted by Wilson, who recently proposes a cooperative work[6] to search the possible algorithms in the theoretical area, a statistic method may be one of the candidate to the approach.

There can be two advantages in statistic algorithm:

(1) In contrast with the "mean field" assumption of HF method,[2] the energy calculation in statistic method is taken by sampling the electrons in random position, and averaging the energies obtained in each of the particular position of the electrons. Thus, the energy measurement taken in each picture at one moment, the interaction between all the particles (electrons and atoms) are fully counted, and the correlation between these particles are also involved. According to our results, the energies calculated by this method can recover 90 - 100% of the correlation energies.

(2) The way that statistic method solves the Schrödinger equation is by a

simulation of particle random walk. The multi-center-integral which causes a more than 4th power increasing of computal time vs the increasing of the number of the electrons in conventional *ab initio* method (HF, CI, and MC) is replaced by a Green's function which treats the motion of the electrons as a transition probability. Therefore, the relation of the increasing computal time vs the number of electrons is estimated as a quadratic to a cubic power that improves greatly the situation in applying to a large molecule.

With the introduction of importance sampling[7] quantum Monte Carlo simulations (QMC)[8−13] have become of increased interest for the determination of the electronic structure of molecular systems. Two variants, fixed-node and released node[12], have been developed to treat the nodal problem which arises from the discrepancy between the positive-density particle simulation and the true wavefunction with nodes. In recent years the fixed-node quantum Monte Carlo method[10−15](FNQMC) has been successfully applied to the calculation of the electronic energies of small molecules.[10,13−19] The attractive feature of this method is that with a relatively modest basis set and often only a single-Slater determinant with correlation factor (correlated molecular orbital wavefunction), one typically recovers over 90% of the correlation energy.[12−14,17−19]

In the FNQMC approach the trial function ψ_t plays a central role. (1) As a guiding function it preferentially samples regions of high probability during the random walk process. (2) It imposes the appropriate symmetry on the desired state. (3) The antisymmetry character of ψ_t imposes that property on the FNQMC

solution. (4) As a boundary condition to the Schroedinger equation, the nodes of the FNQMC solution, which ultimately determine the quality of the results, are fixed by ψ_t.

I have developed an optimization algorithm to improve FNQMC trial functions. In the approach a projection operator is used to impose the desired symmetry on the ground- or excited-state trial function. By using a projection operator constructed from certain Young tableux of the permutation group, the electron exchange properties of a desired multiplet are obtained.

This chapter is organized as follows. A diffusion quantum Monte Carlo and FNQMC method is introduced in Sec. B. A trial function optimization algorithm based on energy minimization is described in Sec. C. The symmetry restrained by the projection operator of the group theory is given in Sec. D, Application of these operators to ground- and excited-state pyramidal H_4 is presented in Sec. E. Illustrative applications to $H_2(X^1\sum_g^+)$, $H_2(B^1\sum_u^+)$ and Li_2 are interspersed in these sections which are followed by a brief summary in Sec. F.

B. Quantum Monte Carlo Method

Introducing an imaginary time $\tau = it$ the time-dependent Schrödinger equation can be treated as a diffusion-reaction equation

$$\frac{\partial\psi}{\partial\tau} = D\nabla^2\psi - V\psi \tag{5.1}$$

where the Laplacian term can be simulated by a particle random walk with a diffusion coefficient D = 1/2, and the second term can be treated as a death and birth process depanding on whether the potential V less than zero or greater than one.

This diffusion quantum Monte Carlo method has been applied to several simple examples such as a particle in box, harmonic oscillator, and etc., and was found a bad convergency in more complicate cases since many of the samplings were taken in the space where the wavefunction has a low probability distribution.

By introducing a trial function ψ_t and define $f = \psi\psi_t$ the Eq. (5.1) can be re-written by a trasformation and one obtains

$$-\frac{\partial f}{\partial \tau} = -D\nabla^2 f + D\vec{\nabla}\cdot\vec{F}_D f + (E_L - E_t)f \tag{5.2}$$

Monte Carlo sampling of Eq. (5.2) in 3N-dimensional space is dominated by three factors corresponding to the three terms on the right-hand-side of Eq. (5.3), namely, (1) diffusion; (2) particle drift under the influence of a "quantum force"

$$\vec{F}_D = \nabla(ln\psi_t^2) = \frac{2\nabla\psi_t}{\psi_t}; \tag{5.3}$$

and (3) a branching process. Here $D \equiv \hbar^2/2m_e$ where m_e is the electron mass and E_t is a constant shift of the zero of energy that is useful for present purposes.

The local energy

$$E_L \equiv \frac{H\psi_t}{\psi_t} \tag{5.4}$$

is sampled throughout 3N-dimensional space. If one carrys out the random walk in the absence of the branching process, the usual variational energy is obtained,[12] i.e.,

$$< E >_V = \frac{< \psi_t \mid H \mid \psi_t >}{< \psi_t \mid \psi_t >} \tag{5.5}$$

Inclusion of the branching step leads to the fixed-node energy[11,12]

$$< E >_{FN} = \frac{< \psi \mid H \mid \psi_t >}{< \psi \mid \psi_t >} \tag{5.6}$$

It is well established that Eq. (5.5) yields an upper bound to the ground-state energy in ref. 12 it is shown that Eq. (5.6) also provides an upper bound. Because the Hamiltonian is hermitean, Eq. (5.6) can yield, in principle, the exact energy of the system regardless of the discrepancy between the trial and exact wavefunctions.

This calculation procedure can be done as the following: Take 100-200 sampling points in 3n-dimensional space in which each sampling point represents a set of the coordinates of n electrons, let these points take a random walk, and at each step a "local energy" measurement is carried out and be averaged. The acceptance of a random walk step should be determined by comparing the Green's function

$$\begin{aligned} G(R \rightarrow R', \tau) &= (4\pi D\tau)^{-3N/2} \\ &\times exp[-\tau((E_L(R) + E_L(R'))/2 - E_T)] \\ &\times exp[-(R' - R - D\tau F_D(R))^2/4D\tau] \end{aligned} \tag{5.7}$$

to a random number. The branching should be determined by $E_L - E_T$. Compared with Eq. (5.1) the branching coefficient (or birth/death probability) V is replaced by $E - E_t$, where the sigularity in V which causes a bad statistics has been removed.

C. Optimization

1. Correlation function

As I discussed in Sec. A, the trial function ψ_t plays a central role in FNQMC. According to Eq. (5.6) a finite basis set does not cause bias in energy calculation. This desired character makes the relative energy calculation such as barrier, well depth more meaningful, because in conventional method the same basis set does not always mean the same quality when it is applied for different gemetries or states. However, one still needs a good ψ_t to reduce variance in this statistic method. Thinking of such a case that when a ψ_t which is the exact eigen function (in most case it is impossible!) of Hamiltonian is applied to Eq. (5.4), the constant eigen value causes no variance at all. In general, a large size of basis set and a multi-determinant trial function may help a better result, but the inconvenient in pre-calculation to obtaine these trial functions and the increasing cost induced by a complicate form of ψ_t be calculated tens of thousands time in Eq. (5.4) would reduce the interest of this method. By checking balance, one appreciates a fairly simple form of ψ_t but expects all the parameters to be optimized. This is the idea came to my mind to think of a possible optimization algorithm in statistic environment.

The other demand of optimization comes from the using of correlation function. The widely using two-body (electron-electron and electron-nuclear) correlation

form, namely, Jastrow function[20] is

$$S = exp\left(\sum_{ij} \frac{ar_{ij}}{(1+br_{ij})}\right) \tag{5.8}$$

Another more effective Zhiwei's form[13] for electron-electron correlation is

$$S = 1 - a_1 exp(-r_{ij}/b_1) - a_2 exp(-r_{ij}^2/b_2) \tag{5.9}$$

Using one of these explicit forms as a multiplied factor to the usual Slater-determinant of wavefunction one may recover 50 - 80% of the correlation energy in variational energy calculation (Eq. (5.5)). Lester did an *ab initio* study[21] of the "columbs hole" between the two electrons of H_3^+. The correlation function he used was a Gaussian type form in order to perform the analytic integrals. The variational QMC offers greater flexibility than the traditional *ab initio* approach because, as shown previously,[12] there are only function and derivative evaluations needed for QMC calculations - no integral evaluation is encountered. However, the optimization of the parameters in these correlation functions is stiil a problem because of the statistic uncertainty.

Thinking of only one-parameter optimization, the uncertainty in both the varied parameter and the refered parameter calculations makes one hard to make judgement on that which parameter is better. One may increase the independent calculations to reduce the error bar, but it is tedious to run many computer hours just for making sure that one paremeter should or should not move with a small step. Therefore, a special optimization algorithm based on random walk needs be designed in order to meet the needs of the optimization of the correlation parameters.

2. Virial Theorem

Besides the optimization of the correlation function parameters, there is a demand to re-optimize the parameters in Slater-determinant part though these parameters (the linear and exponential basis set parameters) has been optmized in *ab initio* calculation. I am going to show the perturbation introduced by incorporating the Slater-determinant with a correlation factor.

There can be many effects by that perturbation, however, I just focus on the scalling effect here. Introducing a scale factor λ into the wavefunction, the total energy corresponding to the scaled wavefunction $\psi'(r) \equiv \psi(\lambda r)$ will be a quadratic form in λ,[24] i.e.,

$$E' = \lambda^2 < T > + \lambda < V > \tag{5.10}$$

where T is the kinetic energy and V is the potential energy. In this form, the total energy has a minimum for $\lambda = - < V > /2 < T >$. If $\lambda \neq 1$ the wavefunction can be scaled thereby lowering the energy by an amount $\Delta E = -(1-\lambda)^2 E$.

In the other hand, from the virial theorem

$$2 < T > = - < V > - \sum_{\alpha} q_{\alpha} \frac{\partial U}{\partial q_{\alpha}} \tag{5.11}$$

and letting the quantum force $\partial U / \partial q = 0$ at equilibrium geometry, it also results in $- < V > /2 < T > = 1$. Hence, $\lambda = 1$ can be taken as a necessary criterion for an optimal wavefunction.

A HF wavefunction should satisfy this criterion according to the variational principle. But how about the HF wavefunction which is incorporated with an

electron-electron (e-e) correlation function, or with an electron-nuclear (e-n) correlation function? I take 3 type of trial functions of $H_2(B)$ moleculae at the equilibrium separation r = 2.43 a.u.:

(1) HF wavefunction incorporated with e-e correlation function;

(2) HF wavefunction incorporated with both the e-e and e-n correlation functions;

(3) HF wavefunction with e-e correlation function only, but all the parameters in Slater-determinant and correlation factor have been optimized.

Each of these trial functions has been taken 5 independent QMC (variational and FNQMC) calculations. The parameters and results of the calculations are shown in Tab. 5.1 and Tab. 5.2 respectively. From Tab. 5.2 the $\lambda = 1.0437$ resulted from using trial function (1) shows that this trial function is not optimal, the molecular size determined by HF is overly expanded. Also, the result by using trial function (2) shows that the molecular size is overly contracted ($\lambda = 0.9834$) when the electron-nuclear correlation is taken consideration. A conclusion can be immediately drawn as: the HF wavefunction needs be re-optimized by the introducing of the correlation factors, the parameters should be adjusted such that to reducing the scale with the inclusion of e-e correlation and enlarge the scale with the inclusion of e-n correlation. Using the fully optimized trial function which is done by my algorithm (not by scaling technique), the results show a perfect satisfaction of λ (1.0021 for variational QMC and 1.0032 for FNQMC). The FNQMC energy by using trial function (3) gives an excellent agreement with the exact energy (-0.7565

a.u.). It is the best achievment for a single-determinant trial function with a DZP basis set.

Now I am going to show that it is a general rule that the e-e correlation always makes the wavefunction in need of reducing the scale ($\lambda > 1$), and the e-n correlation does the opposit direction ($\lambda < 1$). Let us start with

$$\lambda = -\frac{<V>}{2<T>} = 1 \tag{5.12}$$

where

$$<V> = \sum V_{nn} + \sum V_{en} + \sum V_{ee}$$

and

$$\sum V_{ee} = \sum_{r_{ij}>b} V_{ee} + \sum_{r_{ij}\leq b} V_{ee}$$

where b is the electron-electron (e-e) effective correlation radius. All the potential energy terms except the repulsive e-e term for $r_{ij} < b$ remain unchanged by the introduction of the e-e correlation factor. The change in the last term makes $< V >$ smaller so that

$$\lambda' = -\frac{<V>'}{2<T>} > 1 \tag{5.13}$$

Consider now the introduction of an electron-nucleus correlation function of the Jastrow form[20]

$$S = exp\left(-\frac{ar_{i\alpha}}{1+br_{i\alpha}}\right) \tag{5.14}$$

where a and b are parameters. The effect of the attractive factor is to bring electrons closer to the nuclei with an increase of the kinetic energy and concomitant reduction

of the potential energy

$$V' = V - \delta, \qquad and \qquad T' = T + \delta \tag{5.15}$$

where δ is the changing amount due to the motion of electrons, which results in

$$\lambda' = -\frac{< V > -\delta}{2(< T > +\delta)} = \frac{2 < T > +\delta}{2 < T > +2\delta} < 1 \tag{5.16}$$

The physical meaning of this general rule can be interpreted as the following: The HF wavefunction is obtained by variational principle without the consideration of the e-e correlation. The modified HF wavefunction which is the product of the Slater-determinant multiplied an e-e correlation factor must be re-optimized, because the additional repulsive force introduced by the e-e factor must be canceled out by contracting the molecular size that can be done by either re-scaling the wavefunction by a factor $\lambda > 1$ or a parameter optimization procedure. The excessive repulsive can be also canceled out by introducing an attractive e-n correlation factor, but the trial function's nodal position which is established without the e-e correlation would not be improved by the nodeless e-n correlation factor.

In my algorithm, I don't suggest to introduce an e-n correlation factor since the atom-centered coordinate dependence of the e-n correlation function should be included by that of the basis set. Any adjustment of the e-n correlation factor should be covered by optimizing the Slater-determinant. The introducing of the e-n correlation factor is good only when one wants the e-e correlation but finds difficulty to adjust the Slater-determinant with the presence of the e-e correlation function.

The purpose of this section is also not to suggest a scaling though this technique dramatically improves the total energy. The reason why I discuss the scaling

here is to show the necessity of the optimization and to realize what direction of the optimization should to go, and finally to establish one of the criterion of the optimization. The optimization by scaling is only one aspect that is the overall molecular size for optimization. The criterion $\lambda = 1$ is necessary but not sufficient. The optimization we carried out on $H_2(B)$ molecule shows (see Tab. 5.1) that the larger exponential coefficient ζs (ground-state $\zeta_s = 1.154$ with linear coefficient 1.0, excited-state $\zeta'_s = 0.402$ with linear coefficient 1.0) are achieved by my algorithm that fits the requirement of contracting the molecule size but does not necessarily increase the other ζs (see Tab. 5.1). The algorithm for optimization I have been using will be described in next.

3. Algorithm

As we discussed in Sec. C.1 the difficulty of the optimization in statistic problem is caused by uncertainty. To solve the problem I have developed a many-parameter optimization method based on the use of random walks. There are two major key points of this algorithm:

(1) The optimization is made by gradually moving the parameters along the steepest descent direction in parameter-space based on minimizing the variational energy. Instead of making decision in each step by the end of the random walks, the moving of parameter is determined by a incomplete statistics within a "block" which is formed by several hundred steps. The correct results can be eventually achieved by the accumulation of these small step motion.

(2) To fulfil the camparison between the energies of refered parameter and that in which one of the parameter varies with a small amount, these energy measurements are taken based on a single random walk process. That is, the moving of the electrons in coordinate space has only one process, and the measurement of the refered energy, together with all the comparing energies, are taken simultaneously.

Suppose $\psi_0 = \psi_t(\vec{C}, R)$ is a trial function where $\vec{C} \equiv (c_1, c_2, \ldots\ldots, c_m)$ denotes the set of parameters to be optimized and R identifies the coordinate space of electrons. Let us construct m functions, each differing slightly in the value of one parameter,

$$\psi_j = \psi_t(C_j, R) \qquad (j = 1, 2, \ldots\ldots, m) \tag{5.17}$$

where

$$C_j = (c_1, ..., c_j + \delta c_j, ..., c_m) \tag{5.18}$$

To determine the steepest descent direction in the parameter space, m total energies-one for each ψ_j-must be evaluated.

When the variational energy of a wavefunction other than the guiding function ψ_g is evaluated, a weight factor $w_j = (\psi_j/\psi_g)^2$ is required to obtain proper sampling, i.e.,

$$< E_j > = \frac{< \psi_j \mid H \mid \psi_j >}{< \psi_j \mid \psi_j >} = \frac{\int \left(\frac{H\psi_j}{\psi_j}\right) \left(\frac{\psi_j}{\psi_g}\right)^2 \psi_g^2 d\vec{r}}{\int \left(\frac{\psi_j}{\psi_g}\right)^2 \psi_g^2 d\vec{r}}$$

$$\approx \frac{\sum_{R\in f} \left(\frac{H\psi_j}{\psi_j}\right) w_j}{\sum_{R\in f} w_j} \tag{5.19}$$

The optimization procedure may be summarized as follows:

(1) Run several hundred random walk steps governed by a guiding function ψ_g (initially $\psi_g \equiv \psi_0$) to form a block. In each step m E_js and E_0 are evaluated by Eq. (5.19), and the averages for each E_j are taken over the block.

(2) At the end of a block, all parameters are moved in the steepest descents direction

$$\vec{C}' = \vec{C} - \vec{N}$$

where

$$\vec{N} = (\partial E/\partial c_1, \partial E/\partial c_2, ..., \partial E/\partial c_m);$$

the derivatives are determined as finite differences of averaged energies.

(3) When several blocks have been computed, the guiding function may be updated with current parameters. This keeps the weights w_j close to unity maintaining numerical stability. The collection of blocks forms a "section."

The above procedure, steps (1-3), is repeated until all parameters converge to within a preset limit. Typically the optimized parameters are determined from 10-15 sections.

The optimization procedure has been applied to $H_2(X) \equiv H_2(X^1 \sum_g^+)$, $H_2(B) \equiv H_2(B^1 \sum_u^+)$, and $Li_2(^1\sum_g^+)$. Results for these systems are shown in Figs. 5.1-5.4. Fig. 5.1 shows how the correlation parameters are modified by optimization. The parameters of Eq. (5.9) are chosen to satisfy the *cusp* condition,[11] i.e., $b_1 = -2a_1/(1-a_1)$, and $b_2 = -2a_2/(1-a_2)$. The time step for the variational QMC calculation is set to 1.5 a.u.. A run of 60 sections (each section has 20 blocks; each block contains 500 steps) takes about 1 *cpu* hour on a VAX11/780. The converged values, a = 4 and b = 0.24, agree with a previous trial-and-error optimization. With randomly chosen initial values, rapid convergence is obtained to the variational energy of -1.168 a.u. (vs. exact[36] -1.1745 a.u.) for $H_2(X)$.

Fig. 5.2 plots the optimization of linear coefficients for $H_2(X)$. The basis set consists of 1s, 2s, and 2p atom-centered Slater basis functions with $\zeta = 1.12$, 1.64, and 2.0 respectively. The coefficient of the 1s function is set to unity.

The parameters for $H_2(B)$ appear in Table 5.2. By symmetry there are only four coefficients, two of σ_g and two of σ_u symmetries, that need to be optimized. Figure 3 shows the optimization process. The optimization of the Li_2 correlation

function is presented in Fig. 5.4.

D. Symmetry Restrained by Group Theory

1. Projection Operator: Point Group

The failure to obtain exact excited state energies with FNQMC is due to errors in the nodal description and lack of orthogonality of the excited state trial function to the exact ground state wavefunction. Kalos *et al.* have suggested[15] a "transient estimates" method to remove this deficiency in which the first excited state is constrained to be totally antisymmetric in the electronic coordinate space. Coker and Watt[25] suggest keeping the excited state wavefunction orthogonal to all lower states. These authors had some sucessful examples in appling to solve the nuclear motion problems. Applying to electronic state calculation, the difficulty with the former approach is that various excited states cannot be simply totally antisymmetric. In the latter case, no prescription is available to provide the exact ground state wave function, thus the orthogonality restriction does not always provide a useful alternative in electronic state calculation.

By introducing a projection operator defined from group theory[27,37] for a given symmetry,

$$\hat{P}_i^{(\lambda)} = \frac{n_\lambda}{g} \sum_R \Gamma_{ii}^{(\lambda)}(R)^* \hat{R} \tag{5.20}$$

one can obtain a function with the desired symmetry properties for the state of interest. Here g is the dimension of the group, n_λ is the dimension of λ-th irreducible representation (IR), and Γ is the matrix representing the group operator $\hat{R}$ such

that

$$\hat{R}\psi_i^\lambda = \sum_{j=1}^{n_\lambda} \Gamma_\lambda^{ij}(R)\psi_j^\lambda , \tag{5.21}$$

One means to distinguish the states and maintain orthogonality arises from the projection operator property,

$$\hat{P}_\mu^i \cdot \hat{P}_\lambda^j = 0,$$

for $i \neq j$ and $\mu \neq \lambda$.

In general, Eq.(5.20) may be replaced by

$$\hat{P}_\lambda = \frac{n_\lambda}{g} \sum_R \chi_\lambda(R) \cdot \hat{R} \tag{5.22}$$

where χ is the *character* of λ-th IR without specifying the particular basis function within the λ-th IR.

During optimization, the projection operator is applied to constrain the trial function to have the symmetry of the desired state. Instead of using Eq. (5.20) or (5.22) directly, a set of constraint relations are deduced from

$$P_\lambda^2 \vec{C} = P_\lambda \vec{C} \tag{5.23}$$

or

$$(P_\lambda - 1)\, \vec{C} = 0 \tag{5.24}$$

where $\vec{C}$ is a vector of linear coefficients, and P_λ is defined by

$$P_\lambda = \frac{n_\lambda}{g} \sum_R \chi_\lambda(R) \cdot D(R) \tag{5.25}$$

Here D is the representation matrix in the given molecular frame and basis set. The example of pyramidal H_4 in C_{3v} symmetry is provided in Appendix 1. Table

5.3 shows the number of independent parameters to be optimized for the lowest electronic states. By using the projection operator definition Eq. (5.20), we can, in particular, obtain both components of the doubly degenerate E state (denoted E_1 and E_2). When the optimization is carried out solely with these independent parameters, not only is the process simplified, but the state is also constrained to have the proper symmetry by the projection operator.

2. Projection Operator: Permutation Group

For a totally antisymmetric wavefunction the spatial function Ψ and the spin function S belong to conjugate permutation IR's[28,29,37]. In the Young diagram (YD) representation, the conjugate IR's are denoted by several blocks, and the number of blocks in each column of one equals the number of blocks in each row of the other. Since an electron spin function has only 2 spin states, the YD representing spin function S can have at most 2 rows (hence the spatial function YD is allowed at most 2 columns). In a four electron system (S_4) only the following three pairs of conjugate YD are allowed: $(e) \otimes (a)$, $(d) \otimes (b)$, and $(c) \otimes (c)$ (see Fig. 5.5) are able to describe the real total wavefunctions. Among them $(e) \otimes (a)$ represents a quintuplet state, $(d) \otimes (b)$ represents a triply degenerate triplet state, and the last self-conjugate YD represents a doubly degenerate singlet state.

As illustrated by the above examples, the total wavefunction may be expressed by the direct product of a spatial YD and a spin YD[29]

$$\Theta = \sum_f C^{f\bar{f}}_{\lambda\bar{\lambda}} \, \Psi^{\lambda}_f \, S^{\lambda}_{\bar{f}} \tag{5.26}$$

where f is the λ-th YD Yamanuchi symbol.[29] The tilde denotes the conjugate rep-

resentation, C is the coupling coefficient, and the sum is taken over the dimension of the degeneracy. For a spin-free Hamiltonian only the spatial function is taken to be a trial function and it is generated by a projection operator according to the definition (5.20). The linear coefficients are taken from the character table of the permutation group. Application to pyramidal H_4 (S_4 symmetry) is given in Appendix 2. The A_1, E (doubly degenerate E_1, E_2), and GVB form of the A states are obtained by operating on different configurations of MOs. Note that the GVB form is immediately treated by the method.

E. Application to H_4

The quenching of excited $H_2(B)$ state by ground $H_2(X)$ has been found to be a very efficient process. Moore *et al.* measured[44] a quenching cross section 9 times larger than that due to rare gases. A number of theoretical studies have been carried out of excited states[45-50] and, in particular the quenching mechanism. A significant advance was achieved by Nicolaides *et al.*[39] with the discovery of a "maximum ionicity excited state" (MIES) of H_4 that has pyramidal geometry. (see Fig. 5.6) According to them, and confirmed by our calculations, at the geometries deformed from C_{3v} symmetry, where r ranges 1.65 - 1.70 a.u. which is similar to the equilibrium H_3^+ length, and R ranges 3.6 - 4.0 a.u. there is an avoided curve crossing between the ground state (X^1A') and the first excited state ($2^1A'$) pes. Especially there may be a minimum existed in the excited pes. The stability can be thought caused by Columb's attraction of the two ionic pieces (H_3^+ and H^-).

As a first step in characterizing the H_4 system we determined the $H_3 + H$ asymptotes. Present results and comparisons with other work are presented in Tab. 5.5. for R = 3.4 a.u. contains HF, MCHF, variational QMC with an optimized trial function, and FNQMC total energies. One finds a large improvement with the optimized trial function. In Fig. 5.7 the two lowest-lying QMC potential energy curves are compared with those of Nicolaides *et al.*. The present FNQMC results are found to lie 0.6-0.8 ev lower than NTP's for R = 3.2 - 5.0 a.u.. and attest to the capability of the approach. An singles and doubles CI result is to provide a further basis of comparison.

F. Summary

(1) An algorithm for optimizing the parameters of variational and FNQMC trial functions has been developed based on random walks.

(2) Several examples show that an optimized correlated molecular orbital wavefunction (product of HF and correlation function) provides an improved nodal description. The FNQMC energies calculated with optimized trial functions are considerably lower than those obtained with unoptimized functions.

(3) The optimization procedure can be constrained by symmetry. The application of a projection operator technique provides a powerful tool to distinquish different states. In a calculation of pyramidal H_4, the technique is able to provide converged ground- and excited-state energies in a surface-crossing region.

Appendix 1: Molecular Orbitals and Projection Operator for Pyramidal H_4

Fig. 5.7 shows the molecular geometry with in assumed equilateral triangle H_3 base in the Y-Z plane and one H on the X-axis. We chose a TZP basis set (24 linear coefficients in all) and the molecular orbital is shown as the following:

$$\psi_\lambda = \sum_{\alpha j} C_{\alpha j}^{(\lambda)} \phi_{\alpha j} \qquad (C1.1)$$

where $\alpha = a.b.c.d$ representing the atom-center location (see Fig. 5.7), $j = 1s, 1s'$, $1s''$, $2p_x$, $2p_y$, $2p_z$ representing the type of the atom-centered Slater basis function, and $\lambda = 1a, 2a, e$ are the states with different symmetries. A brieve notation of the linear coefficients will be used throughout this section as the following: all the s-type basis function ($1s$, $1s'$, $1s''$) are denoted by 's', and all the p-type basis function ($2p_x$, $2p_y$, $2p_z$) are denoted by 'x','y','z' respectively. For example: C_{ax} represents the coefficient of a $2p_x$ basis function with its center at atom H_a.

Using the C_{3v} character table (see Tab. 5.6) and Eq. (5.22), one can obtain the following projection operators for the A and E states

$$\hat{P}_A = \frac{1}{6}(\hat{e} + \hat{C}_3^1 + \hat{C}_3^2 + \hat{\sigma}_1 + \hat{\sigma}_2 + \hat{\sigma}_3) \qquad (C1.2.1)$$

$$\hat{P}_E = \frac{1}{3}(2\hat{e} - \hat{C}_3^1 - \hat{C}_3^2) \qquad (C1.2.2)$$

Solving Eq. (5.24) yields 9 free parameters for the A state, and 14 free parameters for the E state.

(a) A state:

free parameters: C_{as}, C_{ax}, C_{bs}, C_{bx}, C_{by}

symmetry restrictions:

$$C_{ay} = C_{az} = C_{bz} = 0;$$

$$C_{ds} = C_{cs} = C_{bs};$$

$$C_{dx} = C_{cx} = C_{bx};$$

$$C_{cy} = -\tfrac{1}{2}C_{by};$$

$$C_{cz} = \tfrac{\sqrt{3}}{2}C_{by};$$

$$C_{dy} = -\tfrac{1}{2}C_{by};$$

$$C_{dz} = -\tfrac{\sqrt{3}}{2}C_{by};$$

(b) E state:

free parameters: C_{ay}, C_{az}, C_{cs}, C_{cx}, C_{cy},

C_{cz}, C_{ds}, C_{dx}, C_{dy}, C_{dz};

symmetry restrictions:

$$C_{as} = C_{ax} = 0;$$

$$C_{bs} = -(C_{cs} + C_{ds});$$

$$C_{bx} = -(C_{cx} + C_{dx});$$

$$C_{by} = \tfrac{1}{2}C_{cy} + \tfrac{\sqrt{3}}{2}C_{cz} + \tfrac{1}{2}C_{dy} + \tfrac{\sqrt{3}}{2}C_{dz};$$

$$C_{bz} = \tfrac{\sqrt{3}}{2}C_{cy} + \tfrac{1}{2}C_{cz} - \tfrac{\sqrt{3}}{2}C_{dy} + \tfrac{1}{2}C_{dz};$$

The E state is doubly degenerate, Using Eq.(5.20) instead of (5.22) we can treat the two components separately. Tab. 5.7 is the two-dimensional matrix representation of the E state:

The description of the two components of the E state, E_1 and E_2, follows

(c) E_1 component (symmetric):

free parameters: C_{ay}, C_{ds}, C_{dx}, C_{dy}, C_{dz};

symmetry restrictions:

$$C_{as} = C_{ax} = C_{az} = Cbz = 0;$$

$$C_{bs} = -2C_{ds};$$

$$C_{bx} = -2C_{dx};$$

$$C_{by} = C_{dy} + \sqrt{3}C_{dz};$$

$$C_{cs} = C_{ds};$$

$$C_{cx} = C_{dx};$$

$$C_{cy} = C_{dy};$$

$$C_{cz} = -C_{dz};$$

(d) E_2 component (antisymmetric):

free parameters: C_{az}, C_{ds}, C_{dx}, C_{dy}, C_{dz};

restrictions:

$$C_{as} = C_{ax} = C_{ay} = C_{bs} = C_{bx} = C_{by} = 0;$$

$$C_{bz} = -\sqrt{3}C_{dy} + C_{dz};$$

$$C_{cs} = -C_{ds};$$

$$C_{cx} = -C_{dx};$$

$$C_{cy} = -C_{dy};$$

$$C_{cz} = C_{dz};$$

Appendix 2: H_4 Wavefunction from Permutation Group Projection Operator

The character table for YD-c (S_4) is presented in Tab. 5.8.

If we allow the spin-free Hamiltonian to operate on Eq. (5.26) and consider the linear independence of the spin function, we can write the spatial function as

$$\begin{aligned} \Psi &= \sum_{f=1}^{2} C_c^f \psi_c^f \\ &= \sum_{f=1}^{2} C_c^f \hat{P}_c^f \psi(1,2,3,4) \end{aligned} \qquad (C2.1)$$

where $C_c^1 = 1$, $C_c^2 = -1$, and $\hat{P}_c^f$ is a permutation group projection operator defined by Eq. (5.22). Using the character table of the permutation group S_4 (Tab. 5.8) one obtains

(a) ^1A *state (closed shell)*

The configuration is $\mid 1a^2, 2a^2 \mid$, and

$$\psi(1,2,3,4) = \psi_{1a}(1)\psi_{1a}(2)\psi_{2a}(3)\psi_{2a}(4).$$

The trial function is

$$\Psi = \psi_{1a}(1)\psi_{1a}(2)\psi_{2a}(3)\psi_{2a}(4) + \psi_{1a}(3)\psi_{1a}(4)\psi_{2a}(1)\psi_{2a}(2)$$

$$-\psi_{1a}(2)\psi_{1a}(3)\psi_{2a}(1)\psi_{2a}(4) - \psi_{1a}(1)\psi_{1a}(4)\psi_{2a}(2)\psi_{2a}(3)$$

(b) ^1E *state:*

The configuration is $\mid 1a^2, e, 2a \mid$, and

$$\psi(1,2,3,4) = \psi_{1a}(1)\psi_{1a}(2)(\psi_e(3)\psi_{2a}(4) + \psi_e(4)\psi_{2a}(3)).$$

The trial function is

$$\Psi = \psi_{1a}(1)\psi_{1a}(2)(\psi_e(3)\psi_{2a}(4) + \psi_e(4)\psi_{2a}(3))$$

$$+ \psi_{1a}(3)\psi_{1a}(4)(\psi_e(1)\psi_{2a}(2) + \psi_e(2)\psi_{2a}(1))$$

$$- \psi_{1a}(2)\psi_{1a}(3)(\psi_e(1)\psi_{2a}(4) + \psi_e(4)\psi_{2a}(1))$$

$$- \psi_{1a}(1)\psi_{1a}(4)(\psi_e(2)\psi_{2a}(3) + \psi_e(3)\psi_{2a}(2))$$

(c) ^1A *state (GVB)*

The configuration is $\mid 1a^2, 2a, 3a \mid$, and

$$\psi(1,2,3,4) = \psi_{1a}(1)\psi_{1a}(2)(\psi_{2a}(3)\psi_{3a}(4) + \psi_{2a}(4)\psi_{3a}(3)).$$

The trial function is

$$\Psi = \psi_{1a}(1)\psi_{1a}(2)(\psi_{2a}(3)\psi_{3a}(4) + \psi_{2a}(4)\psi_{3a}(3))$$

$$+ \psi_{1a}(3)\psi_{1a}(4)(\psi_{2a}(1)\psi_{3a}(2) + \psi_{2a}(2)\psi_{3a}(1))$$

$$- \psi_{1a}(2)\psi_{1a}(3)(\psi_{2a}(1)\psi_{3a}(4) + \psi_{2a}(4)\psi_{3a}(1))$$

$$- \psi_{1a}(1)\psi_{1a}(4)(\psi_{2a}(2)\psi_{3a}(3) + \psi_{2a}(3)\psi_{3a}(2))$$

References

(1) A. Abraham, Scient. Amer. **257-4**, 57 (1987).

(2) J. A. Pople and D. L. Beveridge, "*Approximate Molecular Orbital Theory*", McGraw-Hill, 1970.

(3) P-O. Löwding, "*Advances in Chemical Physics*" editd by I. Prigogine, (Interscience, New York, 1959), Vol 2.

(4) I. Shavitt, "*Method of Electronic Structure Theory*", edit. by H. F. Schaefer III, Chapt. 6, 1977.

(5) A. C. Wahl and G. Das, "*Method of Electronic Structure Theory*", edit. by H. F. Schaefer III, Chapt. 3,1977.

(6) K. G. Wilson, "*propsal*", private communication with W. A. Lester, jr.

(7) J. M. Hammersley and D. C. Handscomb, *Monte Carlo Methods*, Chapman and Halls, London, 1964, pp. 57-59.

(8) N. Metropolis and S. M. Ulam,J. Am. Stat. Assoc., **44**, 247 (1949).

(9) R. C. Grimm and R. G. Storer, J. Comp. Phys., **7**, 134 (1971).

(10) J. B. Anderson, J. Chem. Phys., **63**, 1499 (1975); **65**, 4121 (1976).

(11) D. M. Ceperley and B. J. Alder, Phys. Rev. Lett., **45**, 566 (1980); Physica B, **108**, 875 (1981); J. Chem. Phys., **81**, 5833 (1984).

(12) P. J. Reynolds, D. M. Ceperley, B. J. Alder, W. A. Lester, Jr., J. Chem. Phys., **77**, 5593 (1982).

(13) Z. W. Sun, P. J. Reynolds, and W. A. Lester, Jr., to be published.

(14) P. J. Reynolds, M. Dupuis, and W. A. Lester, Jr., J. Chem. Phys. **82**, 1983

(1985).

(15) J. W. Moskowitz and M. H. Kalos, Int. J. Quantum Chem. **20**, 1107 (1981); J. W. Moskowitz, K. E. Schmidt, M. A. Lee, and M. H. Kalos, J. Chem. Phys. **76**, 1064 (1982).

(16) R. N. Barnett, P. J. Reynolds, and W. A. Lester, Jr., J. Chem. Phys. **82**, 2700 (1985).

(17) R. J. Harrison and N. C. Handy, Chem. Phys. Lett. **113**, 257 (1985).

(18) R. M. Grimes, B. L. Hammond, P. J. Reynolds, and W. A. Lester, Jr., J. Chem. Phys., **85**, 4749 (1986).

(19) D. R. Garmer and J. B. Anderson, J. Chem. Phys. **86**, 4025 (1987).

(20) R. Jastrow, Phys Rev. **98**, 1479 (1955); R. B. Dingle, Philos. Mag. **40**, 573 (1949).

(21) W. A. Lester, Jr. and M. Krauss, J. Chem. Phys. **44**, 207 (1966).

(22) C. C. J. Roothaan and P. S. Bagus, "*Methods in Computational Physics*", edited by B. Alder, S. Fernbach, and M. Rotenberg, (Academic Press: London, 1963). Vol. 2, pp. 67.

(23) I. N. Levine, "*Quantum Chemistry*", Chapt. 14.

(24) P-O. Lowdin, "*Advances in Chemical Physics*", editd by I. Prigogine (Interscience, New York, 1959), Vol 2; see also ref. 13.

(25) D. F. Coker and R. O. Watts, Mol. Phys. **58**, 1113 (1986).

(26) J. Carlson and M. H. Kalos, Phys. Rev. C **32**, 1735 (1985).

(27) F. Albert Cotton, "*Chemical Applications of Group Theory*", Wiley, 1971.

(28) A. C. Tang, J. Z. Sun, Y. S. Jiang, Z. H. Deng, R. Z. Liu, Q. R. Zheng, G. S.

Yian, Z. Gu, and S. S. Dai, "*Legand method*", (Chinese), Sciences Publishing House, Beijing, 1979.

(29) B. F. Bayman, "*Some Lectures on Groups and Their Applications to Spectroscopy*", Nordita, 1960.

(30) W. L. Mcmillan, Phys. Rev. **A138**, 442 (1965).

(31) D. M. Ceperley, G. V. Chester, and M. H. Kalos, Phys. Rev. **B 16**, 3081 (1977).

(32) D. J. Klein and H. M. Pickett, J. Chem. Phys. **64**, 4811 (1976).

(33) R. J. Harrison and N. C. Handy, Chem. Phys. Lett. **113**, 257 (1985).

(34) W. L. Mcmillan, Phys. Rev. **A138**, 442 (1965).

(35) D. M. Ceperley, G. V. Chester, and M. H. Kalos, Phys. Rev. **B 16**, 3081 (1977).

(36) W. Kolos and L. Wolniewicz, J. Mol. Spectrosc. **54**, 303 (1975).

(37) M. Hamermesh, "*Group Theory and Its Application to Physical Problems*", Addison-Wesley, 1964.

(38) W. Kolos and L. Wolniewicz, J. Chem. Phys. **43**, 2429 (1965).

(39) C. A. Nicolaides, G. Theodorakopoulos, and I. D. Petsalakis, J. Chem. Phys. **80**, 1705 (1984); **81**, 748 (1984).

(40) R. J. Harrison and N. C. Handy, Chem. Phys. Lett., **113**, 257 (1985).

(41) J. W. Moskowitz and K. E. Schmidt, "*Monte Carlo Method in Quantum Problems*", pp. 59 edited by M. H. Kalos, (1982).

(42) B. L. Hammond, P. J. Reynolds, and W. A. Lester, Jr., J. Chem. Phys. **87**, 1130 (1987).

(43) M. M. Hurley and P. A. Christianson, J. Chem. Phys. **86**, 1069 (1987).

(44) E. H. Fink, D. L. Akins, and C. B. Moore, J. Chem. Phys. **56**, 900 (1972).

(45) G. Theodorakopoulos, I. D. Petsalakis, and C. A. Nicolaides, J. Mole. Stru. (Theochem), **149**, 23 (1987).

(46) E. Kassab, E. M. Evleth, G. Chambaud, and B. Levy, "*Photochemistry and Photobiology*", Vol. II, 1307, (1984).

(47) J. A. Montgomery, Jr. and H. H. Michels, J. Chem. Phys. **86**, 5882 (1987).

(48) A. Metropoulos and C. A. Nicolaides, Z. Phys. D - Atom. Mole. Clus. **5**, 175 (1987).

(49) W. Gerhartz, R. D. Poshusta, and J. Michl, J. Amer. Chem. Soc. **98**, 6427 (1976).

(50) J. D. Goddard and I. G. Csizmadia, Chem. Phys. Lett. **43**, 73 (1976); **64**, 219 (1979).

Table 5.1 Wavefunction Parameters: $H_2(B^1\sum_u^+)$ (R = 2.43 a.u.).

parameters		$HF \times e-e^a$	$HF \times e-e \times e-n^b$	$HF \times e-e, optimized^c$
	ζ_s	1.147	1.147	1.154 (1.000^d)
				1.142 (0.075)
SCF	ζ_s'	0.349	0.349	0.349 (-0.025)
				0.402 (1.000)
	ζ_p	1.200	1.200	1.200 (0.206)
				1.187 (0.018)
e-e^e	a_1	0.5	0.5	0.5
	a_2	5.5	5.5	5.5
e-n	λ_0	0.0	0.1	0.0
	μ	0.0	0.8	0.0

[a] Correlated molecular orbital wavefunction: product of HF wavefunction and electron-electron (e-e) Jastrow factor, Eq. (5.8).

[b] Same as footnote a times an electron-nucleus (e-n) Jastrow factor, see Eq. (5.13).

[c] Same as footnote a except for orbitals σ_g and σ_u which are allowed to optimize having different exponential coefficients. Parameters of upper row correspond to the σ_g orbital and the lower row correspond to the σ_u orbital.

[d] Numbers in parenthesis are the optimized linear coefficients.

[e] The parameters b_1 and b_2 of Eq. (5.9) are determined by the *cusp* conditions: $b_i = -2a_i/(1-a_i)$, (i = 1,2).

Table 5.2 Energies and scaling factors λ for $H_2(B^1 \sum_u^+)$ for trial wavefunctions of Tab. 5.1.

wavefunction	$< V >$	$< T >$	E	λ
$HF \times e - e$	-1.3894(74)[a]	0.6648(55)	-0.7227(11)	1.0437(37)
$HF \times e - e \times e - n$	-1.4656(154)[a]	0.7451(152)	-0.7205(16)	0.9834(90)
$HF \times e - e$, opt.	-1.4927(63)[a]	0.7447(66)	-0.7479(3)	1.0021(42)
	-1.5081(65)[b]	0.7516(62)	-0.7565(10)	1.0032(36)

* Energies in Hartrees. Numbers in parentheses are statistical variances.

** The average values are taken from 5 independent QMC runs.

[a] Variational QMC.

[b] Fixed-node QMC.

Table 5.3 Independent linear coefficients of a TZP basis set for H_4.

state	No. of independent parameters	No. of constraint equations
A	9	15
E	14	10
E_1	7	17
E_2	7	17

Table 5.4 Total energies of H_3 and H_3^+ (D_{3h} symmetry)[a]

R(a.u.)	$H_3(E)$	$H_3(A)$	H_3^+
1.65	-1.5354(6)		-1.3327(4)
	-1.5586(18)		-1.3433(5)
1.655	-1.5363(12)	-1.4493(19)	-1.3317(5)
	-1.5626(9)	-1.4822(13)	-1.3433(7)
			(-1.3428)[e]
1.70	-1.5400(5)[b]	-1.4426(8)	-1.3317(4)
	-1.5694(8)[c]	-1.4745(9)	-1.3419(3)
	(-1.5665)[d]		

[a] All energies are in a.u.; 1 a.u. = 27.21 eV.

[b] Variational energy; this study.

[c] FNQMC energy; this study.

[d] P. Siegbahn and B. Liu, J. C. Phys., **68**, 2457 (1978).

[e] C. E. Dykstra and W. C. Swope, J. C. Phys., **79**, 111 (1983).

Table 5.5 Total Energies of Pyramidal H_4, R = 3.4 a.u. , r = 1.7 a.u.[a]

Wavefunction	Total Energy[f]
SCF (1)[b]	-1.9868
MCSCF (3)[b]	-2.0017
MRD-CI[c]	-2.0430
Variational (1)[d]	-2.0471(32)
SDCI(1035)[e]	-2.0583
FNQMC	-2.0872(42)

[a] R is the distance from the center of the H_3 equilateral triangle base to the apex H atom and r is the length of the side of the trianle.

[b] DZP basis set. Digits in parentheses are number of configurations.

[c] Reference [39].

[d] See Eq. (5.5) for definition.

[e] The calculation includes single and double excitations from a MCSCF wavefunction.

[f] Numbers in parentheses are the statistical uncertainties.

Table 5.6 C_{3v} character table.

C_{3v}	e	C_3^1	C_3^2	σ_1	σ_2	σ_3
A	1	1	1	1	1	1
E	2	-1	-1	0	0	0

Table 5.7 E representation of C_{3v} group

C_{3v}	e	C_3^1	C_3^2	σ_1	σ_2	σ_3
E_1	1 0	$-\frac{1}{2}$ $-\frac{\sqrt{3}}{2}$	$-\frac{1}{2}$ $\frac{\sqrt{3}}{2}$	1 0	$-\frac{1}{2}$ $\frac{\sqrt{3}}{2}$	$-\frac{1}{2}$ $-\frac{\sqrt{3}}{2}$
E_2	0 1	$\frac{\sqrt{3}}{2}$ $-\frac{1}{2}$	$-\frac{\sqrt{3}}{2}$ $-\frac{1}{2}$	0 -1	$\frac{\sqrt{3}}{2}$ $\frac{1}{2}$	$-\frac{\sqrt{3}}{2}$ $\frac{1}{2}$

Table 5.8 S_4 character table

S_4	$1(1^4)$	$6(2,1^2)$	$3(2^2)$	8(3,1)	6(4)*
a	1	1	1	1	1
b	3	1	-1	0	-1
c	2	0	2	-1	0
d	3	-1	-1	0	1
e	1	-1	1	1	-1

* The notation, x^y, where x is the length of the exchange section and y is the number of exchange sections, denotes a permutation operator. For example, (2,1sup2) represents the operator (a,b)(c)(d) that interchanges a and b, and retains c and d unchanged.

Caption

Fig. 5.1 Optimization of the electron-electron correlation function parameters a and b (see Eq. 7) of $H_2(X^1 \sum_g^+)$ where b is scaled by a factor of 10. The lower panel plots the variational energy vs the number of random walks during the optimization.

Fig. 5.2 Optimization of linear coefficients of the $H_2(X^1 \sum_g^+)$ wavefunction. The σ_g molecular orbital is formed with a basis set of 1S, 2S, and 2PZ where the 1S coefficient is set to unity. The lower panel plots the variational energy vs the number of random walks during the optimization.

Fig. 5.3 Optimization of linear coefficients of the $H_2(B^1 \sum_u^+)$ wavefunction. Both molecular orbitals (σ_g and σ_u) are formed with a basis set of 1S, 2S, and 2PZ where the 1S coefficients (σ_g, denoted by 1S 1) and 2S (σ_u, denoted by 2S 2) are set to unit. The lower panel plots the variational energy vs the number of random walks during the optimization.

Fig. 5.4 Optimization of the electron-electron correlation function parameters a and b (see Eq. 7) of Li_2. The lower panel plots the variational energy vs the number of random walks during the optimization.

Fig. 5.5 Pyramidal H_4 and the C_{3v} symmetry.

Fig. 5.6 Potential energy curves of pyramidal H_4 vs the distance

between H and the H_3 triangular base. The QMC trial wavefunctions of the E and A states are taken from a symmetry-constrained optimization. The dashed curves are from ref. 33.

Fig. 5.7 Young diagram (YD) of S_4 permutation group. Both ^1A and ^1E states of H_4 belong to YD-c. The lower part of the figure shows the two Young tableaux of the doubly degenerate self-conjugate YD-c.

OPTIMIZATION OF LINEAR COEFFICIENTS OF H2(X)

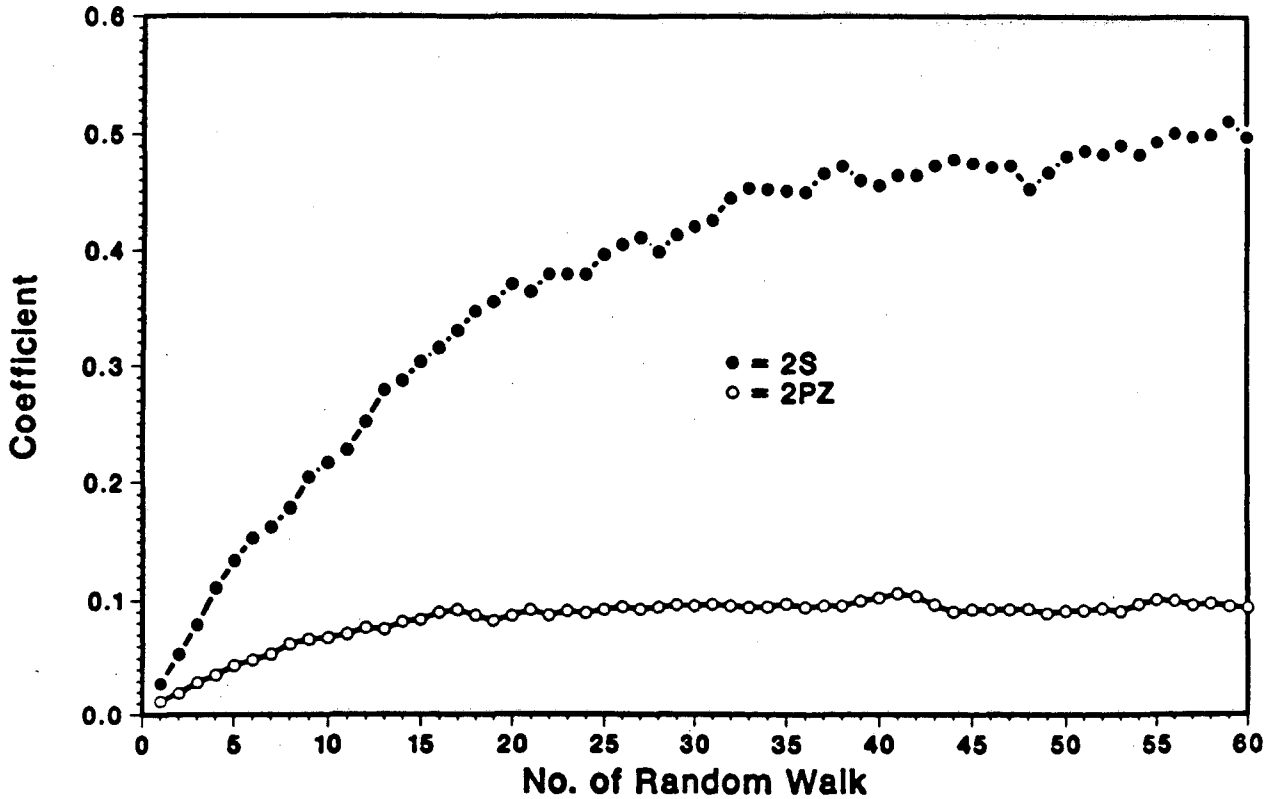

VARIATIONAL ENERGY OF H2(X)

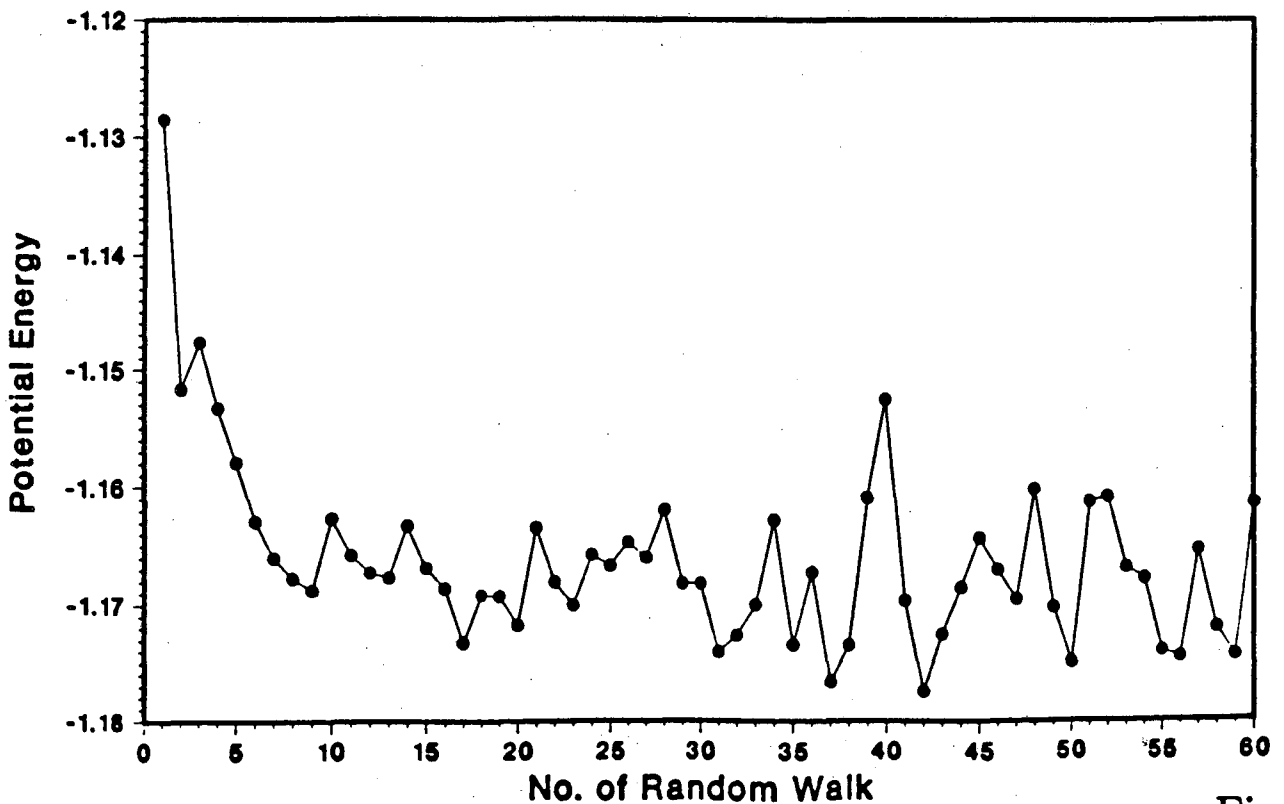

Fig. 5.1

e-e OPTIMIZATION FOR H2(X)

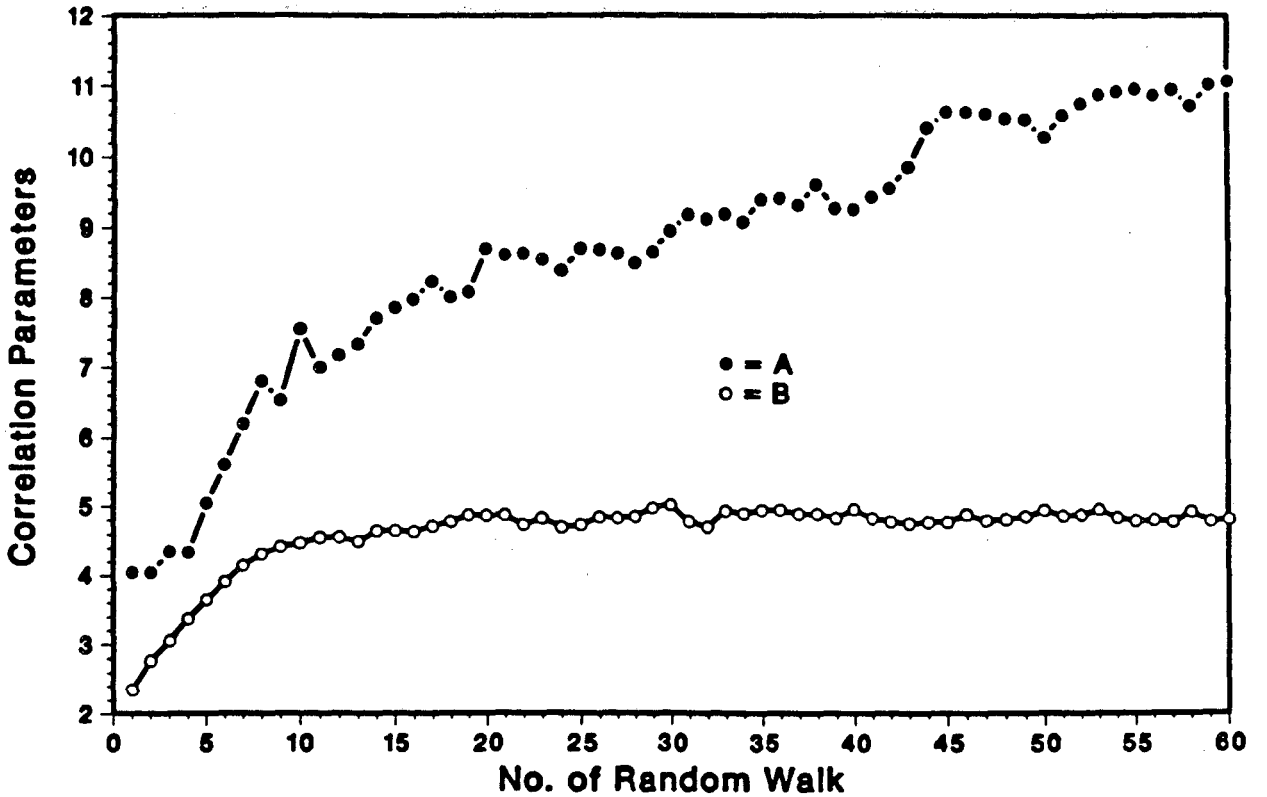

VARIATIONAL ENERGY OF H2(X)

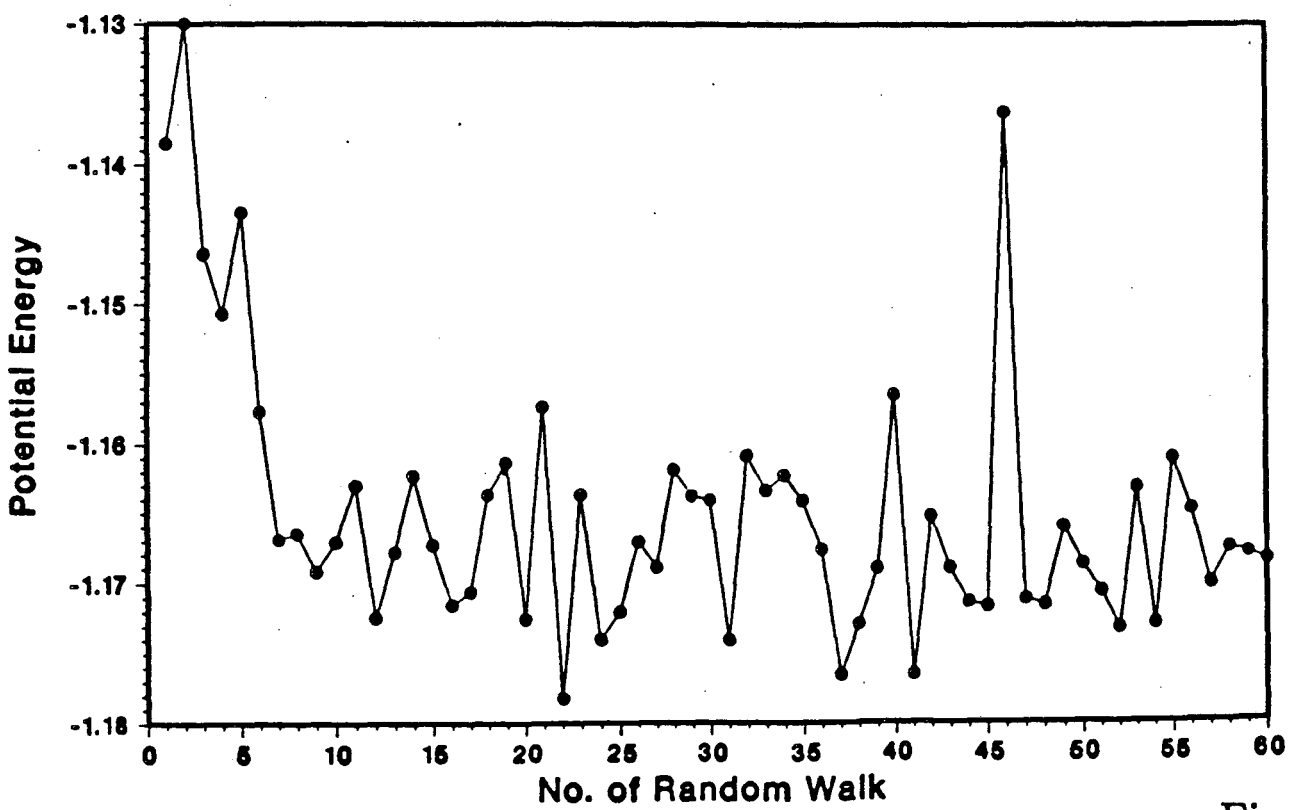

Fig. 5.2

OPTIMIZATION OF LINEAR COEFFICIENTS OF H2(B)

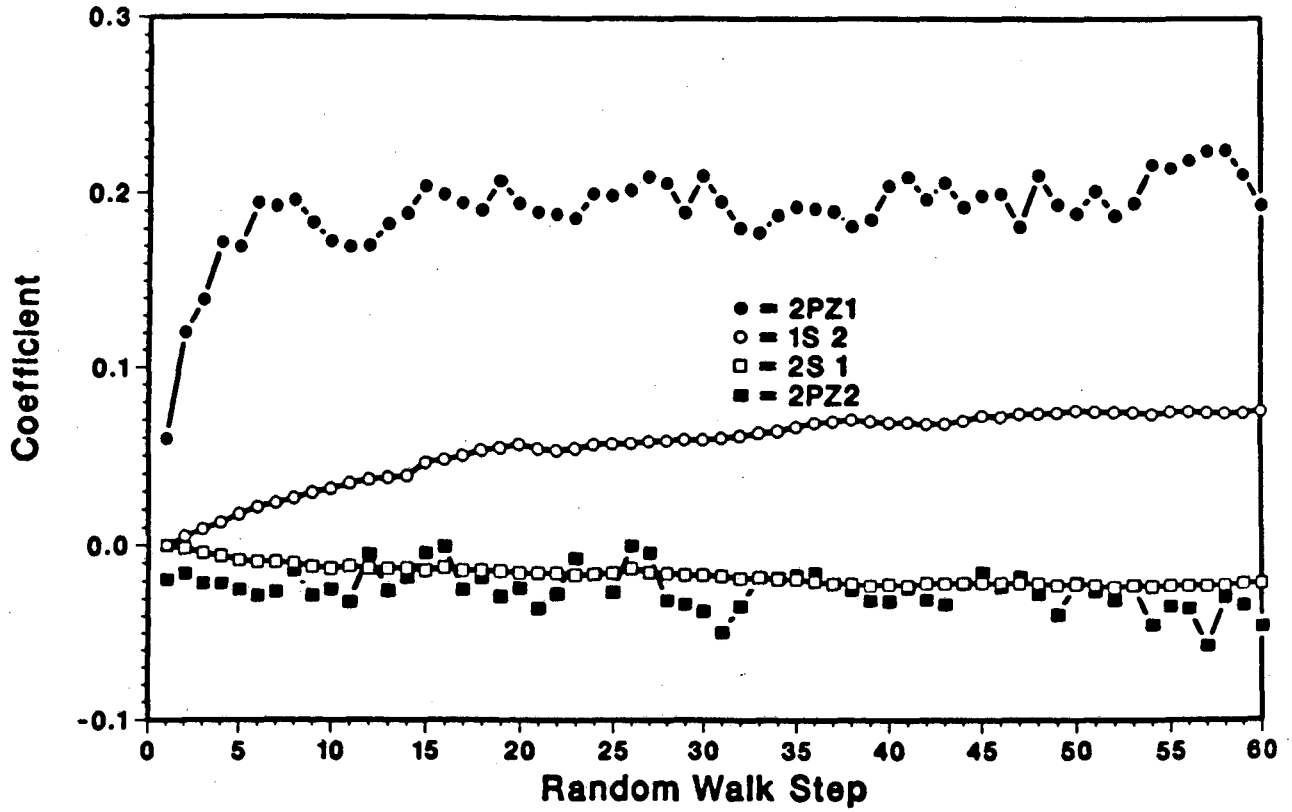

VARIATIONAL ENERGY OF H2(B)

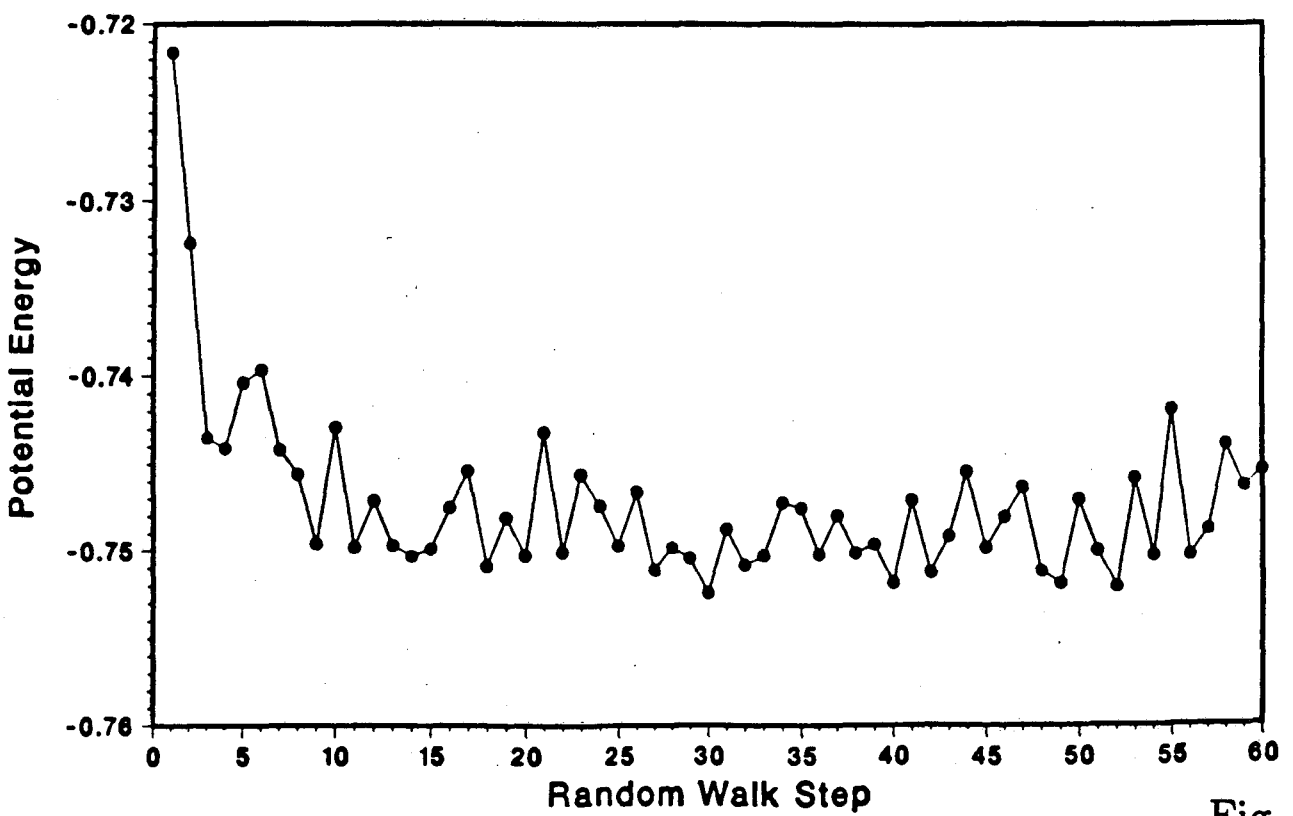

Fig. 5.3

e-e OPTIMIZATION FOR LI2

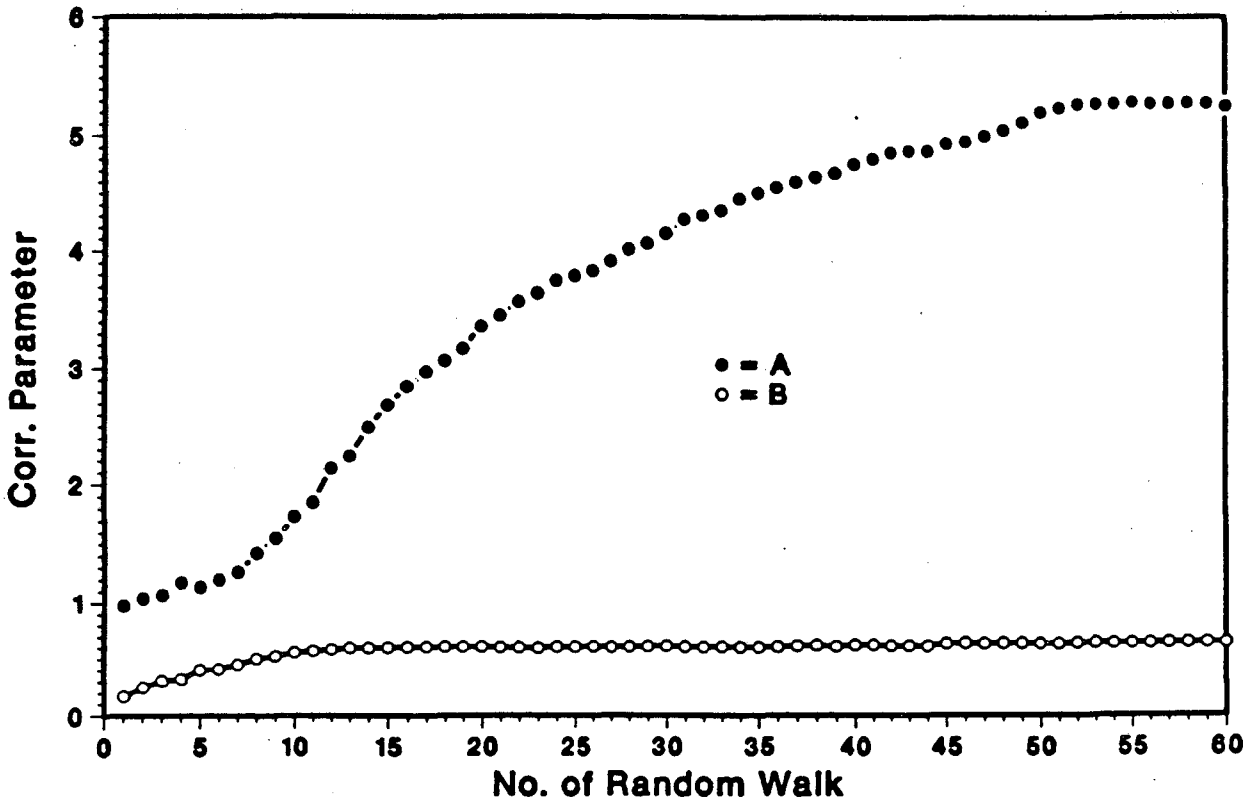

VARIATIONAL ENERGY OF LI2

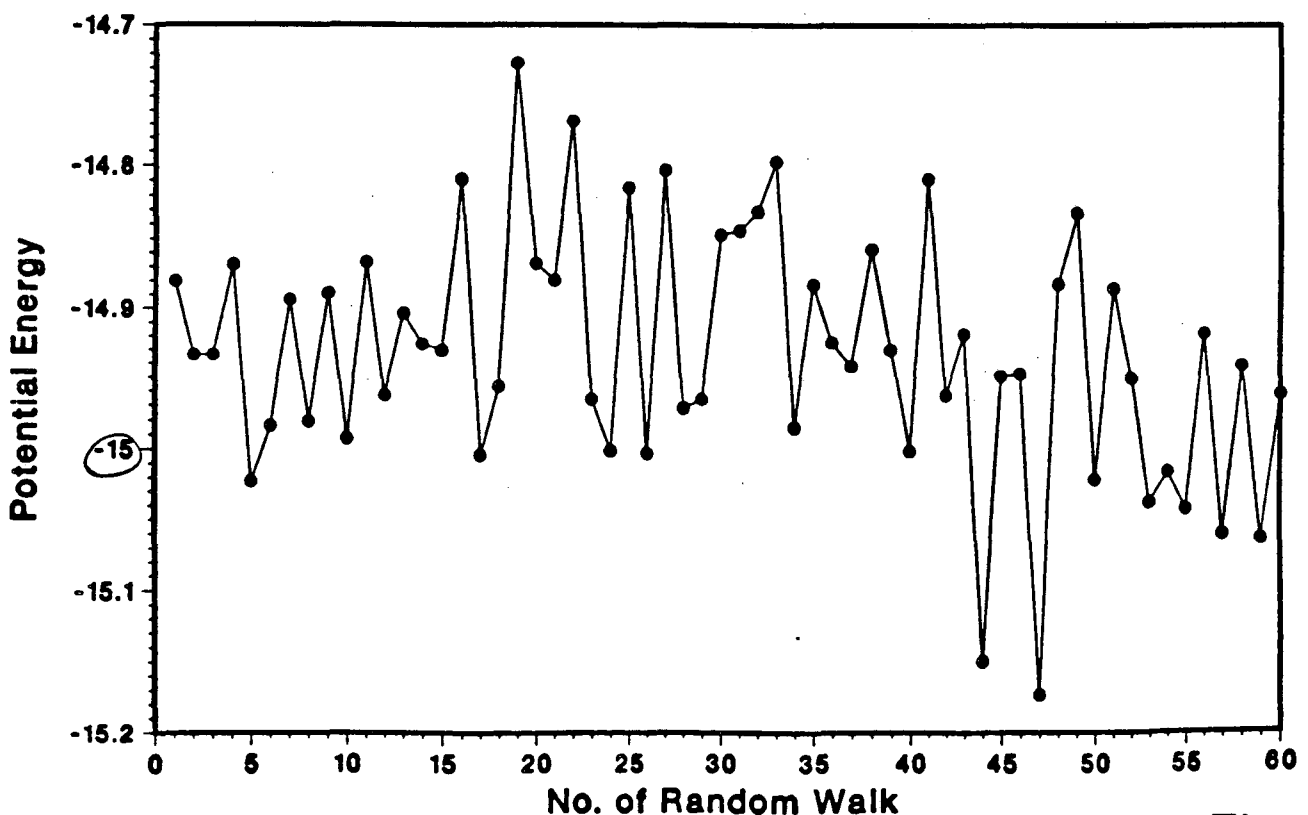

Fig. 5.4

POTENTIAL ENERGY OF PYRAMIDAL H4

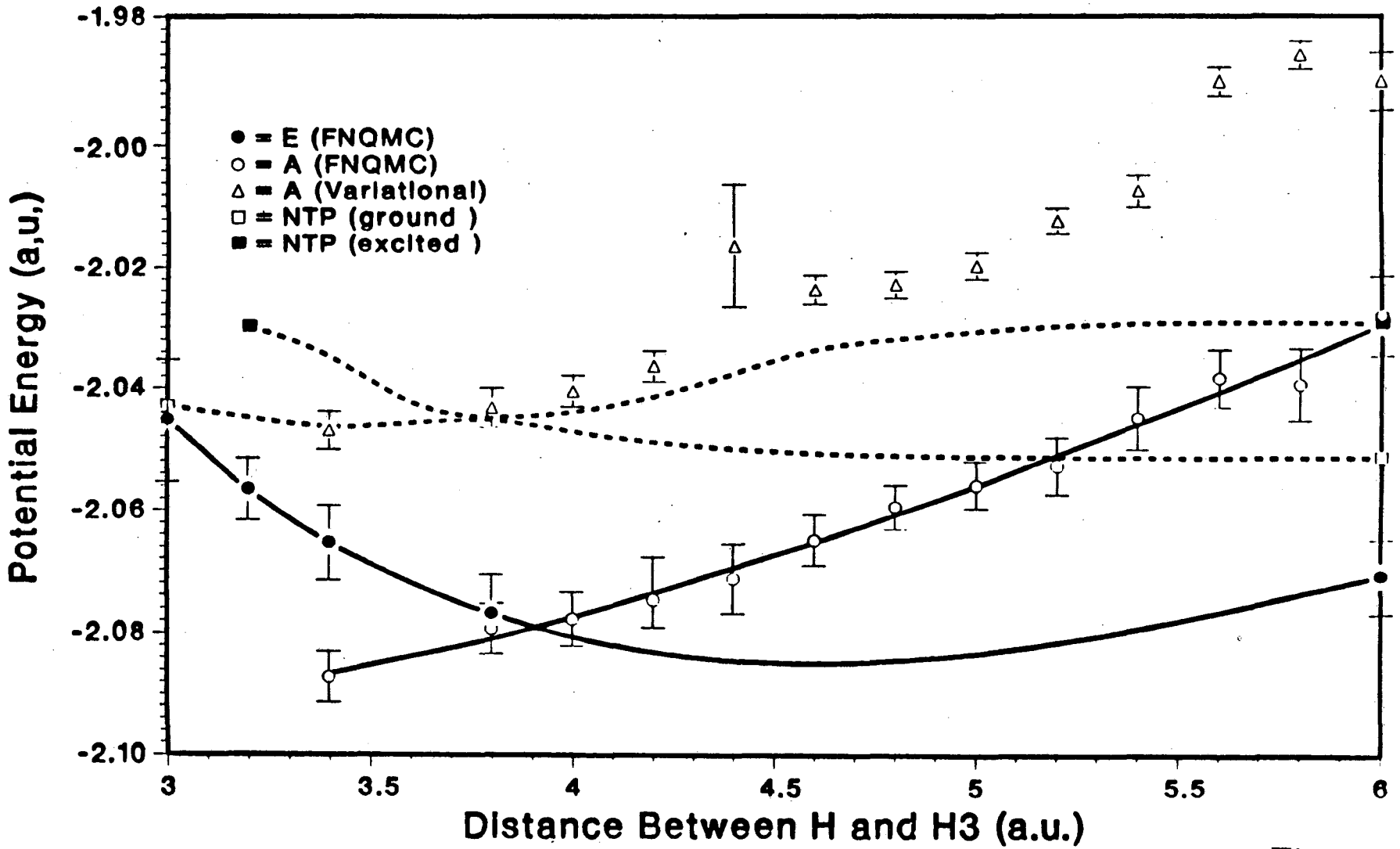

Fig. 5.5

LAWRENCE BERKELEY LABORATORY
TECHNICAL INFORMATION DEPARTMENT
1 CYCLOTRON ROAD
BERKELEY, CALIFORNIA 94720